Multiscale modeling of strain rate effects in FRP laminated composites

Liu, Y.

DOI
10.4233/uuid:92db8fa0-bba1-431a-866e-f05151753632

Publication date
2020

Document Version
Final published version

Citation (APA)
Liu, Y. (2020). *Multiscale modeling of strain rate effects in FRP laminated composites*. [Dissertation (TU Delft), Delft University of Technology]. https://doi.org/10.4233/uuid:92db8fa0-bba1-431a-866e-f05151753632

Important note
To cite this publication, please use the final published version (if applicable).
Please check the document version above.

Multiscale modeling of strain rate effects in FRP laminated composites

Multiscale modeling of strain rate effects in FRP laminated composites

Proefschrift

ter verkrijging van de graad van doctor
aan de Technische Universiteit Delft,
op gezag van de Rector Magnificus prof. dr. ir. T.H.J.J. van der Hagen,
voorzitter van het College voor Promoties

door

Yaolu Liu

Master in Civil Engineering,
geboren te Jishui, China

Dit proefschrift is goedgekeurd door de

promotor: prof. dr. ir. Lambertus J. Sluys
copromotor: dr. ir. Frans. P. van der Meer

Onafhankelijke leden:

Rector Magnificus,	voorzitter
Prof. dr. ir. Lambertus J. Sluys,	Technische Universiteit Delft
Dr. ir. Frans. P. van der Meer,	Technische Universiteit Delft
Prof. dr. Chiara Bisagni,	Technische Universiteit Delft
Dr. Martin Fagerström,	Chalmers University of Technology
Prof. dr. Stephen Hallett,	University of Bristol
Prof. dr. ir. Akke S. J. Suiker,	TU Eindhoven
Dr. ir. Jaap Weerheijm,	Technische Universiteit Delft
Prof. dr. Milan Veljkovic,	Technische Universiteit Delft, reservelid

Contents

Summary

Fiber reinforced polymer composites are increasingly used in impact-resistant devices, automotives, and aircraft structures due to their high strength-to-weight ratios and their potential for impact energy absorption. Dynamic impact loading causes complex deformation and failure phenomena in composite laminates. Moreover, the high loading rates in impact scenarios give rise to a significant change in mechanical properties (e.g. elastic modulus, strength, fracture energy) and failure characteristics (e.g. failure mechanisms, energy dissipation) of polymer composites. In other words, both mechanical deformation and failure are strain-rate dependent. The contributing mechanisms can be roughly classified as viscous material behavior, changes in failure mechanism, inertia effects and thermomechanical effects. These effects involve multiple length and time scales. In experiments it is difficult to isolate single mechanisms contributing to the overall rate-dependency. Therefore, it is difficult to quantify the contribution of each mechanism at different scales.

The aim of this thesis is to establish a multiscale numerical framework in which three of the contributing mechanisms, i.e. the viscous material behavior, changes in fracture mechanisms and inertia effects, can be investigated at different scales. The research in this thesis is divided into four parts, one related to the macroscale, where the composite material is treated as homogeneous, and three on exploring possibilities to include microscale information, taking into account the microstructure of fibers and matrix.

The macroscale study concerns investigation of a series of dynamic double cantilever beam (DCB) tests of a unidirectional fiber-reinforced polymer (FRP) composite laminate at different loading rates. A rate-dependent cohesive zone model and an interfacial thick level set (ITLS) model are used to reproduce the dynamic crack propagation and energy dissipation in the tests. It is found that the introduced rate-dependent cohesive zone model is capable of capturing the average crack propagation speed with a single set of material parameters. For the ITLS model a dynamics solution scheme is introduced which relates crack speed to energy release rate. It is found that this approach can provide a very good match with experimentally observed arrest and reinitiation phenomena with carefully calibrated parameters and it is concluded that the relation between crack speed and energy release rate is a useful ingredient for describing dynamic crack growth.

The following three parts of the work aim at connecting the macroscale to the microscale. Firstly, a dispersive multiscale model using the asymptotic homogenization technique is introduced to capture micro-inertia effects of composites. The homogenized macroscopic linear momentum equation is enriched with a micro-inertia term scaled by a so-called "dispersion tensor" that is determined by the composite microstructure and its elastic properties. Elastic wave propagation problems are studied and it is found that the dispersive multiscale model shows a considerable

improvement over the non-dispersive model in capturing the dynamic response of heterogeneous materials. The existence of a representative volume element (RVE) for unidirectional fiber-reinforced composites is tested by computing the homogenized properties for micromodels of different size. Convergence is found but only with a relatively large micromodel. Moreover, it is found that the convergence of the dispersion tensor is sensitive to the spatial distribution pattern.

Secondly, a numerical homogenization technique is developed for describing the contribution of the viscous properties of polymer resin on macroscopic transverse response of unidirectional composite plies. A step-by-step numerical homogenization procedure is introduced to calibrate a homogenized viscoelastic-viscoplastic (VE-VP) model. The response of the calibrated VE-VP model is compared against that of the RVE model for different loading scenarios. It shows that: (1) the homogenized model captures viscoelastic deformation, rate-dependent yielding, stress relaxation and unloading behavior of the polymer composite well, although the assumptions of a single plastic Poisson's ratio and pure isotropic hardening are over-simplifications of the composite behavior; (2) the novel step-by-step numerical homogenization procedure provides an efficient and accurate way for obtaining material parameters of a VE-VP model.

Thirdly, an embedded cell model of the single-edge-notched-tension (SENT) geometry is used to study the mode-I dynamic fracture energy and failure mechanisms of fiber-reinforced polymer composites. In the vicinity of the initial notch tip, a composite microstructure of repeating RVEs is embedded in a homogenized medium. A series of SENT tests is simulated for different loading velocities and specimen sizes while the dynamic energy release rate is evaluated using the dynamic version of the J-integral. The influence and interaction of loading rate, time-dependent material nonlinearity, structural inertia and matrix ligament bridging on the failure mechanisms and the fracture toughness are evaluated. It is found that with the given material parameters and studied loading rate range, the failure type is brittle with many microcracks but limited plasticity in the fracture process zone and a trend of increasing brittleness for higher strain rates is observed. The inertia effect is evident for higher strain rates but it is not dominating the response. An R-curve in the average sense is found to be strain-rate independent before the fracture process zone is fully developed and afterwards a velocity-toughness mechanism is dictating crack growth.

Samenvatting

Vezel versterkte kunststof composieten worden gebruikt in de auto en vliegtuig industrie vanwege hun hoge sterkte-gewichtsverhouding en hun vermogen om impact energie te absorberen. Dynamische belasting als gevolg van impact resulteert in complexe vervorming en falen van de composieten. Vooral de hoge belastingsnelheid in impact situaties leidt tot een significante verandering in mechanische eigenschappen (b.v. elasticiteitsmodulus, materiaal sterkte, scheur energie) en faal eigenschappen (b.v. faal mechanismes, energie dissipatie) in polymeer composiet. In andere woorden, zowel de mechanische deformatie en faal eigenschappen zijn rek snelheid afhankelijk. De bijdragende mechanismes kunnen verdeeld worden in viskeus materiaal gedrag, veranderingen in faal mechanismes, inertie effecten en thermo-mechanische effecten. Deze effecten zijn betrokken over meerdere lengte- en tijdsschalen. Het is moeilijk om in een experiment de bijdrage op de totale rek-afhankelijkheid van één enkel mechanisme te isoleren. Dit maakt het lastig om de bijdrage van elk mechanisme te kwantificeren voor verschillende schalen.

Het doel van deze thesis is het ontwikkelen van een multi-schaal numerieke methode waarmee de drie mechanismes: viskeus materiaal gedrag, veranderingen in faal mechanismes en inertie effecten, kunnen worden onderzocht in verschillende schalen. Het onderzoek in deze thesis is onderverdeeld in vier delen. Een daarvan is gerelateerd aan de macro-schaal, waar het composieten materiaal is behandeld als homogeen. De andere drie delen onderzoeken de mogelijkheid in het toevoegen van micro-schaal informatie, waarbij de microstructuur van de vezels en het matrix materiaal wordt meegenomen.

De macro-schaal studie onderzoekt een serie van *double cantilever beam* (DCB) testen gemaakt van uni-directioneel vezel versterkt polymeer composiet voor verschillende belastingsnelheden. Een snelheidsafhankelijk *cohesive zone* (CZ) model en een *interfacial thick level set* (ITLS) model zijn gebruikt om de dynamische scheur propagatie en energie dissipatie te reproduceren zoals geobserveerd in de experimenten. Het CZ model kan de gemiddelde scheurgroei snelheid reproduceren met een enkele set van materiaal parameters. Voor het ITLS model is een dynamische oplossingsschema geïntroduceerd welke de scheursnelheid relateert aan de *energy release rate* (ERR). Deze methode leidt met zorgvuldig gekalibreerde parameters tot een zeer goede overeenkomst met experiment op het gebied van scheur-stops en het opnieuw initialiseren van scheuren. Hierbij is geconcludeerd dat de relatie tussen scheurgroei snelheid en ERR zeer nuttig is om het dynamische scheurgroei proces te beschrijven.

De volgende drie delen van het onderzoek richten zich op het verbinden van de macroschaal met de microschaal. Ten eerste, een dispersie multi-schaal model met een asymptotische homogenisatie techniek is geïntroduceerd om de effecten van micro-inertie van composieten te simuleren. De gehomogeniseerde macroscopische

lineaire momentum relatie is verrijkt met een micro-inertie contributie geschaald bij een dispersie tensor welke is bepaald door de composieten micro-structuur en zijn elastische eigenschappen. Elastische golf propagatie problemen zijn bestudeerd, en het is gevonden dat het dispersie multi-schaal model een aanzienlijke verbetering is voor het modelleren van het dynamische gedrag van heterogene materialen ten opzichte van een non-dispersie model. Het bestaan van een representatief volume element (RVE) voor uni-directioneel vezel versterkte composieten is getest door de homogene eigenschappen van micromodellen van verschillende grote te berekenen. Convergentie werd alleen gevonden met een relatief groot micromodel. Daarnaast, convergentie van de dispersie tensor is gevoelig voor het ruimtelijk verdelingspatroon.

Ten tweede, een numerieke homogenisatie techniek is ontwikkeld welke de bijdrage van de viskeuze eigenschappen van het polymeer hars op de macroscopische dwars reactie van uni-directioneel composieten kan beschrijven. Een homogenisatie procedure is geïntroduceerd om het gehomogeniseerde viskeus elastisch-viskeus plastisch (VE-VP) model te kalibreren. De reactie van het gekalibreerde VE-VP model is vergeleken met het RVE model voor verschillende belastingscenario's. Het is aangetoond dat: (1) het gehomogeniseerde model kan viskeuze deformatie, snelheid-afhankelijk vloeien, spannings vermindering en belasting verminderingsgedrag van polymeer composieten goed simuleren, hoewel, de aannames van een enkele plastische Poisson ratio en pure isotropische verharding een over simplificatie zijn van het composieten gedrag; (2) de nieuw geïntroduceerde numerieke homogenisatie procedure geeft een efficiënte en nauwkeurige methode om de materiaal parameters voor het VE-VP model te verkrijgen.

Ten derde, een ingebed cel model van een *single-edge-notched-tension* (SENT) is gebruikt voor het bestuderen van de mode-I dynamische scheur energie en faal mechanismes van vezel versterkte polymeer composieten. In de nabijheid van de initiële inkepingspunt, een composieten microstructuur van herhalende RVEs is ingebed in een gehomogeniseerd medium. Een serie van SENT testen is gesimuleerd voor verschillende belastingsnelheden en proefstuk afmetingen terwijl de dynamische ERR is geëvalueerd gebruikmakende van de dynamische J-integraal. De invloed en interactie van de belastingsnelheid, tijds-afhankelijke materiaal nonlineariteit, structurele inertie en matrix vezel overbrugging op de faal mechanismes en de scheur taaiheid is geëvalueerd. Het is gevonden dat met de gegeven materiaal parameters en bestuurde belastingsnelheid bereik, resulteert in een bros faalmechanisme met veel microscheuren, hoewel beperkte plasticiteit in het scheur proces gebied en een trend van toenemende brosheid voor hogere rek snelheid is geobserveerd. De inertie effect is zichtbaar voor hogere rek snelheden, maar is niet reactie dominerend. Uit de studie volgt dat een algemene R-curve is rek snelheid onafhankelijk voordat het scheur proces gebied volledig ontwikkeld is waarna een snelheid-taaiheid mechanisme de scheurgroei controleert.

1

Introduction

1.1. Background

Fiber reinforced polymer composites are increasingly used in impact-resistant devices, automotives, aircraft structures due to their potential for high strength-to-weight ratios and impact energy absorption. The multiscale structure of a composite laminate is shown in Fig. 1.1. At the macroscale, the composite laminate is observed as a homogeneous structure while at the mesoscale it can be seen that the laminate consists of a number of unidirectional plies. At the microscale, a typical microstructure is found with fibers embedded in a polymer resin.

Impact (dynamic) loadings can result in complex deformation and failure behavior in composite laminates. For instance, the impact response of laminated composites can exhibit complex failure mechanisms with various forms of damage such as matrix cracks, delaminations and fiber breakages at various locations in the laminate (see Figure 1.2). Importantly, a high loading rate generated by impact loading can cause a significant change of mechanical properties (e.g. elastic modulus, strength, fracture energy) and failure mechanisms for both thermoset and thermoplastic fiber reinforced polymer composites [2, 3].

The underlying mechanisms of the observed rate-dependent deformation and failure of composite laminates take place among multiple length and time scales. The contributing mechanisms can be roughly classified as:

- Viscosity of composite constituents (polymer, fiber and interfaces) [5, 6].
- Rate-dependency of the fracture mechanism as it is constituted by the different failure processes (e.g. fiber failure with fiber pullout, matrix damage, fiber/matrix interface failure) occurring at microscale level under different loading rates [3, 7, 8].
- inertia effects characterized as inertia resistance against rapid deformation, damage formation and crack propagation. Due to material heterogeneity,

1

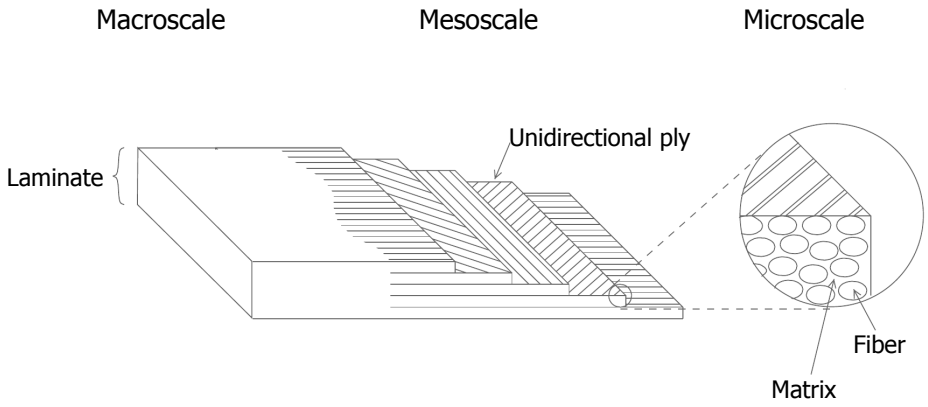

Figure 1.1: Three levels of observation for a composite laminate [1]

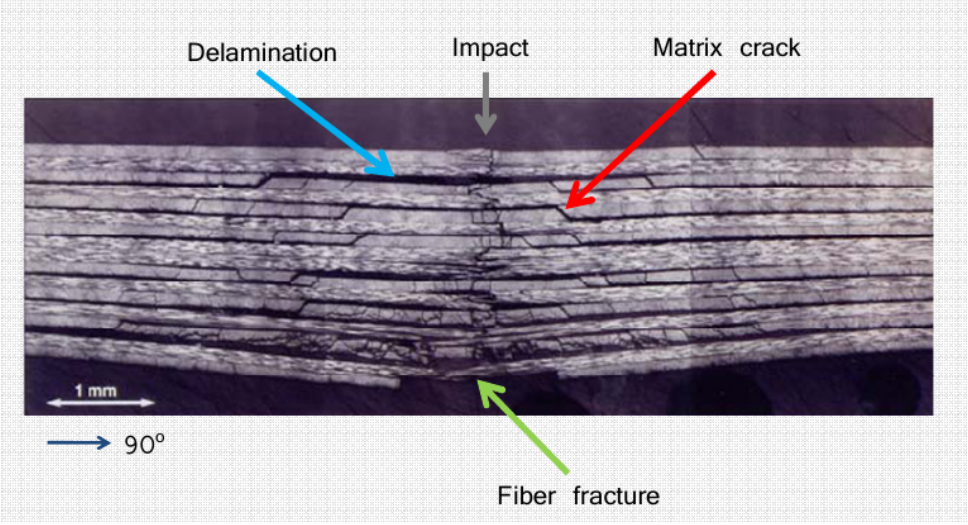

Figure 1.2: Different types of impact induced damage in a [(0/90)4]s Carbon/Epoxy laminate [4]

micro-inertia effects also arise as a result of wave reflection and transmission occurring at the interfaces between the constituents, which can result in complex spatiotemporal scenarios of damage and failure evolution, initiated at multiple spots [9–12].

- thermomechanical dissipation as a transition from isothermal to adiabatic deformation and failure process is expected for increasing loading rate [13, 14].

1.2. Aim of the thesis

In experiments it is hard to isolate single mechanisms contributing to the rate-dependency. The aim of this thesis is to establish a multiscale numerical framework where three of the contributing mechanisms, i.e. inertia effects, the viscous material behavior, and microscale failure pattern, can be investigated at different length scales. This multiscale numerical framework should be capable of including components used for describing each mechanism with enough detail while have lower computational cost than direct numerical simulation models. With this multiscale framework we should be able to quantify the contribution of each mechanism independently and to study the interaction between these mechanisms. In the remainder of this chapter an overview of the state of the art is presented. It is noted that special attention is put on the establishment of the numerical framework rather than calibration of material parameters for a specific type of polymer composites.

1.3. Experimental characterization

Various experimental setups have been employed for investigating the dynamic response of composites, such as the Charpy pendulum, the drop weight, and the split Hopkinson bar. These setups are designed to generate impact loads focusing on different test rates. A variety of contradictory observations and conclusions have resulted from these experimental studies [15]. It has been found that the dynamic deformation properties (e.g. stiffness modulus, strength, ultimate strain) of composites can show evident positive rate-dependency, rate-insensitive behavior or negative rate-dependency, depending on the composite system (the type of fiber and matrix), the test rate range, loading type (tensile, compressive, shear, flexural etc.) and load direction (longitudinal, transverse or off-axis) [16–19].

One way to define loading rate is to use the time rate of stress intensity factor $\dot{K}_I$ and it can be computed by using the equation $\dot{K}_I = K_{Id}/t_f$, where K_{Id} is the dynamic initiation toughness and t_f is the time spent before crack initiation. Table 1.1 shows a summary of commonly used experimental techniques and the corresponding range of loading rate. Most of the experimental studies on interlaminar cracking are focused on the determination of rate-dependent mode-I interlaminar fracture energy (or toughness), as it is the most basic fracture mode [7, 20–22]. No universal trend in the effect of increased loading rate on the toughness is found [23].

Loading method	Loading rate $\dot{K}_I$	Experimental technique
Quasistatic loading	$< 10^4$ MPa $\sqrt{\mathrm{m}}$/s	Servohydraulic testing machine
Dynamic loading	10^5 MPa $\sqrt{\mathrm{m}}$/s	Charpy impact and drop-weight impact
Stress-wave loading	$10^6 - 10^7$ MPa $\sqrt{\mathrm{m}}$/s	Hopkinson bar apparatus
Shock-wave loading	$> 10^8$ MPa $\sqrt{\mathrm{m}}$/s	Plane impact test

Table 1.1: Experimental techniques for dynamic fracture tests and their loading rate ranges [24]

1.4. Rate-dependent deformation and failure

Experimental tests of polymer composites under different loading types, such as fatigue, impact etc., reveal that polymer composites can show evident viscoelastic deformation and viscoplastic flow before damage and failure emerge [5]. The underlying mechanism of the viscoelastic and viscoplastic behavior of polymer composites is dominated by the viscosity of the polymeric matrix [5, 25]. The polymeric matrix typically develops pressure-dependent plastic yielding with the motion of segments of chain molecules, which are strain-rate and temperature dependent as well. According to Eyring [26], the deformation of a polymer is a thermally activated rate process involving the motion of segments of chain molecules over potential barriers. The macroscopic deformation results from basic processes that are either intermolecular (e.g. chain-sliding) or intramolecular (e.g. a change in the conformation of the chain), whose frequency depends on the ease with which a chain segment can surmount a potential energy barrier. Applying a stress effectively lowers the activation barrier for these jumps which leads to a coordinated motion known as yielding. The rate of change of plastic flow is therefore related to the applied stress. Therefore, viscoelastic and viscoplastic constitutive models have been developed to describe the constitutive behavior of polymers [27–29]. For instance, in Rocha et al. [27], a viscoelastic-viscoplastic constitutive model is developed for an epoxy resin (see Fig. 1.3). In this model, the elastic behavior is represented by a generalized Maxwell model consisting of n parallel Maxwell elements connected along with an extra isolated long-term spring. In each Maxwell element, a spring with modulus E_i and a dashpot with viscosity parameter η_i are connected in series. The plastic behavior is represented by a sliding element with yield stress σ_y and a dashpot with viscosity parameter η_p. Overstress is allowed to develop due to the dashpot component that is placed in parallel to the sliding element. The reinforcement inclusions, e.g. tough particles or carbon fiber, are usually much stiffer and more brittle than the surrounding matrix and the mechanical properties of the inclusions are barely rate-sensitive. The interface between inclusion and matrix is usually very complex which may involve both physical and chemical bonding [30, 31].

Failure in composites is also a rate-dependent process occurring across multiple length scales and time scales. For instance, for quasi-static tests delamination is often dominated by fiber/matrix interface failure while resin rich brittle fracture zones have been found more dominant in dynamic tests [32]. The extent of plastic deformation may decrease with increased loading rate, which represents a

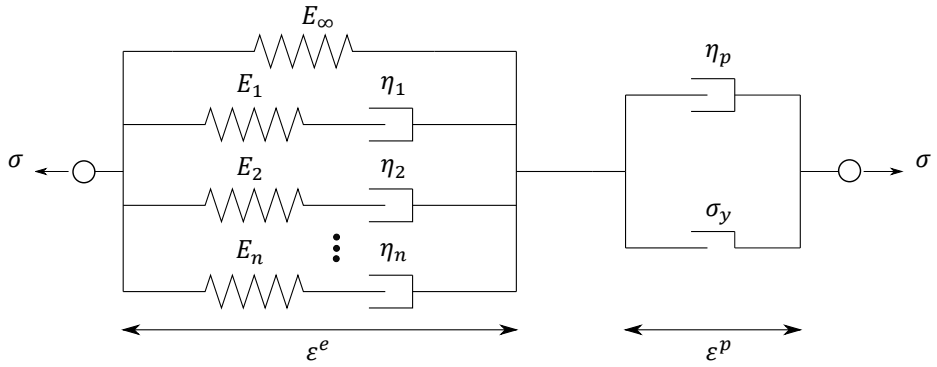

Figure 1.3: Schematic representation of the viscoelastic-viscoplastic polymer model in one-dimension.

ductile-to-brittle transition in the fracture process zone. These observations have motivated the development of rate-dependent cohesive zone models in which rate-dependency of the cohesive strength and the fracture energy are introduced, e.g. see May [33]. Alternatively, a phenomenological relation between the dynamic fracture energy G_c and the crack speed V has been proposed and implemented in numerical models [34, 35]. Experimental studies show that for pure polymeric matrix, corresponding to different levels of propagation velocity, the crack surface roughness is observed to demonstrate different features since materials in the fracture process zone might experience high strain-rate plasticity, microcrack nucleation, thermomechanical interaction and other complex deformation/failure mechanisms [35, 36]. Besides, in laminated composites due to fiber bridging behind the crack tip, the fracture toughness can increase for a certain distance of crack growth (see Fig. 1.4). As shown in Fig. 1.5, with the increase of crack speed, the crack surface appears first to be almost flat (mirror regime), after which a rougher surface with conic marks appears (mist regime), and finally (micro)branching takes place (hackle regime). The increase of the apparent fracture toughness with crack extension is usually described by a function of crack growth resistance vs. crack extension, i.e. the so-called R-curve [37].

1.5. Homogeneous model and multiscale model

To quantify the rate-dependency of composites, using numerical models based on the finite element method (FEM) is a good approach. An implicit dynamic analysis with a fine FEM mesh of the details of a composite microstructure with well calibrated rate-dependent constitutive laws is potentially very accurate in capturing the mechanical response of composite laminates. However, considering that the diameter of a fiber is usually around 5-50 μm, the computational cost of an FEM model with the complete microstructure of a composite laminate is prohibitively high. A homogeneous model or a multiscale model using a homogenization technique improves the feasibility of the computational approach by reducing the computational cost while maintaining an adequate level of accuracy (see Fig. 1.6).

1

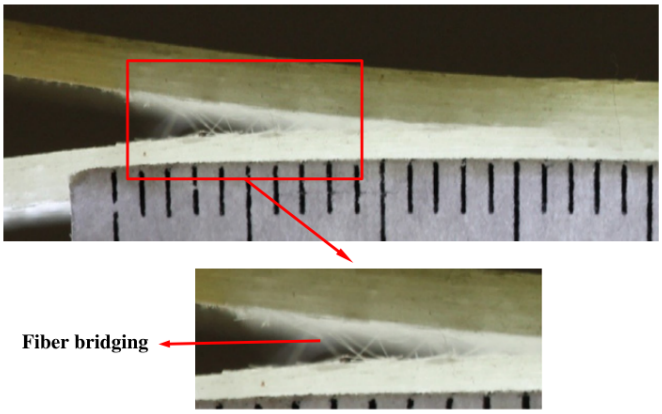

Figure 1.4: Enlarged bridging zone in unidirectional double cantilever beam (DCB) specimen [37]

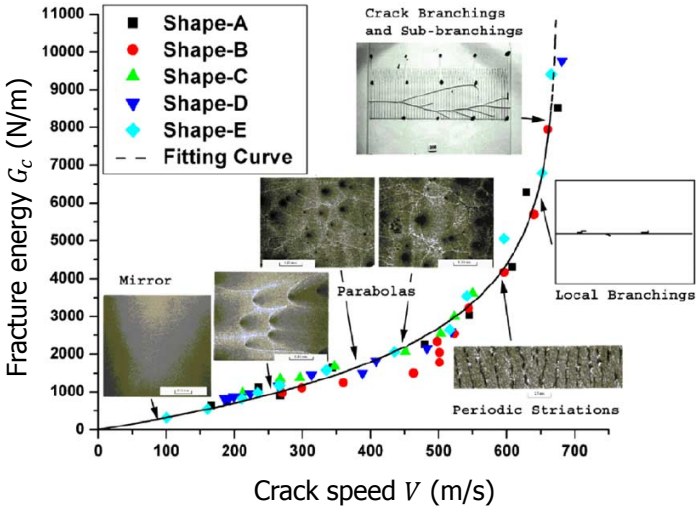

Figure 1.5: Fracture energy G_c and the fracture characteristics corresponding to different crack speed regions for a Polymethyl Methacrylate (PMMA) plate [35]

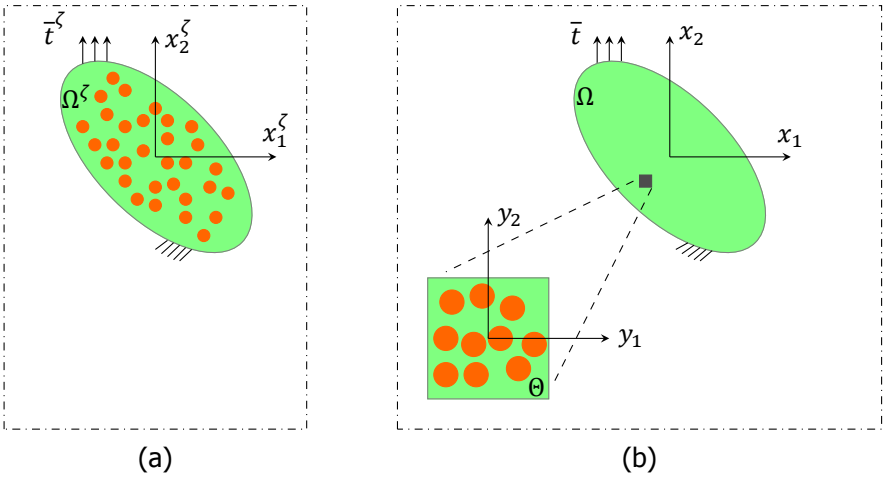

Figure 1.6: Problem statement. (a) original composite problem; (b) equivalent two-scale problem statement.

The rigorous way to consider a complex random microstructure or material nonlinearity is through representative volume element (RVE) based multiscale approaches. Initiated by Hill [38], an RVE can be defined as a characteristic sample of heterogeneous material. It should be large enough to contain sufficient composite micro-heterogeneities in order to be representative but it should be much smaller than the size of the macroscopic structure. RVE based homogenization methods can be divided roughly into: mathematical (asymptotic) homogenization, computational homogenization and numerical homogenization.

The mathematical homogenization method represents the physical fields by asymptotic expansion in powers of a small parameter, which is the ratio of a characteristic size of the heterogeneities and a measure of the macrostructure. By using asymptotic expansions, it allows a decomposition of the final solution into a series of governing equations, which can be evaluated successively from a sequence of (initial) boundary-value problems within an RVE domain. Afterwards, the effective properties are obtained through volume averaging operations [39–41].

In the computational homogenization method, the local macroscopic constitutive response is derived from the solution of a microstructural boundary value problem in an RVE and information of the microscale is passed to the macroscale by bridging laws. There is no need to define any explicit format of the macroscopic constitutive equations in this method since the macroscopic stress is determined from the mechanical deformation state of the associated RVE [42–44].

For the numerical homogenization method, a macroscopic canonical constitutive law is assumed a priori for the macroscale model. The material parameters are then determined from the averaged microscopic stress-strain fields calculated from the computational analysis of an RVE model subjected to fundamental load cases [45–47]. This method greatly reduces the computational cost as the calibrated macro-

scopic constitutive model can be used for modeling composite structures without explicitly representing the microstructure.

Finally, it is possible to abandon the RVE concept and use a detailed micro-model embedded in a homogenized model in concurrent multiscale analysis. This approach is particularly interesting for crack growth problems, where the region of interest is relatively small, while localization of deformations breaks the concept of separation of scales.

1.6. Outline of the thesis

In this thesis, various numerical methods are proposed and tested for describing the rate-dependent deformation and failure of composite laminates under dynamic (impact) loading. There is no single numerical framework found that can completely describe dynamic crack growth in composites for all relevant loading rates. Instead, the mechanisms of strain-rate dependent of composites across different scales are studied by a number of numerical techniques at different scales of observation. Starting from Chapter 2, the strain-rate effect of delamination crack growth is investigated at macroscale. In this chapter, a rate-dependent cohesive zone model (CZM) and an interfacial thick level set (ITLS) model are used to capture the rate-dependency of the fracture energy and stable/unstable dynamic crack propagations observed in dynamic double cantilever beam (DCB) tests of a carbon/PEEK composite laminate. This study uses a homogeneous model without taking the composite microstructure explicitly into account and the introduced rate-dependency laws are phenomenological.

Considering the multiscale nature of underlying phenomena for the strain-rate mechanism studied in Chapter 2, it has been found that microscale mechanisms need to be better understood. In this thesis, special attention is put on inertia effects, viscous material behavior and dynamic fracture energy. Chapter 3 discusses micro-inertia effects of composites with a dispersive homogenization model employing mathematical homogenization concepts. The applicability of the introduced multiscale model is examined by studying the existence of an RVE with a statistical analysis. The aim is to introduce a numerical model which can capture the influence of the microstructure on stress wave propagation phenomenon. In Chapter 4, a numerical homogenization model is developed to derive a homogenized viscoelastic-viscoplastic model for the transverse response of a fiber reinforced composite material. This model allows for quantification of the rate-dependent deformation of polymer composites. In Chapter 5, the mode-I dynamic fracture energy and failure mechanisms of fiber-reinforced polymer composites are investigated with an embedded cell model of the single-edge-notched-tension (SENT) geometry. The thesis ends with concluding remarks on the research as well as recommendations for future research.

References

[1] F. P. van der Meer, *Mesolevel Modeling of Failure in Composite Laminates: Constitutive, Kinematic and Algorithmic Aspects,* Archives of Computational

Methods in Engineering **19**, 381 (2012).

[2] J. T. Fan, J. Weerheijm, and L. J. Sluys, *Compressive response of a glass–polymer system at various strain rates,* Mechanics of Materials **95**, 49 (2016).

[3] O. I. Okoli, *The effects of strain rate and failure modes on the failure energy of fibre reinforced composites,* Composite Structures **54**, 299 (2001).

[4] L. Iannucci, *Dynamic delamination modelling using interface elements,* Computers & Structures **84**, 1029 (2006).

[5] J. Fitoussi, M. Bocquet, and F. Meraghni, *Effect of the matrix behavior on the damage of ethylene–propylene glass fiber reinforced composite subjected to high strain rate tension,* Composites Part B: Engineering **45**, 1181 (2013), 0812.0143v2 .

[6] Z. Jendli, F. Meraghni, J. Fitoussi, and D. Baptiste, *Multi-scales modelling of dynamic behaviour for discontinuous fibre SMC composites,* Composites Science and Technology **69**, 97 (2009).

[7] L. F. M. Leite, B. M. Leite, V. L. Reis, N. N. Alves da Silveira, and M. V. Donadon, *Strain rate effects on the intralaminar fracture toughness of composite laminates subjected to tensile load,* Composite Structures **201**, 455 (2018).

[8] J. Hoffmann, H. Cui, and N. Petrinic, *Determination of the strain-energy release rate of a composite laminate under high-rate tensile deformation in fibre direction,* Composites Science and Technology **164**, 110 (2018).

[9] Y. Chen and S. Ghosh, *Micromechanical analysis of strain rate-dependent deformation and failure in composite microstructures under dynamic loading conditions,* International Journal of Plasticity **32-33**, 218 (2012).

[10] E. E. Nishida, *Distinguishing inertia effects from the intrinsic mechanical behavior of soft materials at high strain rates by Kolsky bar experiments*, Ph.D. thesis, Purdue University (2010).

[11] Z.-P. Wang and C. T. Sun, *Modeling micro-inertia in heterogeneous materials under dynamic loading,* Wave Motion **36**, 473 (2002).

[12] T. Hui and C. Oskay, *A high order homogenization model for transient dynamics of heterogeneous media including micro-inertia effects,* Computer Methods in Applied Mechanics and Engineering **273**, 181 (2014).

[13] Z. Li and J. Lambros, *Dynamic thermomechanical behavior of fiber reinforced composites,* Composites Part A: Applied Science and Manufacturing **31**, 537 (2000).

[14] J. Wang, L. Wen, J. Xiao, T. Liang, X. Hu, and P. Li, *The mechanical properties and constitutive model of two woven composites including the influences of temperature, strain rate and damage growth,* Composites Part B: Engineering **161**, 502 (2019).

[15] G. C. Jacob, J. M. Starbuck, J. F. Fellers, S. Simunovic, and R. G. Boeman, *Strain rate effects on the mechanical properties of polymer composite materials,* Journal of Applied Polymer Science **94**, 296 (2004).

[16] R. L. Sierakowski, *Strain Rate Effects in Composites,* Applied Mechanics Reviews **50**, 741 (1997).

[17] T. Schmack, T. Filipe, G. Deinzer, C. Kassapoglou, and F. Walther, *Experimental and numerical investigation of the strain rate-dependent compression behaviour of a carbon-epoxy structure,* Composite Structures **189**, 256 (2018).

[18] B. Sun, Z. Niu, L. Zhu, and B. Gu, *Mechanical behaviors of 2D and 3D basalt fiber woven composites under various strain rates,* Journal of Composite Materials **44**, 1779 (2010).

[19] M. M. Shokrieh and M. J. Omidi, *Compressive response of glass–fiber reinforced polymeric composites to increasing compressive strain rates,* Composite Structures **89**, 517 (2009).

[20] M. May and T. Lässig, *Rate-dependent mode I delamination in ballistic composites – Experiment and simulation,* Composite Structures **180**, 596 (2017).

[21] P. Kuhn, G. Catalanotti, J. Xavier, M. Ploeckl, and H. Koerber, *Determination of the crack resistance curve for intralaminar fiber tensile failure mode in polymer composites under high rate loading,* Composite Structures **204**, 276 (2018).

[22] P. Kuhn, G. Catalanotti, J. Xavier, P. P. Camanho, and H. Koerber, *Fracture toughness and crack resistance curves for fiber compressive failure mode in polymer composites under high rate loading,* Composite Structures **182**, 164 (2017).

[23] G. C. Jacob, J. M. Starbuck, J. F. Fellers, S. Simunovic, and R. G. Boeman, *The effect of loading rate on the fracture toughness of fiber reinforced polymer composites,* Journal of Applied Polymer Science **96**, 899 (2005).

[24] F. Jiang and K. S. Vecchio, *Hopkinson bar loaded fracture experimental technique: A critical review of dynamic fracture toughness tests,* Applied Mechanics Reviews **62**, 060802 (2009).

[25] M. Shirinbayan, J. Fitoussi, M. Bocquet, F. Meraghni, B. Surowiec, and A. Tcharkhtchi, *Multi-scale experimental investigation of the viscous nature of damage in Advanced Sheet Molding Compound (A-SMC) submitted to high strain rates,* Composites Part B: Engineering **115**, 3 (2017).

[26] H. Eyring, *Viscosity, Plasticity, and Diffusion as Examples of Absolute Reaction Rates,* The Journal of Chemical Physics **4**, 283 (1936).

[27] I. B. C. M. Rocha, F. P. van der Meer, S. Raijmaekers, F. Lahuerta, R. P. L. Nijssen, and L. J. Sluys, *Numerical/experimental study of the monotonic and cyclic viscoelastic/viscoplastic/fracture behavior of an epoxy resin,* International Journal of Solids and Structures **168**, 153 (2019).

[28] R. K. Goldberg, K. S. Carney, P. DuBois, C. Hoffarth, J. Harrington, S. Rajan, and G. Blankenhorn, *Development of an orthotropic elasto-plastic generalized composite material model suitable for impact problems,* Journal of Aerospace Engineering **29**, 04015083 (2016).

[29] A. D. Mulliken and M. C. Boyce, *Mechanics of the rate-dependent elastic–plastic deformation of glassy polymers from low to high strain rates,* International Journal of Solids and Structures **43**, 1331 (2006).

[30] J.-K. Kim and Y.-W. Mai, *Engineered interfaces in fiber reinforced composites* (Elsevier, 1998).

[31] A. Paknahad, D. G. Petre, S. C. Leeuwenburgh, and L. J. Sluys, *Interfacial characterization of poly (vinyl alcohol) fibers embedded in a calcium phosphate cement matrix: An experimental and numerical investigation,* Acta Biomaterialia **96**, 582 (2019).

[32] W. J. Cantwell and M. Blyton, *Influence of Loading Rate on the Interlaminar Fracture Properties of High Performance Composites - A Review,* Applied Mechanics Reviews **52**, 199 (1999).

[33] M. May, *Numerical evaluation of cohesive zone models for modeling impact induced delamination in composite materials,* Composite Structures **133**, 16 (2015).

[34] Y. Liu, F. P. van der Meer, and L. J. Sluys, *Cohesive zone and interfacial thick level set modeling of the dynamic double cantilever beam test of composite laminate,* Theoretical and Applied Fracture Mechanics **96**, 617 (2018).

[35] F. Zhou, J.-F. Molinari, and T. Shioya, *A rate-dependent cohesive model for simulating dynamic crack propagation in brittle materials,* Engineering Fracture Mechanics **72**, 1383 (2005).

[36] X. Zhang, H. Y. Liu, and Y. W. Mai, *Rate-dependent bridging law and its application to dynamic crack growth in brittle-matrix composite materials,* Composites Part A: Applied Science and Manufacturing **34**, 1053 (2003).

[37] M. Heidari-Rarani, M. M. Shokrieh, and P. P. Camanho, *Finite element modeling of mode I delamination growth in laminated DCB specimens with R-curve effects,* Composites Part B: Engineering **45**, 897 (2013).

[38] R. Hill, *Elastic properties of reinforced solids: Some theoretical principles,* Journal of the Mechanics and Physics of Solids **11**, 357 (1963).

[39] J. Fish and K. Shek, *Computational plasticity and viscoplasticity for composite materials and structures,* Composites Part B: Engineering **29**, 613 (1998).

[40] G. J. Dvorak and Y. Benveniste, *On transformation strains and uniform fields in multiphase elastic media,* Proceedings of the Royal Society of London. Series A: Mathematical and Physical Sciences **437**, 291 (1992).

[41] I. V. Andrianov, V. I. Bolshakov, V. V. Danishevs'kyy, and D. Weichert, *Higher order asymptotic homogenization and wave propagation in periodic composite materials,* Proceedings of the Royal Society A: Mathematical, Physical and Engineering Sciences **464**, 1181 (2008).

[42] F. Feyel and J.-L. Chaboche, *FE^2 multiscale approach for modelling the elastoviscoplastic behaviour of long fibre SiC/Ti composite materials,* Computer Methods in Applied Mechanics and Engineering **183**, 309 (2000).

[43] V. Kouznetsova, W. A. M. Brekelmans, and F. P. T. Baaijens, *An approach to micro-macro modeling of heterogeneous materials,* Computational Mechanics **27**, 37 (2001).

[44] E. Tikarrouchine, G. Chatzigeorgiou, F. Praud, B. Piotrowski, Y. Chemisky, and F. Meraghni, *Three-dimensional FE^2 method for the simulation of non-linear, rate-dependent response of composite structures,* Composite Structures **193**, 165 (2018).

[45] O. van der Sluis, P. J. G. Schreurs, W. A. M. Brekelmans, and H. E. H. Meijer, *Overall behaviour of heterogeneous elastoviscoplastic materials: effect of microstructural modelling,* Mechanics of Materials **32**, 449 (2000).

[46] A. Karamnejad, A. Ahmed, and L. J. Sluys, *A numerical homogenization scheme for glass particle-toughened polymers under dynamic loading,* Journal of Multiscale Modelling **08**, 1750001 (2017).

[47] V. Tvergaard, *Analysis of tensile properties for a whisker-reinforced metal-matrix composite,* Acta Metallurgica et Materialia **38**, 185 (1990).

2

Cohesive zone and interfacial thick level set modeling of the dynamic double cantilever beam test of composite laminate

2.1. Introduction

Delamination is one of the crucial degradation mechanisms of composite laminates [2]. Engineering composite laminates can be subjected to complex working load conditions including quasi-static and dynamic loading (e.g. low velocity impact). In order to predict the extent of delamination under given load conditions, it is important to quantify the interlaminar fracture toughness of composite laminates for both quasi-static and dynamic loading.

The double cantilever beam (DCB) test is one of the most commonly used experimental methods for determining the mode-I interlaminar fracture toughness [3]. Studies on measurement of the mode-II, mode-III interlaminar fracture toughness can be found in [4–9]. Based on published results on the DCB test with a smallest test rate of 1.67×10^{-7} m/s in [10] and a largest test rate of 15 m/s in [11, 12], the following observations can be made. Firstly, depending on the investigated test rate and composite system, the crack propagation in the DCB test could be either stable or unstable ("stick/slip") [4, 10, 11, 13–15]. In [10], where a carbon/epoxy composite material, T300/2500, was tested within the crosshead speed range of 1.67×10^{-7} to 8.33×10^{-3} m/s, the delamination crack growth was unstable for test

This chapter is based on [1]

rates lower than 8.33 $\times 10^{-6}$ m/s and became stable for higher test rates. In [13], a unidirectional and a woven carbon/epoxy composite laminate with 19% inclusion of transversal E-glass fibres was tested with different crosshead velocities ranging from 8.3×10^{-5} m/s to 0.19 m/s. For both materials and all loading rates, the crack propagated in an unstable fashion. Secondly, the loading rate may influence the fracture toughness although there is no universal trend in increased loading rate effects on the toughness. Aliyu and Daniel [16] investigated an AS-4/3501-6 carbon/epoxy system with DCB tests at a crosshead displacement rate up to 8.5×10^{-3} m/s. It was found that the mode-I interlaminar fracture toughness increased 28% over three orders of magnitude of loading rate. Smiley and Pipes [14] found that the mode-I interlaminar fracture toughness for APC-2 carbon/PEEK composite remains constant over four decades of low loading rates while further increase in loading rate caused a decrease up to 70% over the next decade of loading rate. This inconsistency in the trends might be attributed to differences in material constituent, specimen geometry, data-reduction scheme, measurement technique and definition of the rate parameter [17, 18].

In terms of numerical modeling, the cohesive zone model (CZM) is widely used for modeling delamination. Motivated by the possible rate-sensitivity of composite laminates or polymeric adhesives, rate-dependent cohesive laws have been proposed. They can be roughly divided into four categories, namely, the dynamic increase factor (DIF) models, the damage-delay models, the viscoplasticity models and the viscoelasticity models. The first category of models assumes that some characteristic parameters (e.g. the fracture energy) of a chosen cohesive law are functions of the separation rate of the cohesive surface [19–25]. The second category modifies the classical damage evolution formulation into a rate form, thus limiting the damage rate to a certain maximum [8, 26, 27]. The third category introduces an overstress function to the rate-independent softening plasticity law [28–30]. The fourth category combines viscoelastic components (e.g. Maxwell element) with a damage-type of rate-independent cohesive law [31–33].

Rather than treating damage along the interface as a result of a local displacement jump as it is done for the CZM model, the damage can be driven by a non-local energy release rate. This approach is possible with the interfacial thick level set (ITLS) model. The thick level set (TLS) model was first introduced by Möes et al. [34] for the modeling of damage growth in a continuum under quasi-static loading conditions. Contrary to conventional continuum damage mechanics, the damage d in the TLS is not a direct function of the local strain but rather a function of a level set field ϕ, whose definition is the signed distance to a moving damage front. This damage band has a predefined fixed length acting as an intrinsic length scale to avoid spurious localization and the associated pathological mesh-dependency observed in local damage models. Recent developments and applications of the TLS method include an improved numerical implementation scheme [35], 3D crack simulation for quasi-brittle materials [36], shear failure simulation of sandwich structures [37] and simulation of fragmentation under impact [38, 39]. The TLS model was translated to interface element by Latifi et al. [40] to provide an alternative to the CZM for interfacial cracking. The damage in this interfacial thick level set (ITLS)

model is a function of a level set field defined on the interface. The ITLS allows for non-local evaluation of the energy release rate. Consequently, the damage growth criterion can be related to a fracture mechanics based crack growth criterion. The ITLS model, in this sense, is advantageous since it provides a robust numerical tool for straightforward implementation of energy release rate based crack growth relations. The application of the ITLS model for simulating fatigue crack growth, where the Paris relation gives such a relation, was reported in [41, 42].

This paper is organized as follows: in Section 2.2, a rate-independent and a rate-dependent cohesive law are introduced and their ability to reproduce experimental observations is evaluated. The formulation, solution scheme and relevant details of the ITLS model are presented in Section 2.3. The capability of this method is demonstrated by modeling the dynamic DCB test with a parametric study in Section 2.4. The final section gives a short comparison and summary about the CZM model and the ITLS model.

2.2. Cohesive zone modeling

In this section, both rate-independent and rate-dependent cohesive modeling are used to simulate the DCB tests on unidirectional PEEK/carbon composite laminate reported by Blackman et al. [11, 12]. Starting point is the cohesive law by Turon et al. [43]. Rate-dependency is introduced for the cohesive strength and fracture energy following May [22, 23]. By setting the rate sensitivity parameters in the rate-dependent cohesive law to be zero, the cohesive law introduced by Turon et al. [43] is recovered.

2.2.1. Rate-independent cohesive law

For the sake of completeness, the rate-independent cohesive law is first reviewed. The studied DCB test is assumed to be a plane strain problem, so only a two-dimensional formulation is introduced below. The following relation between traction t_i and displacement jump $[\![u]\!]_i$ is used:

$$t_i = (1-d)\,K\delta_{ij}[\![u]\!]_j - dK\langle -[\![u]\!]_1\rangle\delta_{1i}, \qquad i=1,2;\ j=1,2 \tag{2.1}$$

where index 1 represents the normal direction, 2 is the shear direction, d is a scalar damage variable, K is a penalty stiffness, δ_{ij} is the Kronecker delta and the MacAuley bracket is defined as $\langle x\rangle = \frac{1}{2}(x+|x|)$.

The displacement jump when damage initiates, $[\![u]\!]_i^0$, is given as,

$$[\![u]\!]_i^0 = \frac{\sigma_i}{K}, \quad i=1,2 \tag{2.2}$$

in which σ_i is the cohesive strength. The displacement jump when full decohesion occurs, $[\![u]\!]_i^f$, reads

$$[\![u]\!]_i^f = \begin{cases} \frac{2G_{Ic}}{\sigma_i}, & i=1 \\ \frac{2G_{IIc}}{\sigma_i}, & i=2 \end{cases} \tag{2.3}$$

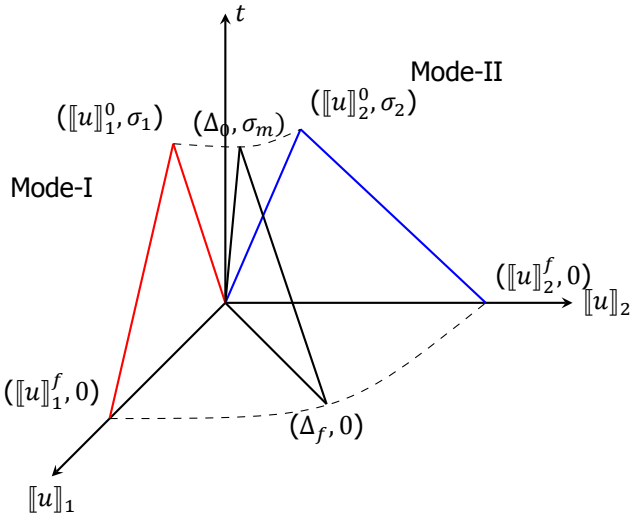

Figure 2.1: Mixed-mode cohesive law.

where G_{Ic} is the mode-I fracture energy and G_{IIc} is the mode-II fracture energy.

The coupling between independent modes is demonstrated in Fig. 2.1. For a given mixed-mode ratio defined as

$$\beta = \frac{|\llbracket u \rrbracket_2|}{\langle \llbracket u \rrbracket_1 \rangle + |\llbracket u \rrbracket_2|} \tag{2.4}$$

The mixed-mode crack initiation criterion is introduced as $\Delta = \Delta_0$, in which the equivalent displacement jump Δ is

$$\Delta = \sqrt{\left(\langle \llbracket u \rrbracket_1 \rangle\right)^2 + \left(|\llbracket u \rrbracket_2|\right)^2} \tag{2.5}$$

and,

$$\Delta_0 = \sqrt{\left(\llbracket u \rrbracket_1^0\right)^2 + \left(\left(\llbracket u \rrbracket_2^0\right)^2 - \left(\llbracket u \rrbracket_1^0\right)^2\right) B^\eta} \tag{2.6}$$

where η is a mode interaction coefficient and

$$B = \frac{\beta^2}{1 + 2\beta^2 - 2\beta} \tag{2.7}$$

The crack propagation criterion is imposed by $\Delta = \Delta_f$ where

$$\Delta_f = \frac{\llbracket u \rrbracket_1^0 \llbracket u \rrbracket_1^f + \left(\llbracket u \rrbracket_2^0 \llbracket u \rrbracket_2^f - \llbracket u \rrbracket_1^0 \llbracket u \rrbracket_1^f\right) B^\eta}{\Delta_0} \tag{2.8}$$

and the mixed-mode fracture energy G_c is calculated as

$$G_c = G_{Ic} + (G_{IIc} - G_{Ic}) B^\eta \tag{2.9}$$

The damage at time T is defined as,

$$d(T) = \max_{\tau \le T} \begin{cases} 0, & \Delta \le \Delta_0 \\ \frac{\Delta_f(\Delta-\Delta_0)}{\Delta(\Delta_f-\Delta_0)}, & \Delta_0 < \Delta < \Delta_f \\ 1, & \Delta \ge \Delta_f \end{cases} \tag{2.10}$$

Detailed derivations on the above relations can be found in [43].

2.2.2. Rate-dependency relation

Rate dependency is introduced for both the cohesive strength and the fracture energy of independent modes with a Johnson-Cook law similar to May [22, 23]. For pure mode-I or mode-II, the following relation is introduced,

$$\sigma_i(\dot{\Delta}) = \begin{cases} \sigma_i^0 \left(1 + c_i \ln\left(\frac{\dot{\Delta}_i}{\dot{\Delta}_i^{\text{ref}}}\right)\right), & \dot{\Delta}_i \ge \dot{\Delta}_i^{\text{ref}} \\ \sigma_i^0, & \dot{\Delta}_i < \dot{\Delta}_i^{\text{ref}} \end{cases}, \quad i = 1, 2 \tag{2.11}$$

where σ_i is the rate-dependent cohesive strength, σ_i^0 is the quasi-static cohesive strength, c_i is a rate-sensitivity constant, $\dot{\Delta}_i$ is the displacement jump rate defined as $\dot{\Delta}_1 = \partial\langle[\![u]\!]_1\rangle/\partial T$ and $\dot{\Delta}_2 = \partial|[u]_2|/\partial T$, and $\dot{\Delta}_i^{\text{ref}}$ is a reference displacement jump rate.

The rate dependency of the fracture toughness is assumed to be,

$$G_{Ic}(\dot{\Delta}) = \begin{cases} G_{Ic}^0, & \dot{\Delta}_1 < \dot{\Delta}_1^{\text{ref}} \\ G_{Ic}^0 \left(1 + m_1 \ln\left(\frac{\dot{\Delta}_1}{\dot{\Delta}_1^{\text{ref}}}\right)\right), & \dot{\Delta}_1^{\text{ref}} \le \dot{\Delta}_1 \le \dot{\Delta}_1^{\text{inf}} \\ G_{Ic}^{\text{inf}}, & \dot{\Delta}_1 > \dot{\Delta}_1^{\text{inf}} \end{cases} \tag{2.12}$$

$$G_{IIc}(\dot{\Delta}) = \begin{cases} G_{IIc}^0, & \dot{\Delta}_2 < \dot{\Delta}_2^{\text{ref}} \\ G_{IIc}^0 \left(1 + m_2 \ln\left(\frac{\dot{\Delta}_2}{\dot{\Delta}_2^{\text{ref}}}\right)\right), & \dot{\Delta}_2^{\text{ref}} \le \dot{\Delta}_2 \le \dot{\Delta}_2^{\text{inf}} \\ G_{IIc}^{\text{inf}}, & \dot{\Delta}_2 > \dot{\Delta}_2^{\text{inf}} \end{cases} \tag{2.13}$$

where G_{Ic}^0 and G_{IIc}^0 are the mode-I and mode-II fracture energy under quasi-static loading, m_1 and m_2 are rate-sensitivity constants, $\dot{\Delta}_1^{\text{inf}}$ and $\dot{\Delta}_2^{\text{inf}}$ are the reference displacement rates for defining constants G_{Ic}^{inf} and G_{IIc}^{inf} that are introduced to bound the fracture energy when negative rate-dependency parameters are used such that $G_{Ic}^{\text{inf}} = G_{Ic}^0 \left(1 + m_1 \ln\left(\frac{\dot{\Delta}_1^{\text{inf}}}{\dot{\Delta}_1^{\text{ref}}}\right)\right)$ and $G_{IIc}^{\text{inf}} = G_{IIc}^0 \left(1 + m_2 \ln\left(\frac{\dot{\Delta}_2^{\text{inf}}}{\dot{\Delta}_2^{\text{ref}}}\right)\right)$. It is further assumed that when rate dependency is activated, the coupling between independent modes introduced in the previous section is still valid. An advantage of the phenomenological DIF formulation in Eq. (2.12) and (2.13) is that it can accommodate both a positive and negative influence of displacement jump rate on either cohesive strength or fracture energy while the existing rate-dependent CZMs developed with damage-delay [8, 26, 27] or viscosity formulation [28–33] can only capture a positive influence. This versatility provides more possibilities in describing different

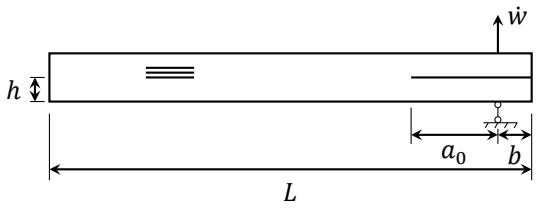

Figure 2.2: Geometry and boundary conditions of the double cantilever beam test under dynamic loading.

failure mechanisms in different composite material system and loading conditions. The measurements by Blackman et al. [11, 12] which show a decrease in fracture energy for increasing loading rate are exemplary of this advantage of the chosen cohesive formulation.

2.2.3. Model description

Numerical models have been created to simulate both dynamic and quasi-static DCB tests. Depending on the type of loading, i.e. dynamic or quasi-static, the numerical model set-ups have differences.

The geometry and boundary conditions of the numerical model used for simulating dynamic DCB tests are depicted in Fig. 2.2. Load is applied at a point on the top surface, the velocity of which is raised to a constant test rate $\dot{w}$ within a short time and maintained until the end of the simulation. The vertical degree-of-freedom of the node symmetric to the loading point with the crack plane is constrained. The bulk material of the beam is represented by plane strain triangular elements with an orthotropic linear elastic constitutive model. The initially intact section of the middle surface between the two arms is modeled by zero-thickness cohesive zone elements with the cohesive law introduced in the previous section. The precracked section of middle surface is considered by zero-thickness interface elements with penalty stiffness in case of a negative $[\![u]\!]_1$ to enforce the contact condition. Implicit dynamic analysis is performed with a Newmark time integration scheme. When the rate-dependent cohesive law is used, the displacement jump rate in Eqs. (2.11), (2.12) and (2.13) is calculated with the Euler-backward scheme, which means that the displacement jump rate is implicitly updated at the end of each load step. The derivation of the consistent tangent is given in Appendix A.

For quasi-static DCB tests, the numerical model differs from the model used for dynamic loading at three points. Firstly, the horizontal degree-of-freedom of the loading point and supported point is constrained to eliminate the rigid body motion of the system. Secondly, the loading velocity is instantly set to the constant test speed $\dot{w}$ at the start of the simulation. Thirdly, no time integration scheme is needed as inertia is not considered.

2.2.4. Material parameters

The experiments from [11, 12] were preformed on a unidirectional PEEK/carbon composite laminate (APC-2) with a nominal fiber volume fraction of 65%. The bulk material is assumed to be orthotropic linear elastic with parameters as defined in Table 2.1. Of these, the longitudinal Young's modulus E_1, density ρ and a major Poisson's ratio ν_{12} are taken from the measured value in [11] while the other values which are taken from typical values in [44] have limited influence on the response.

The parameters needed to be determined for the rate-dependent cohesive law can be divided into: parameters related to the rate-independent cohesive law and parameters related to the rate-dependency. Considering that the simulated DCB test is mode-I dominated, the material properties for mode-I and mode-II are assumed to be the same. The quasi-static fracture energies, G_{Ic}^0 and G_{IIc}^0, are determined to be 1.5 N/mm from the range of measurement values shown in Fig. 12 in [11]. Typical values are used for σ_1^0, σ_2^0 and η. A high value is prescribed for the penalty stiffness K.

Concerning rate-dependency, the quasi-static reference displacement jump rates, $\dot{\Delta}_1^{\text{ref}}$ and $\dot{\Delta}_2^{\text{ref}}$, determine the threshold value for the rate effect comes into play. Several trial simulations of a quasi-static DCB test, with a loading rate of 3.3×10^{-5} m/s, using different reference displacement jump rates are performed and the results are compared with the rate-independent cohesive model. The smallest value adopted in the rate-dependent CZM model that results in the same response as the rate-independent CZM model is determined to be the quasi-static reference displacement jump rates. Finally, the limit jump rate $\dot{\Delta}_1^{\text{inf}}$ and $\dot{\Delta}_2^{\text{inf}}$ are set sufficiently high not to be reached in the presented simulations. They are included in the formulation only to exclude the possibility of negative fracture energy from the model. The calibrations of c_1, c_2, m_1 and m_2 are done by trial simulations to find the best match with the time vs. crack length of the studied four DCB tests. A summary of CZM related parameters is shown in Table 2.2. The rate-dependency parameters for cohesive strength are found to be positive. This means that the cohesive strength increases with the displacement jump rate, which could be due to the viscosity of the PEEK polymer matrix [14, 45, 46]. The rate-dependency parameters for fracture energy are negative, meaning that a decrease of fracture energy with increasing displacement jump rate is found. This increased brittleness is possibly due to lack of time for plasticity to develop. The strain rate dependency of a brittle crack results in a smaller dissipated energy with larger strain rate [46].

Table 2.1: Bulk material parameters: E_1, ρ and ν_{12} from [11], G_{12}, E_2 and ν_{23} from [44].

elastic modulus	$E_1 = 115000$ N/mm^2	$E_2 = 8000$ N/mm^2
Poission's ratio	$\nu_{12} = 0.28$	$\nu_{23} = 0.43$
shear modulus	$G_{12} = 5000$ N/mm^2	
density	$\rho = 1540$ Kg/m^3	

Table 2.2: CZM related properties.

Quasi-static cohesive strength (mode-I/II)	$\sigma_1^0 = \sigma_2^0 = 60$ N/mm^2
Quasi-static fracture energy (mode-I/II)	$G_{Ic}^0 = G_{IIc}^0 = 1.5$ N/mm
Interface penalty stiffness	$K = 100000$ N/mm^3
Mode interaction coefficient	$\eta = 2.284$
Quasi-static reference displacement jump rate (mode-I/II)	$\dot{\Delta}_1^{\text{ref}} = \dot{\Delta}_2^{\text{ref}} = 0.02$ m/s
Strength coefficient (mode-I/II)	$c_1 = c_2 = 0.22$
Fracture energy coefficient (mode-I/II)	$m_1 = m_2 = -0.0783$
Maximum reference displacement jump rate (mode-I/II)	$\dot{\Delta}_1^{\text{inf}} = \dot{\Delta}_2^{\text{inf}} = 100.0$ m/s
Limit fracture energy (mode-I/II)	$G_{Ic}^{\text{inf}} = G_{IIc}^{\text{inf}} = 0.5$ N/mm

2.2.5. Simulation results

The numerical models are used to simulate four DCB tests of a unidirectional PEEK/carbon composite laminate with different test rates reported in [11, 12]: 3.3×10^{-5}, 1.0, 6.5 and 10.0 m/s. Both the rate-independent and rate-dependent cohesive law are considered for each analysis. The dimensions for the first three test cases are the same, i.e. L = 200.0 mm, h = 1.5 mm, a_0 = 35.0 mm, b = 7.1 mm (Fig. 2.2), while the dimensions for the last test case only differ in its initial crack length, i.e. $a_0 = 30$ mm. The time vs. crack length curve for the four simulated cases are plotted in Fig. 2.3a-2.3d. It can be observed that both the rate-independent (denoted in the figure with $c = m = 0$) and rate-dependent cohesive model predict a continuous crack propagation process for all the analysis. The model fails to capture the crack arrest phenomenon that was observed experimentally at the test rates of 1.0 and 6.5 m/s. It can be seen from Fig. 2.3a that the rate-independent model and rate-dependent model produce almost the same time vs. crack length curve for the lowest loading rate. They both match reasonably well with the measured curve. For the 1.0 m/s case (see Fig. 2.3b), the rate-dependent model produces a time vs. crack length curve which is almost coincident with the left boundary of the test curve. The average crack speed from the calibrated rate-dependent model matches with the measurement and the only difference is that in the test the crack does not propagate continuously. The rate-independent cohesive model matches the right boundary of the test curve and the overall crack propagation is slower than the measurement. For the 6.5 m/s case (see Fig. 2.3c), the time vs. crack length curve obtained with the rate-dependent cohesive model follows the measurement well except that it can not capture the crack arrest event for a crack length of around 81 mm. For this loading rate, the time vs. crack length curve produced by the rate-independent cohesive model has a relatively large deviation from the experimental curve. The model predicts a later crack initiation and the crack speed is slower. For the test rate of 10.0 m/s (Fig. 2.3d), the time vs. crack length curve obtained with the rate-dependent model still matches reasonably well with the measurement in terms of crack speed, while the rate-independent model significantly underpredicts the crack speed. In conclusion, the rate-dependent model can reproduce the measurements except for the crack arrests which are not captured. The mismatch between measurements and rate-independent model result

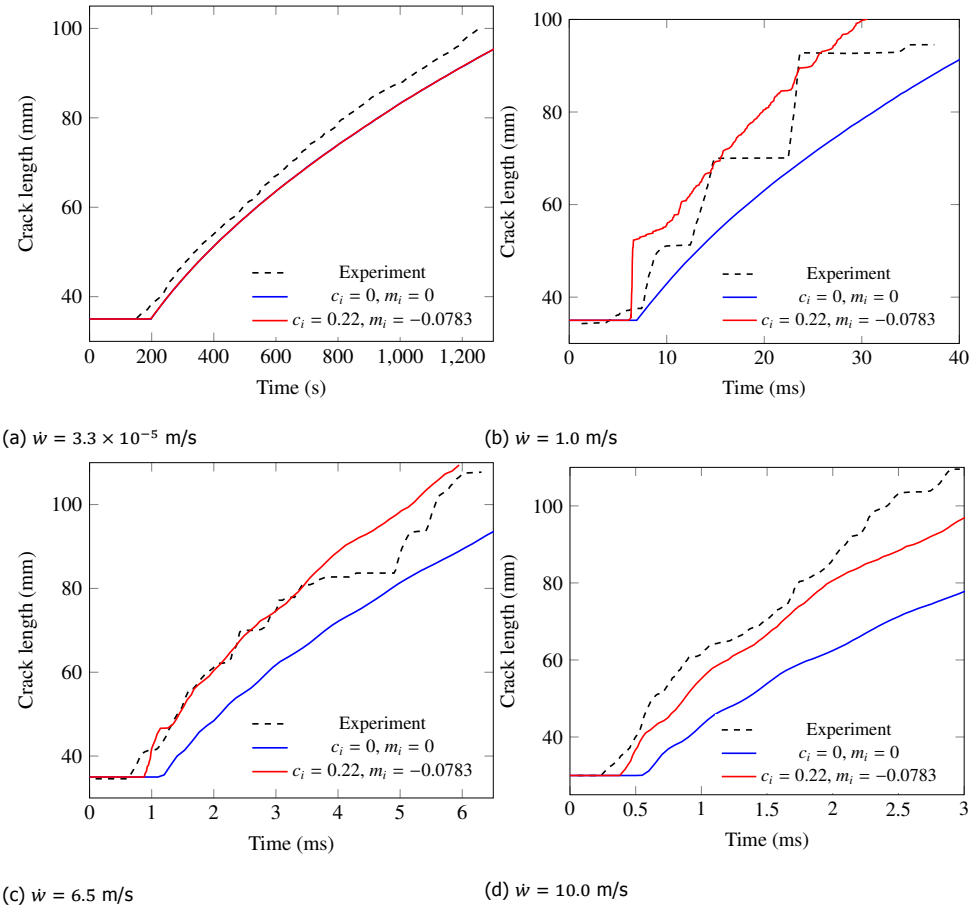

(a) $\dot{w} = 3.3 \times 10^{-5}$ m/s

(b) $\dot{w} = 1.0$ m/s

(c) $\dot{w} = 6.5$ m/s

(d) $\dot{w} = 10.0$ m/s

Figure 2.3: Comparison between experimental and cohesive zone modeling result for test rate of (a) $\dot{w} = 3.3 \times 10^{-5}$ m/s; (b) $\dot{w} = 1.0$ m/s; (c) $\dot{w} = 6.5$ m/s; (d) $\dot{w} = 10.0$ m/s.

indicates the significance of rate dependency for this series of experiments.

2.3. Interfacial thick level set modeling

As an alternative to the CZM, the ITLS model proposed by Latifi et al. [40] is introduced here to simulate the dynamic DCB tests. Similar to the CZM, a traction-separation relation with damage is assumed as the constitutive model of the interface. However, unlike the CZM, damage in the ITLS is not a function of the displacement jump across the surface but a function of a level set field ϕ on the interface. The level set function is defined as a signed distance function from a damage front. In 2D the damage front collapses into a point and ϕ gives the signed distance along the line of the interface to this point. The damage band has a fixed length l_c over which damage d increases from 0 to 1 as the distance to the

front grows from 0 to l_c. This band separates uncracked material with $d = 0$ from cracked material with $d = 1$. Because the damage distribution is fixed, the energy release rate for crack growth can be computed. Moreover, a crack growth rate can be imposed as the front velocity. This makes the method suitable for implementation of crack growth relations that relate crack growth rate to energy release rate, such as the Paris law for fatigue crack growth [41, 42]. In this section, the formulation and solution scheme for the ITLS method are described.

2.3.1. Local governing equation

Following Latifi et al. [40], the free energy per unit surface of interface is defined as:

$$\psi(\llbracket \mathbf{u} \rrbracket, d) = (1-d)\,\psi_0(\llbracket \mathbf{u} \rrbracket) + \frac{1}{2} dK \langle -\llbracket u \rrbracket_1 \rangle^2 \tag{2.14}$$

where $\llbracket \mathbf{u} \rrbracket = (\llbracket u \rrbracket_1, \llbracket u \rrbracket_2)^T$ is the displacement jump vector between the two facets of the interface, $\llbracket u \rrbracket_1$ is the normal displacement jump, $\llbracket u \rrbracket_2$ is the shear displacement jump and d is a scalar damage variable. The variable ψ_0 is defined as:

$$\psi_0(\llbracket \mathbf{u} \rrbracket) = \frac{1}{2} \llbracket u \rrbracket_i K \delta_{ij} \llbracket u \rrbracket_j \tag{2.15}$$

where K is a penalty stiffness and δ_{ij} is the Kronecker delta.

The relation between the traction $\mathbf{t}$ and the displacement jump $\llbracket \mathbf{u} \rrbracket$ across the surface is obtained by:

$$t_i = \frac{\partial \psi}{\partial \llbracket u \rrbracket_i} = (1-d)\,K \llbracket u \rrbracket_i - dK \langle -\llbracket u \rrbracket_1 \rangle \delta_{1i}, \quad i = 1, 2 \tag{2.16}$$

The local driving force for damage growth is obtained by differentiating the free energy function with respect to the damage variable:

$$Y = -\frac{\partial \psi}{\partial d} = \psi_0(\llbracket \mathbf{u} \rrbracket) - \frac{1}{2} K \langle -\llbracket u \rrbracket_1 \rangle^2 \tag{2.17}$$

2.3.2. Damage definition

Fig. 2.4 shows the damage band, the level set field ϕ defined on the interface and its associated damage distribution. The damage function proposed by Voormeeren et al. [42] is adopted.

$$d(\phi) = \begin{cases} 0, & \phi < 0 \\ \arctan\left(\gamma \frac{\phi}{l_c}\right) \arctan^{-1}(\gamma), & 0 < \phi < l_c \\ 1, & \phi > l_c \end{cases} \tag{2.18}$$

where γ is a shape constant. For the current study a value of $\gamma = 15$ is used following Voormeeren et al. [42]. The adopted damage function is plotted in Fig. 2.5.

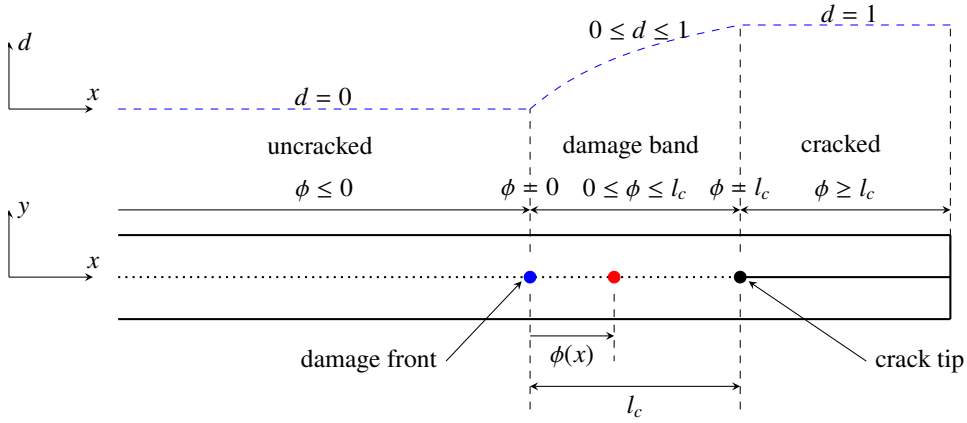

Figure 2.4: Initial level set field and damage distribution: The level set field at one point (red point) is defined as the signed distance to the damage band front (blue point).

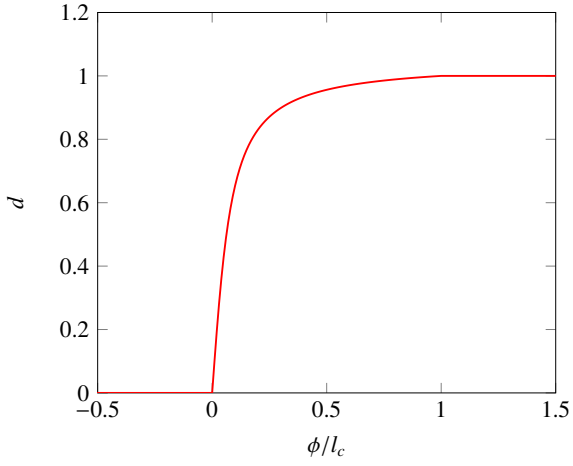

Figure 2.5: Damage function $d(\phi)$ with $\gamma = 15$.

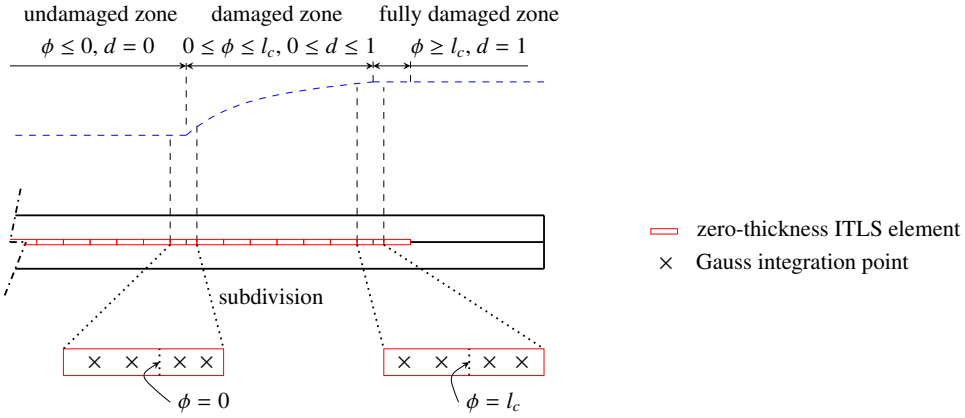

Figure 2.6: Subdivision of zero-thickness ITLS element.

2.3.3. Energy release rate

Because the damage distribution inside the band is given, the energy release rate for crack growth or movement of the band can be calculated by integrating the local driving force over the damage band. In 2D, the integration takes place along a line:

$$G = -\int_0^{l_c} \frac{\partial \psi}{\partial \phi} d\phi = -\int_0^{l_c} \frac{\partial \psi}{\partial d} \frac{\partial d}{\partial \phi} d\phi = \int_0^{l_c} Y \frac{\partial d}{\partial \phi} d\phi \tag{2.19}$$

A two-point Gauss integration scheme is used for elementwise numerical integration of Eq. (2.19). However, during the movement of the damage band, its front ($\phi = 0$) and wake ($\phi = l_c$) can intersect the interface element causing an unsmooth damage distribution inside the element. In order to improve the accuracy of numerical integration for Eq. (2.19) with discontinuous $\frac{\partial d}{\partial \phi}$, the ITLS element crossed by the damage band front or wake is subdivided into two sub-elements. In each of the two elements, two-point Gauss integration is applied (Fig. 2.6).

2.3.4. Crack speed

Completing the ITLS formulation requires a relation between the crack speed V and the energy release rate G. This can be an advantage. For instance, for fatigue crack growth experimental observations can be described well with the Paris law, which gives such a relation. In [41, 42], the ITLS method has been validated for the calculation of energy release rate and prediction of fatigue crack growth. In this paper, a function between energy release rate G and crack speed V for dynamic crack growth with possible stick/slip behavior is introduced (see Fig. 2.7). This function is inspired by the relation between the dynamic stress intensity factor K and crack speed V proposed by Ravi-Chandar [47] for describing dynamic crack growth. Similar to Ravi-Chandar [47], we explicitly differentiate three states for dynamic crack growth, namely, crack initiation, propagation and arrest. The crack

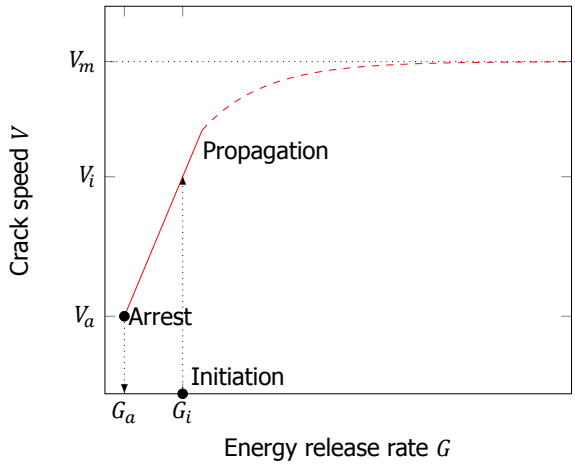

Figure 2.7: Relation between crack velocity V and energy release rate G (the dashed line schematically represents the shape for larger crack speed range [19, 51]).

starts to grow when the energy release rate G reaches the crack initiation toughness G_i. Crack growth starts at a nonzero crack speed V_i. During crack growth, the crack speed V is related to the energy release rate G according to a phenomenological relation which possesses three features: (1) the crack speed has an asympototic maximum value V_m [47, 48]; (2) the $V(G)$ curve has a positive slope, representing the influence of increased microcracking on the fracture toughness [8, 47, 49]; (3) the crack speed jumps from a finite value V_a to zero when the energy release rate drops below the crack arrest toughness G_a [50]. The crack initiation point is not on the curve characterizing the dynamic crack growth criterion is possibly due to bluntness of the initial crack, intrinsic rate dependence of the material, or inertia effects [47]. This difference between crack initiation and growth toughness causes the crack growth rate to jump to a finite speed immediately upon initiation. This behaviour has been observed experimentally for crack growth in polymers [50].

For the studied DCB tests, the Rayleigh wave speed c_R is the theoretical crack speed limit V_m [48]. In the experiments the crack speed is smaller than 85.0 m/s which is far from the theoretic limit ($c_R = 2523$ m/s). Therefore, we introduce a simple linear relation for the studied range of tests as (see Fig. 2.7)

$$V = V_i + \frac{V_i - V_a}{G_i - G_a}(G - G_i) \tag{2.20}$$

2.3.5. Solution scheme

The numerical model is created to simulate the delamination crack in dynamic DCB tests. The model is the same as mentioned in Section 2.2 except that the constitutive behavior of the cohesive elements inserted along the middle surface of the beam is now described with the ITLS.

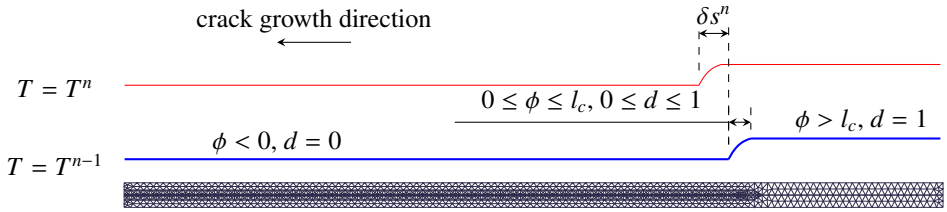

Figure 2.8: Movement of damage band within the nth time step (from time T^{n-1} to T^n): triangular meshes are used for discretization.

The program flow is illustrated in Box 1. There are a few items to be noted: (1) a damage band of length l_c is predefined ahead of the initial crack tip before the first load increment is applied; (2) the Newmark time integration scheme is used for computing displacements for a given damage distribution; (3) a staggered solution scheme is used for the damage update and the displacement field because of its robustness and simplicity. The translational distance of the damage band at the end of time step n is determined by the speed at the time step $n-1$. Therefore, when solving the dynamic equilibrium equation with the Newton-Raphson scheme, the damage is only updated when global convergence is achieved through the update of the level set field.

2.4. Simulation of dynamic DCB tests

The ITLS model is used to simulate the same series of DCB tests discussed in Section 2.2.4 except the quasi-static case with a test rate of 3.3×10^{-5} m/s, since the $V(G)$ relation introduced in Section 2.3.4 is a dynamic crack growth criterion assumed for delamination crack growth in the context of dynamic loading. A $V(G)$ relation with artificial viscoscity for simulating delamination crack generated by quasi-static loading with the ITLS has been introduced in [40].

In this section, the accuracy of the ITLS model for calculating the energy release rate is first validated. Afterwards, the influence of parameters used for the dynamic crack growth criterion is discussed and then the ITLS model is used to calibrate the material parameters for the dynamic DCB tests.

2.4.1. Verification of energy release rate computation

The accuracy of the energy release rate calculation in the ITLS model is demonstrated by modeling a quasi-static DCB specimen in which the deflection of the beam w is fixed while the crack length is gradually increased. Bulk material parameters listed in Table 2.1 are used. The value of 15.0 is adopted for the shape constant γ of the damage function. The damage band width l_c is chosen as 0.9 mm in the current study, which is a typical cohesive zone length found in the cohesive modeling study shown in Section 2.2. The interface element size is around 0.125 mm, which ensures 8 elements inside the damage band and a high accuracy in calculating the energy release rate. The interface penalty stiffness $K = 100000$

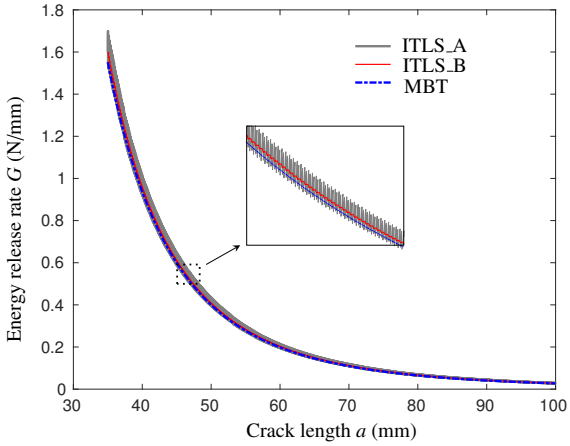

Figure 2.9: Evolution of energy release rate with crack length for ITLS_A (ITLS model without element subdivision used), ITLS_B (ITLS model with subdivision applied) and MBT (modified beam theory solution).

N/mm^3. The energy release rate from Eq. (2.19) is compared with the value from modified beam theory (MBT) introduced in [52]. According to the MBT, the energy release rate for the quasi-static DCB test can be calculated by

$$G = \frac{3}{4}\frac{E_1 h^3 w^2}{(a+\chi h)^4} \tag{2.21}$$

where the correction factor χ is estimated by

$$\chi = \left\{\left(\frac{E_1}{11G_{12}}\right)\left[3-2\left(\frac{\Gamma}{1+\Gamma}\right)^2\right]\right\}^{1/2} \tag{2.22}$$

in which $\Gamma = 1.18\left(\frac{E_1 E_2}{G_{12}}\right)^{1/2}$. Fig. 2.9 shows the crack length vs. energy release rate G calculated by the ITLS model with element subdivision and without element subdivision technique introduced in Section 2.3.3 along with the solution given by the MBT. It is shown that the ITLS model with element subdivision removes, to a large extent, the oscillations that are present for the model without element subdivision. The result by the ITLS model with element subdivision has a good match with the MBT solution, which demonstrates that the ITLS model is capable of calculating the energy release rate accurately.

In order to investigate the influence of the integration scheme on the accuracy of calculating G, a relative error ϵ is introduced as

$$\epsilon = \int_{35}^{55} \frac{|G(a) - \overline{G}(a)|}{\overline{G}(a)} da \tag{2.23}$$

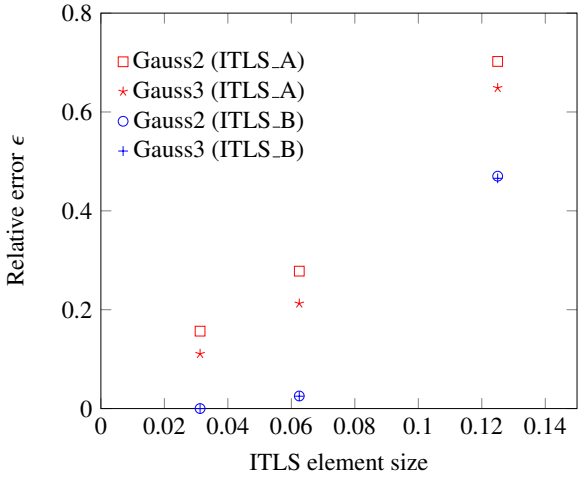

Figure 2.10: Error estimation of the integration scheme

in which $G(a)$ is the calculated energy release rate G at corresponding crack length a and $\overline{G}(a)$ is a reference exact solution. Three different mesh sizes are used for the ITLS model, changing from the coarsest mesh with ITLS interface element size of 0.125 mm, to medium mesh with a size of 0.0625 mm, and to the finest mesh with a size of 0.03125 mm. For each mesh size, four simulations, i.e., ITLS_A with 2-point Gauss, ITLS_A with 3-point Gauss, ITLS_B with 2-point Gauss and ITLS_B with 3-point Gauss, are performed and for each simulation we can calculate the relative error ϵ. In this case, the numerical solution obtained from the ITLS model with interface element size of 0.03125 mm and with 3-point Gauss integration scheme and element-subdivision (ITLS_B) is chosen as the reference exact solution $\overline{G}(a)$ used in Eq. (2.23). This result is plotted in Fig. 2.10 with the horizontal axis showing the number of the elements and the vertical axis showing the relative error ϵ. It can be found that for each mesh size, the ITLS_B model with 3-point Gauss integration scheme has the smallest error while the ITLS_A with 2-point Gauss integration scheme has the biggest error. The use of a 3-point Gauss integration slightly reduces the error for ITLS_A compared with 2-point integration. However, with ITLS_B the influence of higher order integration is limited. The difference of ITLS_B with 2-point and 3-point Gauss integration scheme is minor. It is concluded that 2-point Gauss integration with element subdivision (ITLS_B) is optimal.

2.4.2. Parameter sensitivity study

The influence of the parameters in the dynamic crack growth criterion introduced in Section 2.3.4 on crack growth is clarified by simulating a dynamic DCB test with a loading velocity of 6.5 m/s. An appropriate parameter set is found by trial and error and used as baseline for this parameter study. The baseline values are $G_i = 1.4$ N/mm, $G_a = 0.67$ N/mm, $V_i = 40.0$ m/s and $V_a = 14.5$ m/s. The bulk material

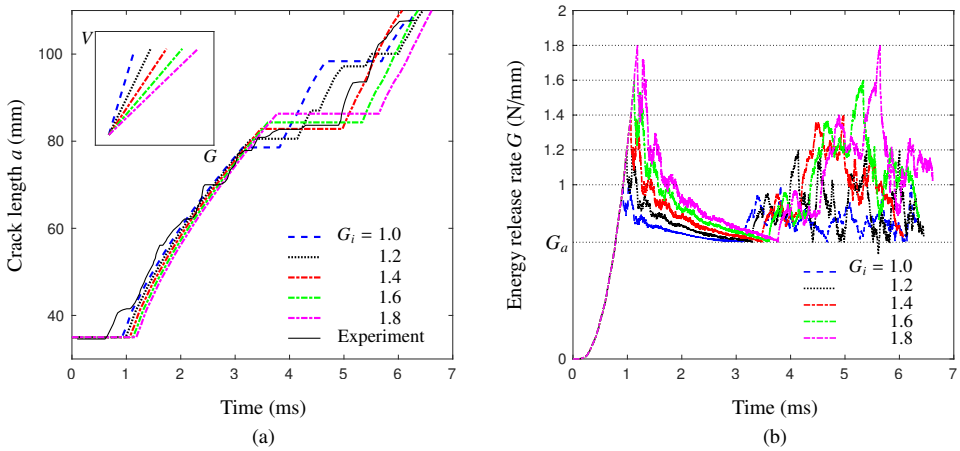

Figure 2.11: (a) Comparison of the time vs. crack length for simulation and experimental test and (b) the evolution of energy release with time for simulation with different G_i.

parameters, mesh discretization, interface parameters, damage function shape parameters γ and damage band length l_c are the same as used in the previous section. The boundary conditions are the same as described in Section 2.2.

Influence of G_i

Five numerical simulations are performed with the initiation toughness G_i increasing from 1.0 to 1.8 N/mm while keeping the other three input parameters (G_a, V_i, V_a) the same as the baseline values. Fig. 2.11a shows the evolution of crack length with time for all the simulations along with the experimental test result. The enclosed subplot illustrates how the $V(G)$ relation changes by varying G_i. Fig. 2.11b depicts the development of the energy release for each simulation. The time needed for crack initiation to occur is the longest for the case of $G_i = 1.8$. The accumulation of energy release rate with time before crack initiation is independent of G_i (see Fig. 2.11b). Therefore it needs more time to reach a larger initiation toughness. This means that G_i can be calibrated from the initiation time in experimental measurements.

Crack arrest is observed for all five simulations. The energy release rate tends to decrease during crack growth and when it reaches G_a crack growth is halted. For the two smallest G_i cases, more than one crack arrest occurred while the other three cases only show one crack arrest event. The first crack arrest happens later for larger G_i. Since the crack speed for the five cases is in the same range $[V_a, V_i]$, the time needed for the energy release rate to drop from G_i to G_a is longer for larger G_i.

Influence of G_a

Next, five numerical simulations in which G_a is varied from 0.47 to 0.87 N/mm are performed. Results are plotted in Fig. 2.12. It is observed from Fig. 2.12a that

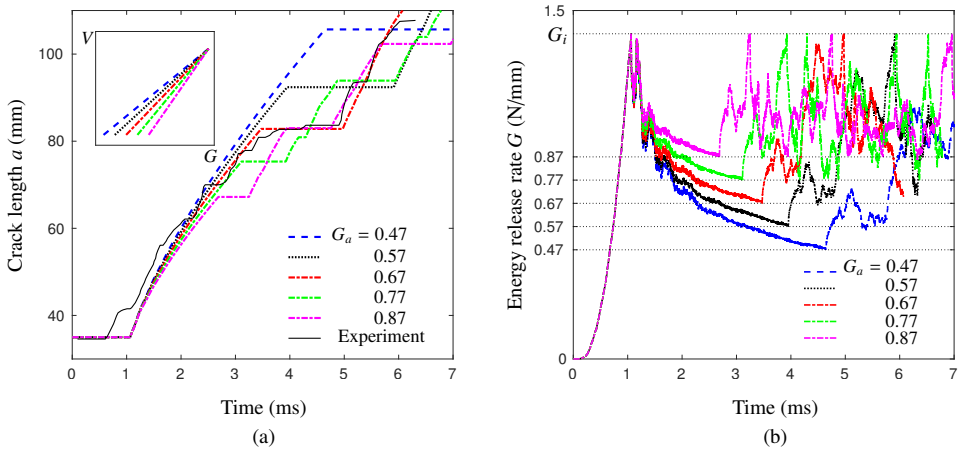

Figure 2.12: (a) Comparison of the time vs. crack length for simulation and experimental test and (b) the evolution of energy release with time for simulation with different G_a.

for all five cases the crack initiation time is the same. More than one crack arrest event appears for the two cases with highest arrest toughness G_a while the first three cases only have one crack arrest. The time at which crack arrest first occurs decreases for increasing G_a. This is a natural outcome of the dynamic crack growth criterion. Since the crack speed range is unchanged, a smaller arrest toughness takes longer to be reached. Another influence of the arrest toughness is that smaller G_a with all other parameters constant leads to lower curvature time vs. crack length curve. This observation helps in calibration of the parameters, as a comparison of the average crack speed between simulation and experimental curve can determine the way of adjusting the value for G_a. The case with $G_a = 0.67$ N/mm gives the best match with the experimental result.

Influence of V_i

The influence of initiation velocity V_i is studied by changing the value from 30 to 50 m/s in five numerical simulations. Fig. 2.13 shows the results. Again, the crack initiation time is the same for the five cases. For smaller initiation velocity V_i, the average crack velocity is also smaller as it is shown in the subplot. The shape of the time vs. crack length curve of the five cases is similar. This means that V_i does not have a big influence on the evolution of the energy release rate after crack initiation. The most notable influence is that increasing V_i decreases the time it takes before the first arrest occurs. This is due to the fact that smaller initiation velocity means smaller averaged crack growth velocity which in turn implies that the energy release rate G decreases slower. The case with $V_i = 40$ m/s shows the best match with the experimental curve.

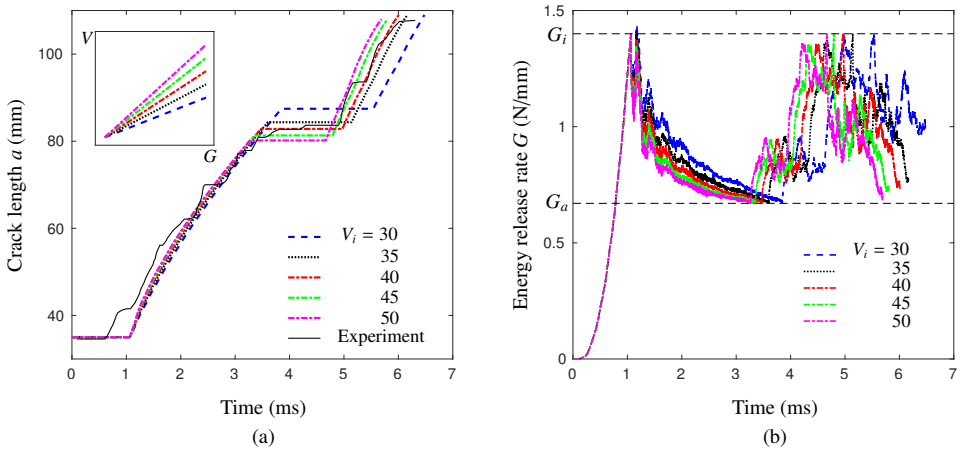

Figure 2.13: (a) Comparison of the time vs. crack length for simulation and experimental test and (b) the evolution of energy release with time for simulation with different V_i.

Influence of V_a

Five simulations with different V_a, ranging from 9.5 m/s to 19.5 m/s, are carried out to study the influence of V_a. Results are displayed in Fig. 2.14. The case with $V_a = 9.5$ m/s shows no crack arrest which can be attributed to the fact that the averaged crack speed is the smallest. For the other four cases, crack arrest is observed to occur earlier with larger V_a. This is because the energy release rate G decreases faster for higher V_a. When compared with the influence of V_i shown in previous section, the time at which crack arrest occurs is more sensitive to V_a. It is shown that the case with $V_a = 14.5$ m/s gives the best match with the experimental test curve.

2.4.3. Calibration results

Based on the parametric sensitivity study, the ITLS model is independently calibrated on the dynamic DCB tests for each of the test rates of 1.0, 6.5 and 10.0 m/s. For each case, the initiation toughness G_i, the arrest toughness G_a, the initiation velocity V_i and the arrest velocity V_a, are determined by comparison with the test curve. All other simulation inputs are the same as those used for the previous section.

Case I: $\dot{w} = 1$ m/s

For the DCB test at $\dot{w} = 1.0$ m/s, the calibrated parameters are $G_i = 1.7$ N/mm, $G_a = 0.7$ N/mm, $V_i = 20$ m/s and $V_a = 4.0$ m/s. The time vs. crack length curve for the experiment and the ITLS simulation are displayed in Fig. 2.15a. The experimental test result shows three major crack arrests events, which are well reproduced by the numerical simulation. The crack length at arrest is also very close to that in the test data. It is also observed that the crack speed, i.e. the slope of the time

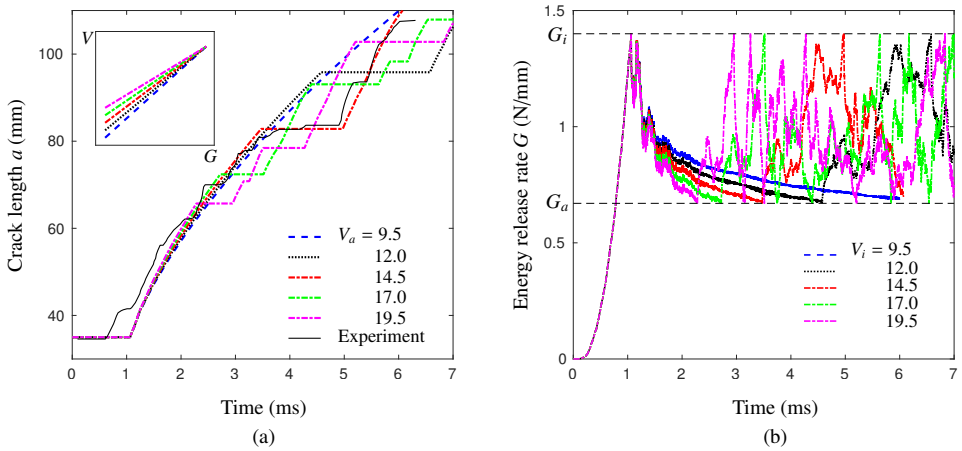

Figure 2.14: (a) Comparison of the time vs. crack length for simulation and experimental test and (b) the evolution of energy release with time for simulation with different V_a.

vs. crack length curve, has a good match between experimental test and numerical simulation.

The numerical model can also show the evolution of energy release rate during the loading process (see Fig. 2.15b). Based on data of the crack length at each time from the ITLS model, the evolution of the energy release rate with time can be calculated by invoking the dynamic version of the MBT [12, 52], i.e. when the crack speed $\dot{a}$ is zero,

$$G = \frac{3}{4}\frac{E_1 h^3 (\dot{w}T)^2}{(a+\chi h)^4} - \frac{33}{140}\frac{E_1 h(\dot{w})^2}{\eta^2} \tag{2.24}$$

and when the crack speed $\dot{a}$ is larger than zero,

$$G = \frac{3}{4}\frac{E_1 h^3 (\dot{w}T)^2}{(a+\chi h)^4} - \frac{111}{280}\frac{E_1 h(\dot{w})^2}{\eta^2} \tag{2.25}$$

where $\eta = \sqrt{E_1/\rho}$ and T is the physical time. A comparison between the energy release rate evaluated in the ITLS model with Eq. (2.19) and the MBT as plotted in Fig. 2.15b reveals that the MBT is still a reasonable approximation for this low loading rate. Hence, the MBT can be a useful tool to gain insight into the energy release rate evolution of the ITLS model. Before crack initiation, the energy release rate keeps increasing until the initiation toughness G_i is reached. The crack initiates with a speed of $V_i = 20$ m/s and the energy release rate G starts to decrease after initiation. This effect can be understood by Eq. (2.25), from which two observations can be made. Firstly, an increase of the crack length a by crack growth has an effect of reducing the energy release rate G. Secondly, the external loading prescribed by the loading velocity $\dot{w}$ causes G to increase with time. Considering that

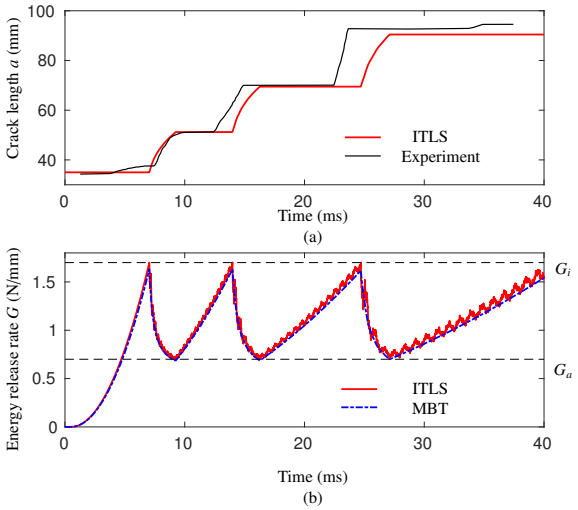

Figure 2.15: (a) Comparison of the time vs. crack length curve for simulation and experimental test at 1.0 m/s and (b) evolution of energy release rate with time for the simulation (solid line) and comparison with the MBT (dash dot line).

$\dot{w}$ for this case is relatively small, the increase of G caused by external loading can not compensate for the loss of G triggered by a fast growing crack. Therefore, G gradually decreases after crack initiation, although a certain amount of fluctuation is present due to dynamic vibration of the structure. When the arrest toughness G_a is reached, the crack is arrested and the crack speed drops to zero from a speed of $V_a = 4$ m/s instantly. It is also observed in Fig. 2.15 that the duration time for the third plateau is the longest while the duration for the first plateau is the shortest. This means that the time needed for the arrested crack to re-initiate becomes longer, which is also in agreement with Eq. (2.25). The crack length at arrest for a later event is longer, hence, it takes more time to increase the energy release rate from G_a to G_i to trigger crack initiation. This feature is visible in experimental measurements as well as in the numerical results. However, it is observed that the reinitiation occurs earlier in the test than in the numerical simulation. This might be due to more complex physics at crack initiation and initial crack tip bluntness.

Case II: $\dot{w} = 6.5$ m/s

The numerical results for the test at $\dot{w} = 6.5$ m/s have been discussed already in detail in Section 2.4.2. The results obtained with calibrated parameters $G_i = 1.4$ N/mm, $G_a = 0.67$ N/mm, $V_i = 40$ m/s and $V_a = 14.5$ m/s are shown in Fig. 2.16. The experimental curve shows one crack arrest at a crack length of 84 mm, which is very close to what is obtained in the numerical simulation. The crack velocity is well captured by the numerical model as the simulation curve follows the path of the test curve. It should be noted that the calibrated arrest toughness $G_a = 0.67$ N/mm differs from the arrest value of around 1.0 N/mm that was extracted from

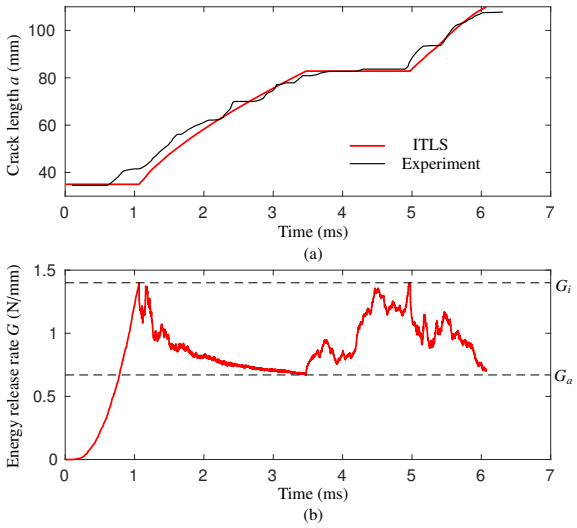

Figure 2.16: (a) Comparison of the time vs. crack length curve for simulation and experimental test at 6.5 m/s and (b) evolution of energy release rate with time for the simulation.

these experimental measurements [11, 12]. The reason for the difference is that in [12] a different definition of the arrest toughness was used for this loading rate, where G_a was determined as a fit through the complete curve, and therefore rather the averaged G during propagation.

The evolution of the energy release rate G during the whole loading process is shown in Fig. 2.16b. Similar to the previous case, the energy release rate G tends to increase when the crack is stationary and to decrease when the crack is growing. However, compared to case I the energy release rate curve has more oscillations especially after the crack is arrested. This oscillation is due to an evident effect of system inertia activated by a larger test rate. When the crack is arrested from a finite crack speed, the system inertia has the tendency to resist the sudden change from a propagation crack state to a stationary crack state. Afterwards, the external loading also has to overcome system inertia to cause the stress at the crack tip to build up and to propagate the arrested crack again. For a larger test rate, the interaction between external loading (which promotes crack propagation) and system inertia (which resists the change of system state) leads to more evident oscillating energy release rate evolution.

Case III: $\dot{w} = 10.0$ m/s

The calibrated material parameters for the test rate of 10.0 m/s are $G_i = 1.3$ N/mm, $G_a = 0.3$ N/mm, $V_i = 85$ m/s and $V_a = 20$ m/s. Fig. 2.17a shows the evolution of crack length with time for experiment and simulation. No clear crack arrest is observed in the experiment, which means that the crack propagation pattern transitions from unstable to stable crack growth as the test rate increases from 1.0

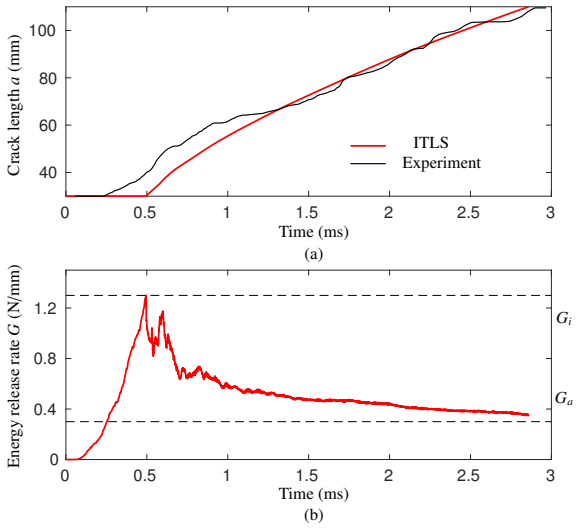

Figure 2.17: (a) Comparison of the time vs. crack length curve for simulation and experimental test at 10.0 m/s and (b) evolution of energy release rate with time for the simulation.

m/s to 10.0 m/s. The numerical simulation also shows no crack arrest. The crack propagation speed is also reasonably well captured. In absence of arrest events in the test data, calibration does not lead a unique set of values for G_a and V_a.

The evolution of energy release rate G with time is shown in Fig. 2.17b. Before crack initiation, the energy release rate already shows visible oscillations compared to case I and II because higher frequency components are activated for higher loading speed. With the high loading rate, G drops more slowly during crack growth than in the previous cases. This offers a possible explanation for the transition from stick/slip to stable crack growth for increasing loading rate.

2.4.4. Discussion

Fig. 2.18 shows the calibrated relation between crack speed V and energy release rate G for the three dynamic DCB tests we have studied. It is shown that the calibrated relation differs significantly for the different test rates. Within the studied test rate range, the initiation toughness G_i for test rate of 1.0, 6.5 and 10.0 m/s is 1.7, 1.4 and 1.3 N/mm respectively. The arrest toughness G_a for the three cases is 0.7, 0.67 and 0.3 N/mm correspondingly although the arrest toughness G_a and arrest velocity V_a for 10.0 m/s case are postulated as the crack propagates in a stable manner. It appears that both G_i and G_a decrease with the test rate where G_i is more sensitive to the loading rate than G_a. The initiation velocity V_i for the three cases is 20, 40 and 85 m/s. The arrest velocity V_a for the three cases is 4, 14.5 and 20 m/s. This shows that both V_i and V_a increase with the test rate and therefore the average crack velocity is also increasing. Although the proposed model performs well in reproducing crack arrest, a single set of parameters does

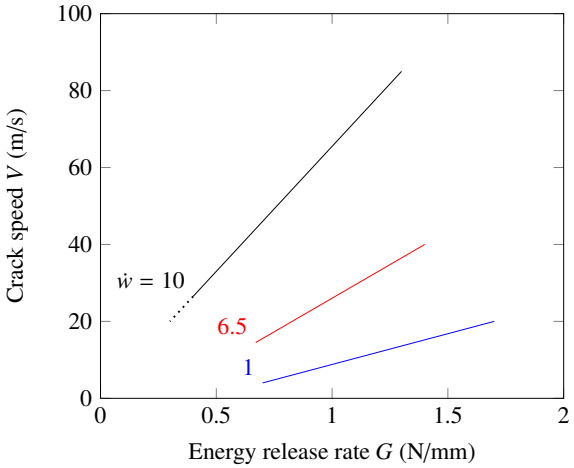

Figure 2.18: Calibrated relation of crack speed V and energy release rate G at $\dot{w}$ = 1.0, 6.5 and 10.0 m/s

not exist to describe the studied dynamic DCB tests at different rates. It can be concluded that in this series of tests, the crack speed is not only a function of the energy release rate at the crack tip. As suggested by Ravi-Chandar [47], strain rate and temperature may influence this relation.

2.5. Conclusion

In this paper, a rate-dependent cohesive zone model (CZM) and the interfacial thick level set (ITLS) model are used to simulate a series of DCB tests carried out over a test rate range of 3.3×10^{-5} to 10.0 m/s on an unidirectional PEEK/carbon composite laminate reported in [11, 12]. Within the studied test rate range and for this composite material, the following conclusions are drawn.

The rate-independent cohesive zone model fails to capture the inherent loading rate dependency of this composite material and therefore cannot capture the crack propagation process well. Unlike other available rate-dependent cohesive laws which can not capture a decrease in fracture energy for increasing loading rate, the presented rate-dependent cohesive zone model is capable of capturing the average crack growth speed. However, it fails to reproduce crack arrests that do occur in some of the experiments.

Using the interfacial thick level set method, an explicit relation between the crack growth speed V and energy release rate G can be implemented to capture both stable crack propagation and unstable crack propagation in DCB tests. With carefully calibrated parameters for this relation, the ITLS model could well reproduce the crack growth process for the different rates. In case of unstable crack growth, the ITLS approach can capture the number of crack arrest events as well as the timing and duration of these events. This indicates that the adopted dynamic fracture cri-

terion with $V(G)$ relation, initiation toughness and arrest toughness is related to the physics of the problem. However, no single $V(G)$ relation could be identified that works for all rates, which means that some physics is still missing in the formulation.

A comparison between the presented rate-dependent CZM and ITLS model shows that: (1) The ITLS method can readily implement a relation of the type $V(G)$, which makes it a good tool for implementing a dynamic crack growth criterion in fracture mechanics. (2) The ITLS model is more advantageous than the rate-dependent cohesive zone model in terms of the capability of capturing unstable crack growth. (3) Instead of adjusting the parameters for the $V(G)$ relation used in ITLS model, the rate-dependent cohesive zone model requires only a single set of parameters to capture the average response of the DCB at different loading rates. Research is thus needed to establish a more general dynamic crack growth criterion that could give the ITLS approach the ability to be more predictive.

The ITLS is for the first time embedded in a dynamics solution scheme which extends the application of this method from quasi-static and cyclic loading to dynamic loading. It is shown that the $V(G)$ relation, inspired by Ravi-Chandar's $V(K)$ relation [47], can provide a very good match with experimentally observed arrests and reinitiation phenomena. The good match that has been observed for individual loading rates points out that the $V(G)$ relation is a useful ingredient for describing dynamic crack growth.

References

[1] Y. Liu, F. P. van der Meer, and L. J. Sluys, *Cohesive zone and interfacial thick level set modeling of the dynamic double cantilever beam test of composite laminate,* Theoretical and Applied Fracture Mechanics **96**, 617 (2018).

[2] M. R. Wisnom, *The role of delamination in failure of fibre-reinforced composites,* Philosophical Transactions of the Royal Society A: Mathematical, Physical and Engineering Sciences **370**, 1850 (2012).

[3] M. May, *Measuring the rate-dependent mode I fracture toughness of composites – A review,* Composites Part A: Applied Science and Manufacturing **81**, 1 (2016).

[4] S. Hashemi, A. J. Kinloch, and J. G. Williams, *The Effects of Geometry, Rate and Temperature on the Mode I, Mode II and Mixed-Mode I/II Interlaminar Fracture of Carbon-Fibre/Poly(ether-ether ketone) Composites,* Journal of Composite Materials **24**, 918 (1990).

[5] H. Zabala, L. Aretxabaleta, G. Castillo, and J. Aurrekoetxea, *Dynamic 4 ENF test for a strain rate dependent mode II interlaminar fracture toughness characterization of unidirectional carbon fibre epoxy composites,* Polymer Testing **55**, 212 (2016).

[6] A. J. Smiley and R. B. Pipes, *Rate sensitivity of mode II interlaminar fracture toughness in graphite/epoxy and graphite/PEEK composite materials,* Composites Science and Technology **29**, 1 (1987).

[7] M. Colin de Verdiere, A. A. Skordos, A. C. Walton, and M. May, *Influence of loading rate on the delamination response of untufted and tufted carbon epoxy non-crimp fabric composites/Mode II,* Engineering Fracture Mechanics **96**, 1 (2012).

[8] J.-M. Guimard, O. Allix, N. Pechnik, and P. Thévenet, *Characterization and modeling of rate effects in the dynamic propagation of mode-II delamination in composite laminates,* International Journal of Fracture **160**, 55 (2009).

[9] D. Pennas, W. J. Cantwell, and P. Compston, *The Influence of Strain Rate on the Mode III Interlaminar Fracture of Composite Materials,* Journal of Composite Materials **41**, 2595 (2007).

[10] T. Kusaka, M. Hojo, Y.-W. Mai, T. Kurokawa, T. Nojima, and S. Ochiai, *Rate dependence of mode I fracture behaviour in carbon-fibre/epoxy composite laminates,* Composites Science and Technology **58**, 591 (1998).

[11] B. R. K. Blackman, J. P. Dear, A. J. Kinloch, H. Macgillivray, Y. Wang, J. G. Williams, and P. Yayla, *The failure of fibre composites and adhesively bonded fibre composites under high rates of test,* Journal of Materials Science **30**, 5885 (1995).

[12] B. R. K. Blackman, A. J. Kinloch, Y. Wang, and J. G. Williams, *The failure of fibre composites and adhesively bonded fibre composites under high rates of test,* Journal of Materials Science **31**, 4451 (1996).

[13] H. Zabala, L. Aretxabaleta, G. Castillo, and J. Aurrekoetxea, *Loading rate dependency on mode I interlaminar fracture toughness of unidirectional and woven carbon fibre epoxy composites,* Composite Structures **121**, 75 (2015).

[14] A. J. Smiley and R. B. Pipes, *Rate Effects on Mode I Interlaminar Fracture Toughness in Composite Materials,* Journal of Composite Materials **21**, 670 (1987).

[15] J. W. Gillespie, L. A. Carlsson, and A. J. Smiley, *Rate-dependent mode I interlaminar crack growth mechanisms in graphite/epoxy and graphite/PEEK,* Composites Science and Technology **28**, 1 (1987).

[16] A. A. Aliyu and I. M. Daniel, *Effects of Strain Rate on Delamination Fracture Toughness of Graphite/Epoxy,* in *Delamination and Debonding of Materials* (ASTM International, 100 Barr Harbor Drive, PO Box C700, West Conshohocken, PA 19428-2959, 1987) pp. 336–336–13.

[17] G. C. Jacob, J. M. Starbuck, J. F. Fellers, S. Simunovic, and R. G. Boeman, *The effect of loading rate on the fracture toughness of fiber reinforced polymer composites,* Journal of Applied Polymer Science **96**, 899 (2005).

[18] W. J. Cantwell and M. Blyton, *Influence of Loading Rate on the Interlaminar Fracture Properties of High Performance Composites - A Review,* Applied Mechanics Reviews **52**, 199 (1999).

[19] F. Zhou, J.-F. Molinari, and T. Shioya, *A rate-dependent cohesive model for simulating dynamic crack propagation in brittle materials,* Engineering Fracture Mechanics **72**, 1383 (2005).

[20] A. Corigliano, S. Mariani, and A. Pandolfi, *Numerical analysis of rate-dependent dynamic composite delamination,* Composites Science and Technology **66**, 766 (2006).

[21] A. Corigliano, S. Mariani, and A. Pandolfi, *Numerical modeling of rate-dependent debonding processes in composites,* Composite Structures **61**, 39 (2003).

[22] M. May, *Numerical evaluation of cohesive zone models for modeling impact induced delamination in composite materials,* Composite Structures **133**, 16 (2015).

[23] M. May, O. Hesebeck, S. Marzi, W. Böhme, J. Lienhard, S. Kilchert, M. Brede, and S. Hiermaier, *Rate dependent behavior of crash-optimized adhesives – Experimental characterization, model development, and simulation,* Engineering Fracture Mechanics **133**, 112 (2015).

[24] X. Wei, A. de Vaucorbeil, P. Tran, and H. D. Espinosa, *A new rate-dependent unidirectional composite model - Application to panels subjected to underwater blast,* Journal of the Mechanics and Physics of Solids **61**, 1305 (2013).

[25] B. Gozluklu and D. Coker, *Modeling of dynamic crack propagation using rate dependent interface model,* Theoretical and Applied Fracture Mechanics **85**, 191 (2016).

[26] O. Allix and J.-F. Deü, *Delayed-damage modelling for fracture prediction of laminated composites under dynamic loading,* Engineering Transactions **45**, 29 (1997).

[27] O. Allix, P. Feissel, and P. Thévenet, *A delay damage mesomodel of laminates under dynamic loading: basic aspects and identification issues,* Computers & Structures **81**, 1177 (2003).

[28] A. Corigliano and M. Ricci, *Rate-dependent interface models: formulation and numerical applications,* International Journal of Solids and Structures **38**, 547 (2001).

[29] C. M. Landis, T. Pardoen, and J. W. Hutchinson, *Crack velocity dependent toughness in rate dependent materials,* Mechanics of Materials **32**, 663 (2000).

[30] G. Giambanco and G. Fileccia Scimemi, *Mixed mode failure analysis of bonded joints with rate-dependent interface models,* International Journal for Numerical Methods in Engineering **67**, 1160 (2006).

[31] J. Wang, Q. H. Qin, Y. L. Kang, X. Q. Li, and Q. Q. Rong, *Viscoelastic adhesive interfacial model and experimental characterization for interfacial parameters,* Mechanics of Materials **42**, 537 (2010).

[32] M. Musto and G. Alfano, *A novel rate-dependent cohesive-zone model combining damage and visco-elasticity,* Computers & Structures **118**, 126 (2013).

[33] C. Xu, T. Siegmund, and K. Ramani, *Rate-dependent crack growth in adhesives: I. modeling approach,* International Journal of Adhesion and Adhesives **23**, 9 (2003).

[34] N. Moës, C. Stolz, P.-E. Bernard, and N. Chevaugeon, *A level set based model for damage growth: The thick level set approach,* International Journal for Numerical Methods in Engineering **86**, 358 (2011).

[35] P. E. Bernard, N. Moës, and N. Chevaugeon, *Damage growth modeling using the Thick Level Set (TLS) approach: Efficient discretization for quasi-static loadings,* Computer Methods in Applied Mechanics and Engineering **233**, 11 (2012).

[36] A. Salzman, N. Moës, and N. Chevaugeon, *On use of the thick level set method in 3D quasi-static crack simulation of quasi-brittle material,* International Journal of Fracture **202**, 21 (2016).

[37] F. P. van der Meer and L. J. Sluys, *The Thick Level Set method: Sliding deformations and damage initiation,* Computer Methods in Applied Mechanics and Engineering **285**, 64 (2015).

[38] K. Moreau, N. Moës, D. Picart, and L. Stainier, *Explicit dynamics with a non-local damage model using the thick level set approach,* International Journal for Numerical Methods in Engineering **102**, 808 (2015).

[39] A. J. Stershic, J. E. Dolbow, and N. Moës, *The Thick Level-Set model for dynamic fragmentation,* Engineering Fracture Mechanics **172**, 39 (2017).

[40] M. Latifi, F. P. van der Meer, and L. J. Sluys, *An interface thick level set model for simulating delamination in composites,* International Journal for Numerical Methods in Engineering **111**, 303 (2017).

[41] M. Latifi, F. P. van der Meer, and L. J. Sluys, *Fatigue modeling in composites with the thick level set interface method,* Composites Part A: Applied Science and Manufacturing **101**, 72 (2017).

[42] L. O. Voormeeren, F. P. van der Meer, J. Maljaars, and L. J. Sluys, *A new method for fatigue life prediction based on the Thick Level Set approach,* Engineering Fracture Mechanics **182**, 449 (2017).

[43] A. Turon, P. P. Camanho, J. Costa, and C. G. Dávila, *A damage model for the simulation of delamination in advanced composites under variable-mode loading,* Mechanics of Materials **38**, 1072 (2006).

[44] I. M. Daniel and O. Ishai, *Engineering mechanics of composite materials* (Oxford University Press, 2006).

[45] K. Friedrich, R. Walter, L. a. Carlsson, a. J. Smiley, and J. W. Gillespie, *Mechanisms for rate effects on interlaminar fracture toughness of carbon/epoxy and carbon/PEEK composites,* Journal of Materials Science **24**, 3387 (1989).

[46] M. A. Meyers, *Dynamic behavior of materials* (John wiley & sons, 1994).

[47] K. Ravi-Chandar, *Energy Balance and Fracture Criteria,* in *Dynamic Fracture*, edited by K. Ravi-Chandar (Elsevier, Oxford, 2004) pp. 71–79.

[48] L. B. Freund, *Energy concepts in dynamic fracture,* in *Dynamic Fracture Mechanics*, Cambridge Monographs on Mechanics (Cambridge University Press, 1990) pp. 221–295.

[49] T. Crump, G. Ferté, A. Jivkov, P. Mummery, and V.-X. Tran, *Dynamic fracture analysis by explicit solid dynamics and implicit crack propagation,* International Journal of Solids and Structures **110-111**, 113 (2017).

[50] K. Ravi-Chandar and W. G. Knauss, *An experimental investigation into dynamic fracture: I. Crack initiation and arrest,* International Journal of Fracture **25**, 247 (1984).

[51] L. Lamberson, V. Eliasson, and A. J. Rosakis, *In Situ Optical Investigations of Hypervelocity Impact Induced Dynamic Fracture,* Experimental Mechanics **52**, 161 (2012).

[52] J. G. Williams, *The fracture mechanics of delamination tests,* The Journal of Strain Analysis for Engineering Design **24**, 207 (1989).

1. Set the time step number $n = 1$;
2. Define a initial damage band with length l_c ahead of the crack tip and calculate the level set field $\phi(x)$;
3. Initialize damage distribution based on the level set field $\phi(x)$ using Eq. (2.18);
4. Set the initial time step δT^1;
5. Apply the nth load/displacement increment;
6. Solve dynamic equilibrium with the Newton-Raphson scheme;
7. Calculate the energy release rate of the nth time step, G^n, using Eq. (2.19);
8. Check the crack state at $(n-1)$th time step, stationary or propagating?
   - Stationary—The crack speed at the end of the nth time step, V^n, is calculated with Eq. (2.20) if the energy release rate G^n is larger than the initiation toughness G_i, otherwise it is zero.
   - Propagating—The V^n is calculated with Eq. (2.20) if G^n is larger than the arrest toughness G_a, otherwise it is zero.
9. Set time step size for the $(n+1)$th time step: $\delta T^n = \min(\delta T^1, 0.6 l_{ie}/V^n)$, where l_{ie} is the minimum interface element size;
10. Move the level set field in the crack growth direction by a distance of δs^n with $\delta s^n = V^{n-1} \cdot \delta T^n$ (see Fig. 2.8);
11. Update the damage distribution with the updated level set field using Eq. (2.18);
12. $n = n + 1$, go to step 5;

Box 1: Staggered solution algorithm for the ITLS model.

3

A dispersive homogenization model for composites and its RVE existence

3.1. Introduction

The heterogeneity of the microstructure of composite materials causes dispersion in wave propagation associated with dynamic loading. This dispersion phenomenon, also referred to as micro-inertia, is a result of local motion of the microstructure driven by multiple wave reflections and transmissions occurring at the interfaces between the constituents. Correct evaluation or tuning of the dispersion properties of composites can be important for engineering applications, for instance impact-resistant components or devices where composites are subject to high-rate loading [2–6] or metamaterials with microstructures designed to show particular effective behavior [7–9].

Computational modelling of composites subjected to stress-wave loading typically involves three length scales, i.e. the size of the macroscopic structure, the characteristic stress wave length and the length scale of the microstructure (in fiber-reinforced composites related to the fiber diameter) [9, 10]. The macroscopic length scale can be much larger than the microstructural length scale. In the case where the stress wave length is also much larger than the typical microstructural size, there is no significant transient effect within the microstructure and micro-inertia is negligible [9]. Therefore, the overall dynamic response can be solely described by averaging density and moduli. However, for a stress wave which is only few times larger than the microstructural length scale, the dispersion becomes evident and averaging properties are not sufficient to describe the dynamic response [9]. In order to account for the dispersion phenomenon, multiple models have

This chapter is based on [1]

been introduced. One type of model is the gradient elasticity model with high-order spatial derivatives of strains, stresses and/or accelerations as reviewed by Askes and Aifantis [11]. However, identification of the length-scale parameters of this method, especially in a multi-dimensional context, is not totally clear. Besides, Willis' elastodynamics homogenization model derives an effective constitutive relation which introduces non-classical coupling between effective stress and effective velocity and coupling between effective momentum and effective strain [12–15]. Recent development of generalized homogenization models enrich the macroscale displacement with additional generalized degrees of freedom of Bloch modes following the lines of Willis' model, see Sridhar et al. [16]. These methods are suitable for linear elastic (layered) periodic materials while an extension to materials with random microstructure is not always straightforward.

An alternative type of method which provides a more flexible framework (e.g. consideration of complex random microstructure or material nonlinearity) is representative volume element (RVE) based multiscale approaches. Initiated by Hill [17], the RVE can be defined as a characteristic sample of heterogeneous material that should be large enough to contain sufficient composite micro-heterogeneities in order to be representative, however it should be much smaller than the macroscopic structure size. Several definitions of an RVE are introduced in literature, as reviewed by Gitman et al. [18]. Generally, a micromodel can be considered representative if further increase of its size of RVE does not lead to changes in the homogenized properties. Typically, statistics studies using numerical computations are used to evaluate the homogenized physical properties (e.g. elastic properties, thermo-conductivity) or effective response (e.g. the effective stress) of a range of micromodels with increasing size, for instance in [18–25]. It should be noted that the size of an RVE depends on the specific investigated morphological (e.g. volume fraction) or physical properties (e.g. thermal or elastic) [19, 21].

Multiscale methods assume multiple (at least two) spatial and (or) temporal scales [26, 27]. In multiscale models finer-scale problems are considered in a (statistically equivalent) representative volume element (RVE) and information of the finer-scale is hierarchically passed into a coarser scale by bridging laws. Based on a multiscale virtual power principle [26] as a notion of a generalized Hill-Mandel lemma, Pham et al. [9] and Roca et al. [28] developed computational homogenization schemes in which the transient dynamics equations are resolved at macroscopic and microscopic scale. Asymptotic homogenization with higher-order (or first-order) expansions was proposed in [29–31] to capture wave dispersion and attenuation within viscoelastic composites. Fish et al. [32] introduced a general purpose asymptotic homogenization scheme in which the micro-inertia is resolved by introducing a eigenstrain term and is valid for nonlinear heterogeneous material. This method was further investigated by Karamnejad and Sluys [33] for impact-induced crack propagation within a heterogeneous medium. The aforementioned methods have shown certain capabilities in capturing wave dispersion for strictly periodic heterogeneous structures with simple microstructures where the RVE can be clearly defined as a unit cell. However, in a realistic composite material, the microstructure has a random nature. Therefore, the question of RVE existence needs

to be answered before multiscale methods can be employed.

In this paper, a dispersive multiscale model based on asymptotic homogenization is reviewed and the existence of an RVE for this method for unidirectional fiber-reinforced composites is investigated. This paper is organized as follows: in Section 3.2, the dispersive model based on asymptotic homogenization technique is introduced. The accuracy of this numerical method for 1D and 2D elastic wave propagation is demonstrated in Section 3.3. In Section 3.4, a statistics study is performed to investigate if an RVE exists for this homogenization approach for realistic fiber reinforce composite microstructures. In Section 3.5, a batch of calibrated numerical samples based on experimentally determined spatial distribution pattern is tested for the convergence of homogenized properties.

3.2. Dispersive homogenization model

In this section, the asymptotic homogenization model originated from Fish et al. [32] and later explored by Karamnejad and Sluys [33] is described. This method allows for a decoupling of the equation of motion into a two-scale formulation. The effect of microscopic dispersion is quantified by a so-called "dispersion tensor", which is related to the acceleration influence function of the microstructure. The acceleration influence functions for microstructures with one and multiple inclusions are demonstrated as examples.

3.2.1. Two-scale formulation

Considering a composite structure that is in dynamic equilibrium with prescribed displacements and stress boundary conditions and given the initial conditions for displacement and velocity (see Fig. 3.1a), the linear momentum equation reads

$$\frac{\partial \sigma_{ij}^{\zeta}}{\partial x_j^{\zeta}} = \rho^{\zeta} \ddot{u}_i^{\zeta}, \qquad \text{in } \Omega^{\zeta} \tag{3.1}$$

with boundary conditions

$$u_i^{\zeta}(\mathbf{x}, t) = \overline{u}_i^{\zeta}(\mathbf{x}, t) \quad \text{on } \partial\Omega^{u\zeta} \tag{3.2}$$

$$\sigma_{ij}^{\zeta}(\mathbf{x}, t) n_j^{\zeta}(\mathbf{x}) = \overline{t}_i^{\zeta}(\mathbf{x}, t) \quad \text{on } \partial\Omega^{t\zeta} \tag{3.3}$$

at the boundary surface $\partial\Omega^{\zeta} = \partial\Omega^{u\zeta} \cup \partial\Omega^{t\zeta}$ and initial displacement and velocity conditions

$$u_i^{\zeta}(\mathbf{x}, 0) = u_i^0(\mathbf{x}) \tag{3.4}$$

$$\dot{u}_i^{\zeta}(\mathbf{x}, 0) = v_i^0(\mathbf{x}) \tag{3.5}$$

where $\boldsymbol{\sigma}^{\zeta}$, ρ^{ζ}, $\mathbf{u}^{\zeta}$, $\ddot{\mathbf{u}}^{\zeta}$ and $\mathbf{n}^{\zeta}$ are stress, density, displacement, acceleration and surface outward normal, respectively. The superscript ζ denotes that quantities are defined within the composite domain. For simplicity, a linear elastic material law is considered herein, namely

$$\sigma_{ij}^{\zeta}(\mathbf{x}, t) = S_{ijkl}^{\zeta}(\mathbf{x}) \varepsilon_{kl}^{\zeta}(\mathbf{x}, t) \tag{3.6}$$

where $\boldsymbol{\varepsilon}^{\zeta}$ is strain and $\mathbf{S}^{\zeta}$ is the elastic stiffness tensor which is for two-phase (i.e. inclusion and matrix) composites a piece-wise constant function of spatial coordinates. Extension to nonlinear material behavior can be done by using the instantaneous stiffness tensor as elaborated in Fish et al. [32]. Perfect bonding between inclusion and matrix is considered here while decohesion can be possibly included through the eigendeformation concept [34] or a cohesive crack formulation [35]. A relevant study on dispersive multiscale formulation with consideration of material damage is introduced by Karamnejad and Sluys [33].

Asymptotic expansions

In the asymptotic expansion approach, two spatial coordinate systems are introduced, macro-scale coordinates $\mathbf{x}$ defined in the macroscopic homogeneous domain Ω and micro-scale coordinates $\mathbf{y}$ in an RVE domain Θ with heterogeneous microstructures, see Fig. 3.1b. The $\mathbf{y}$ coordinate is related to the $\mathbf{x}$ coordinate by $\mathbf{y} = \mathbf{x}/\zeta$ with $0 < \zeta \ll 1$. Any physical field variable, for example, the displacement field $\mathbf{u}$, is a function of spatial coordinate $\mathbf{x}$, $\mathbf{y}$ and also the physical time t. These physical fields are assumed to be $\mathbf{y}$-periodic in RVE domain Θ, namely $f(\mathbf{x},\mathbf{y}) = f(\mathbf{x},\mathbf{y}+\mathbf{k}\mathbf{l}_R)$ in which vector $\mathbf{l}_R = [l_1, l_2]^T$ represents the basic period of the microstructure (in 2D), l_1 and l_2 are the lengths of RVE along the two directions and $\mathbf{k}$ is a 2×2 diagonal matrix with integer components. The choice for periodic boundary conditions for the microscopic field is motivated by superior convergence properties that have been demonstrated by Kanit et al. [19] and Fish [36] among others. Following Fish et al. [32], we can represent this function by an asymptotic expansion around a point $\mathbf{x}$ in powers of ζ, namely,

$$\mathbf{u}^{\zeta}(\mathbf{x},t) = \mathbf{u}^{(0)}(\mathbf{x},t) + \zeta\mathbf{u}^{(1)}(\mathbf{x},\mathbf{y},t) + O(\zeta^2) \tag{3.7}$$

in which the first term on the right hand side represents a macro-scale component while the second term represents a micro-scale component. By applying the two-scale spatial derivative rule $\frac{\partial(\cdot)^{\zeta}}{\partial x_i^{\zeta}} = \frac{\partial(\cdot)}{\partial x_i} + \frac{1}{\zeta}\frac{\partial(\cdot)}{\partial y_i}$, the strain can be expressed as

$$\varepsilon_{ij}^{\zeta}(\mathbf{x},t) \equiv u^{\zeta}_{(i,x_j^{\zeta})}(\mathbf{x},t) = \varepsilon_{ij}^{m}(\mathbf{x},\mathbf{y},t) + O(\zeta) = u^{(0)}_{(i,x_j)}(\mathbf{x},t) + u^{(1)}_{(i,y_j)}(\mathbf{x},\mathbf{y},t) + O(\zeta) \tag{3.8}$$

where ε_{ij}^{m} is the micro-scale strain and $(\cdot)_{(i,x_j)} = \frac{1}{2}\left(\frac{\partial(\cdot)_i}{\partial x_j} + \frac{\partial(\cdot)_j}{\partial x_i}\right)$ means the symmetric gradient of a function with respect to coordinate $\mathbf{x}$. The stress is expanded as

$$\sigma_{ij}^{\zeta}(\mathbf{x},t) = \sigma_{ij}^{m}(\mathbf{x},\mathbf{y},t) + O(\zeta) = \sigma_{ij}^{(0)}(\mathbf{x},t) + \sigma_{ij}^{(1)}(\mathbf{x},\mathbf{y},t) + O(\zeta) \tag{3.9}$$

where σ_{ij}^{m} is the micro-scale stress and the micro-scale perturbation stress $\sigma_{ij}^{(1)}$ satisfies

$$\langle \sigma_{ij}^{(1)}(\mathbf{x},\mathbf{y},t) \rangle = 0 \tag{3.10}$$

where $\langle(\cdot)\rangle = \frac{1}{|\Theta|}\int_{\Theta}(\cdot)d\Theta$ is the volumetric average of $(\cdot)$ within the domain Θ.

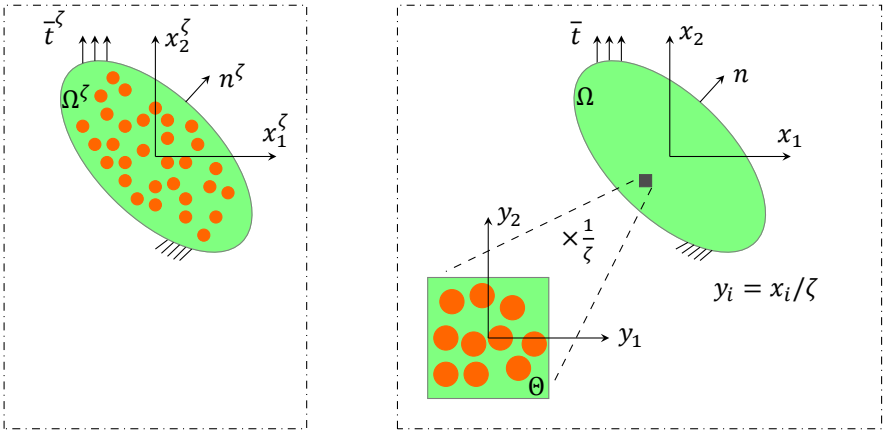

Figure 3.1: Problem statement. (a) original composite problem; (b) equivalent two-scale problem statement.

The inertia is given as the following expansion

$$\begin{aligned}\rho^{\zeta}\ddot{u}_i^{\zeta}(\mathbf{x},\mathbf{y},t) &= \rho^{(0)}\ddot{u}_i^{(0)}(\mathbf{x},t) + \zeta\rho^{(1)}\ddot{u}_i^{(1)}(\mathbf{x},\mathbf{y},t) + O(\zeta^2) \\ &= \rho^{(0)}\ddot{u}_i^{(0)}(\mathbf{x},t) + \zeta\rho^{(0)}h_i^{st}(\mathbf{x},\mathbf{y},t)\ddot{\varepsilon}_{st}^{(0)}(\mathbf{x},t) + O(\zeta^2)\end{aligned} \tag{3.11}$$

where $h_i^{st}(\mathbf{x},\mathbf{y},t)$ is the so-called acceleration influence function which satisfies $\rho^{(1)}\ddot{u}_i^{(1)} = \rho^{(0)}h_i^{st}\ddot{\varepsilon}_{st}^{(0)}$ and $h_i^{st}(\mathbf{x},\mathbf{y},t)$ is a $\mathbf{y}$-periodic function satisfying the normalization condition

$$\langle h_i^{st}(\mathbf{x},\mathbf{y},t)\rangle = 0 \tag{3.12}$$

Weak form

The weak form of Eq. (3.1) reads

$$\int_{\Omega^{\zeta}} \omega_{i,j}^{\zeta}\sigma_{ij}^{\zeta}d\Omega^{\zeta} + \int_{\Omega^{\zeta}} \omega_i^{\zeta}\rho^{\zeta}\ddot{u}_i^{\zeta}d\Omega^{\zeta} = \int_{\partial\Omega^{t\zeta}} \omega_i^{\zeta}\bar{t}_i^{\zeta}d\Gamma^{\zeta} \tag{3.13}$$

in which the test function $\omega_i^{\zeta} \in W^{\zeta} = \{\omega_i^{\zeta} \in C^0(\Omega^{\zeta}), \omega_i^{\zeta} = 0 \text{ on } \partial\Omega^{u\zeta}\}$. Integration of the two-scale functions over the composite domain and its boundary is carried out as

$$\int_{\Omega^{\zeta}}(\cdot)d\Omega^{\zeta} = \lim_{\zeta\to 0}\int_{\Omega}\langle\cdot\rangle_{\Theta}d\Omega \quad \text{and} \quad \int_{\partial\Omega^{\zeta}}(\cdot)d\Gamma^{\zeta} = \int_{\partial\Omega}(\cdot)d\Gamma \tag{3.14}$$

The test function is expanded as

$$\begin{aligned}\omega_i^{\zeta}(\mathbf{x},t) &= \omega_i^{(0)}(\mathbf{x},t) + \zeta\omega_i^{(1)}(\mathbf{x},\mathbf{y},t) + O(\zeta^2) \\ &= \omega_i^{(0)}(\mathbf{x},t) + \zeta h_i^{kl}(\mathbf{x},\mathbf{y},t)\omega_{(k,x_l)}^{(0)}(\mathbf{x},t) + O(\zeta^2)\end{aligned} \tag{3.15}$$

where the relation $\omega_i^{(1)}(\mathbf{x},\mathbf{y},t) = h_i^{kl}(\mathbf{x},\mathbf{y},t)\omega_{(k,x_l)}^{(0)}(\mathbf{x},t)$ is introduced.

By applying the two-scale integration scheme Eq. (3.14) to Eq. (3.13) and using Eq. (3.9), (3.10), (3.11), (3.12) and (3.15) and neglecting higher-order terms, it can be found that

$$\int_\Omega \omega_{(i,x_j)}^{(0)}\left[\sigma_{ij}^{(0)} + \zeta^2 D_{ijst}\ddot{\varepsilon}_{st}^{(0)}\right]d\Omega + \int_\Omega \omega_i^{(0)}\rho^{(0)}\ddot{u}_i^{(0)}d\Omega + \int_\Omega \langle\omega_{(i,y_j)}^{(1)}\sigma_{ij}^m\rangle_\Theta d\Omega = \int_{\partial\Omega^t}\omega_i^{(0)}\bar{t}_i d\Gamma \tag{3.16}$$

where $\omega_i^{(0)} \in W^{(0)} = \{\omega_i^{(0)} \in C^0(\Omega), \omega_i^{(0)} = 0 \text{ on } \partial\Omega^u\}$ and $\omega_i^{(1)} \in W^\Theta = \{\omega_i^{(1)} \in C^0(\Theta), \langle\omega_i^{(1)}\rangle_\Theta = 0, \omega_i^{(1)} = 0 \text{ on } \partial\Theta^u\}$ and the dispersion tensor $\mathbf{D}^M$ is introduced as

$$D_{ijst}^M = \zeta^2 D_{ijst}(\mathbf{x},t) = \rho^{(0)}\langle\, h_p^{ij}(\mathbf{y},t)h_p^{st}(\mathbf{y},t)\,\rangle_\Theta \tag{3.17}$$

where $(\cdot)^M$ denotes the macro-scale quantity. Therefore, the weak form for the two scales can be derived as

$$\int_\Omega \omega_{(i,x_j)}^{(0)}\left[\sigma_{ij}^{(0)} + \zeta^2 D_{ijst}\ddot{\varepsilon}_{st}^{(0)}\right]d\Omega + \int_\Omega \omega_i^{(0)}\rho^{(0)}\ddot{u}_i^{(0)}d\Omega = \int_{\partial\Omega^t}\omega_i^{(0)}\bar{t}_i d\Gamma \quad \text{(macro-scale)} \tag{3.18}$$

$$\frac{1}{|\Theta|}\int_\Theta \omega_{(i,y_j)}^{(1)}\sigma_{ij}^m d\Theta = 0 \quad \text{(micro-scale)} \tag{3.19}$$

The solution of these weak forms is found with separate finite element schemes for the two scales. Details about the extraction of the macro-scale stiffness S_{ijkl}^M are explained in Appendix B and the solution of the micro-scale problem is illustrated in the next section.

Micro-scale problem

It can be observed from Eq. (3.19) that the micro-scale problem is treated as a "quasi-dynamic" formulation following Fish et al. [32]. Considering that $S_{ijkl}^\zeta(\mathbf{x}) = S_{ijkl}^m(\mathbf{y})$ and leaving out the first order remnants in Eq. (3.8) and Eq. (3.9), the constitutive relation Eq. (3.6) can be rewritten as

$$\sigma_{ij}^m(\mathbf{x},\mathbf{y},t) = S_{ijkl}^m(\mathbf{y})\varepsilon_{kl}^m(\mathbf{x},\mathbf{y},t) \tag{3.20}$$

The micro-scale strain $\varepsilon_{kl}^m(\mathbf{x},\mathbf{y},t)$ is divided into two parts: one is caused by the macro-scale strain $u_{(i,x_j)}^{(0)}(\mathbf{x},t)$; the other one is driven by the macro-scale acceleration gradient. The micro-scale strain, from Eq. (3.8), is expressed as

$$\begin{aligned}\varepsilon_{kl}^m(\mathbf{x},\mathbf{y},t) &= u_{(k,x_l)}^{(0)}(\mathbf{x},t) + u_{(k,y_l)}^{(1)}(\mathbf{x},\mathbf{y},t)\\ &= \underbrace{u_{(k,x_l)}^{(0)}(\mathbf{x},t) + H_{(k,y_l)}^{st}(\mathbf{x},\mathbf{y},t)u_{(s,x_t)}^{(0)}(\mathbf{x},t)}_{\text{macro-scale strain related terms}} + \underbrace{\frac{\rho(\mathbf{y})}{\rho^{(0)}}f_{kl}^{(0)}(\mathbf{x},t) + h_{(k,y_l)}^{st}(\mathbf{x},\mathbf{y},t)f_{st}^{(0)}(\mathbf{x},t)}_{\text{macro-scale acceleration gradient related terms}}\end{aligned} \tag{3.21}$$

where H_k^{st} is a displacement influence function satisfying $\mathbf{y}-$periodicity and $\langle H_k^{st}\rangle_\Theta = 0$, and $f_{kl}^{(0)}(\mathbf{x},t)$ is a macroscopic quantity proportional to the macro-scale acceleration gradient so that $f_{kl}^{(0)} \equiv 0$ in the absence of macro-scale acceleration gradient.

It is to be noted that in Eq. (3.21) the first of the macro-scale strain related terms corresponds to a uniform strain on the microstructure while the second term is a fluctuation contribution to keep the microstructure to be in self-balanced state. Similarly, the first term of macro-scale acceleration gradient related parts in Eq. (3.21) represents a uniform acceleration gradient over the microstructure while the second terms refers to a fluctuation contribution to keep the microstructure in equilibrium under the excitation of a macroscopic acceleration gradient.

Substituting Eq. (3.20) and Eq. (3.21) into Eq. (3.19) leads to

$$\int_{\Theta} \omega^{(1)}_{(i,y_j)} \left[S^m_{ijkl}(\mathbf{y}) \left(I_{klst} + H^{st}_{(k,\mathbf{y}_l)}(\mathbf{y},t) \right) u^{(0)}_{(s,x_t)}(\mathbf{x},t) \right] d\Theta + \int_{\Theta} \omega^{(1)}_{(i,y_j)} \left[S^m_{ijkl}(\mathbf{y}) \left(\frac{\rho(\mathbf{y})}{\rho^{(0)}} I_{klst} + h^{st}_{(k,\mathbf{y}_l)}(\mathbf{y},t) \right) f^{(0)}_{st}(\mathbf{x},t) \right] d\Theta = 0 \tag{3.22}$$

where $I_{klst} = \delta_{ks}\delta_{lt}$ and δ_{ks} is the Kronecker delta tensor. Considering the arbitrariness of $u^{(0)}_{(s,x_t)}$ and $f^{(0)}_{st}$, Eq. (3.22) can be split into two separate equations

$$\int_{\Theta} \omega^{(1)}_{(i,y_j)} \left[S^m_{ijkl}(\mathbf{y}) \left(I_{klst} + H^{st}_{(k,\mathbf{y}_l)}(\mathbf{y},t) \right) \right] d\Theta = 0 \tag{3.23}$$

and

$$\int_{\Theta} \omega^{(1)}_{(i,y_j)} \left[S^m_{ijkl}(\mathbf{y}) \left(\frac{\rho(\mathbf{y})}{\rho^{(0)}} I_{klst} + h^{st}_{(k,\mathbf{y}_l)}(\mathbf{y},t) \right) \right] d\Theta = 0 \tag{3.24}$$

Of these, the second one is solved for the acceleration influence function h^{st}_k with finite elements over the micro-scale domain. Details about the solution procedures of Eq. (3.24) are given in Appendix C. By use of Eq. (3.17), h^{st}_k gives the dispersion tensor which is used in the macro-scale weak form, i.e. Eq. (3.18).

3.2.2. Acceleration influence functions

The effect of inertia in the micro-scale is considered by an eigenstrain [37] and therefore only the solution of a typical quasi-static balance problem is needed. As it is pointed out in Fish et al. [32], it is possible to get a closed form solution of the micro-scale balance Eq. (3.19) in the case of a 1D composite bar with two different phases of material with elastic material constants of E_1, ρ_1 and E_2, ρ_2.

For a microstructure with one circular inclusion, the six acceleration influence functions are plotted in figure 3.2. The elastic modulus, Poisson's ratio, mass density of the inclusion and matrix are $E_i = 200$ GPa, $\mu_i = 0.2$, $\rho_i = 10000$ Kg/m^3 and $E_m = 2$ GPa, $\mu_m = 0.2$, $\rho_m = 4000$ Kg/m^3. The volume fraction of the inclusion is 60% and its diameter is 5 μm. From Eq. (3.21), it is known that the acceleration influence functions h^{mn}_k can be interpreted as the first-order microstructural correction to the eigendeformation field as triggered by the macro-scale acceleration gradient. For instance, the negative gradient of h^{11}_1 along y_1-direction in the domain occupied by the stiff inclusion implies that the true acceleration induced strain in the inclusion is smaller than that in the matrix domain. For a microstructure with 25×25 randomly positioned inclusions while keeping the other properties unchanged, the influence

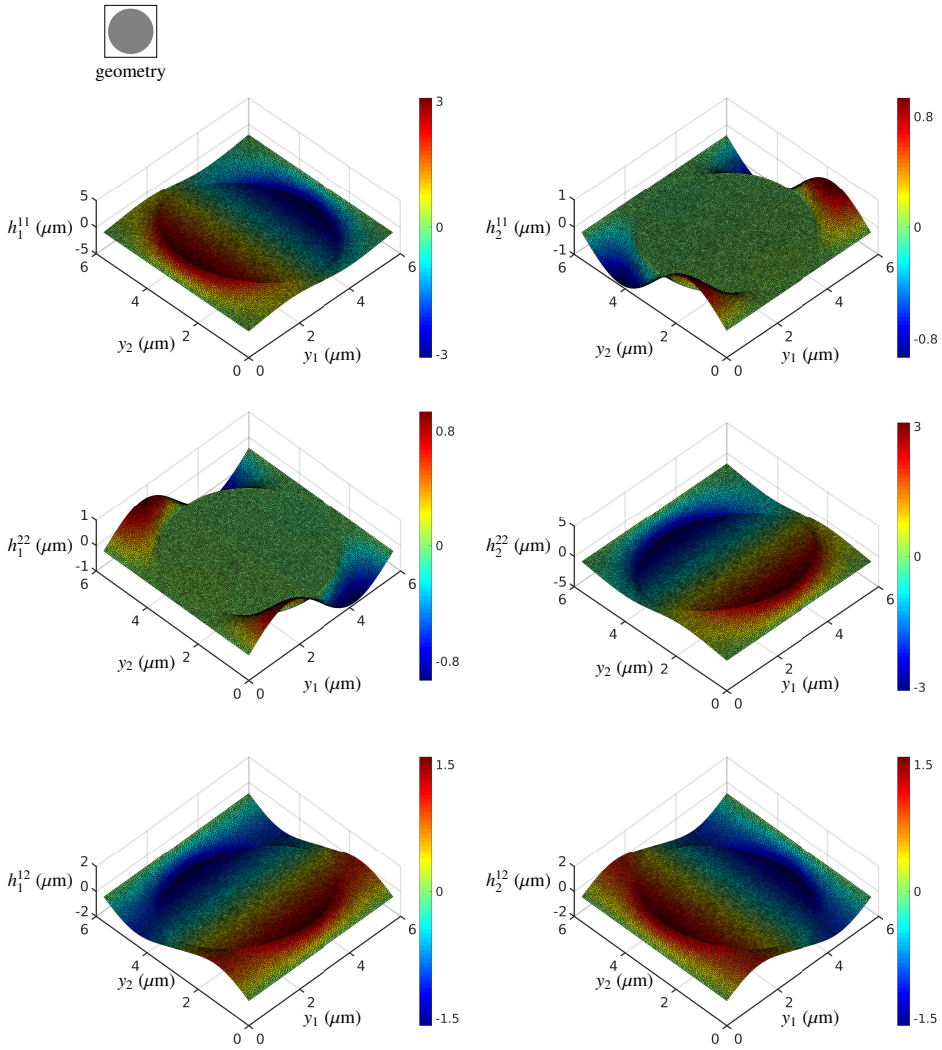

Figure 3.2: Acceleration influence function h_k^{mn} for a one inclusion microstructure (the enclosed subfigure shows the studied microstructure).

function $h_k^{11}(k = 1, 2)$ is plotted in Fig. 3.3. Some observations can be made: (1) the gradient $h_{(1,y_1)}^{11}$ in the inclusions phase is still negative and has similar magnitude among all the inclusions, and (2) both h_1^{11} and h_2^{11} show regions where peaks are higher and regions where peaks are lower as a consequence of the mesostructure.

3.2.3. Properties of dispersion tensor

The magnitude of the dispersion tensor depends on several characteristics of the microstructure. (i) The contrast of material properties between the constituents. In terms of a one-dimensional two-phase composite bar, if the wave impedance is the same for the two phases, the dispersion tensor is null [32]. This is consistent with the fact that when the wave impedance is the same, wave dispersion due to material heterogeneity is not present. To investigate the influence of material contrast on the dispersion tensor, the dispersion tensor is computed for a single microstructure with 15×15 fibers and a fiber volume fraction of 60%. The Young's modulus and density of the inclusion are varied proportionally as $E_i = cE_m$ and $\rho_i = c\rho_m$ for $c \in [2, 4, 9, 16, 30]$, respectively, with the Poisson's ratio unchanged. The six independent components of the dispersion tensor D_{ijkl}^M, normalized with respect to the values of the sample with the lowest property contrast, $D_{ijkl}^M(c = 2)$, for the five cases are shown in Fig. 3.4a. It can be seen that the magnitude of all six components are increasing with larger properties contrast, which means that the expected dispersion effect should be larger for a higher contrast composite. (ii) The diameter of inclusions. Similarly, the dispersion tensor is computed for five cases with the same material properties and microstructure with 15×15 inclusions but with different inclusion diameter, $d_i \in [0.005, 0.025, 0.1, 0.25, 0.5]$ mm. The variation of D_{1111}^M as function of d_i is plotted in Fig. 3.4b along with a quadratic fit. It can be observed that the relation between D_{1111}^M and d_i can be described very well as a quadratic relation and the same was found for the other components of the dispersion tensor. This quadratic relation can also be found in the closed-form solution of the dispersion tensor for a one-dimensional two-phase composite bar given in [32]. This means that for larger inclusions, the influence of dispersion is larger. To ensure a mesh-independent solution of D_{1111}^M, five different mesh sizes of the case with the fiber diameter $d_i = 0.25$ mm are solved, with the number of elements ranging from 22624 to 288800. It is shown in Fig. 3.4c that after the mesh size has reached the medium size, the dispersion tensor component D_{1111}^M has reached converged values. Therefore, this mesh size is adopted for the study described in Section 3.4 and Section 3.5.

3.3. Comparison with direct numerical simulation

In this section, elastic wave propagation in a periodic composite medium is simulated to investigate the performance of the introduced dispersive homogenization model in comparison with direct numerical simulation (DNS). Two cases are considered, one with a one-dimensional microstructure and one with a two-dimensional microstructure.

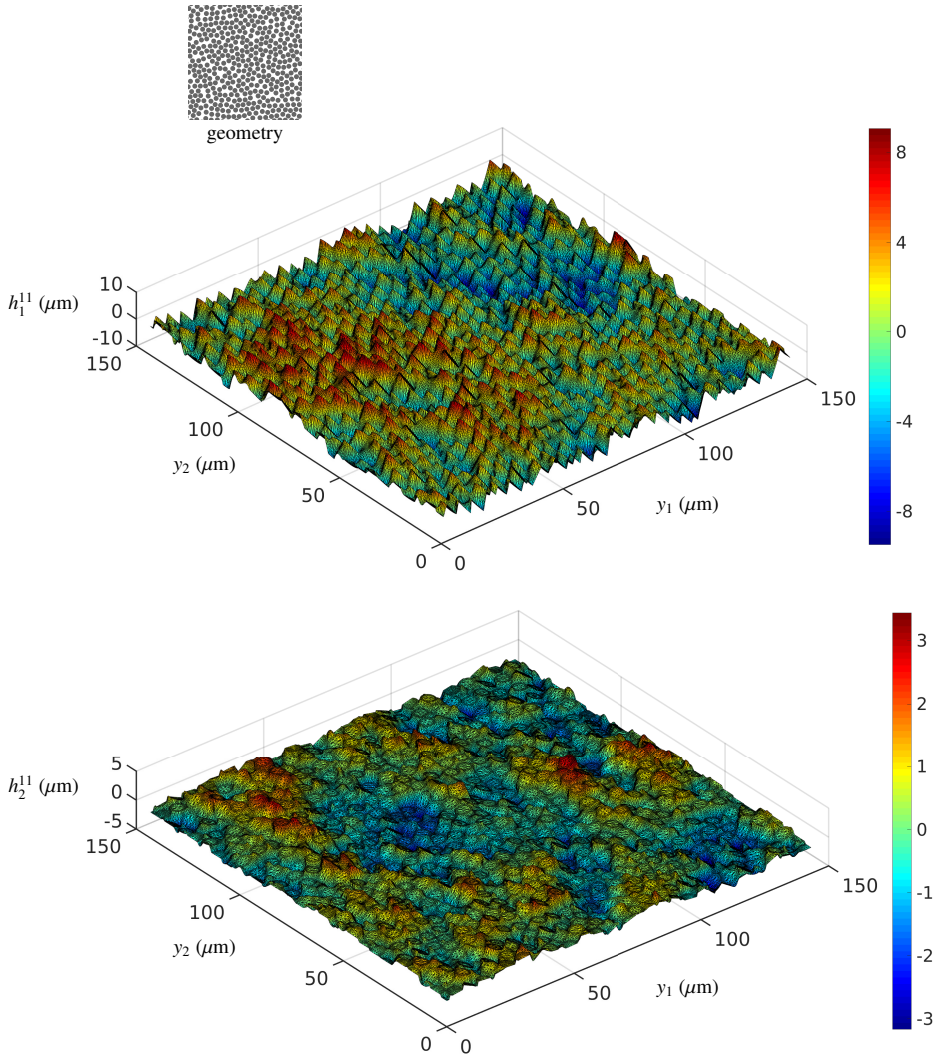

Figure 3.3: Influence function h_1^{11} and h_2^{11} for a 25×25 inclusions microstructure (the enclosed subfigure shows the studied microstructure).

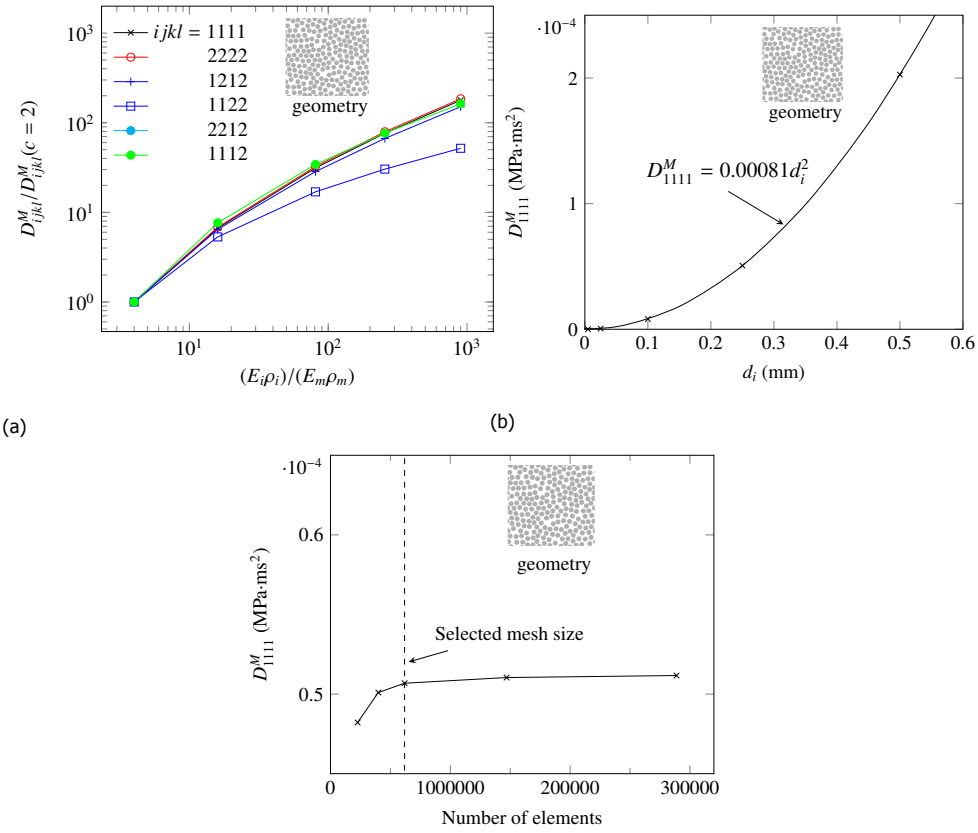

Figure 3.4: Properties of dispersion tensor. (a) Normalized dispersion tensor components; (b) dispersion tensor component D^M_{1111} vs. diameter of inclusion; (c) mesh density influence of D^M_{1111} (the dashed line shows the converged mesh size).

3.3.1. 1D elastic wave propagation

Elastic wave propagation in a periodic two-phase composite bar is studied similar to Karamnejad and Sluys [33]. Geometry and properties are such that wave propagation is purely one-dimensional. The material properties of the two phases are $E_1 = 200$ GPa, $\rho_1 = 10000$ kg/m^3, $\nu_1 = 0$ and $E_2 = 2$ GPa, $\rho_1 = 4000$ kg/m^3, $\nu_2 = 0$. The wave impedance contrast between the two phases is $E_1\rho_1/E_2\rho_2 = 250$. The left end of the bar is fixed. Two types of loading are considered. Firstly, a incoming harmonic wave is imposed on the right end of the bar so that the horizontal displacement $u(t)$ on the right edge satisfies $u(t) = A_0 \sin(2\pi f t)H(\frac{1}{2f} - t)$ in which $A_0 = 0.025$ mm represents the magnitude, $f = 50000$ Hz is the wave frequency and $H(\cdot)$ is the Heaviside step function. The bar consists of 100 repeating unit cells for a total length of 500 mm as shown in Fig. 3.5. Four numerical models are considered: two single-scale models, namely the fine heterogeneous model (DNS) and the fine model with homogenized properties, and two multiscale models, namely the coarse non-dispersive model and the coarse dispersive model. The two fine models consist of 4500 quadrilateral elements. For the one with homogenized properties, the elastic modulus and density of the two phases are prescribed to be the homogenized values, i.e. $E^M = 4.926$ GPa and $\rho^M = 7600$ Kg/m^3, respectively. This model therefore neglects wave reflection and transmission at material interfaces. By contrast, the heterogeneous DNS model considers the heterogeneity of the composite bar and is therefore considered as the reference exact solution of this problem. The two coarse multiscale models use 500 quadrilateral elements with one Gauss-integration point corresponding to a unit cell domain. Homogenized elastic properties are used and the analysis is performed with and without dispersion tensor. The main dispersion tensor component D^M_{1111} for this simple microstructure can be obtained by a closed-form solution following Fish et al. [32]. The dispersion tensor is evaluated numerically as

$$\mathbf{D}^M = \begin{bmatrix} 0.0095 & 0 & 0 \\ 0 & 0 & 0 \\ 0 & 0 & 0.0095 \end{bmatrix} \quad \text{MPa} \cdot \text{ms}^2 \tag{3.25}$$

It is shown in Karamnejad and Sluys [33] and Fish et al. [32] that the ratio between macroscopic wave length l^M and the unit cell size l^m determines the extent of dispersion. If l^M is more than five times larger than l^m, the dispersive effect can be neglected. The dispersive model shows considerably better accuracy than the non-dispersive model within the first pass frequency band[1]. In this case, the wave length is calculated by $l^M = \sqrt{E^M(\rho^M)^{-1}}/f = 16.1$ mm, while the unit cell size $l^m = 5$ mm. Therefore, the ratio $l^m/l^M = 0.3106$ in this case, which corresponds to a shorter wave length than Karamanejad and Sluys [33]. The displacement field along the bar is plotted for four typical time instants in Fig. 3.6. It can be seen in

[1] According to Andrianov et al. [38], a periodic elastic composite behaves like a discrete wave filter. A discrete pass frequency band and stop frequency band structure is formed. Whenever the wave frequency is within the stop frequency band, its magnitude is exponentially attenuated such that the wave is not able to propagate. Only when the wave frequency is within the pass frequency bands, propagation is admissible.

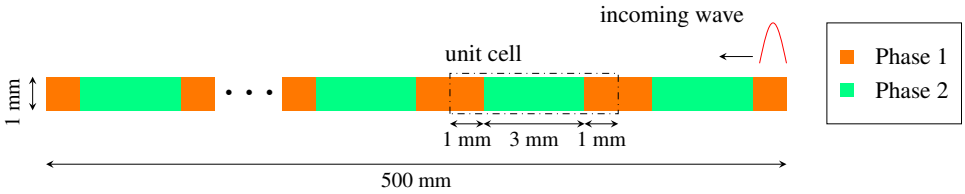

Figure 3.5: Harmonic wave propagating in a periodic bar consisted of 100 unit cells. The microstructure of the unit cell is demonstrated.

the DNS reference solution that the input sinusoidal pulse is not maintained during the propagation and there exists significant amplitude decay. The resultant displacement field shows sharp kinks representing high velocity gradients. This flutter characteristic is mainly due to the high wave impedance contrast between the two phases of the structure, which causes wave reflection. The result of the fine homogenized model shows a well maintained profile although with a small amount of leading oscillation related to the discretization. A comparison between the DNS model and fine homogenized model shows that dispersion is indeed significant for the studied wave length. The solution from the coarse non-dispersive model shows very strong oscillations due to numerical dispersion effects caused by a coarse mesh and the match with the DNS model solution is poor. The coarse dispersive model shows a relatively smooth response. This is because for the dispersive model there is no physical interface in the macro-scale model, so the wave can not "feel" the interface. Nevertheless, there exists reasonably good agreement between the dispersive solution and the DNS model solution before wave reflection at the left edge (a-c) and after reflection (d) although the dispersive model predicts a stronger decay of magnitude for the oscillation at the rear of the wave. A higher order homogenization scheme could result in a higher accuracy but with more computational costs, see for instance [39].

Secondly, loading which mimics an impact-induced loading pulse is considered, to demonstrate the capability of the introduced dispersive numerical model for impact problems. The problem setting is the same as described in Fig. 3.5 except that the horizontal displacement on the right edge is prescribed as

$$u(t) = \begin{cases} \frac{V}{2T}t^2 & , t \leq T \\ \frac{VT}{2} + A \cdot (t - T) & , T < t \leq 2T \\ 2VT - \frac{A}{2T}(3T - t)^2 & , 2T < t \leq 3T \\ 2VT & , t > 3T \end{cases} \tag{3.26}$$

in which V and T are constants. This corresponds to a trapezoidal velocity pulse shown in Fig. 3.7. Two load periods are considered for this type of loading: (1) $T = 0.01$ ms and (2) $T = 0.001$ ms with the same $V = 5.0$ m/s. The displacement field for two typical time instants along the bar for four models, i.e. the fine heterogeneous model (DNS), the fine homogenized model, the coarse non-dispersive multiscale model and the coarse dispersive multiscale model, is plotted in Fig. 3.8

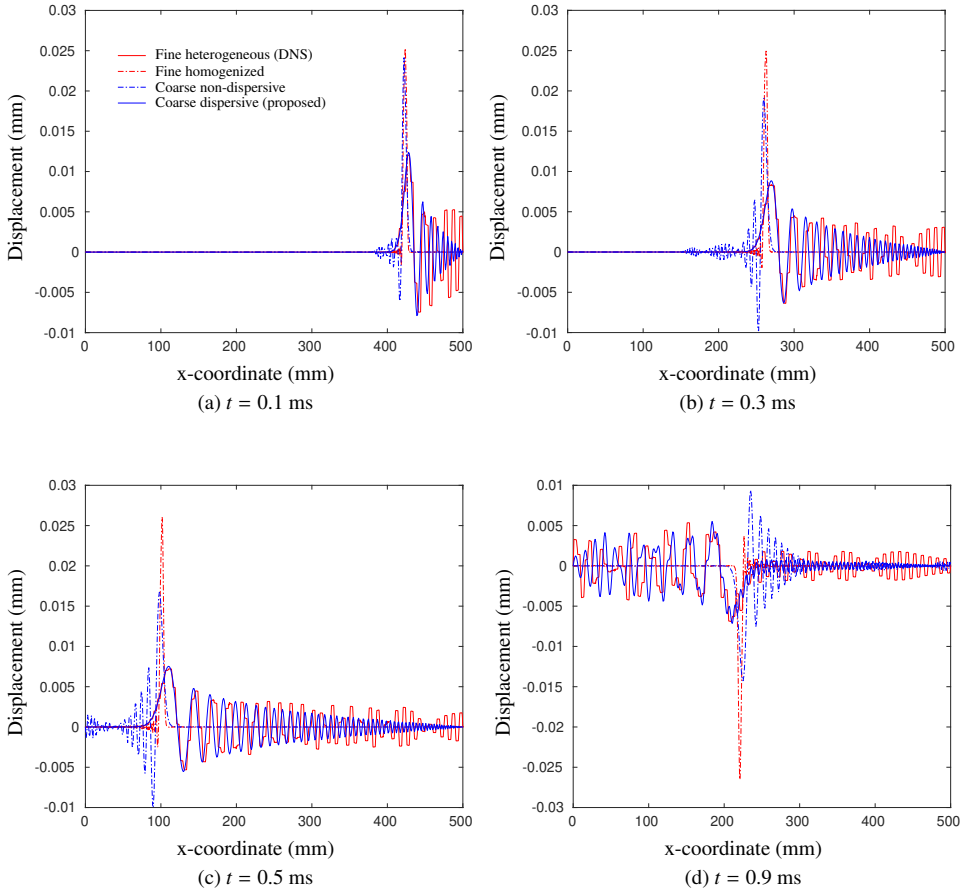

Figure 3.6: plots of displacement field at different time for DNS-heterogeneous, DNS-homogeneous, dispersive multiscale and non-dispersive multiscale model.

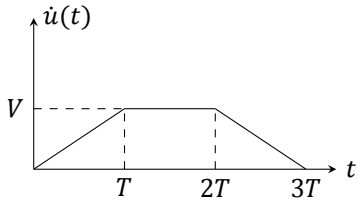

Figure 3.7: Loading pulse of velocity $\dot{u}(t)$ applied at the right edge of the bar.

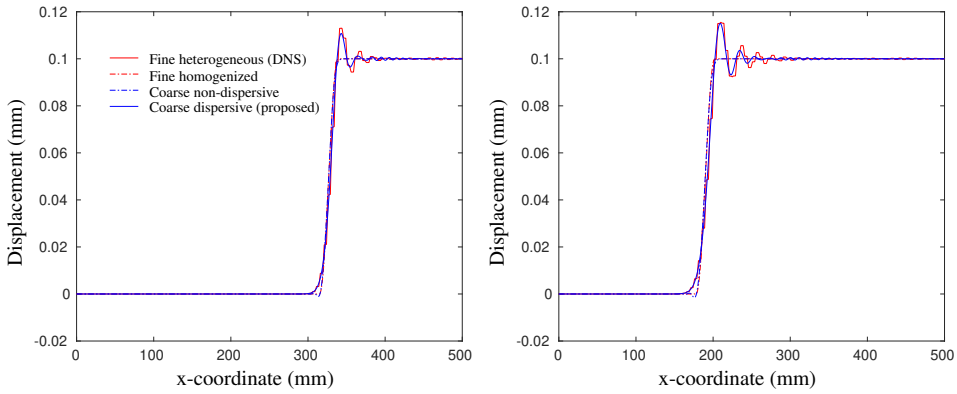

(a) $t = 0.23$ ms (b) $t = 0.4$ ms

Figure 3.8: plots of displacement field at different time instants for loading pulse with $T = 0.01$ ms.

and Fig. 3.9 for the two loading periods. It can be found that dispersion is significant in both cases as the DNS solution is different from the fine homogenized model solution. The second case with shorter time duration shows more evident dispersion. For both cases, the coarse dispersive model shows a better agreement with the DNS model than the non-dispersive model. From the examples of a harmonic loading and a trapezoidal loading, it is concluded that the dispersive multiscale model offers considerable improvements over the non-dispersive model for 1D elastic wave propagation problems. The dispersive multiscale model allows for capturing dispersion with a discretization at macroscale that is coarser than the microstructural resolution.

3.3.2. Two-dimensional wave propagation

Next, elastic wave propagation in a material with a two dimensional microstructure subjected to an incoming sinusoidal wave is considered. The geometry consists of 100 repeating microstructures with a total length of 57.04 mm. There are two phases of materials, circular inclusions with a diameter of 0.5 mm and a surrounding matrix. The top edge and bottom edge of the structure are fixed in vertical direction, which together with plane-strain conditions mimics the state for materi-

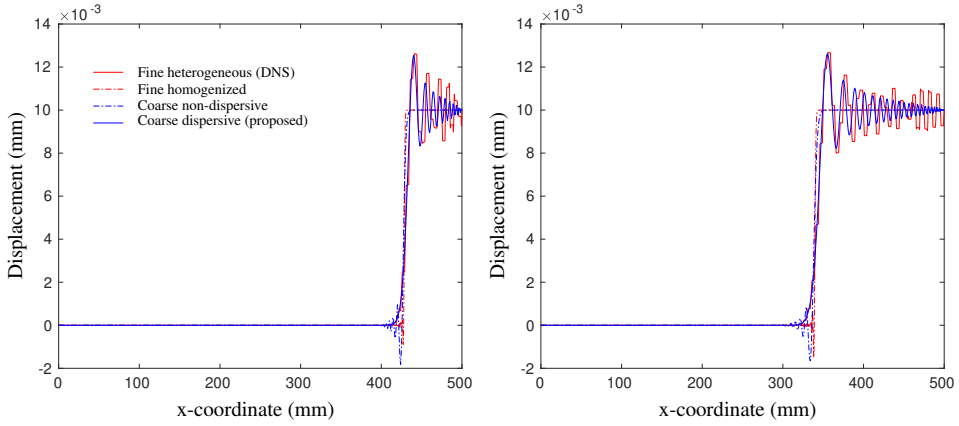

(a) t = 0.09 ms (b) t = 0.2 ms

Figure 3.9: plots of displacement field at different time instants for loading pulse with $T = 0.001$ ms.

als in the middle region along the thickness direction for a plate impact test [40]. The horizontal displacement u_1 of the incoming wave at the right edge satisfies $u_1 = A_0 \sin(2\pi f t) H(\frac{1}{2f} - t)$ with $A_0 = 0.025$ mm and $f = 400$ KHz with constrained vertical displacement $u_2 = 0$. The elastic properties of inclusion and matrix are the Young's modulus $E_i = 200$ GPa, $E_m = 2$ GPa, density $\rho_i = 10000$ Kg/m^3, $\rho_m = 4000$ Kg/m^3, and the Poisson's ratio $\nu_i = 0.2$, $\nu_m = 0.33$. The volume fraction of inclusions V_i is 60%. Similar to Section 3.3.1, four numerical models are considered: the fine heterogeneous model (DNS), the fine model with homogenized properties, the coarse non-dispersive multiscale model and the coarse dispersive multiscale model. The fine models are discretized with 501170 linear triangular elements (see Fig. 3.10). For the homogenized one, the material properties of the complete domain are prescribed to be the homogenized values of each phase. By contrast, the DNS model keeps the different properties of each phase and therefore the dispersion caused by material heterogeneity is naturally included. The coarse models are discretized with 500 linear quadrilateral elements at the macro-scale while each Gauss integration point corresponding to a micro-scale problem solved within a unit cell domain as shown in Fig. 3.11. The coarse non-dispersive model neglects the contribution of dispersion at the macro-scale while the dispersive model adds the dispersion tensor contribution to capture the dispersion effect. The RVE for this structure is clearly identified as the unit cell. The dispersion tensor is found using the procedures illustrated in Appendix C as:

$$\mathbf{D}^M = \begin{bmatrix} 1.529e-4 & 1.770e-5 & -2.762e-8 \\ 1.770e-5 & 1.529e-4 & -1.499e-8 \\ -2.762e-8 & -1.499e-8 & 9.953e-5 \end{bmatrix} \text{ MPa} \cdot \text{ms}^2 \tag{3.27}$$

The averaged horizontal displacement $\overline{u}(x)$, i.e. the volumetric average of hori-

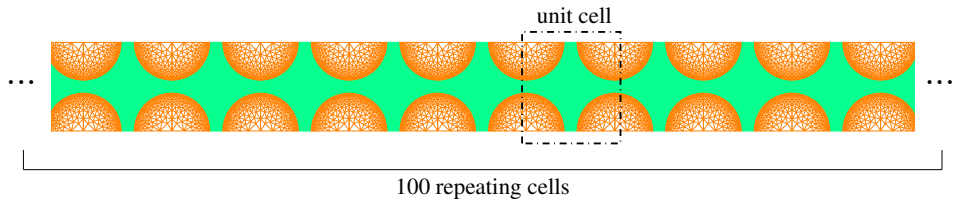

Figure 3.10: The DNS model mesh (501170 linear triangular elements).

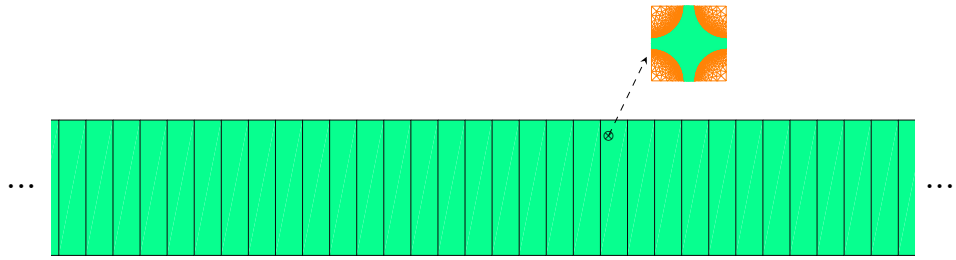

Figure 3.11: The multiscale model (500 linear quadrilateral elements).

zontal displacement within a constant distance l_s, along the bar for two time instants is plotted in Fig. 3.12. In this study, l_s is equal to 1/500 of the total length of the bar. According to the reference DNS solution, the input sinusoidal wave does not maintain its profile during the propagation and it breaks into several pulses with obvious magnitude decay. The profile also shows significant oscillations caused by reflections at material interfaces. The magnitude decay of the DNS model exhibits a more gradual process than the 1D wave propagation problem considered in Section 3.3.1. This is due to the two-dimensional nature of the microstructure. The coarse dispersive model captures the magnitude of the wave well although it predicts a more smooth wave profile. The computational time per time step for the dispersive multiscale model is around 0.04 seconds while for the DNS model around 2.5 seconds is needed on the same system (a PC with a 16 GB of memory and 3.5 GHz Intel Xeon CPU).

3.4. RVE existence study

In the previous section, the accuracy of the introduced dispersive model has been validated for periodic composite structures in which an RVE can be clearly defined as the building unit cell. However, for engineering materials such as fiber reinforced composites, the assumption of a periodic microstructure is not representative. Spatial variations in the fiber distribution can affect the material response. The existence of an RVE for this multiscale approach needs to be assured before the dispersive multiscale model can be applied to simulate realistic composites with

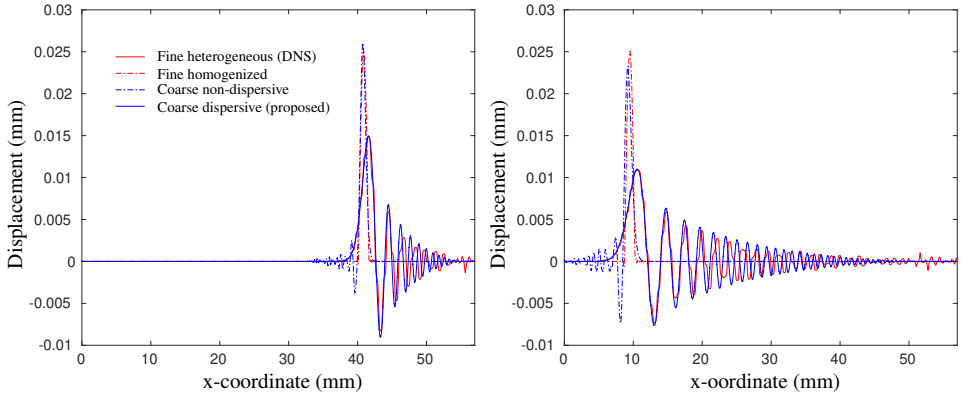

(a) t = 0.014 ms (b) t = 0.04 ms

Figure 3.12: plots of displacement field at different time.

random microstructure. The definition of an RVE prescribes that the size should be sufficiently large such that further increase of the size does not lead to change in the homogenized properties (or effective response). Therefore, the homogenized quantities, i.e. the dispersion tensor and the stiffness tensor, of random microstructures with different sizes are calculated in this study. It is noted that with reference to undirectional fiber-reinforced composites circular inclusions are considered here while non-circular inclusions, for instance, ellipses with different aspect ratio, can be considered for other materials, following Li et al. [41]. In this section, the numerical tool used to generate random microstructures is firstly described, followed by a study of the spatial distribution features of generated numerical samples. Finally, convergence of the dispersion tensor and stiffness tensor for realistic composite microstructure with respect to micromodel dimensions are presented.

3.4.1. Generation of random microstructure with DEM

Following van der Meer [42], a Discrete Element Method (DEM) solver called HADES, developed by Stroeven [43], is used to generate numerical samples of random microstructures. DEM allows for generation of high packing density of granular samples, as the final configuration is a result of stochastic initial conditions and particle-to-particle collisions under external environment force and boundary conditions.

The process for generating a two-dimensional numerical sample with desired packing density V_i is described as follows (see Fig. 3.13): A large box-shaped reference body is created initially, which contains a predefined number of $\mathbf{N_i}$ circular particles with either a given constant diameter D_i or a given diameter distribution curve $f(D_i)$. The initial positions of the particles are random perturbations of horizontally and vertically aligned locations. The initial velocity of any particle is prescribed to be the same in the horizontal and vertical direction but with a randomly

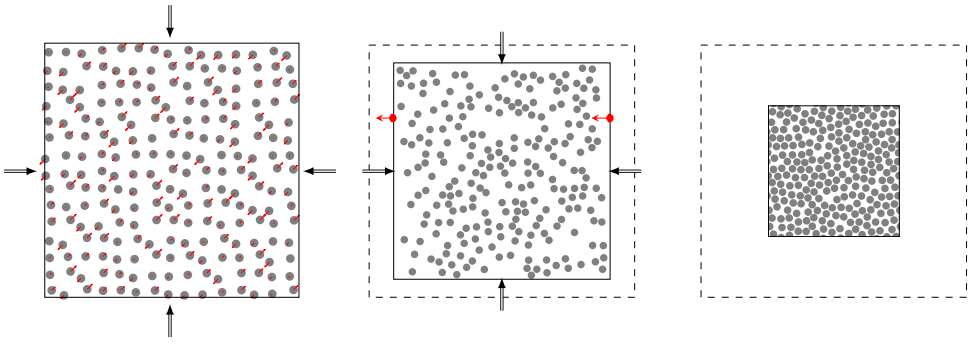

Figure 3.13: Processes for generation of numerical samples with periodic boundary condition. (a) Initial configuration of a particle system (red arrows show a typical initial velocity field of particles and black arrows shows the diminishing motion); (b) intermediate configuration (dashed box shows the undiminished reference body, red particles with arrows denoting the moving direction demonstrate the effect of periodic boundary condition); (c) final configuration: a numerical sample of composite microstructure.

assigned magnitude and sign for each particle. The reference body is gradually diminishing with the same velocity in the horizontal and vertical direction (see Fig. 3.13 (a)). Periodic boundary conditions are applied to the reference body to avoid any wall effect [18]. This means that during the simulation whenever a moving particle is crossing the edge (or corner) of the diminishing reference body, it reappears in the corresponding edge (or corner) during the DEM simulation (see Fig. 3.13 (b)). The collision between particles are treated with the Hertz contact law [43]. The inter-particle contact can introduce energy dissipation characterized by contact damping. In the case that damping coefficients are non-zero, continuous energy loss due to contact results in a clustering effect on the resulting particle system. It will be demonstrated in Section 3.4.2 that this phenomenon can be clearly demonstrated with the spatial distribution pattern of the particle system. A minimum contact distance parameter $d_{\min}$ is enforced so that any two particles can not be closer than this value, following the same hard-core model concept as in [44–47]. It can be expected that decreasing the size of the reference body has the effect of increasing the volume fraction of particles. The simulation stops when the reference body has decreased such that the desired packing density, i.e. volume fraction, is reached (see Fig. 3.13 (c)). After this, a mesh is generated with GMSH [48] for the inclusions and the matrix.

3.4.2. Spatial point distribution analysis

For the random microstructure of composites reinforced with long fibers, the inclusions can be considered as discrete circular objects dispersed into a continuum matrix in a two-dimensional domain. The spatial positioning of these inclusions is stochastic for realistic composites due to the manufacturing processes and conditions. By treating the center of each inclusion as one point, statistical spatial point

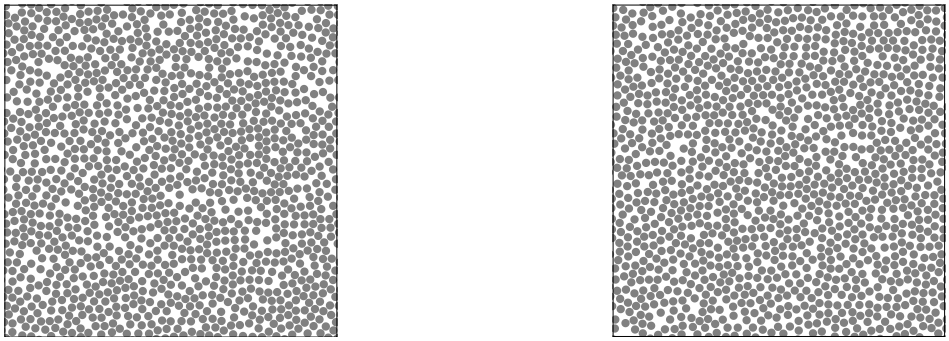

Figure 3.14: A representative sample of (a) batch A and (b) batch B.

pattern analysis can be applied to characterize the microstructure. As it is commented in Bailey and Gatrell [49], the basic interest in analysing the spatial point process is in whether the observed events exhibit any systematic pattern, as opposed to being distributed randomly in space. Possibilities for these patterns are classified as first order or second order effects. First order effects relate to variation in the mean value of the process in space representing a global trend in the distribution of inclusions. Second order effects result from the spatial dependence in the process, representing a local effect. This can be described by the probability density function of the nearest neighbour distances and Ripley's K function [49].

In this study, numerical samples of composite microstructures generated by HADES are first evaluated for their spatial distribution pattern. By introducing the contact damping within the DEM solver, the inter-particle (inclusion) distances become smaller, representing local effects. To demonstrate the influence of contact damping, two batches of numerical samples are considered, one with nonzero contact damping (batch A) and the other with zero contact damping (batch B). The probability density function of the nearest neighbour distances and Ripley's K function are evaluated for these two batches of samples.

Nearest neighbour distances

The nearest neighbour distance (NND) measures the shortest inter-inclusion interaction. The Nth ($N = 1, 2, ...$) nearest neighbour distance is the distance between a randomly chosen inclusion and its Nth closest neighbour in the studied domain [49]. It is assumed that the studied numerical sample is in some sense representative of any region from a realistic composite microstructures. Therefore, it is needed to determine at which size the NND distribution function has converged. Eight different sizes are considered, by varying the number of inclusions per sample N_i with values among $[5 \times 5, 10 \times 10, 15 \times 15, 20 \times 20, 25 \times 25, 30 \times 30, 35 \times 35, 40 \times 40]$. By increasing the number of inclusions while keeping the volume fraction unchanged, the total volume of the micromodel is also changed. For a given size, 100 random

numerical samples are generated to ensure the representativeness of possible spatial distributions. Representative numerical samples of batch A and B are shown in Fig. 3.14. The diameter of the inclusions D_i is kept as a fixed value of 5 μm and their volume fraction V_i is 60%. The minimum contact distance $d_{\min}$ is set to be 0.18 μm.

In Fig. 3.15a, the probability density of the 1st NND at different distances corresponding to different sample sizes for batch A is shown. The value of the probability density at a distance h represents the "chance" of the 1st NND for an inclusion to be h. A detailed view of the probability density of the 1st NND at two typical distances for different sample sizes is plotted in Fig. 3.15b. It is noted that in order to eliminate the influence of the sample boundary on the probability density function of the 1st NND for a given numerical sample (e.g. Fig. 3.13c), a toroidal correction is applied. It assumes that the top and left of the sample domain is connected to the bottom and right, respectively, as if the sample domain is a torus [50, 51]. It can be found from Fig. 3.15 that as the size of sample increases, the mean value of the 1st NND density function gradually converges and the standard deviation decreases. When the sample has 35×35 inclusions, the 1st NND function represents a size-independent function for this batch of samples. The same holds for the numerical samples of batch B. With this converged size, the probability density function of the 1st and 2nd NND for batch A and batch B are evaluated, with the mean value and standard deviation shown in Fig. 3.16. It can be found that the largest probability of 1st NND occurs around 5.21 μm for both batch A and batch B, however, batch A has a larger peak value than batch B. The 2nd NND shows the largest probability around 5.24 μm for batch A while the largest probability for batch B occurs at around 5.38 μm. Again, the peak value of batch A is larger than batch B. These observations show that the spatial distribution of inclusions of batch A is more clustered than that of batch B, which is a result of the contact damping included for batch A.

Ripley's K function

The nearest neighbour distance considers the point pattern on the smallest scale. Information on larger scales is considered by Ripley's K function [49]. The K function is the ratio between the expected number of inclusions within a circle of radius h of an arbitrary inclusion and the mean number of inclusions per unit area. A direct estimate of $K(h)$ from a numerical sample is given by [49]

$$K(h) = \frac{A}{N_i^2} \sum_i \sum_{j \neq i} \frac{I_h(d_{ij} \leq h)}{w_{ij}} \tag{3.28}$$

in which A is the area of the sample, N_i is the total number of inclusions, d_{ij} is the distance between inclusion i and j, $I_h(x)$ is an indicator function which has a value of 1 if the condition x is true otherwise 0, and w_{ij} is a weighting function for edge correction following Zangenberg and Brøndsted [51]. A homogeneous point process with no spatial dependence is the Poisson process with $K = \pi h^2$ [49]. The mean value and standard deviation of the K function for batch A and B are plotted in Fig. 3.17 along with the Poisson solution. The standard deviations for the

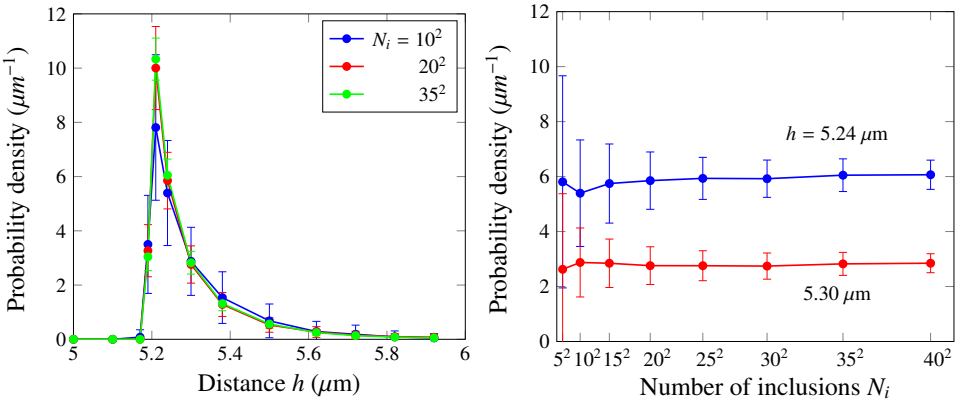

(a) (b)

Figure 3.15: (a) The 1st NND for different sample sizes; (b) 1st NND at two distances for different sample sizes.

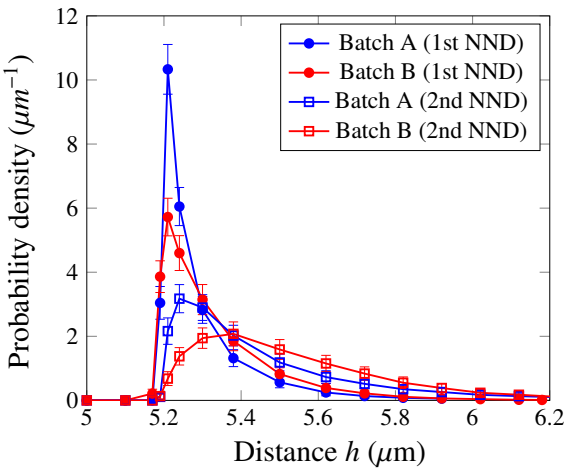

Figure 3.16: The probability density function of the 1st and 2nd NND for sample batch A and sample batch B (35×35 inclusions).

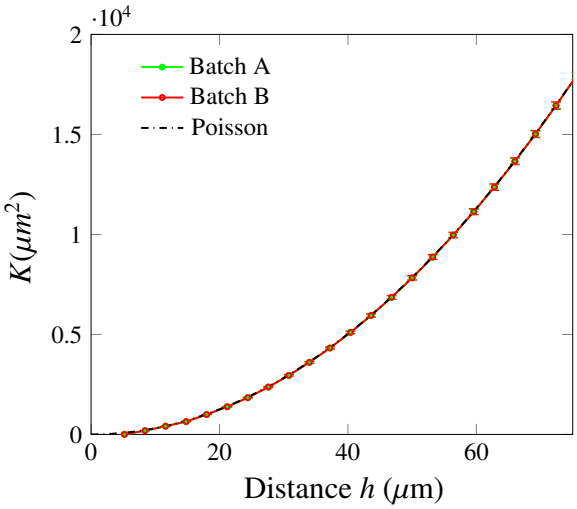

Figure 3.17: The calculated K function at different distances h.

two batches are both very small. The mean value of the K functions for the two batches are very close to each other and both approach the Poisson distribution for larger length scales. It is concluded that the first and second NND provides a good indicator to distinguish between different fiber distributions, while Ripley's K function is less informative.

3.4.3. Convergence of dispersion tensor

The influence of micromodel size on the dispersion tensor for the two batches is investigated to examine the convergence of the dispersion tensor. With the methodology mentioned in Section 3.2, the dispersion tensor can be solved using finite element models. The material properties for inclusions are prescribed as the Young's modulus $E_i = 74$ GPa, Poisson's ratio $\mu_i = 0.2$, density $\rho_i = 2500$ Kg/m^3 and the matrix properties are Young's modulus $E_m = 3.76$ GPa, Poisson's ratio $\mu_m = 0.3$, density $\rho_m = 1200$ Kg/m^3. There are six independent components for the dispersion tensor due to symmetry. Fig. 3.18 shows the mean value and standard deviation of the individual components of the dispersion tensor for the numerical samples of batch A and batch B. Again, 100 realizations of the fiber distribution are solved for each batch and each N_i.

There are several similar observations for the two batches. The mean and standard deviation of $\overline{D}^M_{1111}$ and $\overline{D}^M_{2222}$ are very close to each other, which means that no directional bias is created with either the numerical samples or the dispersive multiscale formulation. The mean values of the cross terms of $\overline{D}^M_{1112}$ and $\overline{D}^M_{2212}$ are calculated to be very close to zero, as expected for a transversely isotropic material. However, certain different findings can be made for the two batches. It is seen that the mean value of the six independent components of the dispersion ten-

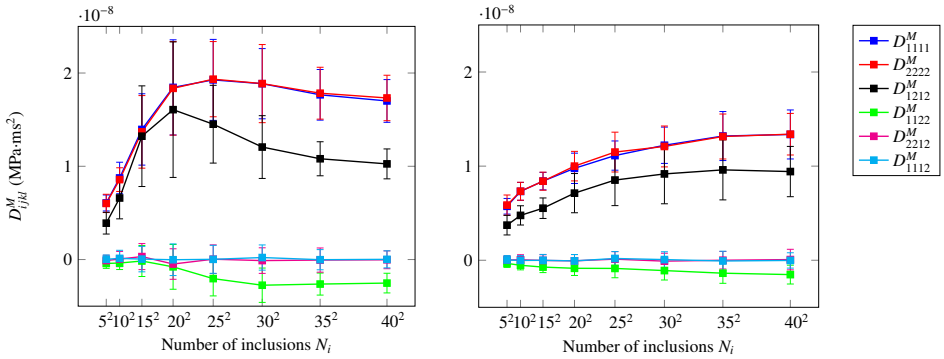

Figure 3.18: The dispersion tensor for sample (a) batch A and (b) batch B.

sor for batch A is gradually approaching a constant value after N_i becomes larger than 20^2 with decreasing standard deviations. For batch B, the mean value of the dispersion tensor components shows the trend of converging to a constant value after N_i becomes larger than 30^2 with the standard deviations tend to decrease as well. The converged values of the dispersion tensor for these two batches seem to be different, which can be possibly due to different spatial distribution patterns. The dispersion tensor converges with a very large size for both these two batches, although for batch A the convergence rate is slightly faster.

3.4.4. Convergence of stiffness tensor

The influence of the numerical micromodel size on the stiffness tensor for the two batches is investigated to also examine convergence of the homogenized stiffness tensor. The stiffness matrix is obtained by using the numerical scheme explained in Appendix B. Plane-strain conditions are assumed herein. The calculated mean and standard deviation of the stiffness tensor is shown in Fig. 3.19. It can be found that for both these two batches, the standard deviation values for the stiffness tensor are small compared with the mean values. The mean values already converge for relatively small micromodel size. The calculated mean values of the stiffness tensor for batch A and batch B in matrix notation are:

$$\bar{\mathbf{S}}^{M(A)} = \begin{bmatrix} 15548.2 & 5302.1 & -3.99049 \\ 5302.1 & 15573.9 & -0.949295 \\ -3.99049 & -0.949295 & 5125.54 \end{bmatrix}, \quad \bar{\mathbf{S}}^{M(B)} = \begin{bmatrix} 15221.1 & 5184.62 & -4.87758 \\ 5184.62 & 15214.1 & 2.89584 \\ -4.87758 & 2.89584 & 5015.75 \end{bmatrix} \tag{3.29}$$

To verify the results, the isotropy of $\mathbf{S}^M$ is checked. It is known that for isotropic material under plane strain condition, the stiffness matrix $\mathbf{S}$ is

$$\mathbf{S}^M = \begin{bmatrix} S^M_{1111} & S^M_{1122} & S^M_{1112} \\ S^M_{2211} & S^M_{2222} & S^M_{2212} \\ S^M_{1211} & S^M_{1222} & S^M_{1212} \end{bmatrix} = \frac{E}{(1+\nu)(1-2\nu)} \begin{bmatrix} 1-\nu & \nu & 0 \\ \nu & 1-\nu & 0 \\ 0 & 0 & \frac{1-2\nu}{2} \end{bmatrix} \tag{3.30}$$

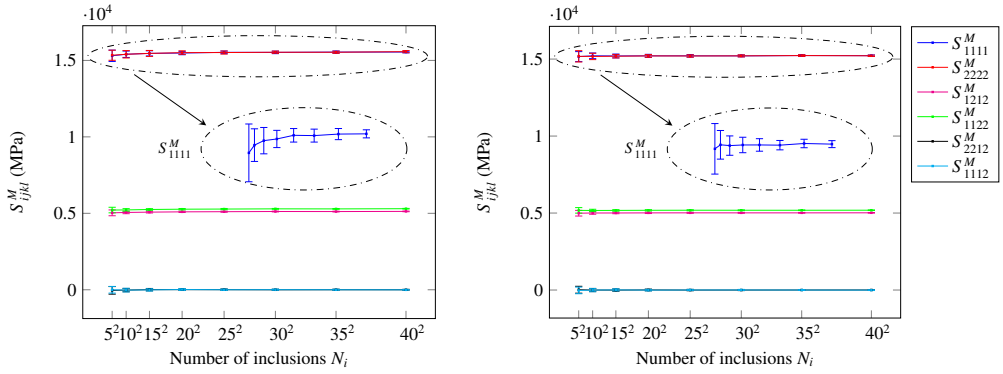

(a) (b)

Figure 3.19: Stiffness tensor for (a) batch A and (b) batch B. Enclosed subplots show the zoomed-in view of stiffness component S^M_{1111}.

where E is the Young's modulus and ν is the Poisson's ratio. Therefore, an isotropic law should satisfy that $2S^M_{1212}/(S^M_{1111}-S^M_{1122})$ is equal to one. An error measurement ϵ_S is introduced as

$$\epsilon_S = \left| \frac{2S^M_{1212}}{(S^M_{1111} - S^M_{1122})} - 1 \right| \times 100\% \tag{3.31}$$

According to Eq. (3.29) and Eq. (3.31), the errors for batch A and batch B are calculated to be 0.0486% and 0.0496%, respectively. This shows that the calculated stiffness is very close to theoretical values. As it is seen in Eq. (3.29), the difference between any component of the calculated stiffness tensor for these two batches is less than 2%, which means that the stiffness tensor is not sensitive to the considered differences in spatial distribution of the microstructure.

3.5. Experimental calibration

It is demonstrated in Section 3.4 that the convergence performance of the dispersion tensor depends on the spatial distribution pattern of the inclusions. Therefore, realistic microstructures should be studied to evaluate the appropriateness of this method to be applied in real composite structures. With image-analysis techniques, spatial distribution patterns can be extracted from snapshots of real composites (see e.g. Czabaj et al. [52]). Computational approaches can thereafter be used to generate random numerical samples according to the experimentally determined spatial patterns.

In this study, numerical samples are generated with the DEM solver HADES for the microstructure of a CFRP composite, HTA/6376, with a fiber volume fraction of 59.2% [53, 54]. First, the DEM settings are calibrated to match experimentally observed NNDs. Then, the RVE existence study from the previous section is repeated with these settings. For the calibration the number of fibers is fixed at 1296 ($=36^2$) in line with the experimental observations on 1300 fibers. The adopted RVE

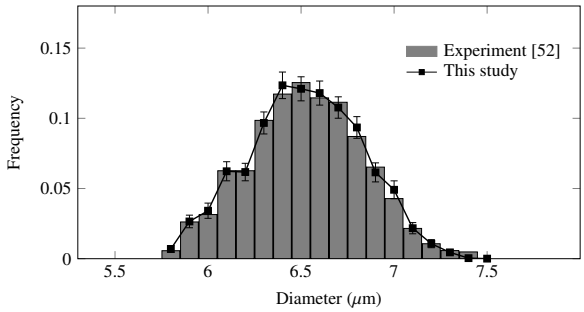

Figure 3.20: Size distribution of fiber diameter.

size is large enough to consider the spatial distribution in the numerical samples as representative based on the observation in Fig. 3.15. A fiber diameter distribution function is predefined according to the experimentally determined size distribution (see Fig. 3.20). The contact parameters, i.e. damping and minimum distance $d_{\min}$ of the DEM simulation are tuned such that the spatial distribution pattern of generated numerical samples can match the experimentally-determined patterns. Herein, 100 numerical samples are generated with the DEM solver. The mean value and standard deviation of the actual fiber diameter distributions used in the DEM simulations are shown in Fig. 3.20 along with the experimental quantification to verify that the input distribution is recovered. The calculated mean and standard deviation of the probability density function of the 1st NND for the calibrated numerical samples are demonstrated in Fig. 3.21 along with the experimental result and two reference solutions from other numerically generated fiber distributions by Yang et al. [44] and Ismail et al. [55]. It is seen that the probability density function of the 1st NND for the generated numerical samples has a good match with the experimental measurements. A considerably better agreement is found for the current study than for the two reference solutions. The mean and standard deviation of the probability density function of the 2nd NND for the numerical samples and the reference solutions are shown in Fig. 3.22. Again, the result for the generated numerical samples matches well with the experiment measurements. A higher agreement is found for this study than Yang et al. [44] while the solution from Ismail et al. [55] also shows a good match. It is therefore validated that the generated numerical samples are sufficiently representative for the real microstructure of the CFRP composite, following the criterion proposed by Liu and Ghoshal [56].

A convergence study on the dispersion tensor is performed next by increasing the size of samples with the same DEM solver settings as the calibrated numerical samples. Again, eight different sizes are considered, and for every size 100 random numerical samples are generated and solved for the dispersion tensor with the FEM model. The influence of the micromodel size on the six independent components of the dispersion tensor is plotted in Fig. 3.23. The standard deviation of all six components shows a decreasing trend as the number of fibers N_f is larger than 400

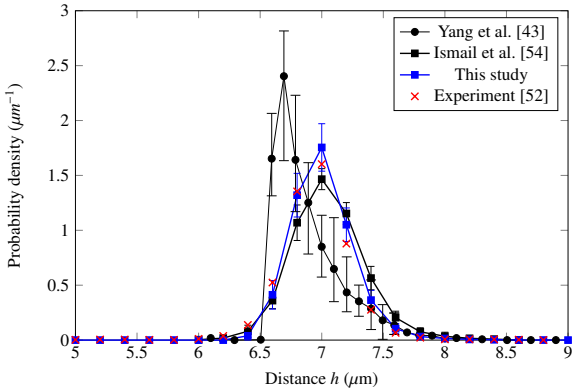

Figure 3.21: The probability density function of 1st NND.

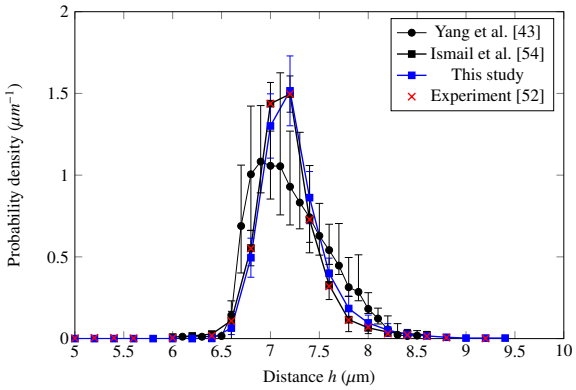

Figure 3.22: The probability density function of 2nd NND.

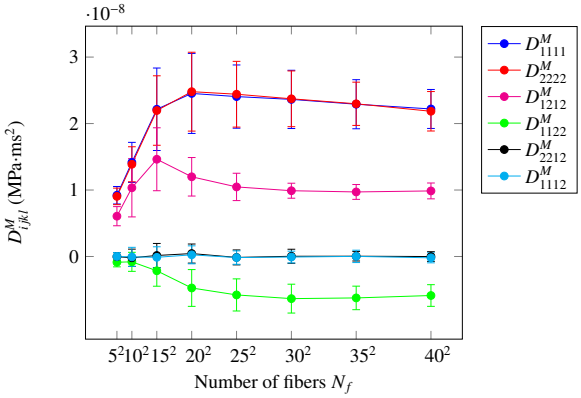

Figure 3.23: Convergence study of calibrated sample.

and the mean values converge to representative values. This means that for this specific composite material the dispersion tensor components converge although convergence is still relatively slow when compared with the stiffness tensor components as shown in Fig. 3.19 or the elasto/plastic response of composites as reported in [42].

3.6. Conclusion

In this paper, a multiscale model is introduced to capture wave dispersion in composites. By using asymptotic homogenization, it is found that the dispersion effect can be characterized by a dispersion tensor, the magnitude of which is dependent on the material property contrast of inclusion/matrix and the size of the inclusion. The dispersive multiscale model is applied to simulate elastic wave propagation problems in a bar with one-dimensional and two-dimension microstructures. Comparison with a DNS model shows that the dispersive multiscale model has a significantly improved accuracy, compared with non-dispersive homogenized models. To test if an RVE can be defined for realistic composites with random microstructures, the dispersion tensor and stiffness tensor are computed for random numerical samples at different sizes. It is found that the convergence performance of the dispersion tensor is considerably slower than that of the stiffness tensor and that the convergence depends on the spatial distribution pattern. Finally, a batch of calibrated numerical samples of CFRP composites is tested for the convergence of the dispersion tensor. It is argued that careful definition of microstructure geometries is required to achieve representativeness.

References

[1] Y. Liu, F. P. van der Meer, and L. J. Sluys, *A dispersive homogenization model for composites and its RVE existence,* Computational Mechanics **65**, 79 (2020).

[2] J. T. Fan, J. Weerheijm, and L. J. Sluys, *Compressive response of a glass-polymer system at various strain rates,* Mechanics of Materials **95**, 49 (2016).

[3] J. T. Fan, J. Weerheijm, and L. J. Sluys, *Compressive response of multiple-particles-polymer systems at various strain rates,* Polymer **91**, 62 (2016).

[4] A. Shams, A. Panteghini, L. Bardella, and M. Porfiri, *A micromechanical model to study failure of polymer-glass syntactic foams at high strain rates,* Computational Materials Science **135**, 189 (2017).

[5] T. Hui and C. Oskay, *Computational modeling of polyurea-coated composites subjected to blast loads,* Journal of Composite Materials **46**, 2167 (2012).

[6] F. V. Souza and D. H. Allen, *Multiscale modeling of impact on heterogeneous viscoelastic solids containing evolving microcracks,* International Journal for Numerical Methods in Engineering **82**, 464 (2010), https://onlinelibrary.wiley.com/doi/pdf/10.1002/nme.2773 .

[7] A. Madeo, P. Neff, I.-D. Ghiba, and G. Rosi, *Reflection and transmission of elastic waves in non-local band-gap metamaterials: A comprehensive study via the relaxed micromorphic model,* Journal of the Mechanics and Physics of Solids **95**, 441 (2016), 1602.05218 .

[8] J. Vondřejc, E. Rohan, and J. Heczko, *Shape optimization of phononic band gap structures using the homogenization approach,* International Journal of Solids and Structures **113-114**, 147 (2017), 1601.02902 .

[9] K. Pham, V. G. Kouznetsova, and M. G. D. Geers, *Transient computational homogenization for heterogeneous materials under dynamic excitation,* Journal of the Mechanics and Physics of Solids **61**, 2125 (2013).

[10] T. Hui and C. Oskay, *A high order homogenization model for transient dynamics of heterogeneous media including micro-inertia effects,* Computer Methods in Applied Mechanics and Engineering **273**, 181 (2014).

[11] H. Askes and E. C. Aifantis, *Gradient elasticity in statics and dynamics: An overview of formulations, length scale identification procedures, finite element implementations and new results,* International Journal of Solids and Structures **48**, 1962 (2011).

[12] H. Nassar, Q.-C. He, and N. Auffray, *Willis elastodynamic homogenization theory revisited for periodic media,* Journal of the Mechanics and Physics of Solids **77**, 158 (2015).

[13] J. R. Willis, *Variational and related methods for the overall properties of composites,* (Elsevier, 1981) pp. 1 – 78.

[14] J. R. Willis, *Variational principles for dynamic problems for inhomogeneous elastic media,* Wave Motion **3**, 1 (1981).

[15] S. Nemat-Nasser and A. Srivastava, *Overall dynamic constitutive relations of layered elastic composites,* Journal of the Mechanics and Physics of Solids **59**, 1953 (2011).

[16] A. Sridhar, V. G. Kouznetsova, and M. G. D. Geers, *A general multiscale framework for the emergent effective elastodynamics of metamaterials,* Journal of the Mechanics and Physics of Solids **111**, 414 (2018).

[17] R. Hill, *Elastic properties of reinforced solids: Some theoretical principles,* Journal of the Mechanics and Physics of Solids **11**, 357 (1963).

[18] I. M. Gitman, H. Askes, and L. J. Sluys, *Representative volume: Existence and size determination,* Engineering Fracture Mechanics **74**, 2518 (2007).

[19] T. Kanit, S. Forest, I. Galliet, V. Mounoury, and D. Jeulin, *Determination of the size of the representative volume element for random composites: statistical and numerical approach,* International Journal of Solids and Structures **40**, 3647 (2003).

[20] M. Stroeven, H. Askes, and L. J. Sluys, *Numerical determination of representative volumes for granular materials,* Computer Methods in Applied Mechanics and Engineering **193**, 3221 (2004).

[21] J. Dirrenberger, S. Forest, and D. Jeulin, *Towards gigantic RVE sizes for 3D stochastic fibrous networks,* International Journal of Solids and Structures **51**, 359 (2014).

[22] T. H. Hoang, M. Guerich, and J. Yvonnet, *Determining the Size of RVE for Nonlinear Random Composites in an Incremental Computational Homogenization Framework,* Journal of Engineering Mechanics **142**, 04016018 (2016).

[23] A. A. Gusev, *Representative volume element size for elastic composites: A numerical study,* Journal of the Mechanics and Physics of Solids **45**, 1449 (1997).

[24] M. Ostoja-Starzewski, *Random field models of heterogeneous materials,* International Journal of Solids and Structures **35**, 2429 (1998).

[25] C. Heinrich, M. Aldridge, A. S. Wineman, J. Kieffer, A. M. Waas, and K. Shahwan, *The influence of the representative volume element (RVE) size on the homogenized response of cured fiber composites,* Modelling and Simulation in Materials Science and Engineering **20**, 075007 (2012).

[26] E. A. de Souza Neto, P. J. Blanco, P. J. Sánchez, and R. A. Feijóo, *An RVE-based multiscale theory of solids with micro-scale inertia and body force effects,* Mechanics of Materials **80**, 136 (2015).

[27] A. Molinari and S. Mercier, *Micromechanical modelling of porous materials under dynamic loading,* Journal of the Mechanics and Physics of Solids **49**, 1497 (2001).

[28] D. Roca, O. Lloberas-Valls, J. Cante, and J. Oliver, *A computational multiscale homogenization framework accounting for inertial effects: Application to acoustic metamaterials modelling,* Computer Methods in Applied Mechanics and Engineering **330**, 415 (2018).

[29] T. Hui and C. Oskay, *A nonlocal homogenization model for wave dispersion in dissipative composite materials,* International Journal of Solids and Structures **50**, 38 (2013).

[30] T. Hui and C. Oskay, *Laplace-domain, high-order homogenization for transient dynamic response of viscoelastic composites,* International Journal for Numerical Methods in Engineering **103**, 937 (2015), 1010.1724 .

[31] R. Hu and C. Oskay, *Nonlocal Homogenization Model for Wave Dispersion and Attenuation in Elastic and Viscoelastic Periodic Layered Media,* Journal of Applied Mechanics **84**, 031003 (2017).

[32] J. Fish, V. Filonova, and S. Kuznetsov, *Micro-inertia effects in nonlinear heterogeneous media,* International Journal for Numerical Methods in Engineering **91**, 1406 (2012), arXiv:1010.1724 .

[33] A. Karamnejad and L. J. Sluys, *A dispersive multi-scale crack model for quasi-brittle heterogeneous materials under impact loading,* Computer Methods in Applied Mechanics and Engineering **278**, 423 (2014).

[34] C. Oskay and J. Fish, *Eigendeformation-based reduced order homogenization for failure analysis of heterogeneous materials,* Computer Methods in Applied Mechanics and Engineering **196**, 1216 (2007).

[35] S. Toro, P. Sánchez, P. Blanco, E. de Souza Neto, A. Huespe, and R. Feijóo, *Multiscale formulation for material failure accounting for cohesive cracks at the macro and micro scales,* International Journal of Plasticity **76**, 75 (2016).

[36] J. Fish, *Practical multiscaling* (John Wiley & Sons, 2013).

[37] T. Mura, *Micromechanics of defects in solids*, Mechanics of Elastic and Inelastic Solids, Vol. 3 (Springer Netherlands, Dordrecht, 1987).

[38] I. V. Andrianov, V. I. Bolshakov, V. V. Danishevs'kyy, and D. Weichert, *Higher order asymptotic homogenization and wave propagation in periodic composite materials,* Proceedings of the Royal Society A: Mathematical, Physical and Engineering Sciences **464**, 1181 (2008).

[39] D. Fafalis and J. Fish, *Computational aspects of dispersive computational continua for elastic heterogeneous media,* Computational Mechanics **56**, 931 (2015).

[40] K. T. Ramesh, *High rates and impact experiments,* in *Springer Handbook of Experimental Solid Mechanics*, edited by W. N. Sharpe (Springer US, Boston, MA, 2008) pp. 929–960.

[41] M. Li, S. Ghosh, O. Richmond, H. Weiland, and T. Rouns, *Three dimensional characterization and modeling of particle reinforced metal matrix composites: part i: Quantitative description of microstructural morphology,* Materials Science and Engineering: A **265**, 153 (1999).

[42] F. P. van der Meer, *Micromechanical validation of a mesomodel for plasticity in composites,* European Journal of Mechanics - A/Solids **60**, 58 (2016).

[43] M. Stroeven, *Discrete Numerical Modelling of Composite Materials - application to cementitious materials*, Ph.D. thesis, Delft University of Technology (1999).

[44] L. Yang, Y. Yan, Z. Ran, and Y. Liu, *A new method for generating random fibre distributions for fibre reinforced composites,* Composites Science and Technology **76**, 14 (2013).

[45] R. Pyrz, *Quantitative description of the microstructure of composites. Part I: Morphology of unidirectional composite systems,* Composites Science and Technology **50**, 197 (1994).

[46] G. Catalanotti, *On the generation of RVE-based models of composites reinforced with long fibres or spherical particles,* Composite Structures **138**, 84 (2016).

[47] A. R. Melro, P. P. Camanho, and S. T. Pinho, *Generation of random distribution of fibres in long-fibre reinforced composites,* Composites Science and Technology **68**, 2092 (2008).

[48] C. Geuzaine and J.-F. Remacle, *Gmsh: A 3-D finite element mesh generator with built-in pre- and post-processing facilities,* International Journal for Numerical Methods in Engineering **79**, 1309 (2009).

[49] T. C. Bailey and A. C. Gatrell, *Interactive spatial data analysis*, Vol. 413 (Longman Scientific & Technical Essex, 1995).

[50] I. Yamada and P. A. Rogerson, *An Empirical Comparison of Edge Effect Correction Methods Applied to K-function Analysis,* Geographical Analysis **35**, 97 (2003).

[51] J. Zangenberg and P. Brøndsted, *Quantitative study on the statistical properties of fibre architecture of genuine and numerical composite microstructures,* Composites Part A: Applied Science and Manufacturing **47**, 124 (2013).

[52] M. W. Czabaj, M. L. Riccio, and W. W. Whitacre, *Numerical reconstruction of graphite/epoxy composite microstructure based on sub-micron resolution X-ray computed tomography,* Composites Science and Technology **105**, 174 (2014).

[53] C. T. McCarthy and T. J. Vaughan, *Micromechanical failure analysis of advanced composite materials,* in *Numerical Modelling of Failure in Advanced Composite Materials* (Elsevier, 2015) pp. 379–409.

[54] T. J. Vaughan and C. T. McCarthy, *A combined experimental–numerical approach for generating statistically equivalent fibre distributions for high strength laminated composite materials,* Composites Science and Technology **70**, 291 (2010).

[55] Y. Ismail, D. Yang, and J. Ye, *Discrete element method for generating random fibre distributions in micromechanical models of fibre reinforced composite laminates,* Composites Part B: Engineering **90**, 485 (2016).

[56] K. C. Liu and A. Ghoshal, *Validity of random microstructures simulation in fiber-reinforced composite materials,* Composites Part B: Engineering **57**, 56 (2014).

4

A numerical homogenization scheme used for derivation of a homogenized viscoelastic-viscoplastic model for the transverse response of fiber-reinforced polymer composites

4.1. Introduction

Fiber-reinforced polymer composites exhibit a complex nonlinear mechanical response in the transverse plane, due to the composition of different types of materials and interfaces between the constituents. By modeling the composite microstructure with a fine numerical model, a virtual testing tool can be established to evaluate the damage and failure of composites in the transverse plane for given constituents and material interfaces instead of performing expensive experiment campaigns. For detailed analysis of crack growth, a direct numerical simulation (DNS) model with a notched configuration is useful as it mimics a typical material characterization experiment. To reduce the computational cost, the composite material away from the notch can be represented by a homogenized model without damage and failure but with possibly rate-dependent nonlinearity. Experimental

This chapter is based on [1]

tests of polymer composites under different loading types, such as fatigue, impact, etc., reveal that polymer composites can show evident viscoelastic deformation and viscoplastic flow before damage and failure emerge [2–4]. The underlying mechanism of the viscoelastic and viscoplastic behavior of polymer composites is related to the nonlinear and time-dependent mechanical properties of the microstructure [5]. Various homogenization strategies exist to calculate the effective properties of polymer composites based on the mechanical properties of the microstructural constituents [6]. The homogenization methods can be divided roughly into: mean-field homogenization, mathematical (asymptotic) homogenization, computational homogenization and numerical homogenization [7, 8].

The mean field homogenization method was first proposed for composites having linear elastic constituents. It is based on assumed relations between volume averages of strain fields in each phase. This relation is typically derived from the exact solution of Eshelby [9] for an ellipsoidal inclusion embedded in an infinite matrix or its extensions with consideration of multiple inclusions by Mori and Tanaka [10], self-consistent scheme by Kröner [11] and Hill [12], and double inclusion schemes [6]. Extension of these schemes to the nonlinear (time-dependent) regime usually requires the linearization of the local constitutive equations and the definition of uniform reference properties for each phase. Popular linearization strategies include secant [13], incremental [14], tangent [15] and affine [16–18] approaches. Examples of the application of mean field homogenization for nonlinear (elasto-plastic, viscoelastic, elasto-visco-plastic) mechanical problems can be found in [16, 19–22]. This semi-analytical method can be very accurate in linear (thermo)elasticity and it is computationally efficient. However, there is no detailed stress/strain field for each phase and accurate extension to nonlinear cases is still challenging.

The mathematical homogenization method represents the physical fields in a composite by asymptotic expansion in powers of a small parameter ζ, which is the ratio of a characteristic size of the heterogeneities and a measure of the macrostructure. The asymptotic expansion allows a decomposition of the final solution into a series of governing equations, which can be evaluated successively from a sequence of (initial) boundary-value problems within a unit cell (or representative volume element) domain. The effective properties are obtained through volume averaging operations [23]. This method is mathematically elegant and rigorous for a periodic microstructure with linear elastic mechanical properties. However, extension to a nonlinear material response is not straightforward although possible with the transformation field analysis [24]. In this method, the inelastic strain field is considered as given eigenstrains, which can be determined from solving linear problems with eigenstrains. Examples can be found for viscoelasticity [25–27] and for viscoplasticity [28–31]

In the computational homogenization method, also referred to as micro-macro analysis or FE^2 [32], the local macroscopic constitutive response is derived from the solution of a microstructural boundary value problem in a (statistically equivalent) representative volume element (RVE) and information of the microscale is hierarchically passed to the macroscale by bridging laws. The RVE is a characteristic sample of heterogeneous material that should be sufficiently large to involve

enough composite micro-heterogeneities in order to be representative, however it should be much smaller than the macroscopic dimensions [33]. This method does not introduce any explicit format of the macroscopic constitutive equations as the macroscopic stress is determined from the mechanical deformation state of the associated RVE. However, the implementation of this method is not readily available in a general-purpose finite element code and the computational cost of this method can be prohibitively high. Computational homogenization has been applied to model amongst others viscoelasticity [34–36] and viscoplasticity [37–40].

For the numerical homogenization method, also called unit cell method [32], a macroscopic canonical constitutive law, e.g. viscoplasticity, is assumed a priori for the macroscale model. The material parameters are then determined from the averaged microscopic stress-strain fields calculated from the computational analysis of a microstructural model (a unit cell or an RVE) subjected to fundamental load cases. The calibrated macroscopic constitutive model is then used for modeling composite structures without explicitly representing the microstructure, which greatly reduces the computational cost. When compared with the computational homogenization method, the numerical homogenization does not need to keep solving boundary value problems of RVEs during a macroscale analysis. This approach has been used for development of the so-called homogenization-based or micromechanically derived classical constitutive models, e.g. plasticity and damage [41–43], as well as for viscoleasticity [44, 45] and viscoplasticity [45–47].

In this paper, a viscoelastic-viscoplastic (VE-VP) model for polymer composites is derived using a numerical homogenization scheme. This paper is organized as follows: in Section 4.2, the basic formulation of the VE-VP model proposed by Rocha et al. [48] is illustrated and the stress update scheme used for implementation of the VE-VP model is introduced. In Section 4.3, novel step-by-step calibration procedures are introduced to calibrate the material parameters of a homogenized VE-VP model based on the response of a representative volume element (RVE) under typical loading conditions. In Section 4.4, the performance of the introduced numerical scheme is demonstrated.

4.2. A viscoelastic-viscoplastic polymer model

Following Rocha et al. [48], a viscoelastic-viscoplastic (VE-VP) model as schematically represented in Fig. 4.1 is used to model the constitutive behavior of an epoxy resin. In this model, the total strain ε_{ij} is decomposed into an elastic part ε_{ij}^{e} and a plastic part ε_{ij}^{p}:

$$\varepsilon_{ij} = \varepsilon_{ij}^{e} + \varepsilon_{ij}^{p} \tag{4.1}$$

The elastic behavior is represented by a generalized Maxwell model consisting of n parallel Maxwell elements connected along with an extra isolated long-term spring. In each Maxwell element, a spring with modulus E_i and a dashpot with viscosity parameter η_i are connected in series. The plastic behavior is represented by a sliding element with yield stress σ_y and a dashpot with viscosity parameter η_p. Overstress is allowed to be developed due to the dashpot component that is placed in parallel to the sliding element. In this section, the mathematical formulation

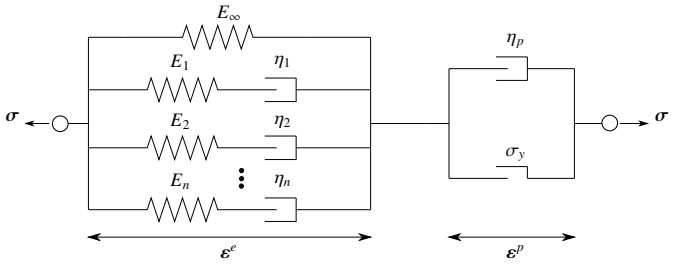

Figure 4.1: Schematic representation of the viscoelastic-viscoplastic polymer model in one-dimension. The coefficients of the elastic and plastic components do not represent the same coefficients used in Section 4.2.1.

for the viscoelasticity and viscoplasticity model is described first, followed by the stress update scheme used for numerical simulation with the finite element method (FEM).

4.2.1. Formulation for the VE-VP model

Following the conceptual representation of the VE-VP model, the mathematical formulations for the VE-VP constitutive model in a three-dimensional setting is detailed in this section. The contribution of the viscoelastic components is described with a linear viscoelastic model. Afterwards, the viscoplastic components are represented by a Perzyna-type overstress formulation with a backbone of a pressure-dependent plasticity model.

Viscoelasticity

Assuming a linear viscoelastic model, the stress is computed with Boltzmann's hereditary integral related to the elastic strain by [49]:

$$\sigma_{ij}(t) = \int_{-\infty}^{t} D_{ijkl}(t-\tilde{t}) \frac{\partial \varepsilon_{kl}^{e}(\tilde{t})}{\partial \tilde{t}} d\tilde{t} \tag{4.2}$$

in which $D_{ijkl}(t)$ is the time-dependent stiffness that can be expressed with the time-dependent shear stiffness $G(t)$ and bulk stiffness $K(t)$:

$$D_{ijkl}(t) = 2G(t) I_{ijkl}^{dev} + 3K(t) I_{ijkl}^{vol} \tag{4.3}$$

where $G(t)$ and $K(t)$ can be further expanded as an addition of a long-term contribution and a Prony series of n_s shear elements and n_r bulk elements:

$$G(t) = G_\infty + \sum_{s=1}^{n_s} G_s \exp\left(-\frac{t}{g_s}\right) \qquad K(t) = K_\infty + \sum_{r=1}^{n_r} K_r \exp\left(-\frac{t}{k_r}\right) \tag{4.4}$$

in which G_∞ and K_∞ represent the long-term shear and bulk stiffness, and G_s , K_r, g_s and k_r are shear and bulk stiffness and relaxation time of the Maxwell elements, respectively. The fourth-order deviatoric and volumetric operator tensors

introduced in Eq. (4.3) are defined as:

$$I_{ijkl}^{dev} = \delta_{ik}\delta_{jl} - \frac{1}{3}\delta_{ij}\delta_{kl} \qquad I_{ijkl}^{vol} = \frac{1}{3}\delta_{ij}\delta_{kl} \tag{4.5}$$

where δ_{ij} is the Kronecker delta. These operator tensors can also be used to decompose the elastic strain ε_{ij}^{e} into a deviatoric part $\varepsilon_{ij}^{e,dev}$ and a hydrostatic part $\varepsilon_{ij}^{e,vol}$:

$$\varepsilon_{ij}^{e} = \varepsilon_{ij}^{e,dev} + \varepsilon_{ij}^{e,vol} = I_{ijkl}^{dev}\varepsilon_{kl}^{e} + I_{ijkl}^{vol}\varepsilon_{kl}^{e} \tag{4.6}$$

By substituting Eqs. (4.4) into Eq. (4.3), the time-dependent stiffness $D_{ijkl}(t)$ can be expressed as:

$$\begin{aligned} D_{ijkl}(t) &= \left(2G_\infty I_{ijkl}^{dev} + 3K_\infty I_{ijkl}^{vol}\right) + \left(\sum_{s=1}^{n_s} 2G_s \exp\left(-\frac{t}{g_s}\right) I_{ijkl}^{dev} + \sum_{r=1}^{n_r} 3K_r \exp\left(-\frac{t}{k_r}\right) I_{ijkl}^{vol}\right) \\ &= D_{ijkl}^{\infty} + D_{ijkl}^{m}(t) \end{aligned} \tag{4.7}$$

where D_{ijkl}^{∞} is the long-term stiffness and $D_{ijkl}^{m}(t)$ is the overall stiffness of the Maxwell elements.

Viscoplasticity

The viscoplasticity model is a Perzyna-type model with a backbone of a hardening plasticity model. Following Rocha et al. [48], the yield function is pressure-dependent and is defined as:

$$f_p(\boldsymbol{\sigma}, \varepsilon_{eq}^{p}) = 6J_2 + 2I_1(\sigma_c - \sigma_t) - 2\sigma_c\sigma_t \tag{4.8}$$

where $I_1 = \sigma_{kk}$ is the first stress invariant, $J_2 = \frac{1}{2}S_{ij}S_{ij}$ is the second invariant of the deviatoric stress S_{ij}, and σ_t and σ_c are the yield stress in tension and compression, respectively. The yield stress values σ_t and σ_c are a function of the accumulated equivalent plastic strain ε_{eq}^{p}, which is in turn related to the plastic strain in an incremental form as:

$$\Delta\varepsilon_{eq}^{p} = \sqrt{\frac{1}{1+2\nu_p^2}\Delta\varepsilon_{ij}^{p}\Delta\varepsilon_{ij}^{p}} \tag{4.9}$$

in which ν_p is the plastic Poisson's ratio. In case of an applied uniaxial loading along direction-1, the incremental plastic strain in the other two perpendicular directions, i.e. $\Delta\varepsilon_{22}^{p}$ and $\Delta\varepsilon_{33}^{p}$, is related to the incremental plastic strain in the loading direction $\Delta\varepsilon_{11}^{p}$:

$$\Delta\varepsilon_{22}^{p} = \Delta\varepsilon_{33}^{p} = -\nu_p\Delta\varepsilon_{11}^{p} \tag{4.10}$$

The desired contraction behavior is implemented through a non-associative flow rule which is written in an incremental form as:

$$\Delta\varepsilon_{ij}^{p} = \Delta\gamma\left(3S_{ij} + \frac{2}{9}\alpha I_1\delta_{ij}\right) \tag{4.11}$$

where $\Delta\gamma$ is the incremental plastic multiplier and the parameter α is:

$$\alpha = \frac{9}{2}\frac{1-2\nu_p}{1+\nu_p} \tag{4.12}$$

A viscous time scale is introduced in the model by allowing the overstress to develop beyond the yield surface. The overstress formulation is of Perzyna-type and the evolution of the plastic multiplier $\Delta\gamma$ can therefore be described by:

$$\Delta\gamma = \begin{cases} \frac{\Delta t}{\eta_p}\left(\frac{f_p}{\sigma_t^0\sigma_c^0}\right)^{m_p} & \text{if } f_p > 0 \\ 0 & \text{if } f_p \leq 0 \end{cases} \tag{4.13}$$

in which σ_t^0 and σ_c^0 are the yield stress values when $\varepsilon_{eq}^p = 0$, Δt is the time increment, and m_p and η_p are viscoplastic coefficients.

4.2.2. Stress update scheme

To facilitate the implementation of the introduced VE-VP model in a FEM framework, an incremental stress update scheme and the consistent tangent used for the Newton-Raphson method are derived. The stress update scheme defines how the stress increment $\Delta\sigma_{ij}$ for a material point is related to a strain increment $\Delta\varepsilon_{ij}$, given that all the state variables from the previous time step are known. For each time step a viscoelastic trial stress is always first computed, assuming that the stress development within this step is not beyond the yield surface. Whenever this assumption is violated, a viscoplastic returning-mapping scheme is used to correct the trial stress.

Viscoelastic stress update

Supposing that all the state variables of a material point at time $t = t_n$ are known and applying a strain increment $\Delta\varepsilon_{ij} = \varepsilon_{ij}(t_{n+1}) - \varepsilon_{ij}(t_n)$, the viscoelastic trial stress is derived as follows: a decomposition of the stress into deviatoric part and hydrostatic part gives:

$$\sigma_{ij}(t_{n+1}) = S_{ij}(t_{n+1}) + 3p(t_{n+1})\delta_{ij} \tag{4.14}$$

in which S_{ij} is the deviatoric stress, p is the hydrostatic stress. By substituting Eqs. (4.3) and (4.4) into Eq. (4.2), the deviatoric and hydrostatic part of the stress at time $t = t_{n+1}$ can be expressed as:

$$\begin{aligned} S_{ij}(t_{n+1}) &= 2G^\infty \varepsilon_{ij}^{e,dev}(t_{n+1}) + \sum_{s=1}^{n_s}\int_0^{t_{n+1}} 2G_s \exp\left(-\frac{t_{n+1}-\tilde{t}}{g_s}\right)\frac{\partial\varepsilon_{ij}^{e,dev}(\tilde{t})}{\partial\tilde{t}}d\tilde{t} \\ &= 2G^\infty \varepsilon_{ij}^{e,dev}(t_{n+1}) + \sum_{s=1}^{n_s}\tau_{ij}^s(t_{n+1}) \end{aligned} \tag{4.15}$$

$$p(t_{n+1}) = K^{\infty}\varepsilon_v^e(t_{n+1}) + \sum_{r=1}^{n_r}\int_0^{t_{n+1}} K_r \exp\left(-\frac{t_{n+1}-\tilde{t}}{k_r}\right)\frac{\partial\varepsilon_v^e(\tilde{t})}{\partial\tilde{t}}d\tilde{t}$$
$$= K^{\infty}\varepsilon_v^e(t_{n+1}) + \sum_{r=1}^{n_r} h^p(t_{n+1}) \tag{4.16}$$

in which $\varepsilon_v^e = \varepsilon_{kk}^e$ is the volumetric part of the elastic strain, $\varepsilon_{ij}^{e,dev} = \varepsilon_{ij}^e - \frac{1}{3}\varepsilon_v^e\delta_{ij}$ is the deviatoric part and the viscous components can be described as:

$$\begin{aligned}\tau_{ij}^s(t_{n+1}) &= \int_0^{t_{n+1}} 2G_s \exp\left(-\tfrac{t_{n+1}-\tilde{t}}{g_s}\right)\frac{\partial\varepsilon_{ij}^{e,dev}(\tilde{t})}{\partial\tilde{t}}d\tilde{t}\\ &= \exp\left(-\tfrac{\Delta t}{g_s}\right)\tau_{ij}^s(t_n) + 2G_s\left[1-\exp\left(-\tfrac{\Delta t}{g_s}\right)\right]\tfrac{g_s}{\Delta t}\Delta\varepsilon_{ij}^{e,dev}\\ &= \exp\left(-\tfrac{\Delta t}{g_s}\right)\tau_{ij}^s(t_n) + 2G_{ve}(\Delta t)\Delta\varepsilon_{ij}^{e,dev}\end{aligned} \tag{4.17}$$

$$\begin{aligned}h^p(t_{n+1}) &= \int_0^{t_{n+1}} K_r \exp\left(-\tfrac{t_{n+1}-\tilde{t}}{k_r}\right)\frac{\partial\varepsilon_v^e(\tilde{t})}{\partial\tilde{t}}d\tilde{t}\\ &= \exp\left(-\tfrac{\Delta t}{k_r}\right)h^p(t_n) + K_r\left[1-\exp\left(-\tfrac{\Delta t}{k_r}\right)\right]\tfrac{k_r}{\Delta t}\Delta\varepsilon_v^e\\ &= \exp\left(-\tfrac{\Delta t}{k_r}\right)h^p(t_n) + K_{ve}(\Delta t)\Delta\varepsilon_v^e\end{aligned} \tag{4.18}$$

with

$$G_{ve}(\Delta t) = G_s\left[1-\exp\left(-\frac{\Delta t}{g_s}\right)\right]\frac{g_s}{\Delta t} \qquad K_{ve}(\Delta t) = K_r\left[1-\exp\left(-\frac{\Delta t}{k_r}\right)\right]\frac{k_r}{\Delta t} \tag{4.19}$$

By using Eqs. (4.15)-(4.19), the stress $\sigma_{ij}(t_{n+1})$ can be expressed as:

$$\begin{aligned}\sigma_{ij}(t_{n+1}) &= S_{ij}(t_{n+1}) + 3p(t_{n+1})\delta_{ij}\\ &= D_{ijkl}^{\infty} : \varepsilon_{kl}^e(t_{n+1}) + D_{ijkl}^{ve}(\Delta t) : \Delta\varepsilon_{kl}^e + \sigma_{ij}^{hist}(t_n)\end{aligned} \tag{4.20}$$

with

$$D_{ijkl}^{ve}(\Delta t) = 2G_{ve}(\Delta t)I_{ijkl}^{dev} + 3K_{ve}(\Delta t)I_{ijkl}^{vol} \tag{4.21}$$

$$\sigma_{ij}^{hist}(t_n) = \sum_{s=1}^{n_s}\exp\left(-\frac{\Delta t}{g_s}\right)\tau_{ij}^s(t_n) + 3\sum_{r=1}^{n_r}\exp\left(-\frac{\Delta t}{k_r}\right)h^p(t_n)\delta_{ij} \tag{4.22}$$

For the trial stress it is assumed that there is no plastic strain increment, i.e. $\Delta\varepsilon_{ij}^p = 0$ and $\Delta\varepsilon_{ij}^e = \Delta\varepsilon_{ij}$. Therefore, by using Eq. (4.20) the viscoelastic trial stress reads:

$$\begin{aligned}\sigma_{ij}^{tr} &= D_{ijkl}^{\infty} : \varepsilon_{kl}^e(t_{n+1}) + D_{ijkl}^{ve} : \Delta\varepsilon_{kl} + \sigma_{ij}^{hist}(t_n)\\ &= D_{ijkl}^{\infty} : \left(\varepsilon_{kl}(t_{n+1}) - \varepsilon_{kl}^p(t_n)\right) + D_{ijkl}^{ve}(\Delta t) : \Delta\varepsilon_{kl} + \sigma_{ij}^{hist}(t_n)\end{aligned} \tag{4.23}$$

The viscoelastic stress is then substituted into the yield function in Eq. (4.8) to check if the yield condition is satisfied. If the yield function is not larger than zero, the stress is equal to the trial stress,

$$\sigma_{ij}(t_{n+1}) = \sigma_{ij}^{tr} \tag{4.24}$$

Otherwise, the stress has to be corrected with the viscoplastic return-mapping scheme outlined in the next section. The consistent tangent operator needed for iterative solving of the global system of equations is given in Appendix D.

Viscoelastic-viscoplastic stress update

If the yield function for a viscoelastic trial stress in Eq. (4.8) is larger than zero, a return-mapping scheme is needed. In this case, plastic flow should occur so that $\Delta\varepsilon_{ij}^{p} \neq 0$ and $\Delta\varepsilon_{ij}^{e} = \Delta\varepsilon_{ij} - \Delta\varepsilon_{ij}^{p}$. According to Eq. (4.20) and Eq. (4.23), the stress can be expressed as:

$$\sigma_{ij} = \sigma_{ij}^{tr} - \left(D_{ijkl}^{\infty} + D_{ijkl}^{ve}(\Delta t)\right)\Delta\varepsilon_{kl}^{p} = \sigma_{ij}^{tr} - \hat{D}_{ijkl}\Delta\varepsilon_{kl}^{p} \tag{4.25}$$

in which

$$\hat{D}_{ijkl} = D_{ijkl}^{\infty} + D_{ijkl}^{ve}(\Delta t) \tag{4.26}$$

Substitution of Eq. (4.26) and replacing the increment of plastic strain defined in Eq. (4.11) in Eq. (4.25) gives:

$$\sigma_{ij}(t_{n+1}) = \sigma_{ij}^{tr} - 6\hat{G}\Delta\gamma S_{ij}(t_{n+1}) - \frac{2}{9}\hat{K}\alpha\Delta\gamma\,(I_1)_{n+1}\,\delta_{ij} \tag{4.27}$$

where

$$\hat{G} = G_{\infty} + G_{ve}(\Delta t) \qquad \hat{K} = K_{\infty} + K_{ve}(\Delta t) \tag{4.28}$$

Splitting Eq. (4.27) into its deviatoric and volumetric components gives:

$$S_{ij}(t_{n+1}) = S_{ij}^{tr} - 6\hat{G}\Delta\gamma S_{ij}(t_{n+1}) \Leftrightarrow S_{ij}(t_{n+1}) = \frac{S_{ij}^{tr}}{1 + 6\hat{G}\Delta\gamma} = \frac{S_{ij}^{tr}}{\zeta_s} \tag{4.29}$$

$$p(t_{n+1}) = p^{tr} - \frac{2}{3}\Delta\gamma\hat{K}\alpha I_1 \Leftrightarrow p(t_{n+1}) = \frac{p^{tr}}{1 + 2\hat{K}\alpha\Delta\gamma} = \frac{p^{tr}}{\zeta_p} \tag{4.30}$$

in which

$$\zeta_s = 1 + 6\hat{G}\Delta\gamma, \quad \zeta_p = 1 + 2\hat{K}\alpha\Delta\gamma \tag{4.31}$$

Considering Eqs. (4.8), (4.9), (4.11), (4.29) and (4.30), the overstress function in Eq. (4.13) is only a function of $\Delta\gamma$:

$$\Phi(\Delta\gamma) = \frac{\Delta t}{\eta_p}\left(\frac{f_p}{\sigma_t^0\sigma_c^0}\right)^{m_p} - \Delta\gamma = 0 \tag{4.32}$$

This equation can be solved by a local Newton-Raphson scheme outlined in Appendix E. After the incremental plastic multiplier $\Delta\gamma$ is obtained, the stress can be computed by a back substitution of its value into Eq. (4.27). The consistent tangent needed for iterative solution of the system of equations in an implicit FEM framework is given in Appendix E.

4.3. Numerical homogenization scheme

In this section, a numerical homogenization scheme for deriving a viscoelastic-viscoplastic model for two-phase polymeric composites is introduced. In this method, the mechanical response of the composites is assumed to be an average response of the two different phases of the material. Therefore, by selecting a characteristic sample of the heterogeneous composite microstructure, i.e. the so-called representative volume element (RVE), the overall response of composites can be extracted from homogenization of the response of the RVE (see Fig. 4.2). In this work, a three-dimensional orthotropic periodic RVE of 5×5 fibers with a volume fraction of 60% is created [1]. The polymer phase of the RVE is assumed to be epoxy and the VE-VP model introduced in Section 4.2 is adopted with given material parameter values. The fiber, which is usually much stiffer and stronger, is assumed to be linear elastic. Perfect bonding is assumed for the interface between the polymer matrix and fibers. This three-dimensional orthotropic RVE is adopted with only the response of the fiber/matrix microstructure in the transverse plane investigated. For that reason we can use an isotropic material for the homogenized response. This isotropic model will only be valid for the 2D response. We choose to do the calibration in plane stress, because this allows for straightforward identification of parameters of the homogenized VE-VP model. For the 3D RVE simulations, global plane stress conditions are applied with periodic boundary conditions with free contraction in the fiber direction, which means that the average stress in fiber direction is equal to zero. Because the nonlinear response of the composite material can be expected to inherit characteristics of the underlying nonlinear model for the polymer matrix, it is assumed that the overall transverse mechanical response of the composite material can be described with the same VE-VP model as the polymer phase alone. Numerical homogenization requires the parameters of the homogenized VE-VP model to be determined from a calibration process. According to the VE-VP model introduced in Section 4.2.1, the following set of material parameters needs to be determined through numerical homogenization schemes: (1) elasticity-related: Young's modulus E_∞ and Poisson's ratio ν; (2) viscoelasticity-related: relaxation modulus (i.e. K_r and G_s) and relaxation times (i.e. k_r and g_s); (3) plasticity-related: plastic Poisson's ratio ν_p and hardening curves; (4) viscoplasticity-related: m_p and η_p.

The adopted strategy is a step-by-step calibration process based on different components of the homogenized VE-VP material model: (a) elasticity; (b) viscoelasticity; (c) plasticity; (d) viscoplasticity. The central premise of this paper is that if we have a micromodel with representative geometry and rich constitutive relations for the constituents, we can calibrate an equally rich constitutive law for an equivalent homogeneous material by separately accounting for the influence of the different constitutive ingredients. The calibration procedure is performed for two-dimensional plane stress simulations. A three-dimensional orthotropic RVE with free contraction in fiber direction is adopted to ensure a consistent macroscopic

[1] A discrete element method generator called HADES is used to generate a stochastic distribution of the fibers with the diameter $D_f = 5\ \mu$m and a minimum distance between fibers $d_{min} = 0.2\ \mu$m, following the procedures in Liu et al. [50]. After this, a mesh is generated with GMSH [51] for the fibers and the matrix.

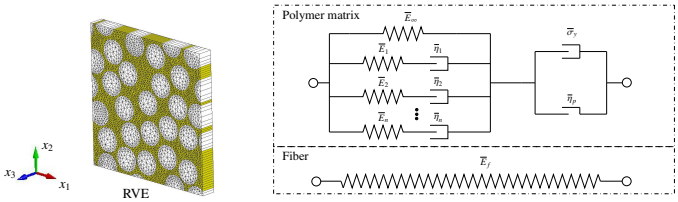

(a) Finite element mesh of the RVE microstructure (the dimensions of the numerical sample are $[l_1, l_2, l_3] = [28.6, 28.6, 0.5]$ μm) and its constitutive models.

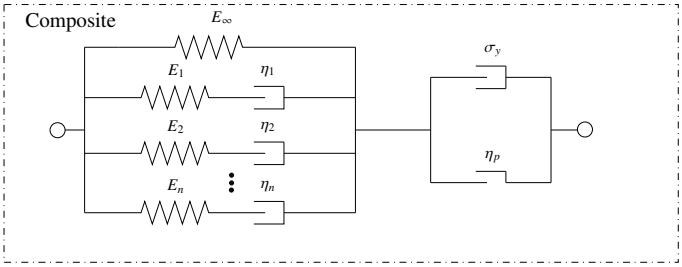

(b) Homogenized VE-VP material model

Figure 4.2: The equivalent homogeneous model with a VE-VP model (b) is assumed to have the same mechanical behavior as the RVE model with heterogeneous material in (a). The parameters in (b) have to be determined by homogenization of the RVE model.

plane stress response.

For each calibration step, only one component of the constitutive model is considered while the others are turned off. In this way, the complexity of coupling different mechanisms is reduced and the material parameters for each component of the homogenized VE-VP model can be calibrated through the corresponding homogenization techniques. Typically, the mechanical response of the RVE model under representative loading conditions is investigated with FEM simulations and the average response of the RVE is considered as the reference exact solution of the homogenized VE-VP model. The value of the material parameters of the homogenized VE-VP model can be determined by matching the averaged RVE response with optimization algorithms. Building upon the parameters calibrated from the previous step, each time a certain number of extra parameters is calibrated by extracting the necessary information from the RVE model during a new calibration step. Finally, the whole set of calibrated parameters of the homogenized VE-VP model is obtained.

4.3.1. Step 1: calibration of elastic component parameters

To calibrate elasticity parameters of the homogenized VE-VP model, only the elasticity components of the RVE model is considered on while the other components are turned off (see Fig. 4.3). The Young's modulus of the fiber $\overline{E}_f$ and matrix $\overline{E}_\infty$

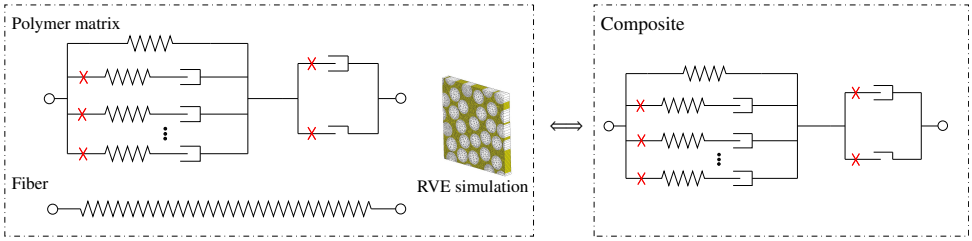

Figure 4.3: Schematic representation of step 1: the calibration of elasticity parameters of the homogenized VE-VP model. The cross sign represents the components that are turned off.

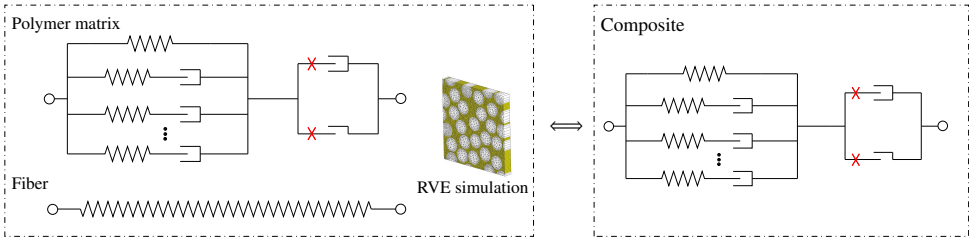

Figure 4.4: Schematic representation of step 2: the calibration of viscoelasticity parameters of the homogenized VE-VP model. The cross sign represents the components that are turned off.

are 74000 MPa and 2500 MPa, respectively. The Poisson's ratio for fiber $\overline{\nu}_f$ and matrix $\overline{\nu}_m$ are 0.2 and 0.37, respectively. The Young's modulus and Poisson's ratio of the homogenized VE-VP model can be extracted by subjecting the RVE to a uniaxial stress state. The boundary conditions illustrated in Appendix F are applied on the RVE shown in Fig. 4.3 with a prescribed unit displacement along direction-1. The Poisson's ratio can therefore be calculated as:

$$\nu = -\varepsilon_{22}/\varepsilon_{11} = 0.42 \tag{4.33}$$

where ε_{22} and ε_{11} are the normal strains along direction-1 and the direction-2, respectively. Similarly, the Young's modulus E_∞ is calculated by:

$$E_\infty = \frac{f_1/(l_2 l_3)}{\varepsilon_{11}} = 10394 \text{ MPa} \tag{4.34}$$

where f_1 is the total nodal force of the right surface of the RVE model, l_2 and l_3 are the length of the RVE along direction-2 and direction-3, respectively.

4.3.2. Step 2: calibration of viscoelastic parameters

To calibrate the viscoelastic parameters of the homogenized VE-VP model, only the viscoelastic components of the RVE model are turned on (see Fig. 4.4). Following [48, 52], a dynamic mechanical analysis (DMA) on the RVE is performed. The basic theory and procedures can be illustrated as follows: it is known that for a

$\bar{\tau}_i$ (ms)	52.7704	2938.8889	5.4080e4	3.9612e7
$\bar{E}_i$ (MPa)	98.5401	142.4348	487.7009	112.2702

Table 4.1: Prony series parameter values for the polymer model

viscoelastic material subjected to a sinusoidal strain $\bar{\varepsilon}^e = \varepsilon_0 \sin(\omega t)$, the resultant stress is also sinusoidal but with a phase shift and can be expressed as:

$$\sigma(t) = \sigma_0 \sin(\omega t + \delta) = E' \varepsilon_0 \sin(\omega t) + E'' \varepsilon_0 \cos(\omega t) \tag{4.35}$$

where E' is called the storage modulus and E'' is called the loss modulus. Under uniaxial loading, the stress is independent of the Poisson's ratio, and the viscoelastic Young's modulus may be described by a Prony series similar to Eq. (4.4):

$$E(t) = E_\infty + \sum_{i=1}^{n} E_i \exp\left(-\frac{t}{\tau_i}\right) \tag{4.36}$$

where $E_\infty = 10394$ MPa is the long-term Young's modulus which is already calibrated in Section 4.3.1, E_i and τ_i are the relaxation Young's modulus and the relaxation time for each Maxwell chain, respectively, and n is the number of Maxwell chains. Following Rocha et al. [48], four Prony series are used for the polymer model and the corresponding parameter values are listed in Table 4.1. For given parameters E_i and τ_i, the stress signal is given as:

$$\sigma(t) = \int_{-\infty}^{t} E(t-\tilde{t}) \frac{\partial \bar{\varepsilon}^e(\tilde{t})}{\partial \tilde{t}} d\tilde{t} = \left(E_\infty + \sum_{i=1}^{4} \frac{E_i \omega^2}{\omega^2 + \frac{1}{\tau_i^2}} \right) \varepsilon_0 \sin(\omega t) + \left(\sum_{i=1}^{4} \frac{E_i \frac{\omega}{\tau_i}}{\omega^2 + \frac{1}{\tau_i^2}} \right) \varepsilon_0 \cos(\omega t) \tag{4.37}$$

from which the storage modulus and loss modulus can be identified as:

$$E'(\omega) = E_\infty + \sum_{i=1}^{4} \frac{E_i \omega^2}{\omega^2 + \frac{1}{\tau_i^2}} \tag{4.38}$$

$$E''(\omega) = \sum_{i=1}^{4} \frac{E_i \frac{\omega}{\tau_i}}{\omega^2 + \frac{1}{\tau_i^2}} \tag{4.39}$$

The closed-form formulations given in Eq. (4.38) and Eq. (4.39) show that both the storage modulus E' and the loss modulus E'' are a function of the applied angular frequency ω.

To calibrate the viscoelastic parameters of the homogenized VE-VP model, 10 DMA simulations with uniaxial tension on the RVE with 10 different angular frequencies $\omega_i \in 2\pi \times [0.05, 0.1, 0.5, 1.0, 2.0, 5.0, 10.0, 15.0, 20.0, 25.0]$ Hz and the same magnitude $\varepsilon_0 = 0.0001$ mm are performed and the overall stress of the RVE is recorded. The boundary conditions illustrated in Appendix F are applied on the RVE

shown in Fig. 4.4 and the overall stress is calculated according to Eq. (45) in the appendix. For each case, the values of E' and E'' can be calculated from the stress of the simulation, considering the closed-form expression Eq. (4.35). These values for the storage modulus and loss modulus are plotted in Fig. 4.5. Meanwhile, a non-linear least-square optimization algorithm implemented in the LSQNONLIN function in MATLAB is used to match the numerical results with the closed-form formulation of E' and E''. The two objective functions that are minimized by running the LSQNONLIN are:

$$y(x) = \begin{bmatrix} \sqrt{\sum_{i=1}^{10} \left(E_i'(\omega_i, x) - \overline{E}_i'(\omega_i) \right)^2} \\ \sum_{i=1}^{10} \left(E_i''(\omega_i, x) - \overline{E}_i''(\omega_i) \right)^2 \end{bmatrix} \tag{4.40}$$

where $x = (E_1, E_2, E_3, E_4, \tau_1, \tau_2, \tau_3, \tau_4)$ are the unknown viscoelastic relaxation modulus and relaxation times needed to be calibrated, $E_i'(\omega_i, x)$ and $E_i''(\omega_i, x)$ are the relaxation modulus and relaxation time calculated from Eq. (4.38) and Eq. (4.39), and $\overline{E}_i'(\omega_i)$ and $\overline{E}_i''(\omega_i)$ are the storage modulus and loss modulus obtained from each RVE simulation. Finally, the calibrated VE parameters are:

$$[E_1, E_2, E_3, E_4, \tau_1, \tau_2, \tau_3, \tau_4]^T = \begin{bmatrix} 256.4811 \\ 188.1201 \\ 2232.8425 \\ 302.9434 \\ 61.1900 \\ 553.0494 \\ 40905.3228 \\ 30015955.2538 \end{bmatrix} \tag{4.41}$$

By substituting the calibrated values in Eq. (4.41) into Eq. (4.38) and Eq. (4.39), the calibrated loss modulus and storage modulus functions are obtained. The comparison between this calibrated solution and the RVE solution shown in Fig. 4.5 verifies the accuracy of the calibration procedure.

Next, the relaxation bulk modulus K_i and shear modulus G_i can be obtained by:

$$G_i = \frac{E_i}{2(1+\nu)}, \qquad K_i = \frac{E_i}{3(1-2\nu)}, \qquad i = 1, 2, 3, 4 \tag{4.42}$$

where $\nu = 0.42$ is the elastic Poisson's ratio calibrated in Section 4.3.1. The relaxation times for bulk modulus and shear modulus are obtained by [53]:

$$g_i = \frac{E_i \tau_i}{G_i}, \qquad k_i = \frac{E_i \tau_i}{K_i}, \qquad i = 1, 2, 3, 4 \tag{4.43}$$

All these data are listed in Table 4.2.

4.3.3. Step 3: homogenized plasticity model

To calibrate the plasticity properties of the homogenized VE-VP model, i.e. the plastic Poisson's ration ν_p and the hardening curves, only the plasticity components

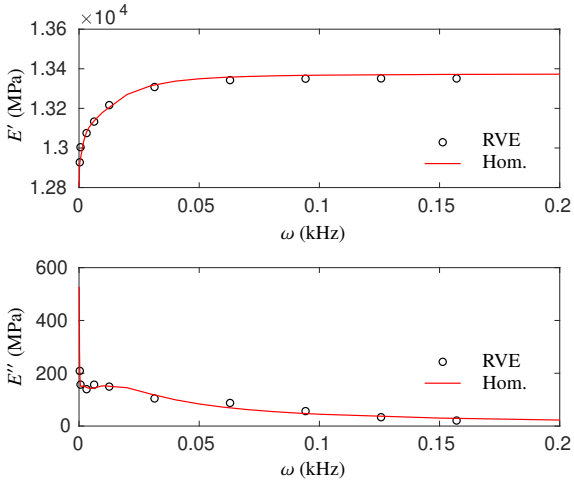

Figure 4.5: Comparison of storage modulus and loss modulus results between RVE model and the homogenized model with calibrated parameters.

G_i (MPa)	90.3102	66.2395	786.2121	106.6702
g_i (ms)	173.7796	1570.6603	116171.1168	85245312.9208
K_i (MPa)	534.3356	391.9169	4651.7552	631.1321
k_i (ms)	29.3712	265.4637	19634.5549	14407658.5218

Table 4.2: Bulk and shear relaxation modulus and relaxation times of four Prony series.

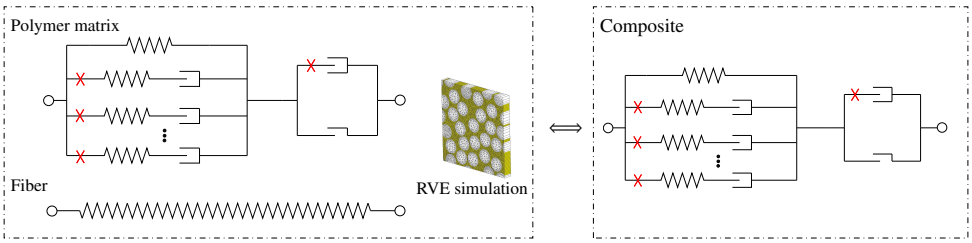

Figure 4.6: Schematic representation of step 3: the calibration of plasticity parameters of the homogenized VE-VP model. The cross sign represents the components that are turned off.

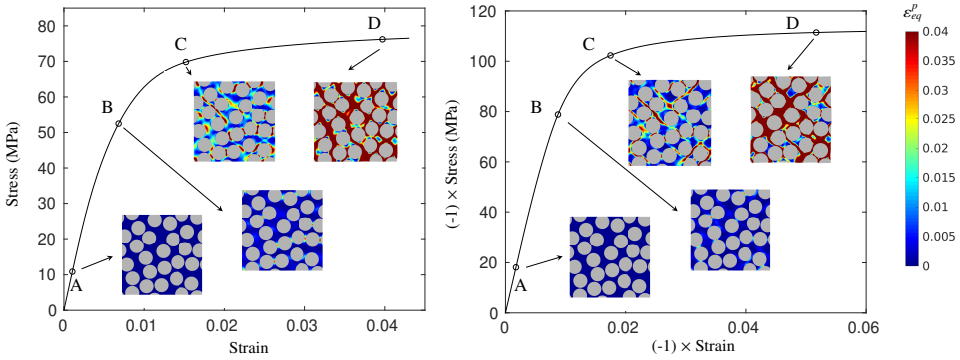

Figure 4.7: Stress vs. strain curve for tension (left) and compression (right). The enclosed subfigures show the distribution of the equivalent plastic strain ε^p_{eq} for typical time instants.

of the RVE model are turned on (see Fig. 4.6) with the homogenized elasticity properties from Section 4.3.1. The plastic Poisson's ratio is 0.32 and the hardening curves of the matrix for tension and compression are $\sigma_t\left(\varepsilon^p_{eq}\right) = 64.80 - 33.6\exp\left(-\varepsilon^p_{eq}/0.003407\right) - 10.21\exp\left(-\varepsilon^p_{eq}/0.06493\right)$ and $\sigma_c = 1.25\sigma_t$ (see Fig. 4.8b). Two types of stress states are applied on the RVE: a uniaxial tensile stress and a uniaxial compressive stress, to account for the hardening plasticity behavior under both tension and compression loading. The boundary conditions illustrated in Appendix C are applied on the RVE shown in Fig. 4.6 with a tensile (and compressive) loading rate $\dot{\bar{u}}$ of 0.003 m/s.

During the RVE simulation, the average stress σ_{11} and strains ε_{11}, ε_{22} are recorded. The stress vs. strain curve and the distribution of the equivalent plastic strain at several representative time instants of the two cases are shown in Fig. 4.7. There is an initial linear region where the material is deforming elastically (see point A in Fig. 4.7). Afterwards, a hardening-type of stress-strain curve is observed while plastic flow occurs and plastic bands start to form (see points B, C, D in Fig. 4.7). The stress increase in compression is faster than that in tension. From the enclosed subfigures, it can be found that the deformation pattern of the RVE with plastic shear bands is similar to what is expected for a isotropic material under a unidirectional stress state. This verifies the effectiveness of the applied boundary conditions. It should also be noted that the detailed strain and stress field are obtained as well, which is one of the advantages over mean-field homogenization approaches.

The plastic Poisson's ratio ν_p for each case can be calculated according to:

$$\nu_p = -\frac{\varepsilon^p_{22}}{\varepsilon^p_{11}} = -\left(\frac{u_2}{l_2} + \nu\cdot\frac{\sigma_{11}}{E_\infty}\right)\Big/\left(\frac{u_1}{l_1} - \frac{\sigma_{11}}{E_\infty}\right) \tag{4.44}$$

where u_1 and u_2 are the displacement along direction-1 and direction-2, respectively, l_1 and l_2 are the length of RVE along direction-1 and direction-2, respectively, and $\nu = 0.42$ is the elastic Poisson's ratio.

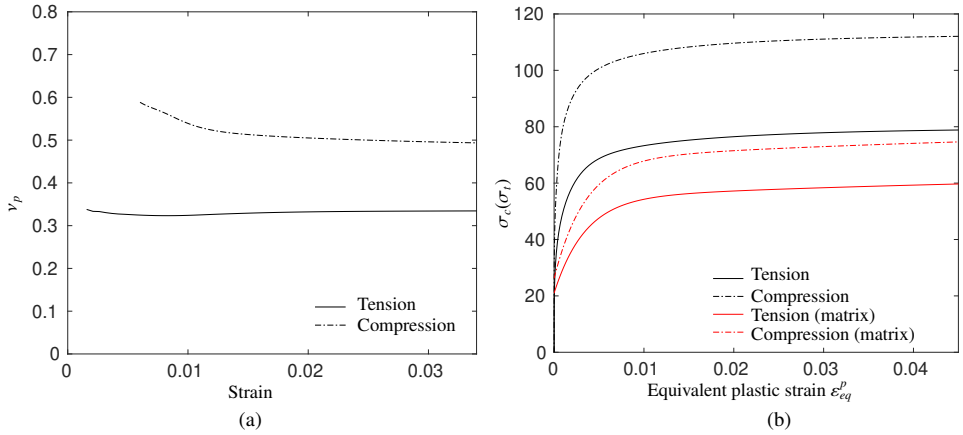

Figure 4.8: (a) Plastic Poisson's ratio under tension and compression (for the matrix, the plastic Poisson's ratio is 0.32); (b) calibrated hardening curves.

The evolution of the plastic Poisson's ratio ν_p with the strain ε_{11} is visualized in Fig. 4.8. The plastic Poisson's ratio for tension and compression gradually stabilizes to a certain value. For tension that is around 0.34 while for compression it is around 0.5. A similar observation was made in micromechanical simulations by van der Meer [54], showing that the assumption of a single plastic Poisson's ratio is an oversimplification for the composite material response.

In this work, the plastic Poisson's ratio extracted from tensile loading is adopted (i.e. $\nu_p = 0.34$) for simplicity. Therefore, the coefficient α in the flow rule, i.e. Eq. (4.11), is found to be 1.075. For this transversely isotropic RVE, the definition of the equivalent plastic strain from Eq. (4.9) is adapted to:

$$\Delta\varepsilon^p_{eq} = \sqrt{\frac{1}{1+\nu_p^2}\Delta\varepsilon^p_{ij}\Delta\varepsilon^p_{ij}} \quad \text{in which } i,j = 1,2 \tag{4.45}$$

so that the same in-plane response is found with an isotropic RVE with the equivalent plastic strain defined in Eq. (4.9). From the unidirectional tension and compression RVE simulations, the hardening curves, i.e. $\sigma_c(\varepsilon^p_{eq})$ and $\sigma_t(\varepsilon^p_{eq})$, can be extracted by taking the stress and equivalent plastic strain data pair $(\sigma^i_{11}, \varepsilon^p_{eq})$ for each time step with:

$$\sigma^i_{11} = \frac{f_1}{l_2 l_3}, \qquad i = c,t \tag{4.46}$$

The calibrated hardening curves for tension and compression are plotted in Fig. 4.8(b) along with the hardening curves of the matrix. It is observed that by adding the fibers, the yield stresses increase.

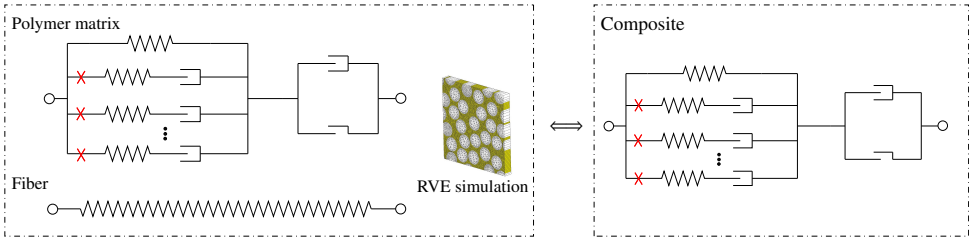

Figure 4.9: Schematic representation of step 4: the calibration of viscoplasticity parameters of the homogenized VE-VP model. The cross sign represents the components that are turned off.

4.3.4. Step 4: homogenized viscoplastic properties

To obtain the viscoplasticity parameters of the homogenized VE-VP model, i.e. m_p and η_p, part of the polymer and the homogenized model are turned off. The RVE is loaded in unidirectional tension and different loadings are considered. The boundary conditions illustrated in Appendix F are applied on the RVE shown in Fig. 4.9. The elasticity and plasticity properties of the polymer in the RVE model have already been introduced in Section 4.3.1 and Section 4.3.3, respectively. The viscoplastic coefficients for the polymer are $\overline{m}_p = 7.305$ and $\overline{\eta}_p = 3.49 \cdot 10^{12}$ MPa·s. Six different cases with the loading rates $\dot{\varepsilon}_{11} \in [0.00035, 0.00175, 0.0035, 0.0175, 0.035, 0.175]$ s^{-1} are applied on the RVE. The stress-strain relations of the six cases are plotted in Fig. 4.10. Single element tests with the homogenized VE-VP model are performed to match the six RVE simulation results with given viscoplastic coefficients m_p and η_p. The elasticity and plasticity properties of the homogenized VE-VP model are already calibrated in Section 4.3.1 and Section 4.3.3. Therefore, only the homogenized viscoplastic parameters m_p and η_p need to be calibrated. In order to find an optimal combination of these parameters, 7×5 simulations of the homogenized VE-VP model with a combination of one of the seven m_p values and one of the five η_p values listed in Table 4.3 are performed. Six objective functions are introduced as:

$$y(m_p, \eta_p) = \begin{bmatrix} \sum_{i=1}^{n_1} \left(\Xi_i^{(1)}(m_p, \eta_p) - \overline{\Xi}_i^{(1)} \right)^2 \\ \sum_{i=1}^{n_2} \left(\Xi_i^{(2)}(m_p, \eta_p) - \overline{\Xi}_i^{(2)} \right)^2 \\ \sum_{i=1}^{n_3} \left(\Xi_i^{(3)}(m_p, \eta_p) - \overline{\Xi}_i^{(3)} \right)^2 \\ \sum_{i=1}^{n_4} \left(\Xi_i^{(4)}(m_p, \eta_p) - \overline{\Xi}_i^{(4)} \right)^2 \\ \sum_{i=1}^{n_5} \left(\Xi_i^{(5)}(m_p, \eta_p) - \overline{\Xi}_i^{(5)} \right)^2 \\ \sum_{i=1}^{n_6} \left(\Xi_i^{(6)}(m_p, \eta_p) - \overline{\Xi}_i^{(6)} \right)^2 \end{bmatrix} \tag{4.47}$$

where $\overline{\Xi}_i^{(k)}$ is the stress of each time increment in each loading rate case $k = 1, 2, ..., 6$ obtained from the RVE simulation, $\Xi_i^{(k)}(m_p, \eta_p)$ denotes the stress of the

$\mathcal{M}$	6.5	6.6	6.7	6.8	6.9	7.0	7.1
$\mathcal{Q}$ (MPa·s)	5.e12	7.e12	1.e13	2.e13	5.e13		

Table 4.3: A list of all the m_p and η_p values used in homogenized model.

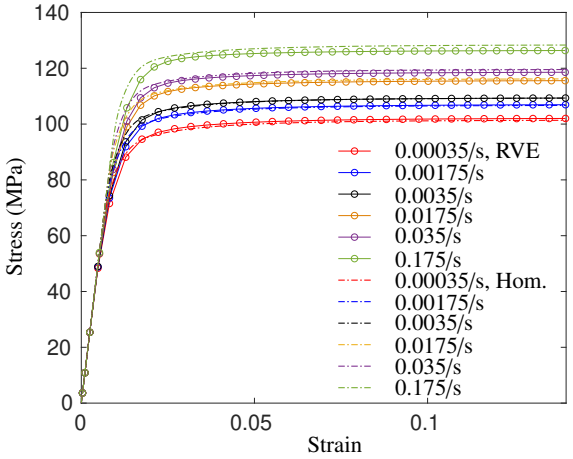

Figure 4.10: Comparison of Stress-strain relation of monotonic loading for six different strain rates between RVE simulation and the homogenized numerical model.

homogenized numerical model for the same time increment as the RVE simulation with the value of m_p and η_p, and n_k is the number of time increments for each loading rate case. Afterwards, the function $\Xi_i^{(k)}\left(m_p,\eta_p\right)$ is defined by the following interpolation/extrapolation scheme:

$$\Xi_i^{(k)}\left(m_p,\eta_p\right)=\sum_{s=1}^{2}\sum_{t=1}^{2}N_s(m_p)N_t(\eta_p)\Xi_i^{(k)}\left(m_p^s,\eta_p^t\right),\qquad m_p^s\in\mathcal{M},\eta_p^t\in\mathcal{Q}\tag{4.48}$$

where $N_s(m_p)$ and $N_t(\eta_p)$ are 1st-order Lagrange interpolation functions of m_p and η_p, respectively, and $\Xi_i^{(k)}\left(m_p^s,\eta_p^t\right)$ is the stress of the homogenized numerical model for each loading rate case at the same time increment as the RVE simulation for $m_p^s\in\mathcal{M}$ and $\eta_p^t\in\mathcal{Q}$. By running the LSQNONLIN function in MATLAB, the optimal values of m_p and η_p are found to be $m_p=6.66$, $\eta_p=1.2\cdot10^{13}$ MPa·s. The stress-strain curves for the homogenized numerical model using the calibrated values are plotted in Fig. 4.10. It is shown that the homogenized model solution matches very well with the RVE simulation results for the studied strain rate ranges.

4.4. Comparison with RVE model

To validate the step-by-step calibration scheme introduced in the previous section, the performance of the homogenized VE-VP model is compared with the RVE model

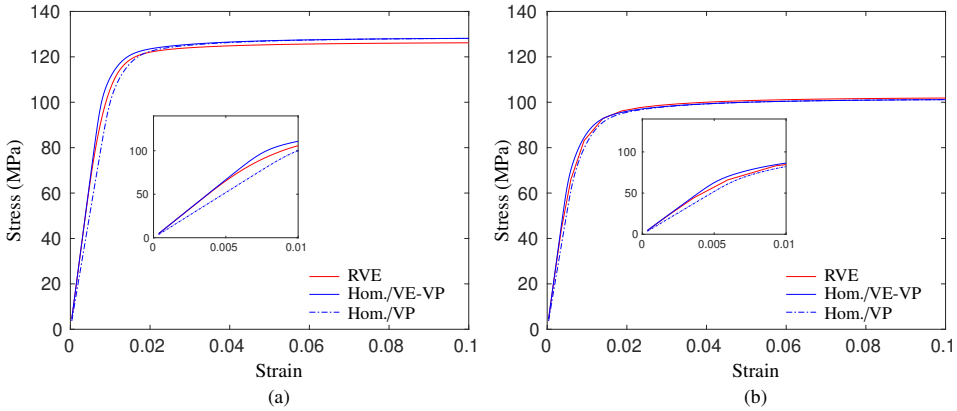

Figure 4.11: Comparison of the RVE model and the homogenized model for the stress-strain relation under monotonic loadings. (a) strain rate is 0.175 /s and (b) strain rate is 0.00035/s.

under a number of characteristic loading conditions.

4.4.1. Rate dependence

The complete homogenized VE-VP model with calibrated parameters from Section 4.3 is now compared against the RVE simulation for a monotonic loading at different rates. All viscoelasticity and viscoplasticity components are turned on for both the homogenized model and the polymer model in the RVE. Both the homogenized model and the RVE model are loaded in unidirectional tension and two different strain rates are considered: 0.00035/s and 0.175/s. The boundary conditions and the calculation of the overall stress illustrated in Appendix F are applied on both models. The comparison in stress vs. strain relation between the RVE model and the homogenized model for these two strain rates is shown in Fig. 4.11. For both cases, an extra computation with the homogenized numerical model but with only the viscoplasticity components turned on is performed and its result is also plotted. For both cases, the response of the composite microstructure is captured very well. This is seen from the good match between the RVE model and the homogenized model with all components turned on. The enclosed subfigure also shows that by turning off the viscoelasticity components, the rate-dependent initial stiffness is not captured correctly in the homogenized model, while the yield stress is still captured well. This verifies that the proposed step-by-step calibration scheme does not lack accuracy due to interaction between the different processes.

4.4.2. Loading/unloading/relaxation behavior

To further validate the calibrated parameters m_p and η_p, the cyclic loading cases shown in Fig. 4.12 are studied. The scenario with loading/unloading (LU) is investigated for two different strain rates: 0.00035/s and 0.175/s. The comparison between the RVE simulation result and the homogenized numerical model is demon-

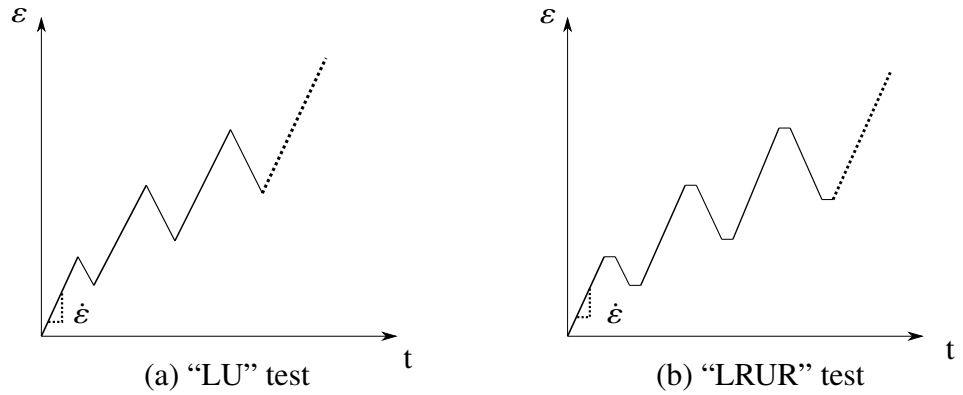

Figure 4.12: Two types of periodic-type of loading with constant loading (unloading) rates. (a) Loading/unloading ("LU") test; (b) Loading/relaxation/unloading/relaxation ("LRUR") test. The strain rate for the unloading part is the same as the loading part and the unloading stops when the strain is unloaded to 2/3 of the strain when the unloading process starts.

strated in Fig. 4.13. It is shown that the stress-strain curve for these two cases has a similar pattern, for the first loading/unloading cycle, the stress is first elastic and after the strain is relatively large, viscoplastic flow starts, followed by elastic unloading. Afterwards, in the next loading/unloading cycle, the material is elastically loaded initially and viscoplastic flow continues to develop followed by elastic unloading again. When strain after unloading is relatively large in the last few cycles, plastic flow also starts in compression as observed from the nonlinear part of the unloading branch of the curve. In both cases, the homogenized model matches very well with the RVE model under tension but if compression also happens, there is some deviation where the model would perform better if (part of) the hardening in the homogenized model would be described as kinematic hardening instead of the same isotropic hardening that is present in the matrix model.

Finally, with the loading/relaxation/unloading/relaxation (LRUR) test, the capability of the homogenized model to capture relaxation is investigated. Both the RVE model and homogenized model are loaded in uniaxial tension under a strain rate of 0.0035/s. As shown in Fig. 4.14, the homogenized numerical model matches very well for both loading and relaxation phases, although again a small deviation is observed for reverse loading when plastic flow in compression starts.

4.5. Conclusion

In this paper, a numerical homogenization scheme is introduced to derive a viscoelastic-viscoplastic material model for polymer composites. It is assumed that the homogenized VE-VP model has the same formulation as the VE-VP model for the polymeric matrix. The material parameters of different components of the homogenized VE-VP model are calibrated by a novel step-by-step numerical homogenization procedure.

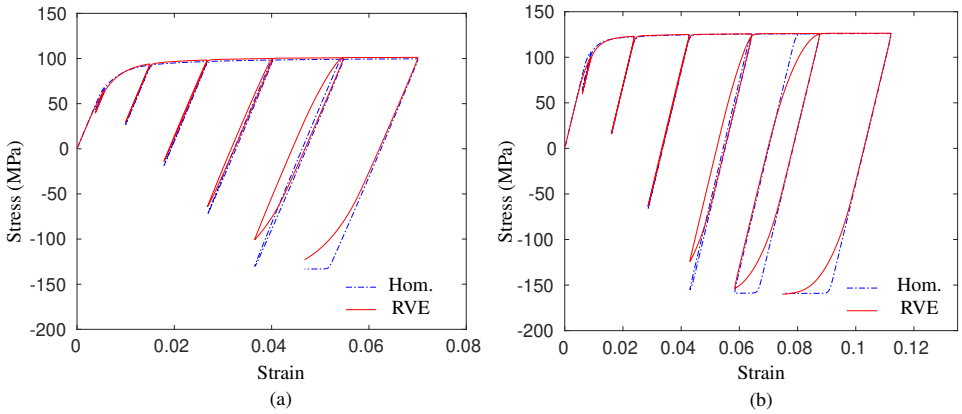

Figure 4.13: Comparison of the RVE model and the homogenized model for the stress-strain relation under "LU" loadings. (a) strain rate 0.00035/s; (b) strain rate 0.175/s.

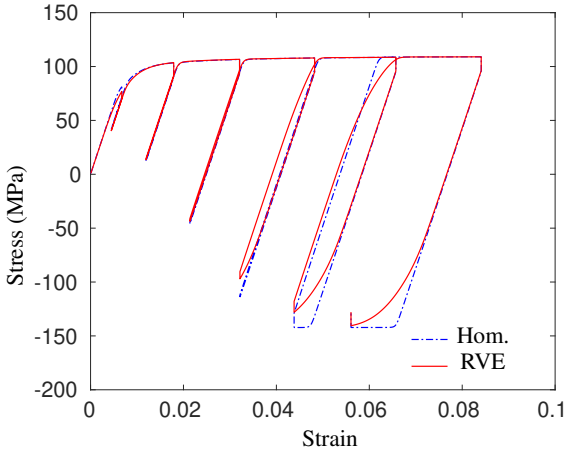

Figure 4.14: Comparison of the RVE model and the homogenized model for the stress-strain relation under a "LRUR" loading. Strain rate 0.0035/s.

The elasticity properties of the homogenized VE-VP model, including the Young's modulus E_∞ and the elastic Poisson's ration ν, are extracted from the stress and strain in the loading direction and strain in the lateral direction when the RVE model with only the elasticity components turned on is subjected to uniaxial loading. Next, the relaxation modulus and relaxation time of the viscoelastic components of the homogenized VE-VP model are calibrated by performing a series of DMA tests on the RVE model with only viscoelasticity components turned on. A good match of the storage modulus and loss modulus at different loading frequencies between the RVE model and the closed-form solutions in Eq. (4.38) and Eq. (4.39) shows that the viscosity of the polymer composites within elastic range is quantified by the calibrated homogenized model accurately. Afterwards, the plastic Poisson's ratio and hardening curves (for both tension and compression) are calibrated by unidirectional load cases with only plasticity components turned on for the RVE model. It is found that the yield stress of the composite is higher than the yield stress of the polymer matrix alone and a single plastic Poisson's ratio is an oversimplification of the polymer composites behavior. The homogenized model with the same isotropic hardening as the matrix model matches very well with the RVE model under monotonic loading. However, if plasticity also happens under reverse loading, there is some deviation where the homogenized model would perform better if (part of) the hardening would be described as kinematic hardening. Next, by turning on the viscoplasticity components of the RVE model, the viscoplasticity related parameters m_p and η_p of the homogenized VE-VP model are calibrated by a series of monotonic tensile tests at different loading rates.

With the calibrated material parameters from the step-by-step numerical homogenization scheme, the homogenized numerical model is compared with the RVE model under characteristic load cases. The capabilities of the homogenized VE-VP model in capturing rate-dependence, loading/unloading and stress relaxation are examined. A good match between these two models demonstrates that the introduced step-by-step numerical homogenization procedure with turning on/off certain components of the material models provides an efficient and accurate way for obtaining material parameters of a VE-VP model. The procedure has been demonstrated for the transverse response of fiber-reinforced composites but can also be used for particle reinforced composites with an appropriate geometry for the RVE.

References

[1] Y. Liu, F. P. van der Meer, L. J. Sluys, and J. T. Fan, *A numerical homogenization scheme used for derivation of a homogenized viscoelastic-viscoplastic model for the transverse response of fiber-reinforced polymer composites,* Composite Structures **252**, 112690 (2020).

[2] T. Schmack, T. Filipe, G. Deinzer, C. Kassapoglou, and F. Walther, *Experimental and numerical investigation of the strain rate-dependent compression behaviour of a carbon-epoxy structure,* Composite Structures **189**, 256 (2018).

[3] D. Garcia-Gonzalez, M. Rodriguez-Millan, A. Rusinek, and A. Arias, *Investi-*

gation of mechanical impact behavior of short carbon-fiber-reinforced PEEK composites, Composite Structures **133**, 1116 (2015).

[4] S. V. Thiruppukuzhi and C. T. Sun, *Models for the strain-rate-dependent behavior of polymer composites,* Composites Science and Technology **61**, 1 (2001).

[5] M. Shirinbayan, J. Fitoussi, M. Bocquet, F. Meraghni, B. Surowiec, and A. Tcharkhtchi, *Multi-scale experimental investigation of the viscous nature of damage in Advanced Sheet Molding Compound (A-SMC) submitted to high strain rates,* Composites Part B: Engineering **115**, 3 (2017).

[6] S. Nemat-Nasser and M. Hori, *Micromechanics: overall properties of heterogeneous materials*, Vol. 37 (Elsevier, 2013).

[7] P. Kanouté, D. P. Boso, J. L. Chaboche, and B. A. Schrefler, *Multiscale methods for composites: a review,* Archives of Computational Methods in Engineering **16**, 31 (2009).

[8] V. P. Nguyen, M. Stroeven, and L. J. Sluys, *Multiscale continuous and discontinuous modeling of heterogeneous materials: a review on recent developments,* Journal of Multiscale Modelling **3**, 229 (2011).

[9] J. D. Eshelby, *The determination of the elastic field of an ellipsoidal inclusion, and related problems,* Proceedings of the Royal Society of London **241**, 376 (1957).

[10] T. Mori and K. Tanaka, *Average stress in matrix and average elastic energy of materials with misfitting inclusions,* Acta Metallurgica **21**, 571 (1973).

[11] E. Kröner, *Berechnung der elastischen konstanten des vielkristalls aus den konstanten des einkristalls,* Zeitschrift für Physik **151**, 504 (1958).

[12] R. Hill, *A self-consistent mechanics of composite materials,* Journal of the Mechanics and Physics of Solids **13**, 213 (1965).

[13] G. P. Tandon and G. J. Weng, *A theory of particle-reinforced plasticity,* Journal of Applied Mechanics **55**, 126 (1988).

[14] R. Hill, *Continuum micro-mechanics of elastoplastic polycrystals,* Journal of the Mechanics and Physics of Solids **13**, 89 (1965).

[15] A. Molinari, G. R. Canova, and S. Ahzi, *A self consistent approach of the large deformation polycrystal viscoplasticity,* Acta Metallurgica **35**, 2983 (1987).

[16] B. Miled, I. Doghri, L. Brassart, and L. Delannay, *Micromechanical modeling of coupled viscoelastic-viscoplastic composites based on an incrementally affine formulation,* International Journal of Solids and Structures **50**, 1755 (2013).

[17] I. Doghri, L. Adam, and N. Bilger, *Mean-field homogenization of elasto-viscoplastic composites based on a general incrementally affine linearization method,* International Journal of Plasticity **26**, 219 (2010).

[18] R. Masson, M. Bornert, P. Suquet, and A. Zaoui, *An affine formulation for the prediction of the effective properties of nonlinear composites and polycrystals,* Journal of the Mechanics and Physics of Solids **48**, 1203 (2000).

[19] O. Pierard and I. Doghri, *An enhanced affine formulation and the corresponding numerical algorithms for the mean-field homogenization of elasto-viscoplastic composites,* International Journal of Plasticity **22**, 131 (2006).

[20] I. Doghri and C. Friebel, *Effective elasto-plastic properties of inclusion-reinforced composites. Study of shape, orientation and cyclic response,* Mechanics of Materials **37**, 45 (2005).

[21] M. Lévesque, K. Derrien, L. Mishnaevski, D. Baptiste, and M. D. Gilchrist, *A micromechanical model for nonlinear viscoelastic particle reinforced polymeric composite materials-undamaged state,* Composites Part A: Applied Science and Manufacturing **35**, 905 (2004).

[22] R. M. Haj-Ali and A. H. Muliana, *A micromechanical constitutive framework for the nonlinear viscoelastic behavior of pultruded composite materials,* International Journal of Solids and Structures **40**, 1037 (2003).

[23] I. V. Andrianov, V. I. Bolshakov, V. V. Danishevs'kyy, and D. Weichert, *Higher order asymptotic homogenization and wave propagation in periodic composite materials,* Proceedings of the Royal Society A: Mathematical, Physical and Engineering Sciences **464**, 1181 (2008).

[24] G. J. Dvorak and Y. Benveniste, *On transformation strains and uniform fields in multiphase elastic media,* Proceedings of the Royal Society of London. Series A: Mathematical and Physical Sciences **437**, 291 (1992).

[25] I. V. Andrianov, V. V. Danishevs'kyy, and D. Weichert, *Homogenization of viscoelastic-matrix fibrous composites with square-lattice reinforcement,* Archive of Applied Mechanics **81**, 1903 (2011).

[26] Y.-M. Yi, S.-H. Park, and S.-K. Youn, *Asymptotic homogenization of viscoelastic composites with periodic microstructures,* International Journal of Solids and Structures **35**, 2039 (1998).

[27] Q. Li, W. Chen, S. Liu, and J. Wang, *A novel implementation of asymptotic homogenization for viscoelastic composites with periodic microstructures,* Composite Structures **208**, 276 (2019).

[28] J. Fish and K. Shek, *Computational plasticity and viscoplasticity for composite materials and structures,* Composites Part B: Engineering **29**, 613 (1998).

[29] G. Chatzigeorgiou, N. Charalambakis, Y. Chemisky, and F. Meraghni, *Periodic homogenization for fully coupled thermomechanical modeling of dissipative generalized standard materials,* International Journal of Plasticity **81**, 18 (2016).

[30] L. Zhang and W. Yu, *A micromechanics approach to homogenizing elasto-viscoplastic heterogeneous materials,* International Journal of Solids and Structures **51**, 3878 (2014).

[31] X. Wu and N. Ohno, *A homogenization theory for time-dependent nonlinear composites with periodic internal structures,* International Journal of Solids and Structures **36**, 4991 (1999).

[32] V. Kouznetsova, W. A. M. Brekelmans, and F. P. T. Baaijens, *An approach to micro-macro modeling of heterogeneous materials,* Computational Mechanics **27**, 37 (2001).

[33] R. Hill, *Elastic properties of reinforced solids: Some theoretical principles,* Journal of the Mechanics and Physics of Solids **11**, 357 (1963).

[34] F. V. Souza and D. H. Allen, *Modeling the transition of microcracks into macrocracks in heterogeneous viscoelastic media using a two-way coupled multiscale model,* International Journal of Solids and Structures **48**, 3160 (2011).

[35] S. Staub, H. Andrä, M. Kabel, and T. Zangmeister, *Multi-scale simulation of viscoelastic fiber-reinforced composites,* Tech. Mech **32**, 70 (2012).

[36] T. Schüler, R. Manke, R. Jänicke, M. Radenberg, and H. Steeb, *Multi-scale modelling of elastic/viscoelastic compounds,* ZAMM-Journal of Applied Mathematics and Mechanics/Zeitschrift für Angewandte Mathematik und Mechanik **93**, 126 (2013).

[37] F. Feyel and J.-L. Chaboche, *FE^2 multiscale approach for modelling the elastoviscoplastic behaviour of long fibre SiC/Ti composite materials,* Computer Methods in Applied Mechanics and Engineering **183**, 309 (2000).

[38] R. Berthelsen and A. Menzel, *Computational homogenisation of thermo-viscoplastic composites: Large strain formulation and weak micro-periodicity,* Computer Methods in Applied Mechanics and Engineering **348**, 575 (2019).

[39] E. Tikarrouchine, G. Chatzigeorgiou, F. Praud, B. Piotrowski, Y. Chemisky, and F. Meraghni, *Three-dimensional FE^2 method for the simulation of non-linear, rate-dependent response of composite structures,* Composite Structures **193**, 165 (2018).

[40] S. Marfia and E. Sacco, *Multiscale technique for nonlinear analysis of elastoplastic and viscoplastic composites,* Composites Part B: Engineering **136**, 241 (2018).

[41] J. R. Brockenbrough, S. Suresh, and H. A. Wienecke, *Deformation of metal-matrix composites with continuous fibers: geometrical effects of fiber distribution and shape,* Acta metallurgica et materialia **39**, 735 (1991).

[42] V. Tvergaard, *Analysis of tensile properties for a whisker-reinforced metal-matrix composite,* Acta metallurgica et materialia **38**, 185 (1990).

[43] G. Bao, J. W. Hutchinson, and R. M. McMeeking, *Particle reinforcement of ductile matrices against plastic flow and creep,* Acta metallurgica et materialia **39**, 1871 (1991).

[44] A. Courtois, L. Marcin, M. Benavente, E. Ruiz, and M. Lévesque, *Numerical multiscale homogenization approach for linearly viscoelastic 3D interlock woven composites,* International Journal of Solids and Structures **163**, 61 (2019).

[45] A. Karamnejad, A. Ahmed, and L. J. Sluys, *A numerical homogenization scheme for glass particle-toughened polymers under dynamic loading,* Journal of Multiscale Modelling **08**, 1750001 (2017).

[46] O. van der Sluis, P. J. G. Schreurs, W. A. M. Brekelmans, and H. E. H. Meijer, *Overall behaviour of heterogeneous elastoviscoplastic materials: effect of microstructural modelling,* Mechanics of Materials **32**, 449 (2000).

[47] O. van der Sluis, P. J. G. Schreurs, and H. E. H. Meijer, *Homogenisation of structured elastoviscoplastic solids at finite strains,* Mechanics of Materials **33**, 499 (2001).

[48] I. B. C. M. Rocha, F. P. van der Meer, S. Raijmaekers, F. Lahuerta, R. P. L. Nijssen, and L. J. Sluys, *Numerical/experimental study of the monotonic and cyclic viscoelastic/viscoplastic/fracture behavior of an epoxy resin,* International Journal of Solids and Structures **168**, 153 (2019).

[49] S. Haouala and I. Doghri, *Modeling and algorithms for two-scale time homogenization of viscoelastic-viscoplastic solids under large numbers of cycles,* International Journal of Plasticity **70**, 98 (2015).

[50] Y. Liu, F. P. van der Meer, and L. J. Sluys, *A dispersive homogenization model for composites and its RVE existence,* Computational Mechanics (2019), 10.1007/s00466-019-01753-9.

[51] C. Geuzaine and J.-F. Remacle, *Gmsh: A 3-D finite element mesh generator with built-in pre- and post-processing facilities,* International Journal for Numerical Methods in Engineering **79**, 1309 (2009).

[52] A. Krairi and I. Doghri, *A thermodynamically-based constitutive model for thermoplastic polymers coupling viscoelasticity, viscoplasticity and ductile damage,* International Journal of Plasticity **60**, 163 (2014).

[53] B. Miled, I. Doghri, and L. Delannay, *Coupled viscoelastic-viscoplastic modeling of homogeneous and isotropic polymers: Numerical algorithm and analytical solutions,* Computer Methods in Applied Mechanics and Engineering **200**, 3381 (2011).

[54] F. P. van der Meer, *Micromechanical validation of a mesomodel for plasticity in composites,* European Journal of Mechanics - A/Solids **60**, 58 (2016).

5

Modeling of dynamic mode I crack growth in glass fiber-reinforced polymer composites: fracture energy and failure mechanism

5.1. Introduction

Fiber reinforced polymer composites have been used in impact-resistant devices, automotives, aircraft structures due to their potential for high strength-to-weight ratios and impact energy absorption. To be able to fully exploit the potential of impact behavior of composites it is necessary to investigate dynamic crack propagation, in particular the underlying mechanisms, microstructural effects and the fracture energy.

Starting from Griffith's ideas postulated for equilibrium cracks [2] and its extension by Mott for dynamic fracture [3], dynamic fracture can be investigated on an energetic basis. The dynamic energy release rate G_d is the energy released into the crack tip process zone per unit crack extension and must be equal to the energy required per unit extension G_c [4]. Generally, both G_d and G_c are functions of crack propagation history, in particular, the crack speed V. Freund [5] showed that for mode-I crack propagation in homogeneous materials under elastodynamic conditions and in plane strain state the dynamic energy release rate G_d can be expressed in the following form: $G_d = A_I(V)\frac{(1-\nu^2)K_I^2}{E}$, where E is the Young's modulus, ν is the Poisson's ratio, K_I is the mode-I dynamic stress intensity factor and A_I is a universal

This chapter is based on [1]

function of crack speed V. The dynamic stress intensity factor K_I tends to zero as V approaches the Rayleigh wave speed c_r, which implies a limiting crack speed of c_r in mode-I. Corresponding to different levels of propagation velocity, the crack surface roughness is observed to show different features since material in the fracture process zone might experience high strain-rate plasticity, microcracks nucleation, thermomechanical interaction and other complex deformation/failure mechanisms. Upon an increase of crack speed, the crack surface first appears to be almost flat (mirror regime), next a rougher surface with conic marks forms (mist regime), and finally (micro)branching takes place (hackle regime). Phenomenologically, a relationship between fracture energy G_c and crack speed V therefore exists.

The relation between the dynamic fracture energy G_c and the crack speed V for composites is determined by the rate-dependent deformation and failure process occurring across multiple length scales and time scales. More specifically, the contributing mechanisms can be roughly classified as viscous material behavior, changes in fracture mechanism, inertia effects and thermomechanical effects. Firstly, there is the role of viscosity of composite constituents (polymer, fiber and interfaces) and its interaction [6, 7]. Shirinbayan et al. [6] postulated that a specific characteristic time for a local damage to occur might exist and this time scale is related to the viscoelastic behavior of the matrix or fiber/matrix interface. Fitoussi et al. [7] argued that for high rate a local strained zone around a debonded interface dissipates the strain energy and accordingly hinders the interfacial crack propagation through the matrix, which causes a delay of the damage at macroscopic scale. Secondly, there can be rate-dependency of the fracture mechanism induced by different failure processes (e.g. fiber failure with fiber pull-out, matrix damage, fiber-matrix interface failure) occuring at microscale level under different loading rates. For instance, for quasi-static tests delamination is often dominated by fiber/matrix interface failure while resin rich brittle fracture zones have been found more dominant in dynamic tests [8–12]. The extent of plastic deformation may decrease with increased loading rate, which represents a ductile-to-brittle transition in the process zone. Thirdly, there are inertia effects characterized as inertia resistance for rapid deformation, damage formation and crack propagation [13, 14]. Due to material heterogeneity, micro-inertia effects also arise as a result of multiple wave reflection and transmission occurring at the interfaces between the constituents, which can result in complex spatiotemporal scenarios of damage and failure evolution, initiated at multiple spots [15, 16]. Finally, there can be thermomechanical dissipation as a transition from isothermal to adiabatic deformation and failure process for composites is expected for increasing loading rate [17–19].

Computational models have been developed on the mesoscale to capture deformation and failure in composites. For such models, the composite ply is considered as a homogenized material where damage and failure can be described by continuum damage models [20, 21] or extended FEM models [22] with failure-mode-based criteria and different stiffness degradation laws for the different failure processes. However, such models inevitably lead to complex constitutive and damage laws that require extensive experimental calibration and the observations obtained at these scales do not provide enough detail about the mechanical processes that

explain the inelastic behavior of the material. Hence, computational micromechanical models are an appealing option for investigating the dynamic fracture energy and the interplay of different mechanisms of dynamic crack growth in composites. Microscale-based approaches can be roughly classified as: the representative volume element (RVE) based multiscale approach, the (modified) boundary layer approach and the embedded cell approach. An RVE is a characteristic sample of heterogeneous material that should be large enough to contain sufficient composite micro-heterogeneities in order to be representative, however it should also be much smaller than the macroscopic structure size [23]. The RVE-based multiscale approach assumes multiple spatial and (or) temporal scales. Solution of finer-scale problems is analyzed in an RVE and information of the finer-scale is hierarchically passed into a coarser scale by bridging laws. For a two-scale scheme, at the macroscopic level the strain localization can be represented by cohesive cracks with strong discontinuity kinematics and a proper kinematical information transfer from the macro-to-micro scales [24–27]. However, the implementation of this method is not readily available in a general-purpose finite element code and the computational cost of this method can be prohibitively high. The (modified) boundary layer formulation considers a small layer of material near the crack tip with well-defined singularity displacement fields applied at the edges of the layer. Numerical solution of this problem allows a quantification of the energy dissipation under such singularity field with energy integrals. This approach has been applied to study elastic–plastic ductile cracking in a homogeneous material [28, 29] and the effective fracture toughness of a heterogeneous material [30–32]. However, it is not clear how to apply the boundary conditions if a singularity field cannot clearly be defined. For the embedded cell approach, full details of the heterogeneous composite microstructure (including the random spatial distribution of the fibers) are explicitly resolved in the fracture region with a finer discretization. Meanwhile, the rest of the model is considered to be a homogeneous medium with simple constitutive equations (obtained a priori with any appropriate homogenization technique) and coarser discretization. The region in which the microstructure is resolved should be small so that the computational cost is affordable. However, it should be sufficiently large to include all the area in which damage occurs during the propagation of the crack, thus energy spent by the different failure micromechanisms (interface debonding, matrix cracking, matrix plastic deformation, etc.) is properly taken into account. This approach has been used in analysis of quasi-static crack propagation of in composite material and to compute the fracture toughness associated to different failure modes [33, 34].

In this paper, a multiscale numerical model using the embedded cell approach is developed to evaluate the mode-I fracture energy of dynamic crack propagation in fiber-reinforced composites and to investigate the associated failure mechanisms. Specifically, the single edge notched tension (SENT) specimen is analyzed. The paper is organized as follows: in Section 5.2, details of the embedded cell model of the SENT specimen are given. Section 5.3 presents the typical deformation and failure phenomena in a series of tests on SENT specimen and the obtained relations between the dynamic fracture energy G_c and crack speed V. The failure

mechanisms in the fracture process zone of the composites are discussed in Section 5.4.

5.2. Numerical model

To compute the mode-I fracture energy of dynamic crack growth in fiber-reinforced polymeric composites, a embedded cell model of an SENT specimen with a width of W and a length of L is developed. It is noted that the crack develops in the transverse plane rather than the fiber direction. The SENT specimen is favored over other Mode-I tests, such as the double cantilever beam test, because the absence of bending deformations (with both tension and compression) in the SENT is beneficial for numerical robustness under dynamic loading condition. As it is shown in Fig. 5.1, an initial notch of length a_0 along x-direction is created on one edge of the specimen and a symmetric displacement loading is applied on the top and bottom edge of the specimen with a prescribed velocity of $\dot{\delta}$. In the vicinity of the initial notch tip, a composite microstructure of M rows and N columns of repeating RVEs is embedded in a homogenized medium of the composites. The RVE has a stochastic distribution of 5×5 fibers with a fiber diameter $D_f = 5\ \mu m$ and a fiber volume fraction of 60%. It is generated by a discrete element method generator called HADES, following the procedures in Liu et al. [35].

The matrix material of the microstructure is assumed to be epoxy modeled as viscoelastic-viscoplastic model as detailed in Section 5.2.1 while the fiber is assumed to be linear elastic. The material around the embedded microstructure is treated as a homogeneous isotropic elastic solid whose behavior is obtained by a standard computational homogenization scheme (see Appendix A in [35]) from elastic constants of the fibers and matrix in an RVE. Cracking is allowed to develop only inside the matrix and on the fiber/matrix interfaces in the embedded cell. Following Camacho and Ortiz [36], a dynamic insertion technique of cohesive elements, introduced in Section 5.2.2, is used to capture cracking. The whole numerical model is solved with an implicit dynamics scheme. A plane strain condition is assumed and the two-dimensional plane is considered as the transverse plane of a fiber-reinforced composite ply. The algorithm is described in detail in Section 5.2.3. The dynamic energy release rate for the composites is computed by utilizing the dynamic version of the J-integral with its formulation shown in Section 5.2.4.

5.2.1. Polymer model

The polymer matrix of the embedded microstructure is assumed to have a constitutive behavior according to a viscoelastic-viscoplastic (VE-VP) model following Rocha et al. [37]. Following the conceptual representation of the VE-VP model in Fig. 5.2, two contributing constitutive models are involved: a linear viscoelastic model and a viscoplastic component represented by a Perzyna-type overstress formulation with a rate-independent backbone of a pressure-dependent plasticity model.

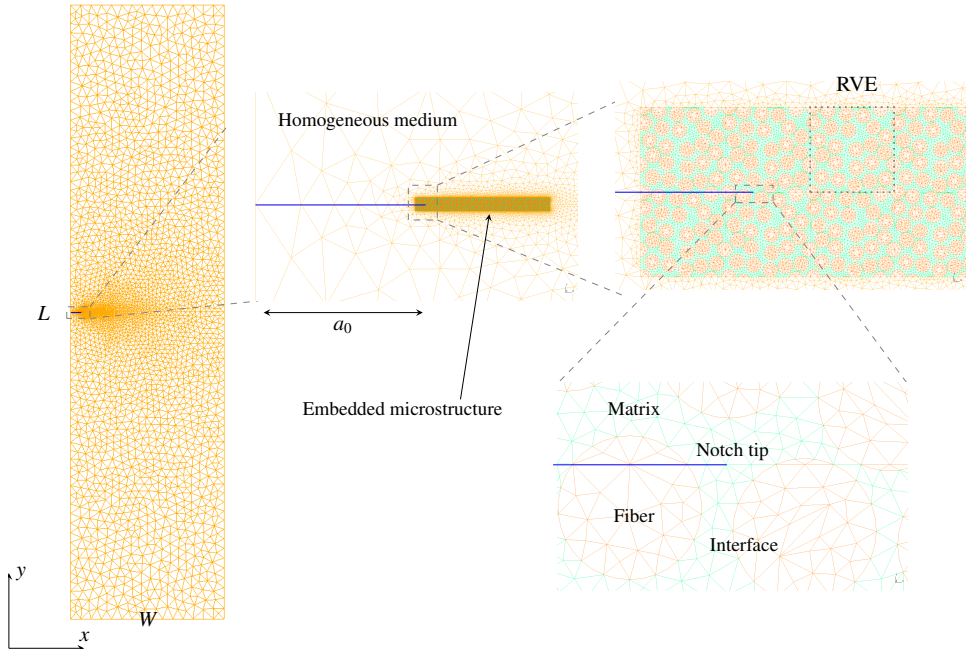

Figure 5.1: Finite element model of the SENT specimen. An initial notch is located on the left side of the specimen with an embedded microstructure represented by a number of repeating RVEs with stochastic fiber distributions. The mesh is discretized with six-node triangular elements. The dotted box on the top right shows the mesh of a RVE. Finer mesh is used for the embedded microstructure zone and coarser mesh is used for the surrounding homogeneous medium.

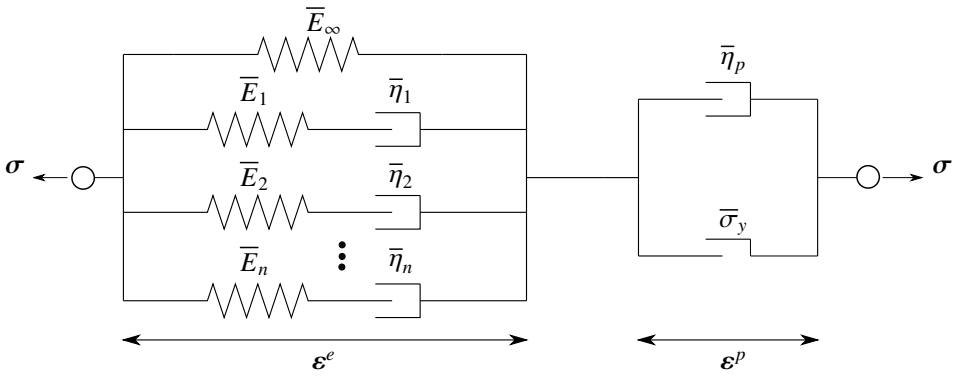

Figure 5.2: Schematic representation of the VE-VP polymer model in one-dimension. It is noted that the coefficients of the elastic and plastic components $\overline{(\cdot)}$ do not represent the same coefficients as used in Section 5.2.1.

Viscoelasticity

By assuming a linear viscoelastic model the stress σ_{ij} for time t is expressed with Boltzmann's hereditary integral of the elastic strain ε_{kl}^{e}:

$$\sigma_{ij}(t) = \int_{-\infty}^{t} D_{ijkl}(t-\tilde{t}) \frac{\partial \varepsilon_{kl}^{e}(\tilde{t})}{\partial \tilde{t}} d\tilde{t} \tag{5.1}$$

in which $D_{ijkl}(t)$ is a time-dependent stiffness which can be expressed with a time-dependent shear stiffness $G(t)$ and bulk stiffness $K(t)$:

$$D_{ijkl}(t) = 2G(t) I_{ijkl}^{dev} + 3K(t) I_{ijkl}^{vol} \tag{5.2}$$

where $G(t)$ and $K(t)$ can be further expanded as a combination of a Prony series of n_s shear elements and n_r bulk elements and a long-term contribution:

$$G(t) = G_{\infty} + \sum_{s=1}^{n_s} G_s \exp\left(-\frac{t}{g_s}\right) \qquad K(t) = K_{\infty} + \sum_{r=1}^{n_r} K_r \exp\left(-\frac{t}{k_r}\right) \tag{5.3}$$

in which G_{∞} and K_{∞} represent the long-term shear and bulk stiffness, and G_s , K_r, g_s and k_r are shear and bulk stiffness and relaxation time of the Maxwell elements, respectively. The fourth-order deviatoric and volumetric operator tensors introduced in Eq. (5.2) are defined as:

$$I_{ijkl}^{dev} = \delta_{ik}\delta_{jl} - \frac{1}{3}\delta_{ij}\delta_{kl} \qquad I_{ijkl}^{vol} = \frac{1}{3}\delta_{ij}\delta_{kl} \tag{5.4}$$

where δ_{ij} is the Kronecker delta. These operator tensors can also be used to decompose the elastic strain ε_{ij}^{e} into a deviatoric part $\varepsilon_{ij}^{e,dev}$ and a hydrostatic part $\varepsilon_{ij}^{e,vol}$:

$$\varepsilon_{ij}^{e} = \varepsilon_{ij}^{e,dev} + \varepsilon_{ij}^{e,vol} = I_{ijkl}^{dev}\varepsilon_{kl}^{e} + I_{ijkl}^{vol}\varepsilon_{kl}^{e} \tag{5.5}$$

By substituting Eqs. (5.2) and (5.3) into Eq. (5.1), the stress can be expressed as:

$$\sigma_{ij}(t) = D_{ijkl}^{\infty}\varepsilon_{kl}^{e}(t) + \sum_{r=1}^{n_r} p_r^{ve}(t)\delta_{ij} + \sum_{s=1}^{n_s} S_{ij,s}^{ve}(t) \tag{5.6}$$

in which the deviatoric viscoelastic stress contribution:

$$S_{ij,s}^{ve}(t) = 2G_s \int_{-\infty}^{t} \exp\left(-\frac{t-\tilde{t}}{g_s}\right) \frac{\partial \varepsilon_{ij}^{e,dev}(\tilde{t})}{\partial \tilde{t}} d\tilde{t} \tag{5.7}$$

and the hydrostatic viscoelastic stress contribution:

$$p_r^{ve}(t) = K_r \int_{-\infty}^{t} \exp\left(-\frac{t-\tilde{t}}{k_r}\right) \frac{\partial \varepsilon_{v}^{e}(\tilde{t})}{\partial \tilde{t}} d\tilde{t} \tag{5.8}$$

Viscoplasticity

The viscoplasticity model is assumed to be a Perzyna-type model with a backbone of a pressure-dependent hardening plasticity model. The yield function of the plasticity model is defined as:

$$f_p(\boldsymbol{\sigma}, \varepsilon_{eq}^p) = 6J_2 + 2I_1(\sigma_c - \sigma_t) - 2\sigma_c\sigma_t \tag{5.9}$$

in which $I_1 = \sigma_{kk}$ is the first stress invariant, $J_2 = \frac{1}{2}S_{ij}S_{ij}$ is the second invariant of the deviatoric stress S_{ij}, and σ_t and σ_c are the yield stress in tension and compression, respectively. The yield stress, σ_t or σ_c, is a function of the accumulated equivalent plastic strain ε_{eq}^p. In an incremental form, the accumulated equivalent plastic strain is defined as:

$$\Delta\varepsilon_{eq}^p = \sqrt{\frac{1}{1+2\nu_p^2}\Delta\varepsilon_{ij}^p\Delta\varepsilon_{ij}^p} \tag{5.10}$$

in which ν_p is the plastic Poisson's ratio. The desired contraction behavior is implemented through a non-associative flow rule which is expressed in an incremental form as:

$$\Delta\varepsilon_{ij}^p = \Delta\gamma\left(3S_{ij} + \frac{2}{9}\alpha I_1\delta_{ij}\right) \tag{5.11}$$

where $\Delta\gamma$ is the incremental plastic multiplier and the parameter α is:

$$\alpha = \frac{9}{2}\frac{1-2\nu_p}{1+\nu_p} \tag{5.12}$$

By allowing the overstress to develop beyond the yield surface, a viscous time scale is introduced in the model. A Perzyna-type of overstress formulation is adopted, which gives the evolution of the plastic multiplier $\Delta\gamma$:

$$\Delta\gamma = \begin{cases} \frac{\Delta t}{\eta_p}\left(\frac{f_p}{\sigma_t^0\sigma_c^0}\right)^{m_p} & \text{if } f_p > 0 \\ 0 & \text{if } f_p \leq 0 \end{cases} \tag{5.13}$$

in which σ_t^0 and σ_c^0 are the yield stress values when $\varepsilon_{eq}^p = 0$, m_p and η_p are viscoplastic coefficients and Δt is the time increment.

Energy dissipation

The free energy Ψ of the VE-VP model can be expressed as:

$$\Psi = \frac{1}{2}\int_0^t\int_0^t \frac{\partial\varepsilon_{ij}^e(\tilde{t})}{\partial\tilde{t}} D_{ijkl}^e(2t-\bar{t}-\tilde{t})\frac{\partial\varepsilon_{kl}^e(\tilde{t})}{\partial\tilde{t}}d\bar{t}d\tilde{t} + \psi^h \tag{5.14}$$

in which ψ^h is the plastic hardening energy. According to the second law of thermodynamics, the Clausius–Duhem inequality for the isothermal case is imposed:

$$\Xi = \sigma_{ij}\dot{\varepsilon}_{ij} - \dot{\Psi} \geq 0 \tag{5.15}$$

Following the derivation in Rocha et al. [37], the work of energy dissipation per unit volume for viscoelasticity and viscoplasticity can be expressed as:

$$\Xi^{ve}(t) = \sum_{s=1}^{n_s} \frac{S_{ij,s}^{ve} S_{ij,s}^{ve}}{2G_s g_s} + \sum_{r=1}^{n_r} \frac{(p_r^{ve})^2}{K_r k_r} \tag{5.16}$$

$$\Xi^{p} = \sigma_{ij}\dot{\varepsilon}_{ij}^{p} - \dot{\psi}^{\mathrm{h}} \tag{5.17}$$

Summing up Eqs. (5.16) and (5.17) and integration over time give the accumulated dissipation per unit volume w^p as:

$$w^p(t) = \int_0^t \left[\Xi^{ve}(\tilde{t}) + \sigma_{ij}(\tilde{t})\dot{\varepsilon}_{ij}^{p}(\tilde{t})\right] d\tilde{t} \tag{5.18}$$

To derive Eq. (5.18) the term $\dot{\psi}^{\mathrm{h}}$ is neglected because the plastic hardening in the polymer also contributes to the energy for growing a macroscopic crack. In the numerical model, the total dissipated energy of the polymer matrix can be computed as the volume integral over the embedded microstructure:

$$W_{diss}^{p} = \int_{\Omega^e} w^p d\Omega \tag{5.19}$$

in which Ω^e is the volume of the embedded microstructure zone.

5.2.2. Cohesive crack with Ortiz model

The microcracks in the embedded zone, representing fiber/matrix debonding and matrix cracking, are modeled with the cohesive zone model. Instead of inserting cohesive elements between element boundaries before the simulation starts, in this study the cohesive elements are placed on the fly following the shifted cohesive law technique described in Camacho and Ortiz [36]. A stress-based failure criterion is introduced to determine when and where the cohesive element should be inserted. The crack always starts at the middle node of edges of six-node triangle elements by splitting the nodes (see Fig. 5.3). Because cohesive elements are inserted on the fly, continuity of the response requires that the adopted cohesive law is an initially rigid linear softening law. As a consequence there is no initial stiffness present, of which the value could otherwise affect the overall compliance of the material or the stress development under dynamic loading conditions.

Cohesive element insertion criterion

Considering mixed-mode fracture, the adopted stress-based failure criterion reads [36]:

$$\sigma^{\mathrm{eff}} \geq f_{\mathrm{t}} \tag{5.20}$$

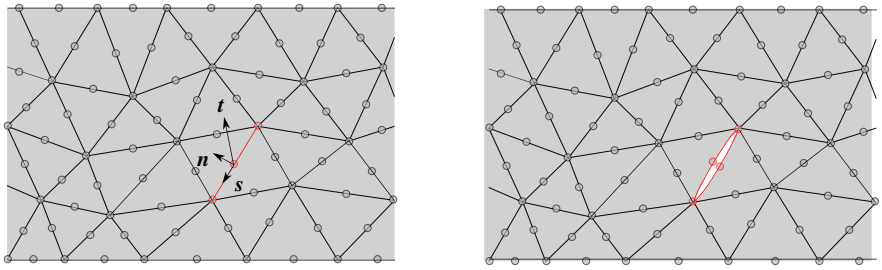

Figure 5.3: Sketch of the dynamic insertion technique of cohesive elements.

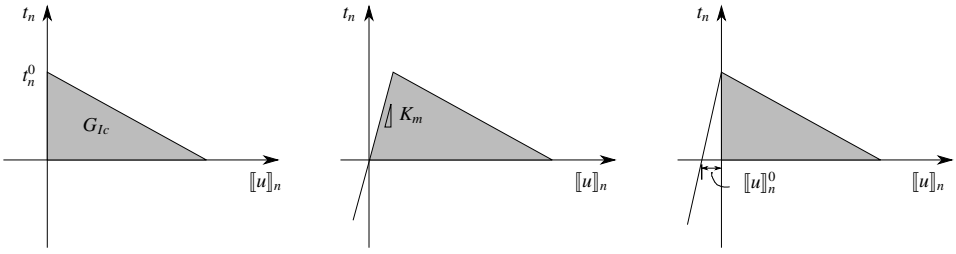

(a) Initially rigid (b) Initially stiff (c) Shifted origin

Figure 5.4: Pure mode I representation of shift in cohesive law to mimic initially rigid behavior.

where f_t is the cohesive strength and the effective stress σ^{eff} is defined as:

$$\sigma^{\text{eff}} = \begin{cases} \sqrt{(t_n)^2 + \theta\,(|t_s|)^2}, & [\![\mathbf{u}]\!]_n \geq 0 \\ \sqrt{\theta}\,(|t_s| - \mu|t_n|)\,, & [\![\mathbf{u}]\!]_n < 0 \end{cases} \tag{5.21}$$

in which $\mathbf{t} = (t_n, t_s)$ is the traction of cohesive surface along the normal direction and shear direction in the local {n,s} frame, $[\![\mathbf{u}]\!] = \left([\![u]\!]_n, [\![u]\!]_s\right)$ is the displacement jump along normal and shear direction, θ is a shear stress factor, and μ is the friction coefficient.

Shifted cohesive law

To construct an initially rigid law without singularity, a shifted cohesive law is adopted [38]. As seen in Fig. 5.4, starting from a traction separation relation with a finite initial stiffness, a shift of this relation is applied such that the traction for zero crack opening is equal to the traction at crack initiation. This leads to the desired initially rigid behavior.

For the shifted cohesive law, the traction is computed not from the actual displacement jump, but from a translated displacement jump $[\![\mathbf{v}]\!]$:

$$[\![\mathbf{v}]\!] = [\![\mathbf{u}]\!] + [\![\mathbf{u}]\!]^0 \tag{5.22}$$

The shift $[\![\mathbf{u}]\!]^0$ is computed from the bulk stress at the moment of crack initiation and can be expressed as:

$$[\![\mathbf{u}]\!]^0 = \frac{\boldsymbol{\sigma}^0 \mathbf{n}}{K_m} \tag{5.23}$$

in which $\boldsymbol{\sigma}^0$ is the stress at crack initiation and K_m is a dummy stiffness.

The traction is updated in the local {n, s} frame as:

$$\mathbf{t} = [\mathbf{I} - \boldsymbol{\Omega}]\mathbf{t}^{\text{eff}} = [\mathbf{I} - \boldsymbol{\Omega}]K_m[\![\mathbf{v}]\!] \tag{5.24}$$

with the effective traction defined as $\mathbf{t}^{\text{eff}} = K_m[\![\mathbf{v}]\!]$ and a damage tensor $\boldsymbol{\Omega}$ is defined as:

$$\Omega_{ij} = \omega_{\text{m}}\delta_{ij}\left(1 - \delta_{i1}\frac{\langle -t_n^{\text{eff}}\rangle}{t_n^{\text{eff}}}\right) \tag{5.25}$$

in which ω_m is a damage variable, $t_n^{\text{eff}} = K_m[\![v]\!]_n$ is the normal component of the effective traction $\mathbf{t}^{\text{eff}}$, δ_{ij} is the Kronecker delta and the MacAuley bracket is define as $\langle x\rangle = \frac{1}{2}(x + |x|)$. The damage evolution is introduced according to the mixed-mode cohesive law introduced in Turon et al. [39].

$$\omega_m = \max_{\tau \le t}\begin{cases} 0, & \Delta \le \Delta_0 \\ \frac{\Delta_f(\Delta - \Delta_0)}{\Delta(\Delta_f - \Delta_0)}, & \Delta_0 < \Delta < \Delta_f \\ 1, & \Delta \ge \Delta_f \end{cases} \tag{5.26}$$

where the equivalent displacement jump Δ is:

$$\Delta = \sqrt{\left(\langle [\![u]\!]_n \rangle\right)^2 + \left(|[\![u]\!]_s|\right)^2} \tag{5.27}$$

and the equivalent displacement representing onset of failure Δ_0 reads:

$$\Delta_0 = t_{eq}^0 / K_m \tag{5.28}$$

and the equivalent displacement representing complete damage Δ_f is:

$$\Delta_f = 2G_c / t_{eq}^0 \tag{5.29}$$

where G_c is the fracture energy. The equivalent traction corresponding to onset of damage t_{eq}^0 is introduced in Eq. (5.28) and Eq. (5.29) with its definition as the norm of the traction at damage initiation $\boldsymbol{\tau}^0$,

$$t_{eq}^0 = \sqrt{(\tau_n^0)^2 + (\tau_s^0)^2} \tag{5.30}$$

Energy dissipation in fiber/matrix interfaces

The total dissipated energy of the cohesive interfaces reads:

$$W_{diss}^c = \int_{\Gamma^c} \Xi dS \tag{5.31}$$

in which Γ^c is the area of the cohesive elements and the incremental dissipation density $d\Xi$ can be computed by:

$$d\Xi = \frac{1}{2}\Delta_f K_m \Delta_0 dD_m \tag{5.32}$$

with the incremental of a variable D_m

$$D_m = \frac{\Delta - \Delta_0}{\Delta_f - \Delta_0} \tag{5.33}$$

5.2.3. Solution scheme

Implicit dynamics analysis is carried out. The adopted semi-discretization scheme includes an implicit time integration of the Newmark-β type and a spatial discretization with six-node triangular elements. The solution program flow is illustrated in Box 2. There are a few items to be noted: (1) in step 5 of the algorithm, the dynamic system of equations is solved with a Newton-Raphson scheme. In certain circumstances, convergence can not obtained by a large time step size. Then, an adaptive stepping algorithm is used such that the time step size is reduced and the system equation is solved with smaller time steps until convergence is reached. (2) when new cohesive elements are inserted, the mesh is updated and the same step is solved again to ensure that the final converged solution for the time step does not violate the failure criterion.

5.2.4. J-integral calculation

Following Anderson [40], for a fast moving crack the amount of energy flowing into the crack tip region through the contour Γ can be calculated by the crack tip energy flux integral (see Fig. 5.5):

$$J^{dyn} = \int_\Gamma Q_{1j} n_j ds = \int_\Gamma \left[(w + e)\delta_{1j} - \sigma_{ij} \frac{\partial u_i}{\partial x_1} \right] n_j ds \tag{5.34}$$

with

$$Q_{1j} = \left[(w + e)\delta_{1j} - \sigma_{ij} \frac{\partial u_i}{\partial x_1} \right] \tag{5.35}$$

and ds is a line segment of path Γ, $w = \int_0^t \sigma_{ij} \dot{\varepsilon}_{ij} dt$ is the stress work density, $e = \frac{1}{2}\rho \dot{u}_i \dot{u}_i$ is kinetic energy density, n_j is the outward unit normal to the contour Γ, σ_{ij} is the stress, u_i is the displacement.

This J-integral formulation is valid for time-dependent as well as history-dependent material behavior because it was derived from a generalized energy balance. In the special case of a constant crack propagation speed and steady-state crack propagation in homogeneous hyperelastic material the dynamic J-integral becomes path-independent [41]. In this study, the integral contour is defined outside of the embedded microstructure similar to what was done in the embedded cell model by Herráez et al. [31].

1. Set the time step number $n = 1$;
2. Set the maximum allowed number of inserted cohesive element per time step N_c and initiate the state variables to be zero;
3. Apply the nth load/displacement increment;
4. Set the nth time step size Δt^n;
5. Solve dynamic equilibrium using a Newton-Raphson scheme and adaptive time stepping;
6. Loop over the edges of elements representing the polymer matrix material in the embedded zone and check if the failure criterion, i.e. Eq. (5.20), evaluated at the middle nodes of edges is satisfied or not?
   - Yes—insert at most N_c cohesive elements at edges starting from the element edge with highest σ^{eff}. Go to step 5;
   - No—go to step 7;
7. Update the state variables;
8. $n = n + 1$, go to step 4;

Box 2: Solution algorithm for the embedded cell model.

To facilitate the application of the dynamic J-integral into a FEM framework, an equivalent domain integral is introduced to replace the line integral introduced [41]. Fig. 5.5 shows an example of the selected path Γ along boundaries of one ring of finite elements alongside with an extra remote path Γ_o, one segment of the initial surface Γ^+ and one segment of the initial surface Γ^-. A closed path $C = \Gamma_o + \Gamma^+ + \Gamma^- - \Gamma$ is therefore constructed in counter-clockwise direction. In addition, a weighting function $q(\mathbf{x})$, which must be continuous and differentiable and fulfills the requirements,

$$q = \begin{cases} 0 & \text{on} \quad \Gamma_o \\ 1 & \text{on} \quad \Gamma \end{cases} \tag{5.36}$$

is introduced. A linear interpolation is applied for the q function for the enclosed domain C. The dynamic J-integral introduced in Eq. (5.34) is reformulated as [41]:

$$J^{dyn} = \int_{\Gamma} Q_{1j} n_j ds = -\int_{C} Q_{1j} q_{,j} dS - \int_{C} Q_{1j,j} q dS + \int_{\Gamma^+ + \Gamma^-} Q_{1j} n_j q ds \tag{5.37}$$

Substitution of Eq. (5.35) into Eq. (5.37) gives the final expression for dynamic J-integral:

$$J^{dyn} = \int_{C} \left\{ \left[\sigma_{ij} \frac{\partial u_i}{\partial x_1} - (w + e)\delta_{1j} \right] q_{,j} + (\rho \ddot{u}_i u_{i,1} - \rho \ddot{u}_i \dot{u}_{i,1}) q \right\} dS \tag{5.38}$$

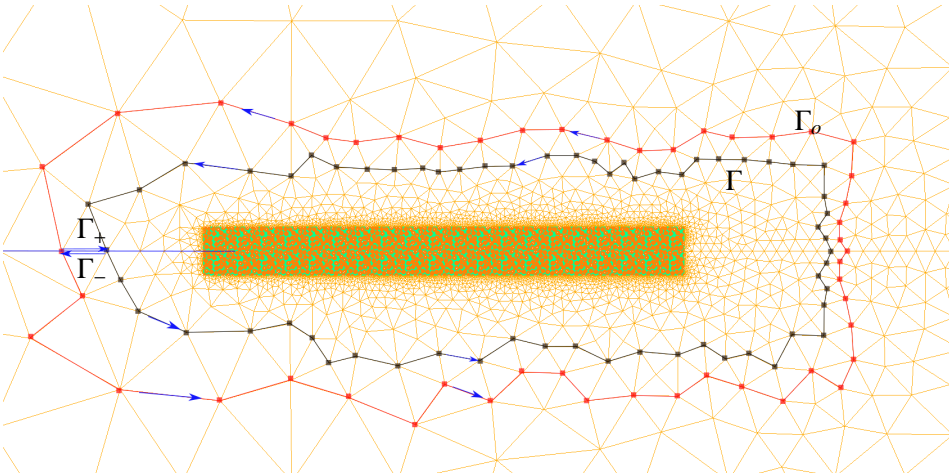

Figure 5.5: Sketch of the equivalent domain integral for the dynamic J-path integral. The q function is equal to 1.0 for the nodes (indicated by black dots) on the path Γ while it equals to 0.0 for the nodes (indicated by red dots) on the path Γ_o. Linear shape functions are used to ensure a linear field of function q inside the elements in domain C.

The conditions that the surfaces Γ^+ and Γ^- are traction-free and the crack growth direction is along the x-direction are used in deriving the above equation.

5.3. Fracture energy and crack speed

In this study, a series of SENT plane strain numerical specimens (see Fig. 5.1) is tested with different loading velocities and different specimen sizes. The considered cases of W and $\dot{\delta}$ are listed in Table 5.1. The maximum nominal strain rate investigated is 250/s, which is intermediate compared with high strain rate testing, such as in plate impact tests where the strain rates up 10^8/s to have been reported [42]. Dimensions are normalized with respect to the length of a single RVE denoted $l_x = 0.02856$ mm. For each case, the geometry of the SENT specimen satisfies that $a_0 = 0.05W$ and $L = 4W$. The number of RVEs in the microstructure is kept fixed at $N_{\text{RVE}} = 2 \times 20$ except where mentioned otherwise (i.e. 2 rows and 20 columns of RVEs). The initial notch tip has a distance of $1.33l_x$ from the left edge of the embedded microstructure zone. The fiber is modeled as a linear elastic material with the elasticity parameters listed in Table 5.2 and the material parameters for the VE-VP polymeric model are listed in Table 5.3. Considering that there might exist a characteristic time for a local damage to occur and this time scale is related to the relaxation times of the matrix as postulated in Shirinbayan et al. [6], it is ensured that the time steps adopted in the numerical simulations are much smaller than the relaxation times. The elastic properties corresponding to the homogenized medium outside of the embedded region determined by a computational homogenization technique are included in Table 5.2. Matrix cracking and fiber/matrix debonding are

Table 5.1: A summary of considered test cases with different specimen width W and loading velocities $\dot{\delta}$.

	$\dot{\delta} = 0.01$ m/s	$\dot{\delta} = 0.1$ m/s	$\dot{\delta} = 1.0$ m/s
$W = 70l_x$	✓	✓	✓
$W = 100l_x$	✓	✓	✓
$W = 200l_x$		✓	
$W = 500l_x$	✓		
$W = 600l_x$	✓	✓	

Table 5.2: Elastic properties of fiber and matrix taken from [45], and composite obtained from computational homogenization

	Fiber	Matrix	Composite
Young's modulus (MPa)	74000	2500	9407
Poisson's ratio	0.2	0.37	0.31
Mass density (g/mm^3)	0.01	0.004	0.0076

considered with the cohesive zone model with the shifted cohesive law described in Section 5.2.2. Considering that the fiber/matrix interface is generally weaker than the pure matrix, a smaller cohesive strength and fracture energy are adopted for the interface (see Table 5.4). The energy release rate is equal to the energy flux into the crack tip, divided by the crack speed [43, 44]. The mode-I energy release rate for dynamic crack growth in composites can be computed by the dynamic J-integral formulation introduced in Section 5.2.4 for all the considered SENT specimens. The crack speed V is the time derivative of the crack length which can be determined from the numerical model. Since the dynamic energy release rate is equal to the dynamic fracture energy G_c for a propagating crack, a relationship between dynamic fracture energy G_c and crack speed V can be established.

In this section, the crack growth process of the SENT specimen under dynamic loading for a typical case with specimen width $W = 600l_x$ and loading velocity $\dot{\delta} = 0.1$ m/s is first described. Then, the influence of the size of the embedded microstructure on the crack growth and energy release rate is discussed. Finally, the energy release rate for different crack speeds extracted from the numerical tests are presented.

5.3.1. Typical observations

For a typical test case with $W = 600l_x$, $a_0 = 0.05W$ and $L = 4W$, the SENT specimen is subjected to a loading velocity $\dot{\delta} = 0.1$ m/s. A total number of 113550 six-node triangular elements is used for the discretization of the numerical sample with a transition from a mesh size of 2 mm to 0.001 mm. Fig. 5.6 shows the initiation and evolution of cohesive cracks and the distribution of the normal stress σ_{yy} of the material near the crack tip for five different time steps. It is found that the applied loading causes the typical plane-strain crack tip stress field with peanut shaped stress concentration. Inside the microstructure, an inhomogeneous stress

Table 5.3: Material properties of the polymeric matrix taken from [37].

viscoelasticity				
G_∞ (MPa)	912.			
K_∞ (MPa)	3205.			
G_i (MPa)	36.	52.	178.	41.
g_i (ms)	146.	8080.	1.48e5	1.09e8
K_i (MPa)	125.	182.	625.	143.
k_i (ms)	41.6	2300.	42200.	3.11e7
viscoplasticity				
ν_p	0.32			
$\sigma_t(\varepsilon^p_{eq})$	$64.80 - 33.6 \times e^{(\varepsilon^p_{eq}/-0.003407)} - 10.21 \times e^{(\varepsilon^p_{eq}/-0.06493)}$			
$\sigma_c(\varepsilon^p_{eq})$	$81.00 - 42.00 \times e^{(\varepsilon^p_{eq}/-0.003407)} - 12.76 \times e^{(\varepsilon^p_{eq}/-0.06493)}$			
m	7.305			
η (MPa·s)	3.49e12			

Table 5.4: Material properties of cohesive cracks taken from [45] and [31].

	Matrix	Fiber/Matrix interface
Interface penalty stiffness K_m (N/mm^3)	1.e7	1.e7
Cohesive strength f_t (MPa)	121.	42.0
Fracture energy G_c (N/mm)	0.09	0.02
Mode interaction coefficient θ	0.4	0.4
Friction coefficient μ	0.1	0.1

distribution is found.

Cracks are formed in the fiber/matrix interfaces in a number of spots near the crack tip rather than the pure matrix (see Fig. 5.6(a)), which is due to lower cohesion strength at fiber/matrix interfaces. The spots where cracks initiate are sparsely distributed near the crack tip due to the inhomogeneous stress distribution caused by the applied dynamic loads and material inhomogeneity of the microstructure.

The material near the crack tip is experiencing complex conditions with interaction between dynamic loading, structural inertia, material nonlinearity and material failure. Importantly, the applied continuous loading generates a loading wave propagating into the structure, while the newly created crack surface unloading waves are generated. The process is also complicated due to structural inertia effects. Therefore, the material near the crack tip including the cohesive surfaces can experience several loading/unloading cycles, as visible in the change of loading/unloading state of the cracks shown in Fig. 5.6(a-c). Finally, a fully developed cohesive zone is formed and a dominant crack close to the mid-plane propagates in a self-similar manner (see Fig. 5.6(d-e)). Many cracks including both fiber/matrix debonding and matrix cracking are formed ahead of the crack tip while the cracks at the wake are unloading. Due to the inhomogeneous distribution of fibers, the growing crack is not straight but shows a certain tortuosity. The deformation of the microstructure is relatively small with a large fracture process zone.

5.3.2. Size of the microstructure

The adopted number of embedded RVEs in the embedded zone is $N_{\text{RVE}} = 2 \times 20$. Justification for this choice was found in a size dependence study which is presented in this section. A study on the influence of the microstructure size on the dynamic crack propagation in the SENT specimen is carried out. The size of the embedded microstructure, represented by the number of embedded RVEs, is changed for a case with the width of the SENT specimen $W = 600 l_x$ and the same loading velocity $\dot{\delta} = 0.1$ m/s. Four different sizes of the microstructure are considered, namely, 2×20 RVEs, 2×30 RVEs, 4×16 RVEs and 4×20 RVEs. The response of the SENT specimen with these four different microstructure sizes under dynamic loading is investigated with emphasis on the crack growth speed and the energy release rate.

The crack tip is defined as as the appearance of the first fully damaged cohesive element with stress free surface ($\omega_m = 1$), as illustrated in Fig. 5.6e (Left). The time derivative of the crack length is the crack speed. To obtain the dynamic energy release rate of the fracture process zone, the path of the J-integral is defined outside of the embedded microstructure zone. The path-dependence of the dynamic J-integral is first investigated for three different prescribed paths, A, B and C shown in Fig. 5.7 for the case with $N_{\text{RVE}} = 2 \times 20$. Path A is the outer boundary of the microstructure while path B is slightly further away from Path A and path C is even further than path B. Fig. 5.8 shows the dynamic J-integral value vs. time for the three paths. It is seen that there are only very minor differences in the dynamic J-integral value for the three different paths, which means that the path-independence is found for paths defined outside the embedded microstructure. It is noted that in the homogenized region where paths A, B and C are defined, the

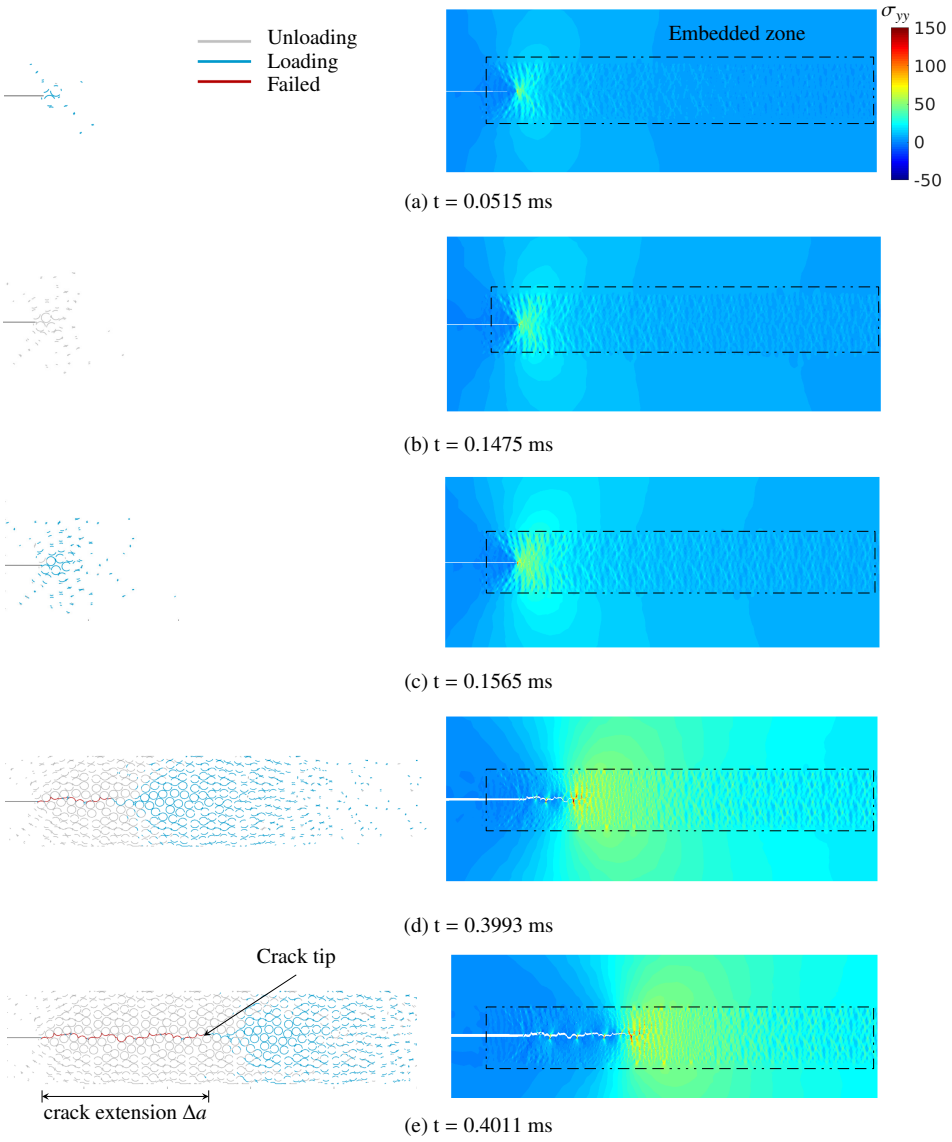

Figure 5.6: Snapshots of the crack distribution and crack state (Left) and σ_{yy} stress distribution (Right).

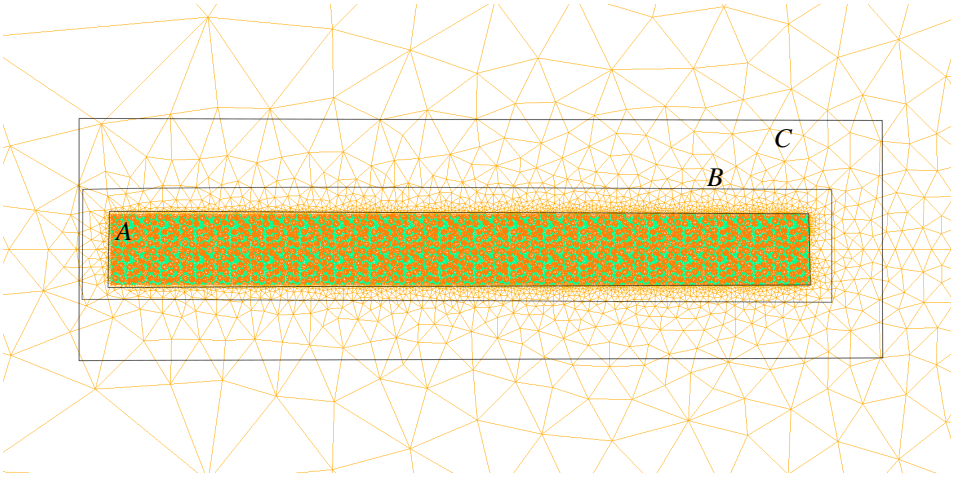

Figure 5.7: J-integral contours: path A, B and C.

material response is modeled as elastic, which attributes to the path-independence observed here. Path A is therefore chosen as the J-integral contour used in this study.

Fig. 5.9 shows the crack extension Δa vs. time and dynamic J-integral for the four cases with different microstructure sizes. It can be observed that the crack extension curve for the four cases are not exactly the same, which is related to the fact that the location where crack occurs is not the same. However, the differences between the four cases are limited. The crack speed, i.e. the slope of the time vs. crack extension curve, seems very close among the four cases. The evolution of the dynamic J for the four cases is also very close. This shows that by either increasing the number of fibers in x-direction from 80 to 150 or in y-direction from 10 to 20, the crack growth process is not evidently different. Therefore, the microstructure with 2×20 RVEs is selected in this study as it is most computationally efficient and provides size-independent responses.

5.3.3. Dynamic energy release rate

The dynamic energy release rate for the series of SENT tests listed in Table 5.1 is summarized in this section. By tracking the crack tip location during the 10 SENT tests, the crack extension a is measured and shown in Fig. 5.10. The discrete time vs. crack extension data obtained in the numerical tests is fitted with smooth functions (e.g. exponential) using the curve fitting toolbox of MATLAB so that a smooth time vs. extension curve is obtained to compute the crack speed. It is observed that all fitted curves for the 10 cases have a R^2 value larger than 0.9928, indicating that good fits are obtained. The crack speed is defined as the slope of the fitted curve, i.e. $V = \partial a/\partial t$ (see Fig. 5.10(j)). It is noted that using numerical differentiation of the discrete time and crack extension points is not a good choice

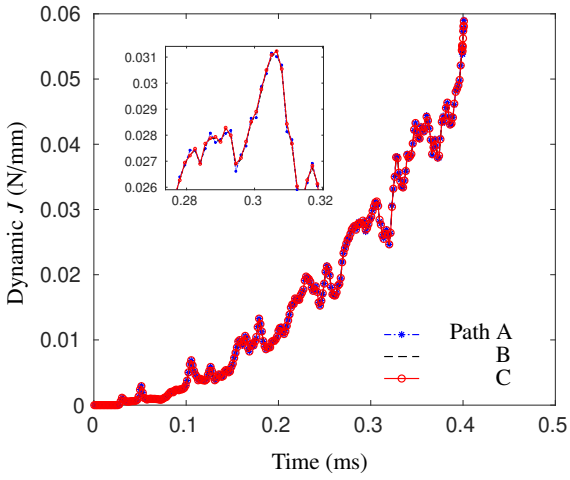

Figure 5.8: The time vs. dynamic J-integral value for three different paths. The maximum time considered corresponds to a crack extension of 0.1 mm.

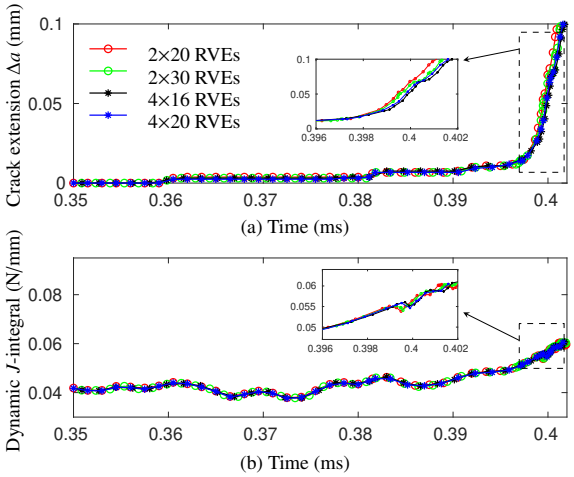

Figure 5.9: Comparison of (a) time vs. crack extension curve and (b) time vs. dynamic J-integral curve for four different microstructure sizes.

for defining the crack speed. Fig. 5.11 shows a comparison of the computed crack speed history with two numerical differentiation schemes and the chosen approach. The considered numerical differentiation methods are the mid-point scheme and the Euler backward scheme. For the mid-point scheme, the crack speed at discrete time t_i $(i = 1, 2, ..., N)$ is calculated as: $V_i = (\Delta a_{i+1} - \Delta a_{i-1})/(t_{i+1} - t_{i-1})$ in which N is the total number of time instants. For the Euler backward scheme, the crack speed at discrete time t_i is calculated as: $V_i = (\Delta a_i - \Delta a_{i-1})/(t_i - t_{i-1})$. It is found that both numerical differentiation schemes give oscillating crack speeds, while the crack speed computed by the chosen approach shows a smooth crack speed history. These oscillations are not necessarily physical and may be attributed to the numerical discretization, numerical time stepping or to the microstructure. In any case, the homogenized response is of particular interest rather than the exact crack speed inside the embedded cell. Therefore, with the chosen approach the crack speed history is smooth and physically regarded as the average crack speed found in the SENT tests [46].

Fig. 5.12 shows the dynamic J-integral value for different crack speeds extracted from the series of numerical tests. A number of observations are made: (1) for the first six cases of with $W = 70l_x, 100l_x$ and $\dot{\delta} = 0.01, 0.1, 1.0$ m/s, there appears to be a unique relation between the dynamic J-integral and the crack speed V, i.e. $J^{dyn}(V)$ or $G_c(V)$. (2) the dynamic J-integral value when crack propagation starts, i.e. when crack speed $V > 0$, among those six cases have small differences and an average value around 0.045 N/mm is identified. This value is between the fracture toughness of the matrix, 0.09 N/mm, and that of the fiber/matrix interface, 0.02 N/mm. (3) for the other four cases, the dynamic J-integral value for the same crack speed is higher than that of the first six cases. (4) the case with $W = 600l_x$ and $\dot{\delta} = 0.01$ m/s has the largest dynamic J-integral value. If a strain rate definition of $\dot{\varepsilon} = \dot{\delta}/2W$ is employed, the case with $W = 600l_x$ and $\dot{\delta} = 0.01$ m/s also has the lowest strain rate. (5) the cases with $W = 70l_x$ and $\dot{\delta} = 1.0$ m/s and $W = 100l_x$ and $\dot{\delta} = 1.0$ m/s, i.e. the cases with the highest strain rate, have shown a more oscillatory response for the dynamic J-integral value. (6) The maximum crack speed is around 265 m/s reached in the case with $W = 70l_x$ and $\dot{\delta} = 1.0$ m/s, which is in the same magnitude as the dynamic crack growth in carbon/epoxy composites with dynamic double cantilever beam tests in [47, 48].

5.4. Discussions of mechanisms

The underlying mechanisms for the observations of the $G_c(V)$ relation shown in Fig. 5.12 are discussed in this section, including inertia effect, ductile/brittle failure type and the R-curve effect.

5.4.1. Inertia effect

Fig. 5.13 shows the time evolution of the dynamic J-integral value before crack initiation for three cases, namely the loading velocity $\dot{\delta} = 0.01, 0.1, 1.0$ m/s with the same width $W = 100l_x$. The dynamic J-integral is gradually increasing for the three cases as a result of applied continuous displacement loading. The case with the

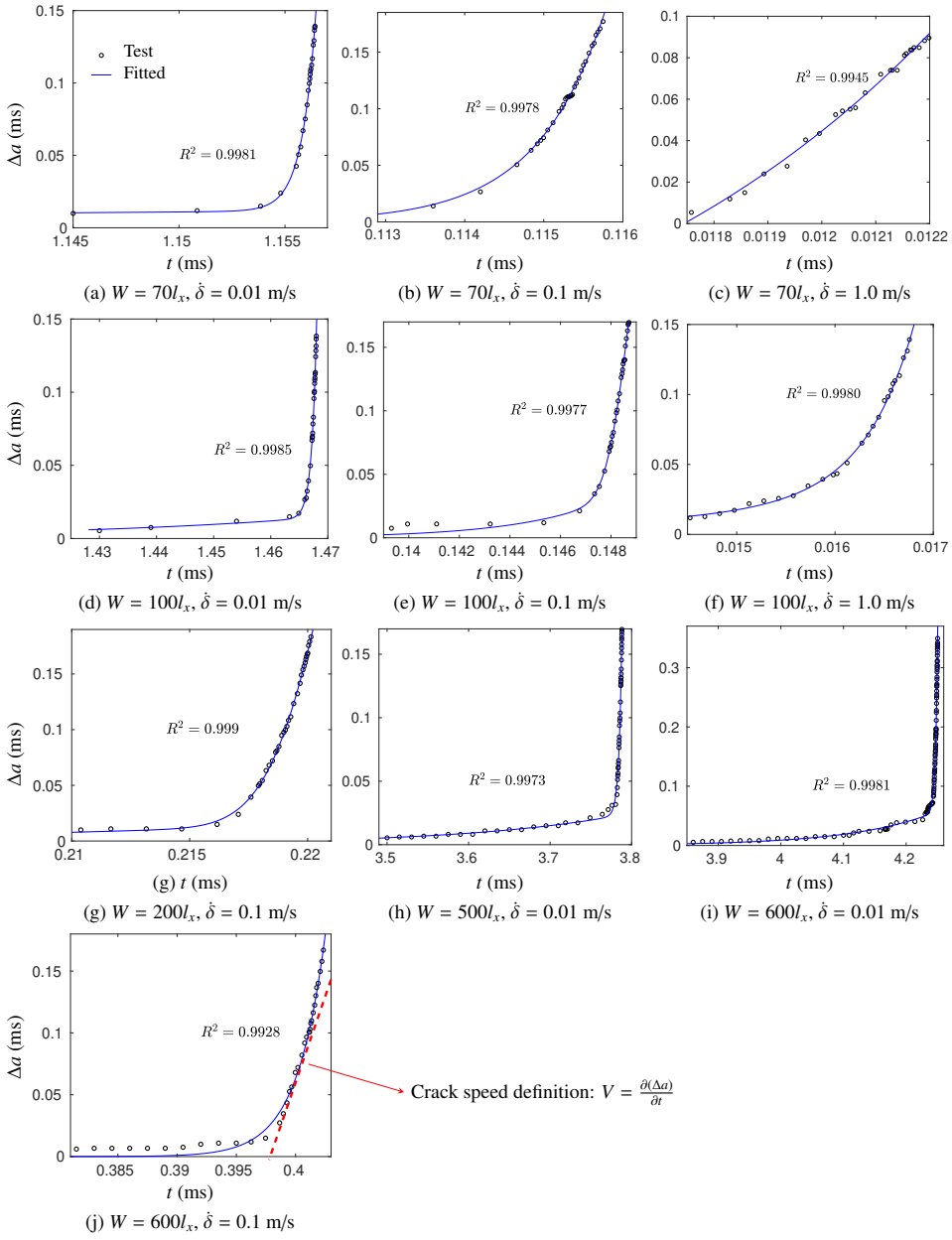

(a) $W = 70l_x$, $\dot{\delta} = 0.01$ m/s (b) $W = 70l_x$, $\dot{\delta} = 0.1$ m/s (c) $W = 70l_x$, $\dot{\delta} = 1.0$ m/s

(d) $W = 100l_x$, $\dot{\delta} = 0.01$ m/s (e) $W = 100l_x$, $\dot{\delta} = 0.1$ m/s (f) $W = 100l_x$, $\dot{\delta} = 1.0$ m/s

(g) t (ms) (g) $W = 200l_x$, $\dot{\delta} = 0.1$ m/s (h) $W = 500l_x$, $\dot{\delta} = 0.01$ m/s (i) $W = 600l_x$, $\dot{\delta} = 0.01$ m/s

(j) $W = 600l_x$, $\dot{\delta} = 0.1$ m/s

Figure 5.10: Time evolution of crack extension for the series of SENT tests and fitted curves.

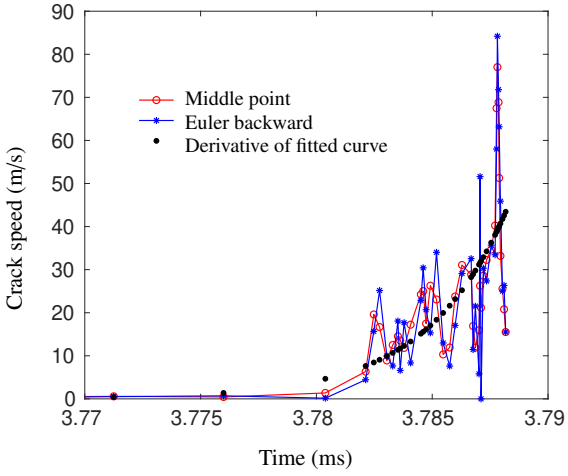

Figure 5.11: Comparison of different approaches for calculating the crack speed.

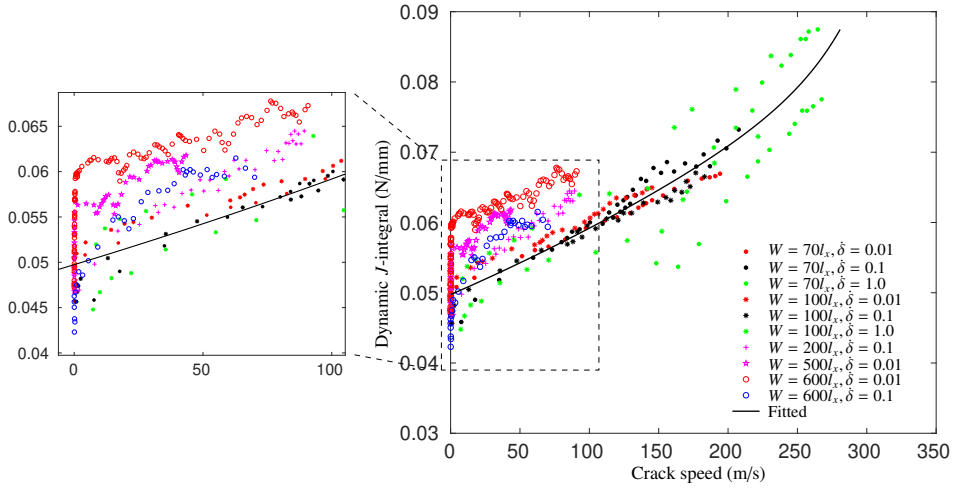

Figure 5.12: The dynamic J-integral for different crack speeds computed from the series of tests. A zoomed-in view of the lower crack speed range is shown on the left.

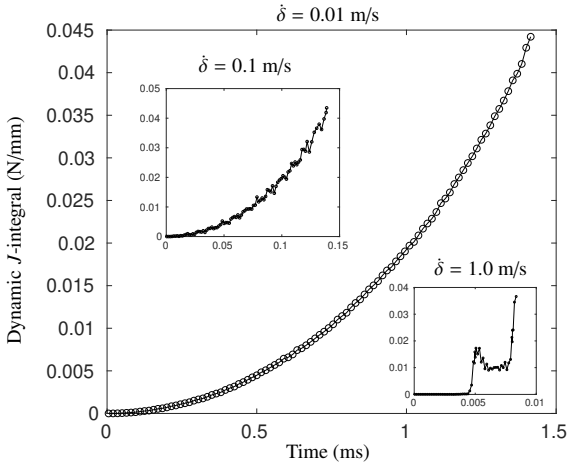

Figure 5.13: Time evolution of the dynamic J value (before crack propagation) for three different cases with $\dot{\delta} = 0.01, 0.1, 1.0$ m/s and the same $W = 100l_x$.

lowest loading velocity $\dot{\delta}$ shows a very smooth profile and a quadratic relation exists between the dynamic J-integral and time. By increasing the loading velocity to 0.1 m/s and 1.0 m/s, the dynamic J-integral clearly shows high frequency oscillations, which is due to an evident effect of system inertia activated by a larger test rate. Similar trends of the dynamic energy release rate for mode-I cracking in composites have been found in Liu et al. [11] with the interfacial thick level set (ITLS) approach.

The formulation for the dynamic J-integral J^{dyn} in Eq. (5.38) can be rewritten as:

$$J^{dyn} = \underbrace{\int_A \left[\sigma_{ij}u_{i,1} - w\delta_{1j}\right] q_{,j} dA}_{J^{static}} - \underbrace{\int_A e\delta_{1j} q_{,j} dA}_{J^{kinetic}} + \underbrace{\int_A \left(\rho\ddot{u}_i u_{i,1} - \rho\dot{u}_i\dot{u}_{i,1}\right) q dA}_{J^{nonsteady}} \tag{5.39}$$

in which three different contributing components can be identified as J^{static}, $J^{kinetic}$ and $J^{nonsteady}$. The J^{static} is the formulation used for quasi-static loading. The $J^{kinetic}$ represents the contribution of kinetic energy flow into the fracture process zone. The $J^{nonsteady}$ is zero in the special case of a constant crack propagation speed and steady-state crack propagation [41] and a nonzero value shows the deviation from that condition. For the case with $\dot{\delta} = 1.0$ m/s, the different components of the dynamic J-integral are shown in Fig. 5.14. The dynamic J-integral J^{dyn} is close to the value of the quasi-static J-integral J^{static} although somewhat oscillatory. Compared with the J^{dyn}, the $J^{kinetic}$ and $J^{nonsteady}$ are much smaller. Of these two, $J^{nonsteady}$ gives the larger contribution. This shows that the effect of nonsteady-state crack propagation or non-constant crack speed is causing a significant inertia effect. However, the inertia effect is not dominant. A similar observation was made by Nakamura et al. [49] who reported for a three-point-bending

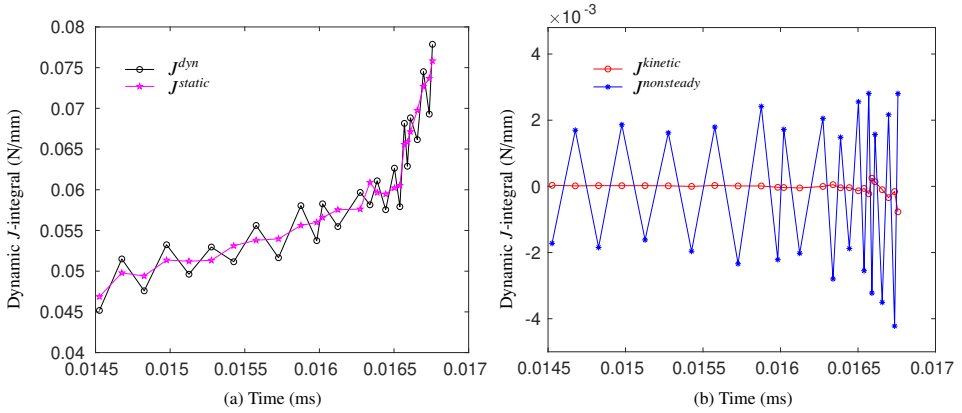

Figure 5.14: Time evolution of (a) J^{dyn}, J^{static}; (b) $J^{kinetic}$ and $J^{nonsteady}$ for a case of $W = 100l_x$ and $\dot{\delta} = 1.0$ m/s.

5

test that the inertia effect is minor when the kinetic energy is a small fraction of the strain energy of the system. Therefore, an average fit of the $J(V)$ data for this case as included in Fig. 5.12 is a reasonable representation of the material response. For a lower test rate with $\dot{\delta} = 0.01$ m/s, the J^{dyn}, J^{static}, $J^{kinetic}$ and $J^{nonsteady}$ are shown in Fig. 5.15. The dynamic J-integral J^{dyn} is almost equal to the static J-integral J^{static} while the other two components $J^{kinetic}$ and $J^{nonsteady}$ are negligible. This shows that for lower rates, the inertia effect vanishes. It is expected that for higher strain rate testing, for instance, Hopkinson Bar loaded fracture experiments, inertia effects become evident and need to be filtered out [50].

5.4.2. Failure type

The failure mode in the embedded microstructure zone is found to be brittle failure with limited plasticity. Fig. 5.16 shows the dissipation for plasticity and cohesive cracks for three cases with $\dot{\delta} = 0.01, 0.1, 1.0$ m/s and the same $W = 100l_x$. They are calculated by Eq. (5.19) and Eq. (5.31) and normalized with $G_c^i l_x b_0$, where $G_c^i = 0.02$ N/mm is the fracture energy of fiber/matrix interface, l_x is the RVE size and $b_0 = 1.0$ mm is a unit thickness. It is observed that the plastic deformation in the matrix dissipates much less energy than the cohesive cracks. For instance, at the same amount of crack extension 0.1 mm, the case with loading velocity $\dot{\delta} = 0.1$ m/s has a plastic dissipation of 4.332×10^{-4} N·mm, while the dissipation for cohesive crack at that point in time is 5.878×10^{-4}N·mm. A comparison of the three cases shows that the case with $\dot{\delta} = 1.0$ m/s has the largest cohesive dissipation W_{diss}^c while the case with $\dot{\delta} = 0.01$ m/s has the largest plastic dissipation. This shows that for a lower loading velocity, plasticity is more developed while for higher loading velocity cohesive cracks dissipate more energy. This phenomenon represents the commonly referred ductile-to-brittle transition for increasing loading rate [10, 51, 52]. Nevertheless, failure in the fracture process zone for the case with

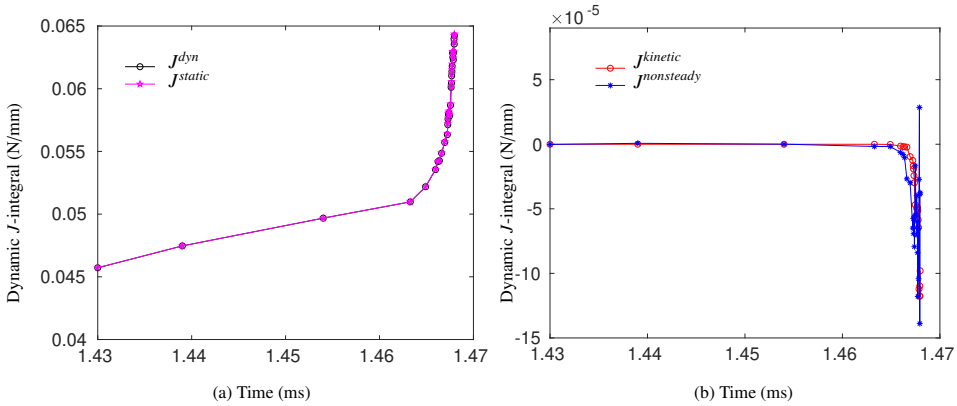

Figure 5.15: Time evolution of (a) J^{dyn}, J^{static}; (b) $J^{kinetic}$ and $J^{nonsteady}$ for a case of $W = 100l_x$ and $\dot{\delta} = 0.01$ m/s.

5

lower loading velocity is still rather brittle. This can be seen from the distribution of the equivalent plastic strain for the case of $\dot{\delta} = 0.01$ m/s shown in Fig. 5.17. The plastic strain is limited to the area close to the crack path. The distribution of normal strain ε_{yy} shown in Fig. 5.18 for the case with $W = 70l_x$ and $\dot{\delta} = 0.1$ m/s reveals that the strain near the crack tip remains small, which indicates a brittle failure.

5.4.3. Dynamic R-curve

It is known that in laminated composites, due to fiber cross-over bridging behind the crack tip the fracture toughness can increase for a certain distance of crack growth. The increase of the apparent fracture toughness with crack extension is usually described by a function of crack growth resistance vs. crack extension, i.e. the so-called R-curve [53]. Even though the crack propagation in this study takes place in the transverse plane, an R-curve also exists here. This is related to the development of the fracture process zone, where microcracking at fiber/matrix interfaces and inside the pure matrix and tearing of matrix ligaments are found. In Fig. 5.19 the R-curve is shown by plotting the evolution of the dynamic J-integral as a function of crack extension. The R-curve for all cases shows a rising trend.

Except for the case with $W = 70l_x$ and $\dot{\delta} = 1.0$ m/and the case with $W = 100l_x$ and $\dot{\delta} = 1.0$ m/s, all cases follow approximately the same R-curve. Considering that structural inertia, cohesive cracking and rate-dependent plasticity are coexisting during the development of the fracture process zone, there are minor differences of the R-curve of the different cases, although, as mentioned in Section 5.4.2, rate-dependent plasticity is less pronounced and does not contribute much to these differences. In the cases with $W = 70l_x$ and $\dot{\delta} = 1.0$ m/s and $W = 100l_x$ and $\dot{\delta} = 1.0$ m/s, which are the two case with the highest nominal strain rates, oscillations are present in the R-curve which are ascribed to inertia effects.

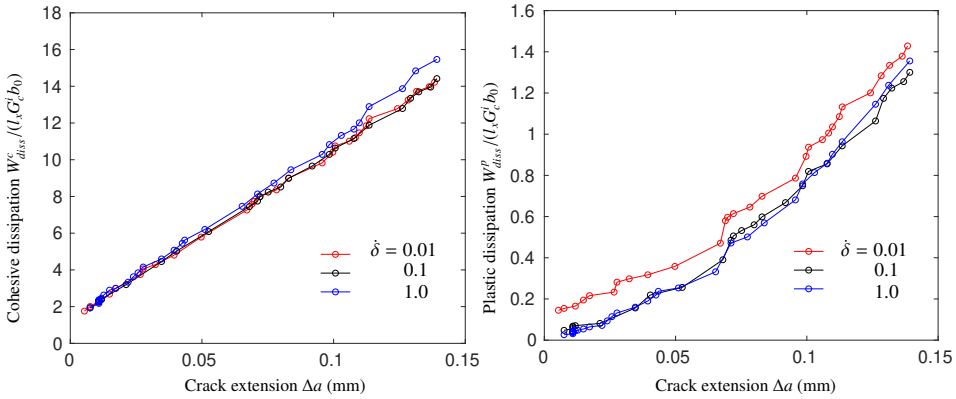

Figure 5.16: (a) Cohesive dissipation and (b) plastic dissipation for a case of $W = 100 l_x$ and loading velocity $\dot{\delta} = 0.01, 0.1, 1.0$ m/s.

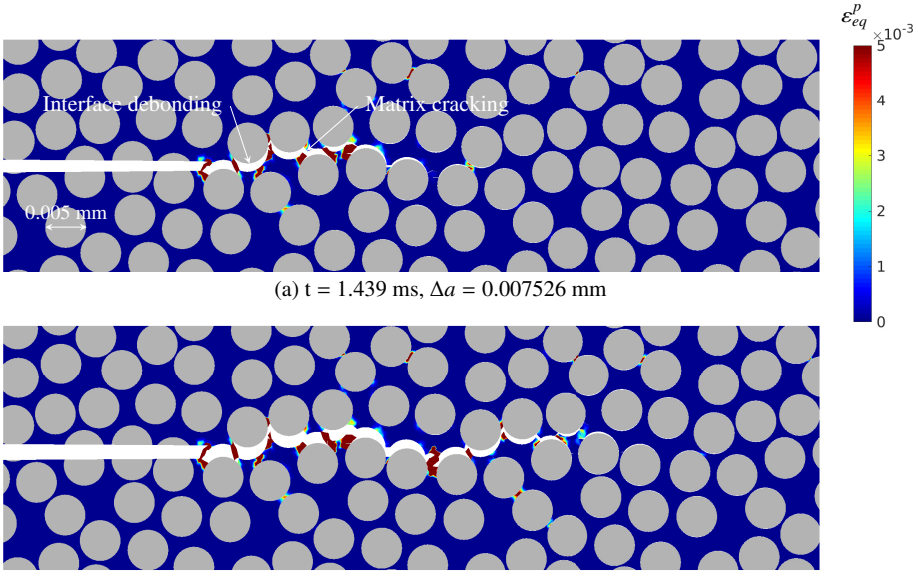

(a) t = 1.439 ms, Δa = 0.007526 mm

(b) t = 1.466 ms, Δa = 0.02767 mm

Figure 5.17: Distribution of equivalent plastic strain ε^p_{eq} for a case with $W = 100 l_x$ and $\dot{\delta} = 0.01$ m/s.

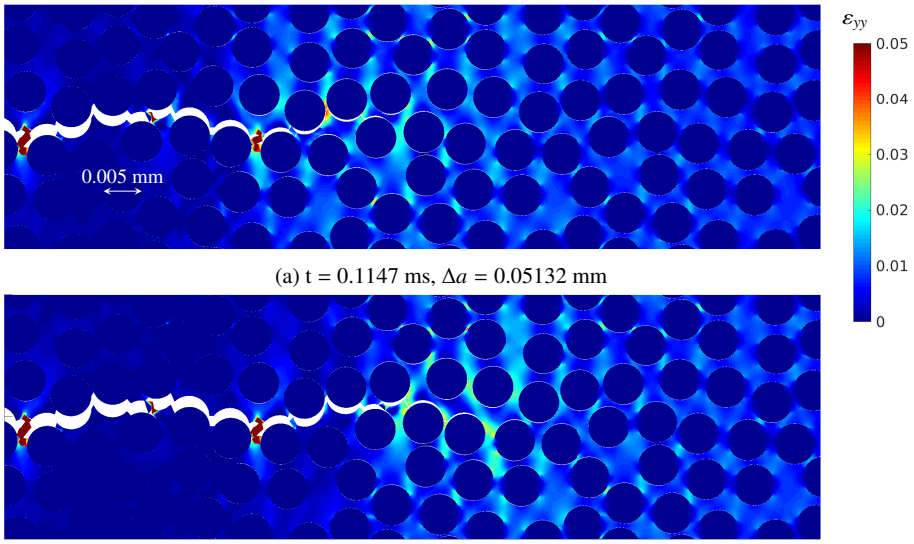

(a) t = 0.1147 ms, Δa = 0.05132 mm

(b) t = 0.1148 ms, Δa = 0.06374 mm

Figure 5.18: Distribution of the normal strain ε_{yy} for a case with $W = 70l_x$ and $\dot{\delta} = 0.1$ m/s.

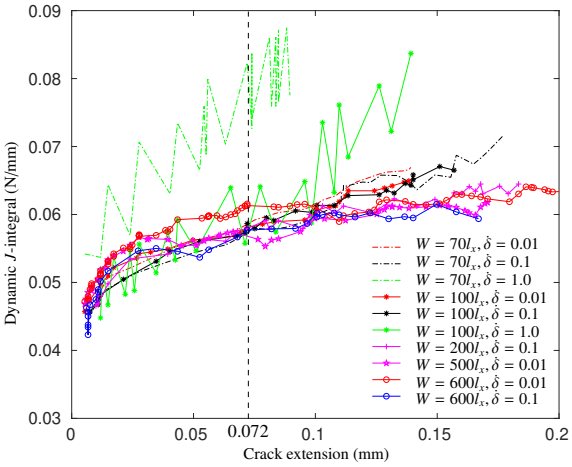

Figure 5.19: R-curves for the series of numerical tests.

In Fig. 5.20, the distribution of normal stress in y-direction σ_{yy} is shown for two lower rate cases, one with $W = 70l_x$ and $\dot{\delta} = 0.1$ m/s and the other with $W = 600l_x$ and $\dot{\delta} = 0.01$ m/s. For both cases, two typical time instants are selected. It shows that the development of the failure zone is a gradual process with the formation of microcracks (along fiber/matrix interfaces and inside the matrix) and ductile tearing of matrix ligaments. The two cases form a very similar crack pattern when the fracture process zone is fully developed and a periodic crack pattern forms as a result of the periodicity of the embedded microstructure. The damage of cohesive cracks corresponding to Fig. 5.20(b) and Fig. 5.20(d) is plotted in Fig. 5.21 when the crack length of both cases is 0.072 mm. The case with higher loading rate only has a slightly wider spreading of cohesive cracks. The similarity of the R-curve for lower rates offers an explanation for the shift observed in the plot of J-integral versus crack speed in Fig. 5.12 for the same cases. Since there is a one-to-one relation between crack length and applied load for these cases, different crack velocities must be found for different applied loading rates.

For the higher rate cases, there are oscillations in the R-curve as well as an increase in the overall fracture resistance. The differences in dynamic J-integral is a numerical representation of the velocity-toughening effect that has been observed experimentally for quasi-brittle materials. Zhou et al. [54] found the failure mechanism of a PMMA plate was found to display increasingly rough crack surfaces for increasing crack propagation velocities. As seen in Fig. 5.10 and Fig. 5.12, the crack speed for the higher nominal strain rate cases is larger than that of lower nominal strain rate cases. Fig. 5.22 shows a comparison of the dissipation of cohesive cracks for three cases, representing the lowest loading rate and the two highest loading rates. It is observed that the higher rate cases have significantly larger cohesive dissipation, pointing at more damage in secondary microcracks.

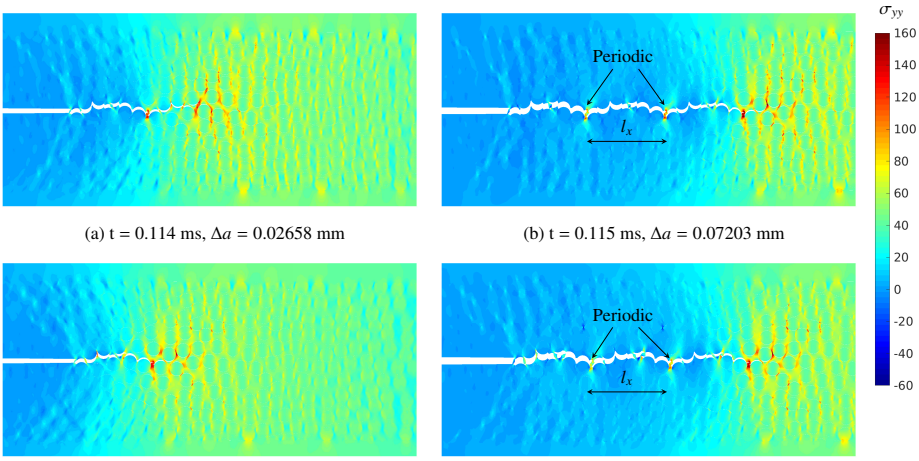

(a) t = 0.114 ms, Δa = 0.02658 mm

(b) t = 0.115 ms, Δa = 0.07203 mm

(c) t = 4.07 ms, Δa = 0.0149 mm

(d) t = 4.24 ms, Δa = 0.07203 mm

Figure 5.20: Normal stress distribution σ_{yy} of the deformed configuration of two typical time instants for two cases: (top) $W = 70l_x$ and $\dot{\delta} = 0.1$ m/s; (bottom) $W = 600l_x$ and $\dot{\delta} = 0.01$ m/s.

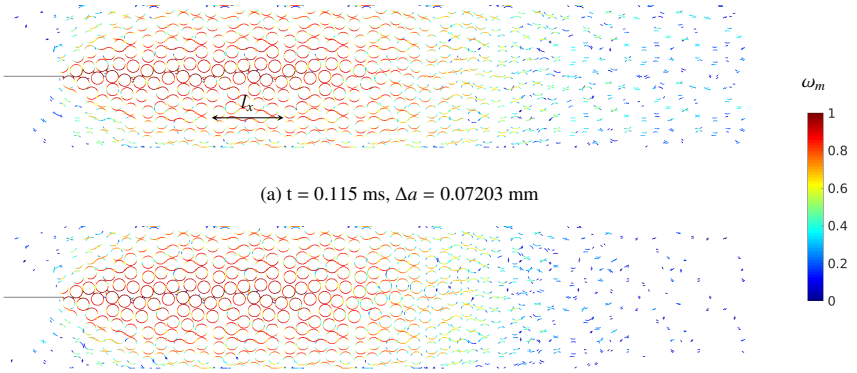

(a) t = 0.115 ms, Δa = 0.07203 mm

(b) t = 4.24 ms, Δa = 0.07203 mm

Figure 5.21: Cohesive damage distribution for two cases: (a) $W = 70l_x$ and $\dot{\delta} = 0.1$ m/s and (b) $W = 600l_x$ and $\dot{\delta} = 0.01$ m/s.

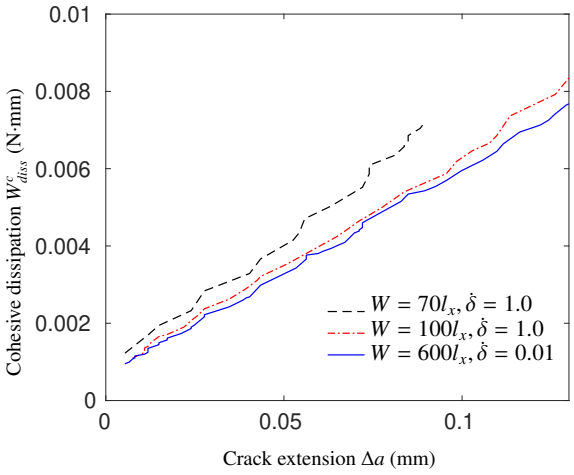

Figure 5.22: Cohesive dissipation for three cases: (a) $W = 70l_x$ and $\dot{\delta} = 1.0$ m/s, (b) $W = 100l_x$ and $\dot{\delta} = 1.0$ m/s and (c) $W = 600l_x$ and $\dot{\delta} = 0.01$ m/s.

5.5. Conclusion

In this paper, a multiscale numerical framework is established to evaluate the fracture energy of dynamic crack propagation in composites. A series of numerical simulations with different specimen sizes and different loading velocities is performed to simulate the deformation and failure process of the SENT specimen with embedded composite microstructure when subjected to continuous dynamic loading. Instead of running explicit dynamics analyses with accumulated divergence from balance of momentum, an implicit dynamics solution scheme is adopted. For each time step the dynamic version of J-integral is evaluated as a measure for the dynamic fracture energy.

The introduced numerical framework allows for a quantitative evaluation of the dynamic fracture energy of composites and for analysis of how rate-dependent plasticity, distributed microcracking and inertia effects contribute to the observed fracture energy.

For all considered cases, microcracks are initially formed in the fiber/matrix interfaces in a number of locations near the crack tip. Materials near the crack tip including the newly created crack surfaces experience a complicated loading process mainly due to interaction of dynamic loading, structural inertia and material failure.

With the given material parameter set, it is seen that an increase of the applied strain rate gives rise to a trend of increasing brittleness for the failure of composites with reduced plastic energy dissipation. However, even for cases with low loading velocity and large specimen size, failure is relatively brittle with a small amount of plasticity occurring near the crack tip and in the wake of the fracture process zone. Therefore, the influence of plasticity on global rate-dependence remains limited.

The dynamic fracture energy G_c shows an increasing trend with the crack speed V but no unique $G_c(V)$ relation is found [47]. For most investigated loading rates, the crack growth follows a rate-independent R-curve, which is related to the fact that the amount of cohesive energy dissipation is the same for different cases with lower loading rates.

Cases with high nominal strain rate show visible inertia effects with oscillating values of J^{dyn}. These cases also show increased microcracking which leads to a higher overall energy dissipation pointing at a velocity toughening effect. Considering that the mode-I fracture toughness is also temperature-dependent [55], incorporation of the temperature effect into the current numerical framework is further needed and can be done by following the idea of [17].

References

[1] Y. Liu, F. P. van der Meer, L. J. Sluys, and L. Ke, *Modeling of dynamic mode I crack growth in glass fiber-reinforced polymer composites: fracture energy and failure mechanism,* Engineering Fracture Mechanics (under revision) .

[2] A. A. Griffith, *Vi. the phenomena of rupture and flow in solids,* Philosophical transactions of the royal society of london. Series A, containing papers of a mathematical or physical character **221**, 163 (1921).

[3] M. F. Mott, *Brittle Fracture in Mild-Steel Plates,* Engineering **165**, 16 (1948).

[4] K. Ravi-Chandar, *Chapter 5 - energy balance and fracture criteria,* in *Dynamic Fracture*, edited by K. Ravi-Chandar (Elsevier, Oxford, 2004) pp. 71 – 79.

[5] L. B. Freund, *Energy flux into the tip of an extending crack in an elastic solid,* Journal of Elasticity **2**, 341 (1972).

[6] M. Shirinbayan, J. Fitoussi, M. Bocquet, F. Meraghni, B. Surowiec, and A. Tcharkhtchi, *Multi-scale experimental investigation of the viscous nature of damage in Advanced Sheet Molding Compound (A-SMC) submitted to high strain rates,* Composites Part B: Engineering **115**, 3 (2017).

[7] J. Fitoussi, M. Bocquet, and F. Meraghni, *Effect of the matrix behavior on the damage of ethylene–propylene glass fiber reinforced composite subjected to high strain rate tension,* Composites Part B: Engineering **45**, 1181 (2013), arXiv:0812.0143v2 .

[8] J. T. Fan, J. Weerheijm, and L. J. Sluys, *Compressive response of a glass–polymer system at various strain rates,* Mechanics of Materials **95**, 49 (2016).

[9] J. Hoffmann, H. Cui, and N. Petrinic, *Determination of the strain-energy release rate of a composite laminate under high-rate tensile deformation in fibre direction,* Composites Science and Technology **164**, 110 (2018).

[10] H. Zabala, L. Aretxabaleta, G. Castillo, and J. Aurrekoetxea, *Loading rate dependency on mode I interlaminar fracture toughness of unidirectional and woven carbon fibre epoxy composites,* Composite Structures **121**, 75 (2015).

[11] Y. Liu, F. P. van der Meer, and L. J. Sluys, *Cohesive zone and interfacial thick level set modeling of the dynamic double cantilever beam test of composite laminate,* Theoretical and Applied Fracture Mechanics **96**, 617 (2018).

[12] W. J. Cantwell and M. Blyton, *Influence of Loading Rate on the Interlaminar Fracture Properties of High Performance Composites - A Review,* Applied Mechanics Reviews **52**, 199 (1999).

[13] E. E. Nishida, *Distinguishing inertia effects from the intrinsic mechanical behavior of soft materials at high strain rates by Kolsky bar experiments*, Ph.D. thesis, Purdue University (2010).

[14] R. Eriksen, C. Berggreen, J. Barton, and H. Toftegaard, *High Strain Rate Characterisation of Composite Materials*, Ph.D. thesis (2014).

[15] Z.-P. Wang and C. T. Sun, *Modeling micro-inertia in heterogeneous materials under dynamic loading,* Wave Motion **36**, 473 (2002).

[16] Y. Chen and S. Ghosh, *Micromechanical analysis of strain rate-dependent deformation and failure in composite microstructures under dynamic loading conditions,* International Journal of Plasticity **32-33**, 218 (2012).

[17] A. Ahmed and L. J. Sluys, *A phantom node formulation for modeling coupled adiabatic-isothermal cracking in FRP composites,* Computer Methods in Applied Mechanics and Engineering **278**, 291 (2014).

[18] J. Wang, L. Wen, J. Xiao, T. Liang, X. Hu, and P. Li, *The mechanical properties and constitutive model of two woven composites including the influences of temperature, strain rate and damage growth,* Composites Part B: Engineering **161**, 502 (2019).

[19] Z. Li and J. Lambros, *Dynamic thermomechanical behavior of fiber reinforced composites,* Composites Part A: Applied Science and Manufacturing **31**, 537 (2000).

[20] E. V. González, P. Maimí, P. P. Camanho, A. Turon, and J. A. Mayugo, *Simulation of drop-weight impact and compression after impact tests on composite laminates,* Composite Structures **94**, 3364 (2012).

[21] O. Allix, *A composite damage meso-model for impact problems,* Composites Science and Technology **61**, 2193 (2001).

[22] A. Ahmed and L. J. Sluys, *A computational model for the simulation of dynamic fracture in laminated composite plates,* Journal of Composite Materials **49**, 1717 (2015).

[23] R. Hill, *Elastic properties of reinforced solids: Some theoretical principles,* Journal of the Mechanics and Physics of Solids **11**, 357 (1963).

[24] S. Toro, P. J. Sánchez, J. M. Podestá, P. J. Blanco, A. E. Huespe, and R. A. Feijóo, *Cohesive surface model for fracture based on a two-scale formulation: computational implementation aspects,* Computational Mechanics **58**, 549 (2016).

[25] J. F. Unger, *An FE2-X1 approach for multiscale localization phenomena,* Journal of the Mechanics and Physics of Solids **61**, 928 (2013).

[26] P. J. Sánchez, P. J. Blanco, A. E. Huespe, and R. A. Feijóo, *Failure-Oriented Multi-scale Variational Formulation: Micro-structures with nucleation and evolution of softening bands,* Computer Methods in Applied Mechanics and Engineering **257**, 221 (2013).

[27] V. P. Nguyen, O. Lloberas-Valls, M. Stroeven, and L. J. Sluys, *Homogenization-based multiscale crack modelling: From micro-diffusive damage to macro-cracks,* Computer Methods in Applied Mechanics and Engineering **200**, 1220 (2011).

[28] C. M. Landis, T. Pardoen, and J. W. Hutchinson, *Crack velocity dependent toughness in rate dependent materials,* Mechanics of Materials **32**, 663 (2000).

[29] S. Tang, T. F. Guo, and L. Cheng, *Mode mixity and nonlinear viscous effects on toughness of interfaces,* International Journal of Solids and Structures **45**, 2493 (2008).

[30] M. Z. Hossain, C.-J. Hsueh, B. Bourdin, and K. Bhattacharya, *Effective toughness of heterogeneous media,* Journal of the Mechanics and Physics of Solids **71**, 15 (2014).

[31] M. Herráez, C. González, and C. S. Lopes, *A numerical framework to analyze fracture in composite materials: From R-curves to homogenized softening laws,* International Journal of Solids and Structures **134**, 216 (2018).

[32] X. Zhang, H. Y. Liu, and Y. W. Mai, *Rate-dependent bridging law and its application to dynamic crack growth in brittle-matrix composite materials,* Composites Part A: Applied Science and Manufacturing **34**, 1053 (2003).

[33] F. Naya, C. S. Lopes, C. González, and J. LLorca, *Computational micromechanics strategies for the analysis of failure in unidirectional composites,* in *Numerical Modelling of Failure in Advanced Composite Materials* (Elsevier, 2015) pp. 411–433.

[34] C. Ruggieri and R. H. Dodds, *A transferability model for brittle fracture including constraint and ductile tearing effects: A probabilistic approach,* International Journal of Fracture **79**, 309 (1996).

[35] Y. Liu, F. P. van der Meer, and L. J. Sluys, *A dispersive homogenization model for composites and its RVE existence,* Computational Mechanics **65**, 79 (2020).

[36] G. T. Camacho and M. Ortiz, *Computational modelling of impact damage in brittle materials,* International Journal of Solids and Structures **33**, 2899 (1996).

[37] I. B. C. M. Rocha, F. P. van der Meer, S. Raijmaekers, F. Lahuerta, R. P. L. Nijssen, and L. J. Sluys, *Numerical/experimental study of the monotonic and cyclic viscoelastic/viscoplastic/fracture behavior of an epoxy resin,* International Journal of Solids and Structures **168**, 153 (2019).

[38] T. S. Hille, A. S. J. Suiker, and S. Turteltaub, *Microcrack nucleation in thermal barrier coating systems,* Engineering Fracture Mechanics **76**, 813 (2009).

[39] A. Turon, P. P. Camanho, J. Costa, and C. G. Dávila, *A damage model for the simulation of delamination in advanced composites under variable-mode loading,* Mechanics of Materials **38**, 1072 (2006).

[40] T. L. Anderson, *Fracture mechanics: fundamentals and applications* (CRC press, 2005).

[41] M. Kuna, *Finite elements in fracture mechanics*, Vol. 10 (Springer, 2013).

[42] J. E. Field, S. M. Walley, W. G. Proud, H. T. Goldrein, and C. R. Siviour, *Review of experimental techniques for high rate deformation and shock studies,* International Journal of Impact Engineering **30**, 725 (2004).

[43] T. Nishioka, *Computational dynamic fracture mechanics,* International Journal of Fracture **86**, 127 (1997).

[44] B. Moran and C. F. Shih, *Crack tip and associated domain integrals from momentum and energy balance,* Engineering Fracture Mechanics **27**, 615 (1987).

[45] A. R. Melro, P. P. Camanho, F. M. Andrade Pires, and S. T. Pinho, *Micromechanical analysis of polymer composites reinforced by unidirectional fibres: Part II – Micromechanical analyses,* International Journal of Solids and Structures **50**, 1906 (2013).

[46] B. R. K. Blackman, A. J. Kinloch, F. S. Rodriguez Sanchez, W. S. Teo, and J. G. Williams, *The fracture behaviour of structural adhesives under high rates of testing,* Engineering Fracture Mechanics **76**, 2868 (2009).

[47] H. Liu, X. Meng, H. Zhang, H. Nie, C. Zhang, and Y. Li, *The dynamic crack propagation behavior of mode I interlaminar crack in unidirectional carbon/epoxy composites,* Engineering Fracture Mechanics **215**, 65 (2019).

[48] B. R. K. Blackman, A. J. Kinloch, Y. Wang, and J. G. Williams, *The failure of fibre composites and adhesively bonded fibre composites under high rates of test,* Journal of Materials Science **31**, 4451 (1996).

[49] T. Nakamura, C. F. Shih, and L. B. Freund, *Analysis of a dynamically loaded three-point-bend ductile fracture specimen,* Engineering Fracture Mechanics **25**, 323 (1986).

[50] E. E. Nishida, *Distinguishing inertia effects from the intrinsic mechanical behavior of soft materials at high strain rates by Kolsky bar experiments*, Ph.D. thesis, Purdue University (2010).

[51] A. J. Smiley and R. B. Pipes, *Rate Effects on Mode I Interlaminar Fracture Toughness in Composite Materials,* Journal of Composite Materials **21**, 670 (1987).

[52] K. Friedrich, R. Walter, L. A. Carlsson, A. J. Smiley, and J. W. Gillespie, *Mechanisms for rate effects on interlaminar fracture toughness of carbon/epoxy and carbon/PEEK composites,* Journal of Materials Science **24**, 3387 (1989).

[53] M. Heidari-Rarani, M. M. Shokrieh, and P. P. Camanho, *Finite element modeling of mode I delamination growth in laminated DCB specimens with R-curve effects,* Composites Part B: Engineering **45**, 897 (2013).

[54] F. Zhou, J.-F. Molinari, and T. Shioya, *A rate-dependent cohesive model for simulating dynamic crack propagation in brittle materials,* Engineering Fracture Mechanics **72**, 1383 (2005).

[55] J. J. M. Machado, A. Hayashi, Y. Sekigushi, R. D. S. G. Campilho, E. A. S. Marques, C. Sato, and L. F. M. da Silva, *Dynamic behaviour in mode I fracture toughness of CFRP as a function of temperature,* Theoretical and Applied Fracture Mechanics **103**, 102257 (2019).

6

Conclusion

6.1. Conclusions and discussions

The main objective of this thesis is to investigate the rate-dependent deformation and failure of composite laminates under dynamic (impact) loads with multiscale numerical models. More specifically, three contributing mechanisms including inertia effects, the viscous material behavior and microscale failure pattern are investigated with multiscale models.

This work started with the investigation of a series of dynamic DCB tests of a unidirectional PEEK/carbon composite laminate over a test rate range of 3.3×10^{-5} to 10.0 m/s with a rate-dependent cohesive zone model (CZM) and an interfacial thick level set (ITLS) model. In the adopted numerical models, the bulk material of the beam is considered to be homogeneous and orthotropic linear elastic without taken the microstructure of the unidirectional composite laminate into account. The rate-dependent failure mechanism and energy dissipation are considered by rate-dependent cohesive laws used in the CZM and the crack speed versus energy release rate ($V(G)$) relation in the ITLS model. It is found that the presented rate-dependent CZM is capable of capturing the average crack growth speed and it fails to reproduce crack arrests that do occur in some of the experiments. However, the $V(G)$ relation can provide a very good match with experimentally observed arrests and reinitiation phenomena with carefully calibrated parameters. No single $V(G)$ relation could be identified that works for all rates, which means that the physical formulation is still incomplete. Further research is needed to investigate other factors that might influence the crack speed, for instance the time rate of the dynamic energy release rate [1].

To obtain a better understanding of the underlying mechanisms at the microscale, multiscale models have been developed to incorporate the effect of composite microstructure and quantify the contribution of various microscale events on macroscopic rate-dependent deformation and failure. Special attention is put on three contributing mechanisms, namely inertia effects, the viscous material behav-

ior and microscale fracture mechanism. Firstly, a dispersive homogenization model which can capture the micro-inertia of composites has been introduced. In this approach, the homogenized macroscopic linear momentum equation is enriched with a micro-inertia term scaled by a so-called "dispersion tensor". This dispersion tensor is computed within a statistically equivalent representative volume element (RVE). It is found that the dispersive multiscale model gives a considerable improvement over the non-dispersive model in capturing the dynamic response of heterogeneous materials. The convergence of the dispersion tensor is found to be sensitive to the spatial distribution pattern. Convergence is obtained in an RVE-size study but only with a relatively large micromodel.

Secondly, a step-by-step numerical homogenization procedure has been introduced to calibrate a homogenized viscoelastic-viscoplastic (VE-VP) model for the transverse response of composites. The calibrated VE-VP model is used in a homogenized FEM model to describe the composite material response and to compare against the RVE model. With a novel step-by-step numerical homogenization procedure, the homogenized model captures the viscoelastic deformation, stress relaxation, the rate-dependent yielding and unloading behavior of the polymer composite well, although the assumptions of a single plastic Poisson's ratio and pure isotropic hardening are over-simplifications of the composite behavior. This model can be further used to model the far-field mechanical response of composites in the transverse plane in a notched configuration in order to avoid high computational costs.

Thirdly, the mode-I dynamic fracture energy and failure mechanisms of polymer composites are investigated with an embedded cell model of the single-edge-notched-tension (SENT) geometry. The influence and interaction of loading rate, time-dependent material nonlinearity, structural inertia and matrix ligament bridging on the fracture toughness and failure mechanisms of composites have been evaluated. It is found that with the given material parameters and studied loading rate range, the failure type is brittle with many microcracks but limited plasticity in the fracture process zone and a trend of increasing brittleness for larger strain rates is observed. The dynamic fracture energy G_c shows an increasing trend with the crack speed V but no unique $G_c(V)$ relation is found. Cases with high nominal strain rate show visible but not very strong inertia effects with oscillating values of the crack growth driving force. The introduced numerical framework allows a quantitative evaluation of the dynamic fracture energy for composites, including macroscopically useful information such as R-curves and velocity-toughening data. Considering that the mode-I fracture toughness is also temperature-dependent [2], incorporation of temperature effects into the current numerical framework is needed which can be achieved following the idea of [3].

Overall, it is concluded that it is possible to capture several phenomena observed for the dynamic response of composites with the appropriate tools. However, no single approach exists that can completely describe dynamic crack growth in composites for all relevant loading rates. Nevertheless, a number of suggestions can be made to help the analysis/design of impact resistant structures in real life: (1) the rate-dependency of fracture energy of composites should be considered for

impact-resistance structures since overlooking such effect could cause an overoptimistic design. (2) Improvement of fracture energy of fiber/matrix interface and the pure matrix could be helpful to increase the overall fracture resistance and the embedded cell model can be used as a numerical tool to evaluate the dynamic fracture energy. (3) The material properties of polymer matrix and fiber determine the viscocity of composites, careful selection of the constituents could help improve the energy dissipation of composite structures. (4) The micro-inertia effect of composites has a remarkable effect on the stress-wave propagation in composites and therefore quantification of such effect should be properly done for designing wave-mitigation structures.

6.2. Novelty and contributions of this work

The new developments in computational methods for describing the dynamic response of composites in this thesis are:

1. The interfacial thick level set (ITLS) method is for the first time embedded in a dynamics solution scheme which extends the application of this method from quasi-static and cyclic loading to dynamic loading.

2. An explicit relation between the crack growth speed V and energy release rate G has been implemented in the ITLS method to capture both stable crack propagation and unstable crack propagation in DCB tests, although a single $V(G)$ that could describe the response at all loading rates could not be found.

3. It is demonstrated that the dispersive multiscale model shows a considerable improvement over the non-dispersive model in capturing the dynamic response of heterogeneous materials by studying elastic wave propagation problems.

4. It has been demonstrated that an RVE exists for the presented dispersive homogenization approach for realistic fiber reinforced composite microstructures, although it was found that careful definition of microstructural geometry is required to achieve representativeness.

5. A numerical homogenization scheme is developed to derive a homogenized viscoelastic-viscoplastic (VE-VP) model for the transverse response of fiber-reinforced epoxy composites, including a novel identification method for homogenized material parameters.

6. An embedded cell model with dynamic J-integral for modeling dynamic crack growth in heterogeneous materials has been developed.

6.3. Recommendations for future work

To be able to predict failure of composites considering high-rate effects, the introduced numerical framework in this thesis needs to be further developed to achieve the goal of an efficient and accurate numerical model. Firstly, a more accurate and

efficient homogenization technique is needed to be used for modeling the constitutive behavior of composites considering high strain rates. The numerical homogenization scheme introduced in Chapter 4 must be extended in fiber-direction and oversimplifications of a single plastic Poisson's ratio and pure isotropic hardening should be corrected. Secondly, a rate-dependent crack growth model (e.g. CZM or ITLS) has to be developed which is capable of capturing the entire physics of dynamic crack growth, including crack initiation, propagation and arrest. Studies in Chapter 2 and 5 have provided useful insights with either the rate-dependent CZM or the ITLS model with a crack speed V vs. dynamic energy release rate G relation. However, there is no unique model that can be established. Thirdly, a homogenization technique is needed to capture different inertia effects of fiber and matrix, especially for high strain rate type of loading cases (e.g. shock wave). The dispersive homogenization model introduced in Chapter 3 is able to capture this effect only when the stress wave is not shorter than a few times of the RVE size. Fourthly, the thermodynamic effect should be considered as it is a critical contribution for cases like impact loading. Therefore, some possible approaches for the above mentioned goals are discussed in this section.

6.3.1. High-rate constitutive modeling

As mentioned in Chapter 4, the developed homogenized VE-VP model with the same isotropic hardening as the matrix model matches very well with the RVE model under monotonic loading. However, if plasticity also happens under reverse loading, there is some deviation observed. Therefore, a mixed hardening rule could be introduced with combined isotropic hardening and kinematic hardening. Meanwhile, to consider the orthotropy of composite laminates, the model needs to be extended to consider the mechanical response in the fiber direction. Therefore, the adopted viscoelasticity and viscoplasticity formulation should be adapted. A possible starting point is to use the transversely-isotropic elastic–plastic constitutive model introduced in Vogler et al. [4] to replace the elastic-plastic components of the VE-VP model in Chapter 4, but additional attention is required to properly introduce viscosity in the orthotropic constitutive law.

6.3.2. Numerical techniques for crack growth

Deriving a rate-dependent cohesive law with cohesive multiscale modeling techniques is also interesting. For instance, with an RVE-based cohesive multiscale approach, information of the finer-scale is hierarchically passed on to a coarser scale by bridging laws. For a two-scale scheme, at the macroscopic level the strain localization can be represented by cohesive cracks with strong discontinuity kinematics and a proper kinematical information transfer from the macro-to-micro scales. Hill–Mandel lemma is extended to relate coarse and fine scale energies with the assumption of separation of scales. Quasistatic crack growth in composites can be studied so that inertia is not needed to be taken into account. With this technique, the material nonlinearity and time-dependence of polymeric resin, rate-dependent fiber/matrix debonding, matrix cracking can be considered and collapsed into a rate-dependent cohesive law. The homogenized rate-dependent cohesive law can

be compared with the DNS model introduced in Chapter 5 to validate the accuracy of the proposed cohesive law. Experimental work is also necessary to be compared with. A further extension could be the study of mixed-mode crack propagation with the above numerical framework.

The ITLS model introduced in Chapter 2 and the embedded cell model introduced in Chapter 5 can be further utilized and developed to study rate-dependent failure of composite laminates. In this thesis a relation is derived between fracture energy G_c and crack speed V from SENT tests in Chapter 5. It would be interesting to see if the ITLS model introduced in Chapter 2 is capable of reproducing the same dynamic crack propagation behavior. The embedded microstructure then has to be homogenized to model the environment of the crack and a possible method is to use the numerical homogenization model introduced in Chapter 4 . In case of short-pulse type of loading when the generated stress wave is a few times of the size of an RVE, the micro-inertia effect becomes evident and the dispersive formulation in Chapter 3 can be included to better capture the response of the homogenized material.

6.3.3. Thermomechanical modeling

As mentioned in Chapter 1, one of the contributing mechanisms of rate-dependent deformation and failure is thermomechanical dissipation, i.e. a transition from isothermal to adiabatic deformation and failure process is expected for composites at increasing loading rates. To account for this, heat production and conduction in bulk material and fracture process zone should be included in the model. Mechanical properties of polymers change dramatically with temperature, going from glass-like brittle behaviour at low temperatures to rubber-like behaviour at high temperatures. This is a typical example of a phenomenon for which multiscale approaches are attractive. Temperature dependent behavior of the matrix can be characterized with tests on pure polymer material, after which RVE simulations can predict how this affects the overall composite material response. Existing thermodynamic constitutive models can be incorporated in the current framework. Homogenization techniques are still needed to derive the connection between the various thermomechanical fields at macroscale and microscale [5].

References

[1] H. Liu, H. Nie, C. Zhang, and Y. Li, *Loading rate dependency of Mode I interlaminar fracture toughness for unidirectional composite laminates,* Composites Science and Technology **167**, 215 (2018).

[2] J. J. M. Machado, A. Hayashi, Y. Sekigushi, R. D. S. G. Campilho, E. A. S. Marques, C. Sato, and L. F. M. da Silva, *Dynamic behaviour in mode I fracture toughness of CFRP as a function of temperature,* Theoretical and Applied Fracture Mechanics **103**, 102257 (2019).

[3] A. Ahmed and L. J. Sluys, *A phantom node formulation for modeling coupled*

adiabatic-isothermal cracking in FRP composites, Computer Methods in Applied Mechanics and Engineering **278**, 291 (2014).

[4] M. Vogler, R. Rolfes, and P. P. Camanho, *Modeling the inelastic deformation and fracture of polymer composites-part I: Plasticity model,* Mechanics of Materials **59**, 50 (2013).

[5] G. Chatzigeorgiou, N. Charalambakis, Y. Chemisky, and F. Meraghni, *Periodic homogenization for fully coupled thermomechanical modeling of dissipative generalized standard materials,* International Journal of Plasticity **81**, 18 (2016).

Acknowledgements

This PhD journey is finally over. To me, it is certainly an important life journey which will influence my whole life. It is interesting and unforgettable. Without the help of many people, I can not imagine that I can achieve this far as being a PhD. Therefore, I would like share my sincere thanks to those who have supported me in any manner during my PhD journey.

First of all, I would like to thank my Promoter, Bert Sluys for your enormous help and the freedom you have given to me. Without you this thesis would simply not have been possible. I enjoyed making presentations to you and the discussions about our research. Your comments on my research are definitely illuminating and your suggestions about my presentation skills lead me in the right path of becoming a better presenter. You are an easygoing person and I certainly like the right of "knocking your door and ask you something without reservation". I would like to thank you for allowing me to stay in Beijing in the last stage of my PhD while still maintaining the supervision and help just like I was in Delft.

I would like to thank my daily supervisor, Frans P. van der Meer for your relentless help. Without the coding environment you provided, I can not even start my PhD project. I can still recall so many discussions we had in your office and you are always so nice to accept me to interrupt you with some "strange" questions. Your suggestions have always helped me to step forward and your comments on the paper always pose a big challenge on me. When I look back, these moments have really progressed the quality of my research. I feel lucky that you are such a nice person to work with and talk with. Your consistent help during my stay in Beijing made the completion of this thesis possible.

I would like to thank those who have shared important research skills with me. I would like to thank Erik Jan, who has provided so many help on JEMJIVE coding. To Martijn, who has shared his knowledge about the DEM solver HADES with me. I would like to thank Iuri for providing me with the implementation of a VE-VP material model.

Thanks the sectary team of the 3MD department, including Anneke, Jaap, Jacqueline, Iris and Sandra. Special thanks go to Anneke who has helped me applying for Visa and build a nice working environment. Special thank also goes to Jaap for being my nice office neighbour and always being so nice to solve my problems.

I would like to thank my colleagues of the computational mechanics group for sharing the PhD journey together. We had nice time having lunch together, talking at the coffee corner, playing sports, going to conferences, eating outside, etc. Special thanks go to my former officemate Erik for having so many discussions on our research, teaching me dutch, coffee breaks, having beer and lunch walks. I would also like to give special thank to Kai and Jitang for helping me get to know the group when I just started my PhD. For Jitang, your financial support during my stay in

Beijing certainly helped me survive. Special thank also goes to Ali for your kindness and friendship, you are a person who is more than willing to provide help and share your skills. You are my gym coach and I hope you enjoy this title. I would like to extend my special thanks to Parashant, dongyu, Richard, Fariborz, Tiziano and Jian for enjoying the basketball time with maybe a bit trash talk and we really had fun. For Richard, you are my gitar teacher, although I am not a good student. I would like to thank Jafar for having beer together and sharing life stories. I would like to thank my officemate Suman for being such a nice person to stay with. I would like to thank Mz and Lu for having nice Chinese food together and the talks we had in Chinese. For Mingjuan, Hongzhi, Chenjie, Tao, Hongxiao and Bingjing, thanks for sharing our Chinese culture and supporting each other while we are studying in the Netherlands. I would like to thank my colleagues: Mohsen, Dragan, Luiz, Bram, Fanxiang, Davide, Lars, Frank, Zheng, Jaap, Arman, Mehdi, Luis, Osvalds, Rafid, Noori, Marcello, Liting, Cao, angelo, Behrouz.

Finally, I would like to thank my parents for giving me so much support both mentally and economically. I have shared so many difficult moments with you. You are always standing by my side with so much patience and encouragements. I would also like to thank Ms. Li Deng for her courage to join my life under such a circumstance. Her love always motivates me to explore my biggest potential.

Yaolu Liu

Appendix A

The cohesive law in this work was implemented in an implicit framework and hence the constitutive tangent matrix was derived. The traction vs. displacement jump relation in Eq. (2.1) can be rewritten in matrix notation as

$$\mathbf{t} = K(\mathbf{I} - d\mathbf{P})[\![\mathbf{u}]\!] \tag{1}$$

in which,

$$\mathbf{I} = \begin{bmatrix} 1 & 0 \\ 0 & 1 \end{bmatrix}, \quad \mathbf{P} = \begin{bmatrix} \frac{\langle [\![u]\!]_1 \rangle}{[\![u]\!]_1} & 0 \\ 0 & 1 \end{bmatrix} \tag{2}$$

During damage growth, the consistent tangent $\mathbf{D}_{\text{cons}}$ for a fixed time step size of T_c is defined as

$$\mathbf{D}_{\text{cons}} = \frac{\partial \mathbf{t}}{\partial [\![\mathbf{u}]\!]} = K\left[\mathbf{I} - d\mathbf{P} - \mathbf{P}[\![\mathbf{u}]\!]\left(\frac{\partial d}{\partial [\![\mathbf{u}]\!]}\right)^T\right] \tag{3}$$

with

$$\frac{\partial d}{\partial [\![\mathbf{u}]\!]} = \frac{\partial d}{\partial \Delta}\frac{\partial \Delta}{\partial [\![\mathbf{u}]\!]} + \frac{\partial d}{\partial \Delta_0}\frac{\partial \Delta_0}{\partial [\![\mathbf{u}]\!]} + \frac{\partial d}{\partial \Delta_f}\frac{\partial \Delta_f}{\partial [\![\mathbf{u}]\!]} \tag{4}$$

The Eq. (4) is expanded as

$$\frac{\partial d}{\partial \Delta} = \frac{\Delta_f \Delta_0}{\Delta^2(\Delta_f - \Delta_0)} \tag{5}$$

$$\frac{\partial \Delta}{\partial [\![\mathbf{u}]\!]} = \frac{1}{\Delta}\left(\langle [\![u]\!]_1 \rangle, [\![u]\!]_2\right)^T \tag{6}$$

$$\frac{\partial d}{\partial \Delta_0} = -\frac{\Delta_f(\Delta_f - \Delta)}{\Delta(\Delta_f - \Delta_0)^2} \tag{7}$$

$$\frac{\partial \Delta_0}{\partial [\![\mathbf{u}]\!]} = \frac{\partial \Delta_0}{\partial B}\frac{\partial B}{\partial [\![\mathbf{u}]\!]} + \frac{\partial \Delta_0}{\partial [\![u]\!]_1^0}\frac{\partial [\![u]\!]_1^0}{\partial \sigma_1}\frac{\partial \sigma_1}{\partial [\![\mathbf{u}]\!]} + \frac{\partial \Delta_0}{\partial [\![u]\!]_2^0}\frac{\partial [\![u]\!]_2^0}{\partial \sigma_2}\frac{\partial \sigma_2}{\partial [\![\mathbf{u}]\!]} \tag{8}$$

$$\frac{\partial d}{\partial \Delta_f} = -\frac{\Delta_0(\Delta - \Delta_0)}{\Delta(\Delta_f - \Delta_0)^2} \tag{9}$$

$$\frac{\partial \Delta_f}{\partial [\![\mathbf{u}]\!]} = \frac{\partial \Delta_f}{\partial B}\frac{\partial B}{\partial [\![\mathbf{u}]\!]} + \frac{\partial \Delta_f}{\partial \Delta_0}\frac{\partial \Delta_0}{\partial [\![\mathbf{u}]\!]} + \frac{\partial \Delta_f}{\partial [\![u]\!]_1^0}\frac{\partial [\![u]\!]_1^0}{\partial \sigma_1}\frac{\partial \sigma_1}{\partial [\![\mathbf{u}]\!]} + \frac{\partial \Delta_f}{\partial [\![u]\!]_2^0}\frac{\partial [\![u]\!]_2^0}{\partial \sigma_2}\frac{\partial \sigma_2}{\partial [\![\mathbf{u}]\!]} + \frac{\partial \Delta_f}{\partial [\![u]\!]_1^f}\frac{\partial [\![u]\!]_1^f}{\partial [\![\mathbf{u}]\!]} + \frac{\partial \Delta_f}{\partial [\![u]\!]_2^f}\frac{\partial [\![u]\!]_2^f}{\partial [\![\mathbf{u}]\!]} \tag{10}$$

with

$$\frac{\partial \Delta_0}{\partial B} = \frac{\eta B^{\eta-1}}{2\Delta_0}\left(([\![u]\!]_2^0)^2 - ([\![u]\!]_1^0)^2\right) \tag{11}$$

$$\frac{\partial B}{\partial [\![\mathbf{u}]\!]} = \left(\frac{\partial B}{\partial [\![u]\!]_1}, \frac{\partial B}{\partial [\![u]\!]_2}\right)^T = \left(-\frac{2\langle [\![u]\!]_1\rangle ([\![u]\!]_2)^2}{\Delta^4}, \frac{2(\langle [\![u]\!]_1\rangle)^2 [\![u]\!]_2}{\Delta^4}\right)^T \tag{12}$$

$$\frac{\partial \Delta_0}{\partial [\![u]\!]_1^0} = \frac{(1-B^\eta)}{\Delta_0} [\![u]\!]_1^0, \quad \frac{\partial \Delta_0}{\partial [\![u]\!]_2^0} = \frac{B^\eta}{\Delta_0} [\![u]\!]_2^0 \tag{13}$$

$$\frac{\partial [\![u]\!]_1^0}{\partial \sigma_1} = \frac{\partial [\![u]\!]_2^0}{\partial \sigma_2} = \frac{1}{K} \tag{14}$$

$$\frac{\partial \sigma_1}{\partial [\![\mathbf{u}]\!]} = \begin{cases} \frac{c_1 \sigma_1^0}{\dot{\Delta}_1 T_c} \left(\frac{\langle [\![u]\!]_1\rangle}{[\![u]\!]_1}, 0\right)^T, & \dot{\Delta}_1 \geq \dot{\Delta}_1^{\text{ref}} \\ 0, & \dot{\Delta}_1 < \dot{\Delta}_1^{\text{ref}} \end{cases}, \quad \frac{\partial \sigma_2}{\partial [\![\mathbf{u}]\!]} = \begin{cases} \frac{c_2 \sigma_2^0}{\dot{\Delta}_2 T_c} \left(0, \frac{|[\![u]\!]_2|}{[\![u]\!]_2}\right)^T, & \dot{\Delta}_2 \geq \dot{\Delta}_2^{\text{ref}} \\ 0, & \dot{\Delta}_2 < \dot{\Delta}_2^{\text{ref}} \end{cases} \tag{15}$$

and

$$\frac{\partial \Delta_f}{\partial B} = \frac{\eta B^{\eta-1}}{\Delta_0} \left([\![u]\!]_2^0 [\![u]\!]_2^f - [\![u]\!]_1^0 [\![u]\!]_1^f\right) \tag{16}$$

$$\frac{\partial \Delta_f}{\partial \Delta_0} = -\frac{\Delta_f}{\Delta_0} \tag{17}$$

$$\frac{\partial \Delta_f}{\partial [\![u]\!]_1^0} = \frac{1-B^\eta}{\Delta_0} [\![u]\!]_1^f, \quad \frac{\partial \Delta_f}{\partial [\![u]\!]_2^0} = \frac{B^\eta}{\Delta_0} [\![u]\!]_2^f \tag{18}$$

$$\frac{\partial \Delta_f}{\partial [\![u]\!]_1^f} = \frac{(1-B^\eta)[\![u]\!]_1^0}{\Delta_0}, \quad \frac{\partial \Delta_f}{\partial [\![u]\!]_2^f} = \frac{B^\eta [\![u]\!]_2^0}{\Delta_0} \tag{19}$$

$$\frac{\partial [\![u]\!]_1^f}{\partial [\![\mathbf{u}]\!]} = \frac{\partial [\![u]\!]_1^f}{\partial G_{IC}} \frac{\partial G_{IC}}{\partial [\![\mathbf{u}]\!]} + \frac{\partial [\![u]\!]_1^f}{\partial \sigma_1} \frac{\partial \sigma_1}{\partial [\![\mathbf{u}]\!]} \tag{20}$$

$$\frac{\partial [\![u]\!]_2^f}{\partial [\![\mathbf{u}]\!]} = \frac{\partial [\![u]\!]_2^f}{\partial G_{IIC}} \frac{\partial G_{IIC}}{\partial [\![\mathbf{u}]\!]} + \frac{\partial [\![u]\!]_2^f}{\partial \sigma_2} \frac{\partial \sigma_2}{\partial [\![\mathbf{u}]\!]} \tag{21}$$

with

$$\frac{\partial [\![u]\!]_1^f}{\partial G_{IC}} = \frac{2}{\sigma_1}, \quad \frac{\partial [\![u]\!]_2^f}{\partial G_{IIC}} = \frac{2}{\sigma_2} \tag{22}$$

$$\frac{\partial [\![u]\!]_1^f}{\partial \sigma_1} = -\frac{2G_{IC}}{(\sigma_1)^2}, \quad \frac{\partial [\![u]\!]_2^f}{\partial \sigma_2} = -\frac{2G_{IIC}}{(\sigma_2)^2} \tag{23}$$

$$\frac{\partial G_{IC}}{\partial [\![\mathbf{u}]\!]} = \begin{cases} \frac{m_1 G_{IC}^0}{\dot{\Delta}_1 T_c} \left(\frac{\langle [\![u]\!]_1\rangle}{[\![u]\!]_1}, 0\right)^T, & \dot{\Delta}_1^{\text{ref}} \leq \dot{\Delta}_1 \leq \dot{\Delta}_1^{\text{inf}} \\ 0, & \text{otherwise} \end{cases} \tag{24}$$

$$\frac{\partial G_{IIC}}{\partial [\![\mathbf{u}]\!]} = \begin{cases} \frac{m_2 G_{IIC}^0}{\dot{\Delta}_2 T_c} \left(0, \frac{|[\![u]\!]_2|}{[\![u]\!]_2}\right)^T, & \dot{\Delta}_2^{\text{ref}} \leq \dot{\Delta}_2 \leq \dot{\Delta}_2^{\text{inf}} \\ 0, & \text{otherwise} \end{cases} \tag{25}$$

Appendix B

The solution of Eq. (3.18) follows a standard FEM formulation with the precomputation of the dispersion tensor via the procedures in Chapter 3.2.1. The stiffness matrix is needed for the calculation of the macro-scale stress $\sigma_{ij}^{(0)}$. This is obtained by a standard computational-homogenization scheme. Periodicity is assumed for the boundary edges and a prescribed displacement is applied to three controlling nodes (see Fig. 1) according to

$$\mathbf{u}_i = \tilde{\mathbf{H}}_i \boldsymbol{\varepsilon}^M, \quad i = 1, 2, 4 \tag{26}$$

where $\boldsymbol{\varepsilon}^M$ is the macro-scale strain and

$$\tilde{\mathbf{H}}_i = \begin{bmatrix} y_1^i & 0 \\ 0 & y_2^i \\ \frac{y_2^i}{2} & \frac{y_1^i}{2} \end{bmatrix} \tag{27}$$

After solving the incremental form of system equation $\mathbf{K}\delta\mathbf{u} = \delta\mathbf{f}$, the stiffness matrix $\mathbf{S}^M$ is obtained by

$$\mathbf{S}^M = \begin{bmatrix} \tilde{\mathbf{H}}_1 & \tilde{\mathbf{H}}_2 & \tilde{\mathbf{H}}_4 \end{bmatrix} \left(\mathbf{K}_{pp} - \mathbf{K}_{pf}(\mathbf{K}_{ff})^{-1}\mathbf{K}_{fp}\right) \begin{bmatrix} \tilde{\mathbf{H}}_1 \\ \tilde{\mathbf{H}}_2 \\ \tilde{\mathbf{H}}_4 \end{bmatrix} \tag{28}$$

in which subscript p denotes the degrees of freedom of the three controlling nodes and subscript f represents the other free nodes.

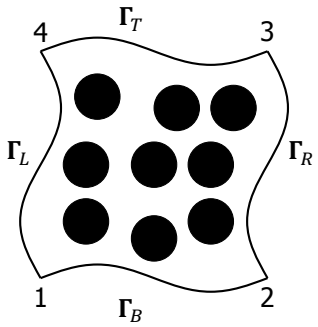

Figure 1: Periodicity of RVE. Two periodicity pairs of edges: Γ_L and Γ_R; Γ_T and Γ_B.

Appendix C

To solve Eq. (3.24), the influence function h_k^{mn} $(mn = 11, 22, 12)$ is treated as nodal variable. In matrix notation, standard FEM formulation with $\mathbf{h}^{mn} := (h_1^{mn}, h_2^{mn})^T = \mathbf{N}\overline{\mathbf{h}}^{mn}$ and $\boldsymbol{\omega} = \mathbf{N}\overline{\boldsymbol{\omega}}$ are introduced where $\mathbf{N}$ is the shape function matrix and $\overline{\mathbf{h}}^{mn}$, $\overline{\boldsymbol{\omega}}$ contain the nodal values of the acceleration influence function and test function, respectively. Eq. (3.24) is further simplified by using the FEM formulation as

$$\int_\Theta \left((L\boldsymbol{\omega})^T \boldsymbol{\sigma}^{mn} + (L\boldsymbol{\omega})^T \mathbf{F}^{mn}\right) d\Theta = \overline{\boldsymbol{\omega}}^T \int_\Theta \left(\mathbf{B}^T \boldsymbol{\sigma}^{mn} + \mathbf{B}^T \mathbf{F}^{mn}\right) d\Theta = 0 \tag{29}$$

where

$$\mathbf{L}\boldsymbol{\omega} = \begin{bmatrix} \frac{\partial}{\partial y_1} & 0 \\ 0 & \frac{\partial}{\partial y_2} \\ \frac{\partial}{\partial y_2} & \frac{\partial}{\partial y_1} \end{bmatrix} \begin{bmatrix} \omega_1 \\ \omega_2 \end{bmatrix} = \begin{bmatrix} \omega_{(1,1)} \\ \omega_{(2,2)} \\ 2\omega_{(1,2)} \end{bmatrix} \quad \boldsymbol{\sigma}^{mn} = \begin{bmatrix} \sigma_{11}^{mn} \\ \sigma_{22}^{mn} \\ \sigma_{12}^{mn} \end{bmatrix} = \begin{bmatrix} S_{1111} & S_{1122} & S_{1112} \\ S_{2211} & S_{2222} & S_{2212} \\ S_{1211} & S_{1222} & S_{1212} \end{bmatrix} \begin{bmatrix} h_{(1,1)}^{mn} \\ h_{(2,2)}^{mn} \\ 2h_{(1,2)}^{mn} \end{bmatrix}$$

$$\mathbf{F}^{mn} = \begin{bmatrix} F_{11}^{mn} \\ F_{22}^{mn} \\ F_{12}^{mn} \end{bmatrix} = \frac{\rho(\mathbf{y})}{\rho^{(0)}} \begin{bmatrix} S_{11mn} \\ S_{22mn} \\ S_{12mn} \end{bmatrix}$$

in which the matrix $\mathbf{B} = \mathbf{LN}$.

The constraint equation Eq. (3.12) is rewritten as

$$\langle h_k^{mn} \rangle_\Theta = \left\langle \mathbf{N}\overline{\mathbf{h}}^{mn} \right\rangle_\Theta = \langle \mathbf{N} \rangle_\Theta \overline{\mathbf{h}}^{mn} = \mathbf{c}\overline{\mathbf{h}}^{mn} = 0 \tag{30}$$

in which the cofficient matrix $\mathbf{c} = \langle \mathbf{N} \rangle_\Theta$. Eq. (30) can then be treated as a constraint for the linear system of equations given by Eq. (29). The $\mathbf{y}-$periodicity condition of h_k^{mn} can be enforced directly by periodicity constraints on corresponding edges of the RVE (see Fig. 1).

Appendix D

According to Eq. (4.20),

$$\sigma_{ij}(t_{n+1}) = D^{\infty}_{ijkl} : \varepsilon^{e}_{kl}(t_{n+1}) + D^{ve}_{ijkl}(\Delta t) : \Delta\varepsilon^{e}_{kl} + \sigma^{hist}_{ij}(t_n) \tag{31}$$

By taking the derivative of the stress $\sigma_{ij}(t_{n+1})$ with respect to the strain $\varepsilon^{e}_{kl}(t_{n+1})$, the consistent tangent can be derived as:

$$D^{con}_{ijkl} = \frac{\partial\sigma_{ij}(t_{n+1})}{\partial\varepsilon_{kl}(t_{n+1})} = \frac{\partial\sigma_{ij}(t_{n+1})}{\partial\varepsilon^{e}_{kl}(t_{n+1})} = D^{\infty}_{ijkl} + D^{ve}_{ijkl}(\Delta t) \tag{32}$$

Appendix E

To solve the local return-mapping scheme, a Newton-Raphson scheme is adopted. Herein, a consistent tangent for the local Newton-Raphson scheme is derived by using:

$$\frac{\partial \Phi}{\partial \Delta\gamma} = \hat{V}\frac{\partial f_p}{\partial \Delta\gamma} - 1 \tag{33}$$

where

$$\hat{V} = \frac{m_p \Delta t}{\eta_p \sigma_t^0 \sigma_c^0}\left(\frac{f_p}{\sigma_t^0 \sigma_c^0}\right)^{m_p - 1} \qquad \frac{\partial f_p}{\partial \Delta\gamma} = -\frac{72\hat{G}J_2^{\mathrm{tr}}}{\zeta_s^3} - \frac{4\left(\sigma_c - \sigma_t\right)\hat{K}\alpha I_1^{\mathrm{tr}}}{\zeta_p^2} + \hat{H}\frac{\partial \Delta\varepsilon_{eq}^{\mathrm{p}}}{\partial \Delta\gamma} \tag{34}$$

with

$$\hat{H} = \frac{\partial f_p}{\partial \varepsilon_{eq}^p} = \frac{2I_1^{tr}}{\zeta_p}\left(\frac{\partial \sigma_c}{\partial \varepsilon_{eq}^p} - \frac{\partial \sigma_t}{\partial \varepsilon_{eq}^p}\right) - 2\left(\sigma_c \frac{\partial \sigma_t}{\partial \varepsilon_{eq}^p} + \sigma_t \frac{\partial \sigma_c}{\partial \varepsilon_{eq}^p}\right) \tag{35}$$

$$\frac{\partial \varepsilon_{\mathrm{eq}}^{\mathrm{p}}}{\partial \Delta\gamma} = \sqrt{\frac{1}{1 + 2\left(\nu_{\mathrm{p}}\right)^2}}\left(\sqrt{\hat{A}} - \frac{\Delta\gamma}{2\sqrt{\hat{A}}}\left(\frac{216\hat{G}J_2^{\mathrm{tr}}}{\zeta_s^3} + \frac{16\alpha^3\hat{K}\left(I_1^{\mathrm{tr}}\right)^2}{27\zeta_p^3}\right)\right) \tag{36}$$

$$\hat{A} = \frac{18J_2^{tr}}{\zeta_s^2} + \frac{4\alpha^2}{27\zeta_p^2}\left(I_1^{tr}\right)^2 \tag{37}$$

Consistent linearization of Eq. (4.25) gives:

$$D_{ijkl}^{con} = \frac{\partial \sigma_{ij}}{\partial \varepsilon_{kl}} = \frac{\widehat{G}}{\zeta_s}\left(\delta_{ik}\delta_{jl} + \delta_{il}\delta_{jk} - \frac{2}{3}\delta_{ij}\delta_{kl}\right) + \frac{\hat{K}}{\zeta_p}\delta_{ij}\delta_{kl} - \frac{72\widehat{V}\widehat{G}^2}{\mu\zeta_s^4}S_{ij}^{\mathrm{tr}}S_{kl}^{\mathrm{tr}} - \frac{36\left(\sigma_c - \sigma_t\right)\widehat{V}\widehat{K}\widehat{G}}{\mu\zeta_p\zeta_s^2}S_{ij}^{\mathrm{tr}}\delta_{kl}$$
$$-\frac{8\alpha I_1^{\mathrm{tr}}\widehat{V}\widehat{K}\widehat{G}}{\mu\zeta_p^2\zeta_s^2}\delta_{ij}S_{kl}^{\mathrm{tr}} - \frac{4\alpha I_1^{\mathrm{tr}}\left(\sigma_c - \sigma_t\right)\widehat{V}\widehat{K}^2}{\mu\zeta_p^3}\delta_{ij}\delta_{kl} - \frac{6\widehat{V}\widehat{G}\widehat{H}}{\mu\zeta_s^2}S_{ij}^{\mathrm{tr}}\widehat{E}_{kl} - \frac{2\alpha I_1^{\mathrm{tr}}\widehat{V}\widehat{K}\widehat{H}}{3\mu\zeta_p^2}\delta_{ij}\widehat{E}_{kl} \tag{38}$$

where

$$\mu = -\frac{\partial \Phi}{\partial \Delta\gamma} \qquad \hat{E}_{ij} = \frac{\partial \varepsilon_{\mathrm{eq}}^{\mathrm{p}}}{\partial \varepsilon_{ij}} = \frac{1}{1 + 2\nu_p^2}\frac{(\Delta\gamma)^2}{\Delta\varepsilon_{\mathrm{eq}}^{\mathrm{p}}}M_{kl}\frac{\partial M_{kl}}{\partial \varepsilon_{ij}} \tag{39}$$

$$M_{kl} = \frac{3S_{kl}^{\mathrm{tr}}}{\zeta_s} + \frac{2\alpha I_1^{\mathrm{tr}}\delta_{kl}}{9\zeta_p} \qquad \frac{\partial M_{ij}}{\partial \varepsilon_{kl}} = \frac{6G\left(\delta_{ijkl}^s - \frac{1}{3}\delta_{ij}\delta_{kl}\right)}{\zeta_s} + \frac{\frac{2}{3}\alpha K\delta_{ij}\delta_{kl}}{\zeta_p} \tag{40}$$

The meaning of other variables can be found in Chapter 4.2.

Appendix F

Periodic boundary conditions are applied on the RVE. For instance, for a schematic finite element model with four hexagonal elements as shown in Fig. 2, this implies that:

$$\mathbf{u}^R - \mathbf{u}^L = \mathbf{u}^{(2)} - \mathbf{u}^{(0)} \tag{41}$$

$$\mathbf{u}^U - \mathbf{u}^D = \mathbf{u}^{(3)} - \mathbf{u}^{(0)} \tag{42}$$

$$\mathbf{u}^F - \mathbf{u}^B = \mathbf{u}^{(1)} - \mathbf{u}^{(0)} \tag{43}$$

where $\mathbf{u}^R$ and $\mathbf{u}^L$ are the displacement of any periodic pair of nodes on the right surface and left surface of the numerical model, respectively, $\mathbf{u}^U$ and $\mathbf{u}^D$ are the displacement of any periodic pair of nodes on the top surface and bottom surface, respectively, $\mathbf{u}^F$ and $\mathbf{u}^B$ are the displacement of any periodic pair of nodes on the front surface and back surface, respectively, $\mathbf{u}^{(0)}$, $\mathbf{u}^{(1)}$, $\mathbf{u}^{(2)}$, $\mathbf{u}^{(3)}$ are the displacement of master nodes {0,1,2,3}, respectively. To ensure that the RVE deformation under unidirectional loading is the same as an isotropic structure under the same loading condition, special care should be taken with respect to the possible shear deformation. The following constraints are applied to prevent possible shear deformation:

$$u_1^{(0)} = u_2^{(0)} = u_3^{(0)} = u_1^{(2)} = u_3^{(2)} = u_1^{(3)} = u_2^{(3)} = u_2^{(1)} = u_3^{(1)} = 0 \tag{44}$$

The incremental average stress for each time step can be calculated by:

$$\delta\sigma = \begin{bmatrix} \delta\sigma_{11} \\ \delta\sigma_{22} \\ \delta\sigma_{33} \\ \delta\sigma_{23} \\ \delta\sigma_{31} \\ \delta\sigma_{12} \end{bmatrix} = \frac{1}{V_0} \begin{bmatrix} \tilde{\mathbf{H}}_0 & \tilde{\mathbf{H}}_1 & \tilde{\mathbf{H}}_2 & \tilde{\mathbf{H}}_3 \end{bmatrix} \begin{bmatrix} \delta\mathbf{f}_0 \\ \delta\mathbf{f}_1 \\ \delta\mathbf{f}_2 \\ \delta\mathbf{f}_3 \end{bmatrix} \tag{45}$$

with

$$\tilde{\mathbf{H}}_q = \begin{bmatrix} x_1^{(q)} & 0 & 0 \\ 0 & x_2^{(q)} & 0 \\ 0 & 0 & x_3^{(q)} \\ 0 & \frac{x_3^{(q)}}{2} & \frac{x_2^{(q)}}{2} \\ \frac{x_3^{(q)}}{2} & 0 & \frac{x_1^{(q)}}{2} \\ \frac{x_2^{(q)}}{2} & \frac{x_1^{(q)}}{2} & 0 \end{bmatrix}, \quad q = 0, 1, 2, 3 \tag{46}$$

in which V_0 is the volume of the RVE, $x_i^{(q)}$ and $\delta \mathbf{f}_i$ are the coordinate and incremental nodal forces of the four control nodes, respectively.

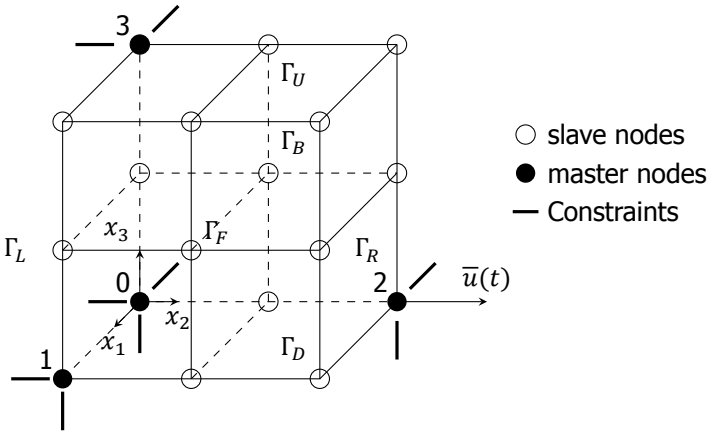

Figure 2: Schematic representation of the periodic and prescribed boundary conditions of a finite element model. Three periodic pairs: top surface $\mathbf{\Gamma_U}$ and bottom surface $\mathbf{\Gamma_D}$, left surface Γ_L and right surface Γ_R, and front surface Γ_F and back surface Γ_B.

Curriculum Vitæ

Yaolu Liu

16-08-1991 Born in Ji Shui, China.

Education

2007–2011 B.Sc. in Hydraulic Engineering
Dalian University of Technology
Dalian, China

2011–2014 M.Sc. in Hydraulic Engineering
Tsinghua University
Beijing, China

2014–2020 Ph.D. candidate
Faculty of Civil Engineering and Geosciences
Delft University of Technology
Delft, the Netherlands

List of Publications

Journal papers

4. Liu, Y., van der Meer, F. P., Sluys, L. J. & Ke, L. Modeling of dynamic crack growth in fiber-reinforced polymer composites: fracture energy and failure mechanism, *Engineering Fracture Mechanics (under revision)*.

3. Liu, Y., Van der Meer, F. P., Sluys, L. J., & Fan, J. T. (2020). A numerical homogenization scheme used for derivation of a homogenized viscoelastic-viscoplastic model for the transverse response of fiber-reinforced polymer composites. *Composite Structures*, 252, 112690.

2. Liu, Y., van der Meer, F. P., & Sluys, L. J. (2020). A dispersive homogenization model for composites and its RVE existence. *Computational Mechanics*, 65(1), 79-98.

1. Liu, Y., van der Meer, F. P. & Sluys, L. J. (2018). Cohesive zone and interfacial thick level set modeling of the dynamic double cantilever beam test of composite laminate. *Theoretical and Applied Fracture Mechanics*, 96, 617–630.

Conferences

2. Liu, Y., van der Meer, F. P. & Sluys, L. J. (2018). Dispersive homogenization model for fiber-reinforced composites, In Proceedings of the 6th European Conference on Computational Mechanics, Glasgow, UK.

1. Liu, Y., van der Meer, F. P. & Sluys, L. J. (2017). Thick-level-set modeling of the dynamic double cantilever beam test, In Proceedings of the 21st International Conference on Composite Materials, Xi'an, China.